Thermal Analysis, Structural Studies and Morphology of Spider Silk-like Block Copolymers

A dissertation submitted by

Wenwen Huang

In partial fulfillment of the requirements for the degree of

Doctor of Philosophy

In

Physics

Tufts University

February, 2013

Advisor: Prof. Peggy Cebe

Abstract

Spider silk is a remarkable natural block copolymer, which offers a unique combination of low density, excellent mechanical properties, and thermal stability over a wide range of temperature, along with biocompatibility and biodegrability. The dragline silk of *Nephila clavipes,* is one of the most well understood and the best characterized spider silk, in which alanine-rich hydrophobic blocks and glycine-rich hydrophilic blocks are linked together generating a functional block copolymer with potential uses in biomedical applications such as guided tissue repair and drug delivery. To provide further insight into the relationships among peptide amino acid sequence, block length, and physical properties, in this thesis, we studied synthetic proteins inspired by the genetic sequences found in spider dragline silks, and used these bioengineered spider silk block copolymers to study thermal, structural and morphological features.

To obtain a fuller understanding of the thermal dynamic properties of these novel materials, we use a model to calculate the heat capacity of spider silk block copolymer in the solid or liquid state, below or above the glass transition temperature, respectively. We characterize the thermal phase transitions by temperature modulated differential scanning calorimetry (TMDSC) and thermogravimetric analysis (TGA). We also determined the crystallinity by TMDSC and compared the result with Fourier transform infrared spectroscopy (FTIR) and wide angle X-ray diffraction (WAXD).

To understand the protein−water interactions with respect to the protein amino acid sequence, we also modeled the specific reversing heat capacity of the protein-water system, $C_p(T)$, based on the vibrational, rotational and translational motions of protein amino acid residues and water molecules. Advanced thermal analysis methods using

TMDSC and TGA show two glass transitions were observed in all samples during heating. The low temperature glass transition, $T_g(1)$, is related to both the bound water removal induced conformational change and the hydrophobicity of the protein sequences, while the high temperature glass transition, $T_g(2)$, above 130 °C is the now dry protein glass transition. Real-time Fourier transform infrared spectroscopy (FTIR) confirmed that conformational change occurred during the two glass transition, with a random coils to beta turns transition during $T_g(1)$ and alpha helices to beta turns transition during $T_g(2)$.

Due to the hydrophobic and hydrophilic nature of the blocks, the spider silk block copolymers tend to self–assemble into various microstructures. To study the morphological features, the spider silk-like block copolymers were treated with hexafluoroisopropanol or methanol, or subjected to thermal treatment. Using scanning electron microscopies, micelles were observed in thermally treated films. Fibrillar networks and hollow vesicles were observed in methanol-cast samples, while no micro-structures were formed in HFIP-cast films, indicating that morphology and crystallinity can be tuned by thermal treatments. Results indicate when we increase the number of repeating unit of A-block in the protein, sample films crystallize more easily and are more thermally stable. Moreover, when samples crystallize, the secondary structure of A-block and B-block become different, thus it will be easier to form bilayer structures which could fold into vesicles or tube structures during drying.

Acknowledgements

I would like to thank my advisor and the chair of my thesis committee, Professor Peggy Cebe, for her great guidance, encouragement, support and help during my Ph.D. study at Tufts.

I am also sincerely grateful to my co-advisor, Professor David Kaplan, for his critical comments, suggestion and support.

I thank all my committee members for their time and advice: Prof. Roger Tobin, Prof. Cristian Staii, Prof. Gary Goldstein, and especially Prof. Christoph Schick from the University of Rostock, Germany, who served as an outside expert.

I would like to acknowledge the National Science Foundation, Division of Chemical, Bioengineering, Environmental, and Transport Systems, for support of this research through grant CBET-0828028, and the MRI Program under DMR-0520655 for thermal analysis instrumentation. I also acknowledge the National Science Foundation, Division of Materials Research, Polymers Program for support of the summer internship projects through grants DMR-0704056 and DMR-0906455. I acknowledge the Harvard University Center for Nanoscale Systems (CNS), for the use of the electron microscopes.

There is a lot of pleasure time with my colleagues, Dr. Xiao Hu, Dr. Seyhan Ince-Gunduz, Dr. Huipeng Chen, Dr. Lei Yu, Dr. Qian Ma, Mr. Bin Mao and Mr. Yazhe Zhu. It is a wonderful experience to work with them. And I also extend my appreciation to Dr. Marek Pyda for his suggestions.

Finally, I would like to thank my family, especially my husband, Nan, for their constant encouragement and help.

Table of Contents

Chapter VII: Conclusions and Future Works

Appendices

List of Tables

List of Figures

Chapter I. Introduction

This chapter provides a general introduction and an overview of this thesis. In the first section of this chapter, basic concepts and the general structure of semi-crystalline polymers, including the crystalline and amorphous structure, concepts of the lamellae and phase transitions of semicrystalline polymers, are reviewed. After that, a variety of protein based polymers are introduced, with detailed description of spider silk and recombinant spider silk-like block copolymers. Finally, the motivation of the thesis and an outline of the subsequent chapters are provided.

1.1 Polymer

Polymer is a term derived from the ancient Greek word which means having many parts [1]. By definition it is a long chain macromolecule consisting of repeating structural units (monomers) typically connected by covalent chemical bonds [2, 3], through a chemical reaction called polymerization [4]. Polymers have been widely studied and applied in our life today, from household tools to high technology applications. Well-known examples of polymers include synthetic polymers used in everyday life, for example, polystyrene (PS) which is used as disposable cutlery, plastic models, CD and DVD cases, foamed packing materials, insulation, and foam drink cups. Other well-known examples includes natural polymers, for example, deoxyribonucleic acids (DNAs) which carry the genetic instructions used in the development and functioning of all known living organisms, and proteins, which perform a vast array of

functions within living organisms. The structure of polystyrene and DNA are shown in **Figure 1.1**.

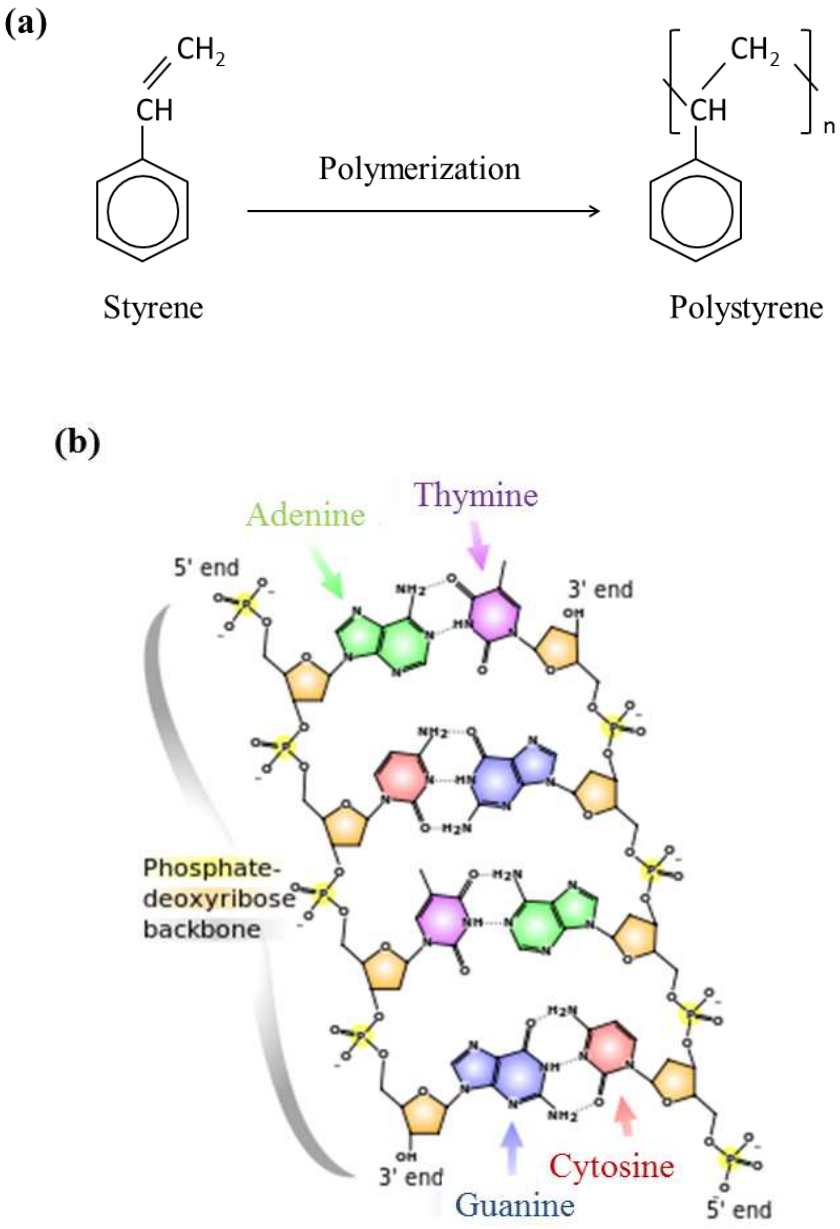

Figure 1.1 (a) Chemical structure of styrene (left) and polystyrene (right), a synthetic polymer. (b) A segment of DNA, a natural polymer, taken from reference [5].

In general, polymers can be classified into natural polymers and synthetic polymers based on their source [2]. Natural polymers, such as DNA, RNA, proteins, cellulose, starch, resins and natural rubbers, can be found in cells, animals or plants and play critical roles in regulating life processes. Synthetic polymers are man-made chemically produced polymers. A variety of synthetic polymers, such as plastics, synthetic rubbers, nylon, Teflon, and epoxy, are examples of man-made polymers extensively used in daily life as well as in industry. In this thesis, the recombinant spider silk-like block copolymers, which are natural polymers, were extensively studied. In the side projects, nanocomposite and polymer blends based on poly (vinylidene fluoride), a synthetic polymer with $–CH_2CF_2-$ repeat units, were also investigated.

Another classification of polymers is based on the chemical types of monomer [2, 3, 6]: homopolymer consists of multiple repetition of a single type of monomer, and copolymers have more than one species of monomer. Furthermore, depending on the arrangement of different types of monomers in the polymer chain, copolymers can be classified into random copolymers, alternating copolymers, block copolymers and graft copolymers. A random copolymer has two or more different types of monomers which are distributed randomly throughout the polymer chain. An alternating copolymer has only two different types of monomers which are arranged alternately along the polymer chain. A block copolymer is a linear copolymer which comprises two or more homopolymer subunits linked by covalent bonds. Finally, a graft copolymer is a branched polymer in which the side chain branches have a different type of monomer to that of the main polymer chain. **Figure 1.2** illustrates different types of polymer chains by a cartoon picture. In this thesis, the recombinant spider silk-like polymer studied is a

type of di-block copolymer. In the side project, the poly (vinylidene fluoride) used is a homopolymer.

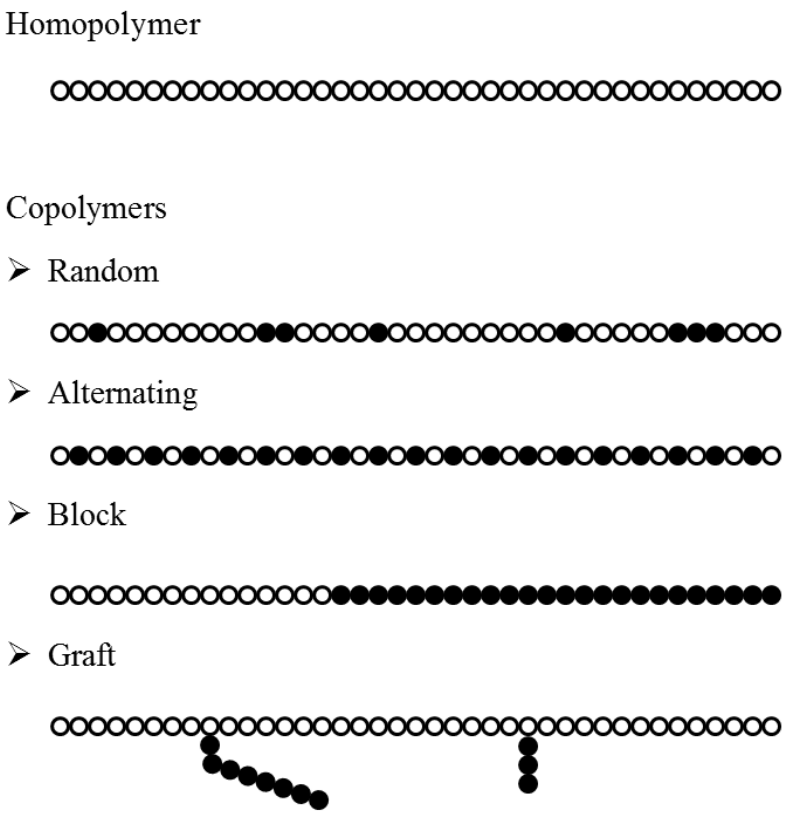

Figure 1.2 Different types of polymer chains. Black and white circles indicate different type of monomers.

The most common way of classifying polymers is based upon their physical properties, especially the thermal properties [2, 3, 6-8]. Thermosets and elastomers are the polymers which undergo permanent change and become intractable when heated. They degrade rather than melt when re-heated to a high temperature. Thermosets are cross linked or heavily branched molecules, which get highly crosslinked upon heating or

adding curing agents and harden permanently once formed. A typical example of thermoset is epoxy resin [8]. Elastomers are crosslinked rubbery polymers in which the polymers chains are held together by weak intermolecular forces, such as Van der Waals forces and hydrogen bonds present in the polymer. Elastomers can be stretched easily to high extensions by applying small stress and they recover their original shape when the stress is released because of the presence of entropic forces. When stretched, the elastomer molecules backbone can undergo torsional motion to permit the uncoiling of the polymer chains, and thus their entropy decreases upon stretching [6], at the same time heat is produced in the elastomer as it is stretched. To spontaneously maintain a state of maximum entropy, the entropic force, which is also proportional to the sample temperature, increases and tends to drive the elastomers back to the original shape (a state of higher entropy). A typical example of elastomer is a rubber band.

Thermoplastics are the polymers which are capable of repeatedly softening on heating and hardening on cooling, and they are usually linear or slightly branched polymers. Many thermoplastics do not crystallize even upon annealing and form wholly amorphous polymers. The thermoplastics which do crystallize form semi-crystalline polymers with both crystalline regions and amorphous regions. They rarely form perfectly 100% crystalline materials due to the imperfect folding at the polymer crystal folding surface, entanglement of long polymer chains, and the effect of the chain ends. The crystalline phase in semi-crystalline polymers is characterized by the melting temperature, T_m, and the crystallization temperature, T_c. The amorphous phase in wholly amorphous polymers and in semi-crystalline polymers is characterized by the glass transition temperature, T_g. The classification of polymers based upon their thermal

properties is summarized in **Figure 1.3**. In this thesis, the recombinant spider silk-like block copolymers studied were found to be either amorphous or semicrystalline thermoplastics. In the side project, the poly (vinylidene fluoride) belongs to the category of semicrystalline thermoplastics.

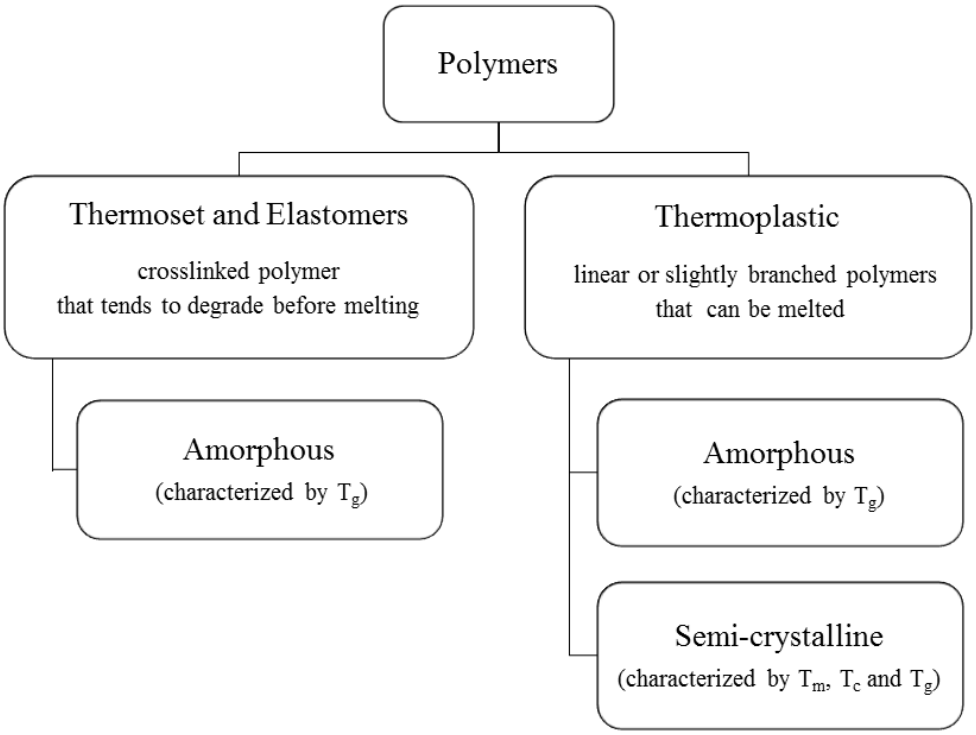

Figure 1.3 Classification of polymers by thermal properties.

Many properties of a polymer are strongly dependent on the size of the polymer chains. For example, when the chain length is increased, the polymer chain mobility decreases as a result of the increase in intermolecular interactions such as Van der Waals attractions and entanglements of the polymer chains which is the topological restriction of molecular motion induced by other chains. Therefore, T_g and T_m increases quickly

with increased chain length [9, 10]. A common expression to characterize the polymer chain length is the molar mass, *M*, which is also known as the molecular weight. The molar mass is the mass of one mole of polymer chains in units of g/mol or kg/mol. The molar mass of a homopolymer can be simply expressed as

$$M = xM_0 \tag{1.1}$$

where M_0 is the molar mass of the monomer, and x is the degree of polymerization, which is the number of monomers in the polymer chain. The molar mass of a copolymer is the sum of $x_i M_{0i}$ for each type of monomer, i,

$$M = \sum_i x_i M_{0i} \tag{1.2}$$

Our spider silk-like block copolymers have *m* A-blocks and *n* B-blocks with a His-tag, and are named as HA_mB_n or HB_nA_m. The molar mass, $M_{HA_mB_n}$ or $M_{HB_nA_m}$, can be calculated as

$$M_{HA_mB_n} = M_{HB_nA_m} = M_H + mM_A + nM_B \tag{1.3}$$

where M_H, M_A and M_B are the molar mass of His-tag block, A-block and B-block, respectively; and *m*, *n* are the number of repeats of A-block and B-block in the block copolymer, respectively.

Synthetic polymerization techniques typically yield a polymer including a wide range of molecular weights with different *x*, therefore the weight is often expressed statistically to describe the distribution of chain lengths. The number average molecular weight is defined as

$$\overline{M_n} = \sum_i X_i M_i = \sum_i [(N_i \Big/ \sum_i N_i) M_i] = \sum_i N_i M_i \Big/ \sum_i N_i \tag{1.4}$$

where X_i is the mole fraction of molecules with molar mass M_i, which can also be expressed as the ratio of N_i to the total number of molecules, $\sum_i N_i$. The weight average molecular weight is defined as

$$\overline{M_w} = \sum_i w_i M_i = \sum_i [(N_i M_i \Big/ \sum_i N_i M_i) M_i] = \sum_i N_i M_i^2 \Big/ \sum_i N_i M_i \qquad (1.5)$$

where w_i is the weight fraction of molecules with molar mass M_i, which can also be expressed as the ratio of N_i M_i to the total weight of molecules, $\sum_i N_i M_i$. The ratio of these two values, $\overline{M_w} \big/ \overline{M_n}$, is the polydispersity index, commonly used to express the "breadth" of the molecular weight distribution. The synthetic polymers are usually polydispersed polymer with a polydispersity greater than unity.

In contrast, the recombinant spider silk-like block copolymers, which were studied in this thesis, are perfectly monodispersed polymers. The number average molecular weight, $\overline{M_n}$, is the same as the weight average molecular weight, $\overline{M_w}$, because the proteins produced by recombinant DNA technology have a uniform length which is strictly controlled by the plasmid DNA [11]. Thus, the polydispersity of recombinant spider silk-like block copolymer is 1.0. The molar mass distribution curves for monodispersed and polydispersed polymers are illustrated by **Figure 1.4**. The contour length, which is used less often, is the length of the chain backbone in its fully extended state.

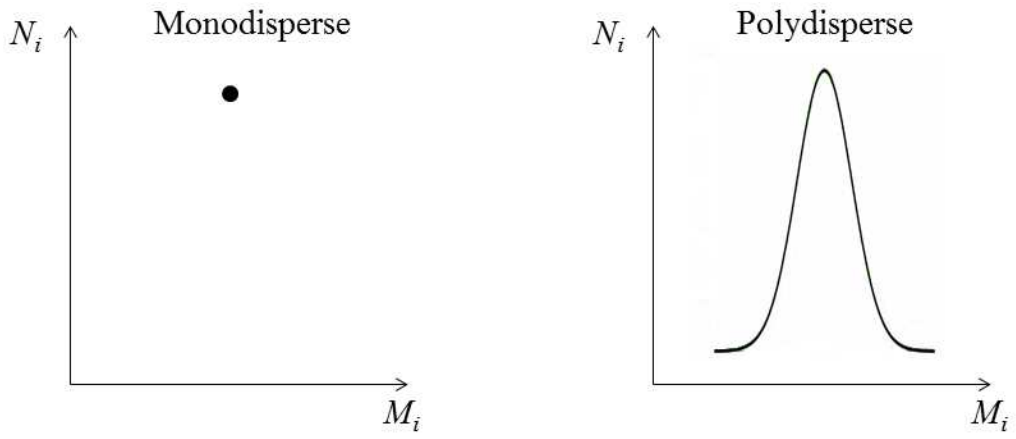

Figure 1.4 Molar mass distribution curves of polymers: monodisperse (left) and polydisperse (right).

1.2 Phases and Phase Transitions in Semi-crystalline Polymers

1.2.1 Two Phase Model and Three Phase Model

Semi-crystalline polymers constitute the largest group of commercially useful polymers and are of enormous technological importance. The reason why these materials are called "semi-crystalline" is that amorphous regions and crystalline regions always coexist in polymers upon crystallization. The degree of crystallinity of a semi-crystalline polymer cannot reach 100%, and this is because of the defects of the polymer chains, such as the two ends of the polymer chains, and entanglement of chains due to the long chain nature of polymers which causes incomplete crystallization.

Generally, in the amorphous region of a semi-crystalline polymer, the polymer chains are oriented randomly and they are entangled as illustrated in **Figure 1.5**, much like cooked spaghetti, and the amorphous regions contribute to polymer's flexibility. In the crystalline regions in a semi-crystalline polymer, the polymer chains adopt a highly

ordered molecular structure by folding and stacking of the polymer chains which is also shown in Figure 1.5. Crystalline regions, which act as physical cross-links, add rigidity to the amorphous regions. Most commercial semi-crystalline polymers have a balance between amorphous and crystalline regions, allowing a balance between flexibility and strength. A two phase model, comprising of the amorphous phase, φ_{MAF}, and the crystalline phase, φ_C, are conventionally used to describe the semicrystalline polymers:

2-Phase: $$\varphi_{MAF} + \varphi_C = 1 \tag{1.6}$$

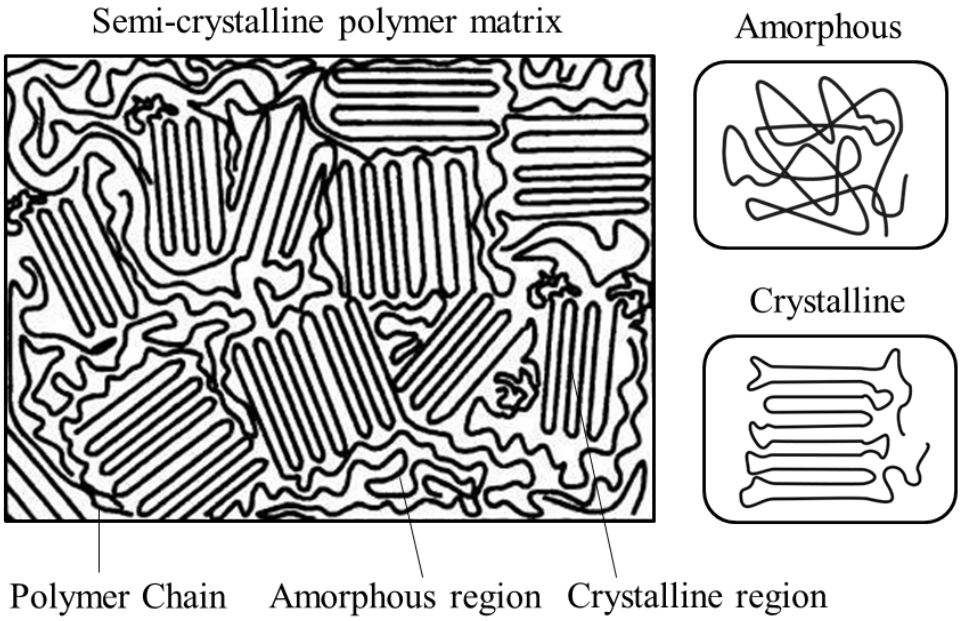

Figure 1.5 Schematic illustration of the folded-chain model [3] of a semicrystalline polymer based on a two phase model.

For some of the semi-crystalline polymers, such as aliphatic nylons [12], poly(ethylene terephthalate) [13, 14], poly(trimethylene terephthalate) [15] and poly(butylene terephthalate) [16], there is a rigid amorphous fraction (RAF) which exists

at the interface of the crystalline and amorphous regions as a result of the imposed geometrical constraints by the incomplete decoupling between the crystals, or a rigid surface, and the amorphous chains. The RAF can be induced due to the crystal or by nano-fillers, such as silica nanoparticles [17]. RAF is an intermediate phase between crystalline and the conventional amorphous phase, the mobile amorphous phase (MAF) [18]. When RAF exists in the polymer matrix, a three phase model [18], comprising the mobile fraction, φ_{MAF}, the crystalline fraction, φ_C, and the rigid amorphous faction, φ_{RAF}, is used to describe the polymer:

$$\text{3-Phase:} \qquad \varphi_{MAF} + \varphi_C + \varphi_{RAF} = 1 \tag{1.7}$$

Figure 1.6 shows a schematic representation about the location of RAF in a semi-crystalline polymer based on a three phase model.

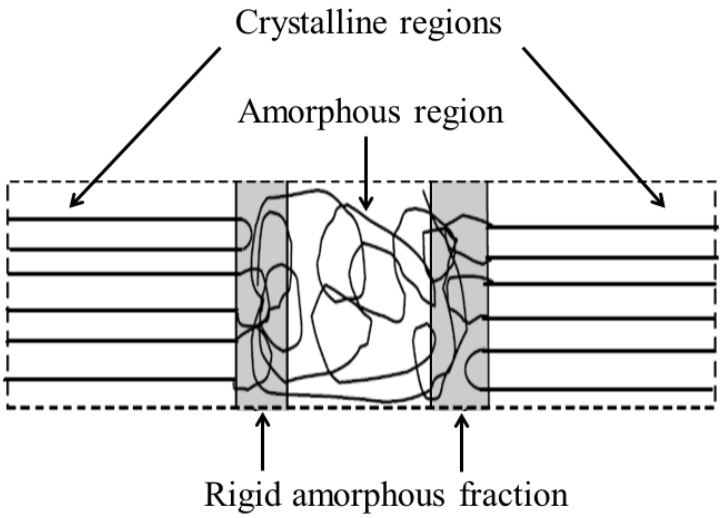

Figure 1.6 A close look at the interface of crystalline and amorphous regions indicating the location of RAF in a semi-crystalline polymer based on a three phase model.

RAF vitrifies or devitrifies during cooling or heating. Devitrification of RAF does not contribute to the heat of fusion. Therefore the thermal transition of RAF is a quasi-second order transition (similar to the glass transition of the MAF, T_g). It is believed that RAF does not participate in the conventional glass transition process as MAF and does not contribute to the heat capacity change at T_g either [18-20]. Generally, the mobility of RAF is lower than that of MAF but higher than that of the crystalline phase.

To determine if RAF exists in a material, the mobile fraction, φ_{MAF}, is determined by the heat capacity step change at the glass transition temperature in a differential scanning calorimetry plot, and the crystalline fraction, φ_C, is determined by the X-ray diffraction pattern. If $\varphi_{MAF} + \varphi_C = 1$, the sample only has two phases. If $\varphi_{MAF} + \varphi_C < 1$, the sample has three phases. In this thesis, the spider silk-like block copolymers do not have RAF, and thus they follow the two phase model. The detail is discussed in Chapter IV.

1.2.2 Phase Transitions

In the study of semi-crystalline polymers, the condensed matter phases (the glassy phase, the crystal phase and the melt phase) are considered to be of most interest in both academic research and industrial applications [6]. At low temperatures, the polymers are in the glassy phase. In this state the polymer molecules are "frozen" in place [2]. They are able to vibrate, but do not have any segmental motion related to polymer backbone conformational changes. When the temperature is raised above the glass transition, T_g, the amorphous region changes to a rubbery state, while the crystalline region has no

change. In this state the polymer molecules in the amorphous region can undergo rotational and translation motion changing the conformation of the backbone [21]. When the temperature increases again to above the melting temperature, T_m, the polymer melts into a viscous liquid. The polymer chains have Gaussian end-to-end statistics and they are disordered in the melt phase. Due to the large molecular weight, polymers degrade into low molecular weight fragments before they reach the gas phase at high temperature, thus polymers do not have a gas phase.

The thermodynamics of phase transition can be characterized by the Gibbs free energy, G, as

$$G = H - TS \tag{1.8}$$

where H is the enthalpy, S is the entropy and T is the temperature of the system. When a phase transition occurs at temperature, T, the change of Gibbs free energy, ΔG, can be expressed as [7]

$$\Delta G = \Delta H - T\Delta S \tag{1.9}$$

where ΔH and ΔS are the heat and entropy of transition, respectively. In the case of melting, ΔH is the heat of fusion and ΔS is the entropy of fusion.

For the first order phase transition:

$$\Delta G = 0 \tag{1.10a}$$

$$\frac{\partial G}{\partial T} = -\Delta S \neq 0 \tag{1.10b}$$

First order phase transitions are those that involve a latent heat [2]. Melting and crystallization are examples of first order transitions in polymers.

For the second order phase transition:

$$\Delta G = 0 \tag{1.11a}$$

$$\frac{\partial G}{\partial T} = -\Delta S = 0 \tag{1.11b}$$

$$\frac{\partial^2 G}{\partial^2 T} = -\frac{\partial \Delta S}{\partial T} = -\frac{\Delta C_p}{T} \neq 0 \tag{1.11c}$$

Second order phase transitions do not involve a latent heat, and they are also called continuous phase transitions [2]. The glass transition is an example of quasi-second order transition in polymer. It is not a true second order transition because it is dependent upon cooling rate. The experimental techniques used for analyzing these phase transitions are discussed in Chapter II and Chapter III.

Crystallization

Crystallization of polymers is a process which involved partial alignment of the polymer chains in the crystalline region of a semi-crystalline polymer [2]. The crystallization process is governed by both thermodynamic and kinetic factors, and it consists of two major events: nucleation and crystal growth [2, 3, 7].

When the temperature of a polymer melt is reduced to the melting temperature, T_m, there is a tendency for the randomly entangled polymer chains in the melt to become aligned and form small ordered regions named nuclei. This process is called nucleation [2] and it is the initiation of the phase change in a small region. Total nucleation is the sum effect of two categories of nucleation: the primary nucleation and the secondary nucleation. Primary nucleation, simply defined, is the growth of a new crystal, which is

classified as being either heterogeneous or homogeneous, while secondary nucleation is the growth of the polymer crystals on a pre-existing crystal surface. During heterogeneous nucleation, a constant number of nuclei arise from self-seeding or foreign bodies [7], such as dust or solid particles or catalyst residue, at the crystallization temperature, T_c. During homogenous nucleation, small nuclei form randomly throughout the polymer melt and increase their size with time [7] in the amorphous regions. The majority of cases of primary nucleation are heterogeneous nucleation, and homogeneous nucleation is relatively rare due to the large free energy cost to form an interface at the boundaries of a new phase.

The second step in the crystallization process is growth whereby the crystal nuclei grow by addition of polymer chains [2]. The growth of a crystal nucleus by the addition of further chains can take place two or three dimensionally. During crystallization, the polymer chains fold together and form ordered two dimensional regions called lamellae. In most synthetic polymer films, lamellae form into larger three dimensional spherical structures named spherulites [22-24]. **Figure 1.7** shows a polarizing optical microscopy image of poly(vinylidene fluoride) where spherulites formed by melt crystallization at 150 ºC for one hour. The image was take at room temperature with analyzer and polarized crossed (A ⊥ P). These spherulites are the characteristic microstructure of semi-crystalline polymer films. Each spherulite grows from a nucleation site, which is strongly affected by impurities, nano-fillers and other additives in the polymer. At the early stage of crystallization, the spherulites are isolated from each other. As the spherulites are growing, impingement occurs in which spherulites come into contact with their neighbors. Spherulite impingements can also be observed in Figure 1.7 at their boundaries. A Maltese cross pattern of light extinction, which arises from the birefringence of the crystalline regions

in the polymer, can also be observed under polarized light. The common feature of lamellar single crystals, lamellae, and spherulites is that the polymer contains both amorphous and crystalline component and it is semi-crystalline. In natural polymers, such as silk, the lamellae, which are called β sheets, stack together to form β sheets crystals [25]. **Figure 1.8** shows a schematic representation of the growth of three dimensional spherulites and β sheet crystals.

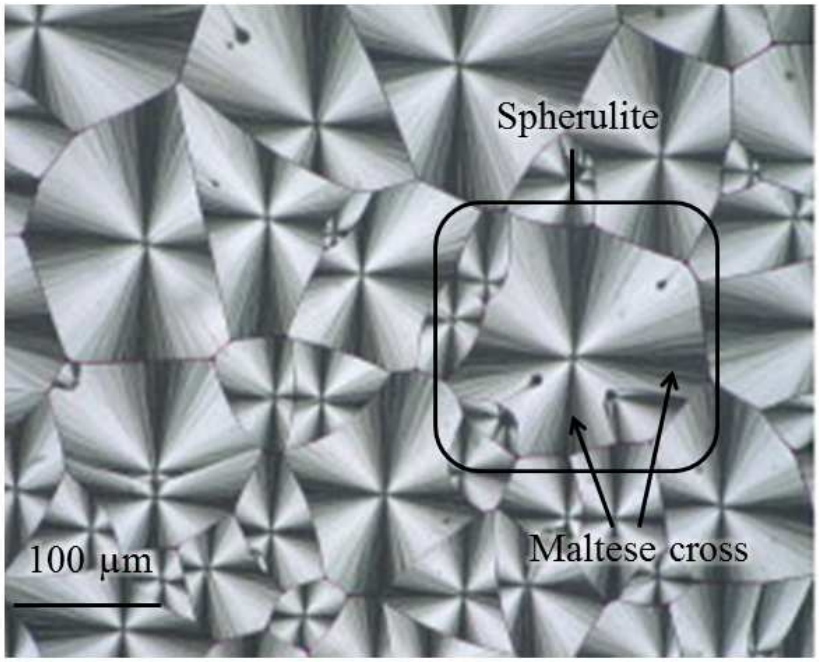

Figure 1.7 Polarizing optical microscopy images (A ⊥ P) of poly(vinylidene fluoride) spherulites formed by melt-crystallized at 150 ºC for 1 h taken from reference [22].

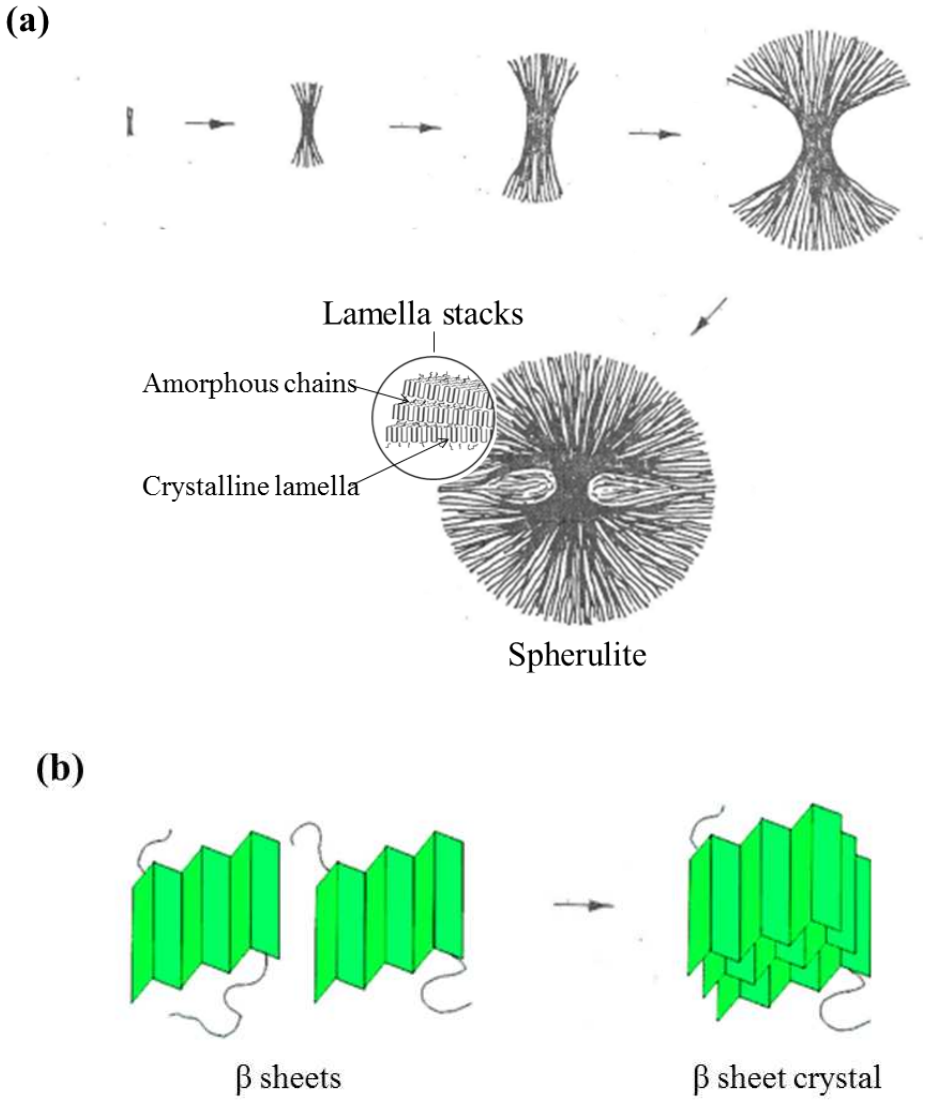

Figure 1.8 Schematic representations of the growth of (a) spherulite and (b) β sheet crystal, taken from references [24, 26].

Avrami analysis is a fairly successful model used in explaining the process of crystal growth, and it is used to roughly determine the overall kinetics of crystallization during isothermal crystallization. The Avrami equation can be written as

$$\chi_c^{rel}(t) = 1 - \exp(-Kt^n) \tag{1.12}$$

where $\chi_c^{rel}(t)$ is the relative crystallinity of the crystallizing sample at different time t, K is the crystallization rate coefficient relating to the crystal growth geometry and the crystallization temperature, and n is the Avrami exponent parameter relating to the nucleation mechanism and crystal growth geometry [27]. The crystallization process is a two dimensional growth when n=2, and a three dimensional growth when n=3. Due to imperfect crystallization, the Avrami exponent, n, usually is not an integer [2].

The semi-crystalline polymers can be crystallized by cold crystallization (by heating), melt crystallization (by cooling) or solution crystallization.

Cold and melt crystallization are the most common processes used to crystalize polymer films [2, 27]. The cold crystallization is achieved by isothermally holding a non-crystalline semi-crystalline polymer film at a temperature above its glass transition temperature, T_g, but below its melting temperature, T_m, at which point the polymer chains gain sufficient mobility to fold and form the crystalline regions in the polymer matrix. Melt crystallization refers to the method in which the semi-crystalline polymer film is melted first by heating above its melting temperature, T_m, and then crystallizing upon cooling from its molten state. After cold or melt crystallization of polymer films, lamellar structures and spherulitic structures can usually be observed.

Solution crystallization is the process of formation of solid crystals precipitating from a polymer solution [2, 6]. Solution-grown polymer crystals usually are very small. **Figure 1.9** shows an isolated chain-folded lamellar polyethylene single crystal grown from a dilute solution [28]. A single crystal does not have amorphous chain inside, but some may exist at the folding surface. A characteristic feature of polymer single crystals is that the crystal edges are straight with well-defined angles to each other. From the

insets (lower right) of Figure 1.9, a chain-folding model of a single crystal, the growth direction of the single crystal is perpendicular to the crystal edges.

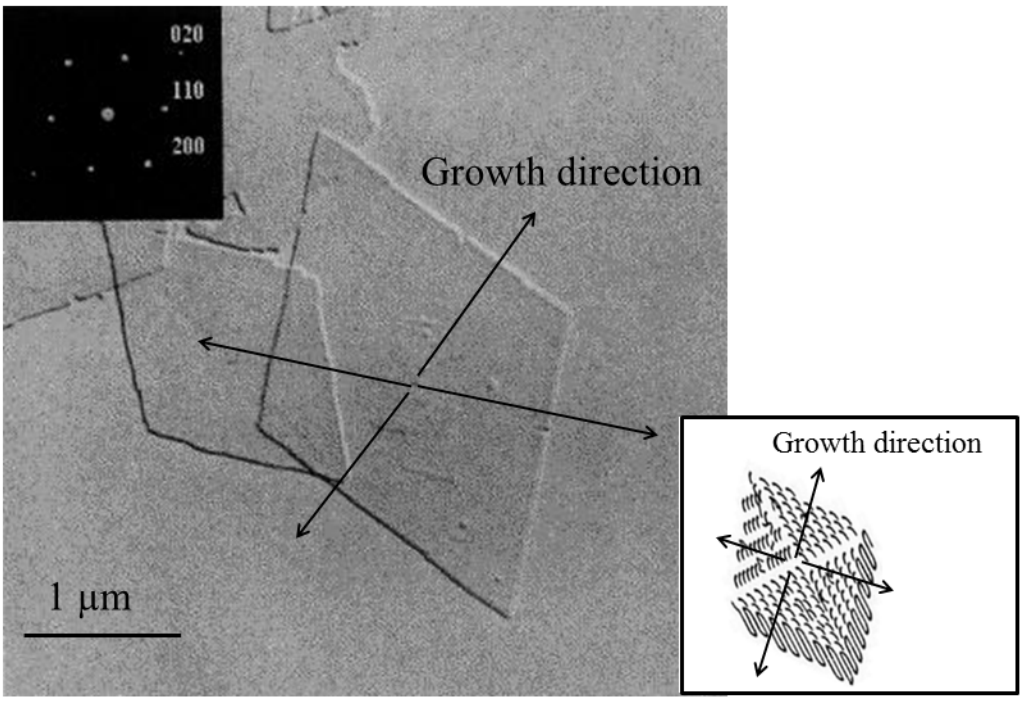

Figure 1.9 TEM micrograph of the rhombic single crystal of linear polyethylene formed from dilute xylene solution, taken from reference [28]. The insets are electron diffraction pattern (upper left) and a chain-folding model of a single crystal (lower right).

Melting

Melting of polymers is a process that is essentially the reverse of crystallization in the crystalline region of a semi-crystalline polymer. During melting, polymer chains change from an ordered state to a disordered state. At the melting temperature, T_m, ΔG equals 0 and T_m equals $\Delta H/\Delta S$ from equations 1.9 and 1.10. Thus, the heat of fusion per unit volume, ΔH_v can be given by [2, 29]:

$$\Delta H_v = \rho T_m^0 (S_L - S_s) \tag{1.13}$$

where T^0_m is defined as the equilibrium melting temperature at which the crystal without any surface would melt [2]; ρ is the lamella density; and S_L and S_S represent the entropy of the polymer in the liquid and solid state, respectively. Following the treatments from reference [2, 29], we assume that the side surface energy is negligible comparing to the fold surface free energy, σ_e, and the width of the lamella, *X*, is much larger than the thickness of the lamella, *l*. Each lamella with a thickness, *l*, cross-sectional area, *A*, and density, ρ, requires *2A* of new surface and $2A\sigma_e$ of surface free enthalpy, where σ_e is the fold surface free energy. Thus, at temperature, T_m, we have[2, 29]

$$G_0 + S_L(T_m^0 - T_m) = G_0 + S_s(T_m^0 - T_m) + \frac{2\sigma_e A}{Al\rho} \tag{1.14}$$

Combining equations 1.13 and 1.14, we have [2, 29]

$$T_m = T_m^0 - \frac{2\sigma_e T_m^0}{l\Delta H_v} \tag{1.15}$$

This equation provides the relationship between the melting temperature, T_m, and the lamellar thickness, *l*, for polymers. The depression of melting temperature for polymers is related to the lamellar thickness, *l*, and different *l* will lead to different melting temperatures [2, 29]. Therefore, the observed melting temperature, T_m, depends upon the crystal thickness, and it also depends upon the thermal history of the sample, especially the crystallization temperature, T_c, which is related to the crystal thickness. T_m versus T_c plot, the Hoffman-Weeks plot [30, 31], usually has a linear relationship as shown in **Figure 1.10**, and the intercept of the extrapolation of the observed T_m versus T_c curve

with the $T_m = T_c$ line gives the upper limit of the melting behavior, T^0_m. The observed melting temperature, T_m, also depends upon the heating rate of the sample due to the thermal lag of the instruments.

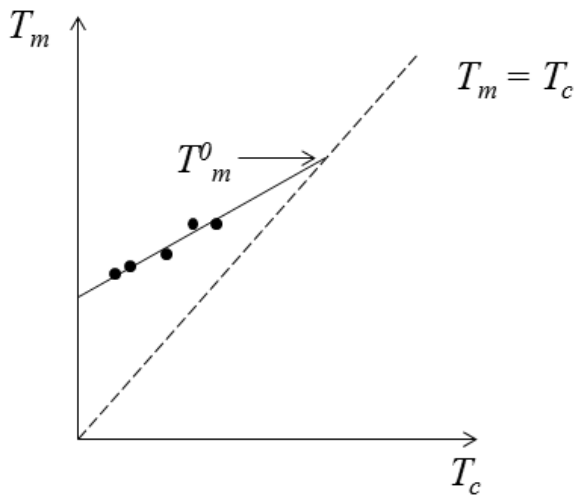

Figure 1.10 Schematic representations of T_m versus T_c plot for poly (dl-propylene oxide), taken from reference [2]. Black dots represent observed data from reference [2] [32].

Glass transition

The glass transition is a reversible transition in an amorphous material, or in the amorphous region of a semicrystalline material, during which the polymer undergoes the transformation from a rubbery state to a glassy state during cooling [2]. During the glass transition, the crystalline portion remains crystalline. The glass transition is a quasi-second order transition, because there is no latent heat involved, but an abrupt change of the heat capacity exists in this process as shown in equation 1.11. The glass transition is also dependent on the thermal history and the cooling rate of the sample, thus it is not a strictly defined second order phase transition, but a quasi-second order phase transition.

It is found that the slower the cooling rate the lower the glass transition temperature, T_g [2].

At low temperatures, below T_g, the glassy sample only has local vibrational motion, thus the vibrational heat capacities of the amorphous and the crystalline region in the sample are approximately the same. The heat capacity of the polymer below the onset of T_g is called the solid heat capacity, $C_p(solid)$, and it can be expressed as

$$C_p^{sc}(solid) = C_p^{amorphous}(solid) = C_p(vibrational), \quad (T < T_g) \tag{1.16}$$

where $C_p^{amorphous}(solid)$ is the solid heat capacity of the amorphous sample, and $C_p^{sc}(solid)$ is the solid heat capacity of the semicrystalline sample. When the temperature is above T_g, the amorphous region of the sample is changed from the glassy state to the rubbery state, and the heat capacity of the amorphous region is larger than that of the crystalline region, because the heat capacity related to the conformational change in the amorphous region needs to be taken into consideration beyond the harmonic vibrations [33]. The heat capacity of the polymer after the end of T_g is called the liquid heat capacity, $C_p(liquid)$, and it can be expressed as

$$C_p^{sc}(liquid) < C_p^{amorphous}(liquid) = C_p(liquid), \quad (T_m > T > T_g) \tag{1.17}$$

where $C_p^{amorphous}(liquid)$ is the liquid heat capacity of the amorphous sample, and $C_p^{sc}(liquid)$ is the liquid heat capacity of the semicrystalline sample. $C_p^{sc}(liquid)$ is smaller than the $C_p^{amorphous}(liquid)$ when the temperature is above T_g but below T_m, because the crystalline region of the sample is still in the solid state, with its heat capacity equal to the solid heat capacity.

$$C_p^{\,crystal} = C_p(solid), \qquad (T_m > T > T_g) \tag{1.18}$$

The heat capacity change at the glass transition in the amorphous polymer, $\Delta C_p^{\,0}$, and in the semicrystalline polymer, $\Delta C_p^{\,sc}$, can be expressed as

$$\Delta C_p^{\,0} = \left(\frac{\partial H}{\partial T}\right)_p\Bigg|_{T_{g(end)}} - \left(\frac{\partial H}{\partial T}\right)_p\Bigg|_{T_{g(onset)}} \tag{1.19a}$$

$$\Delta C_p^{\,sc} = \left(\frac{\partial H}{\partial T}\right)_p\Bigg|_{T_g(end)} - \left(\frac{\partial H}{\partial T}\right)_p\Bigg|_{T_g(onset)} \tag{1.19b}$$

Their ratio can be used to calculate the fraction of the mobile amorphous phase, φ_M, in a semicrystalline polymer as

$$\varphi_M = \frac{\Delta C_p^{\,sc}}{\Delta C_{p0}}\Bigg|_{T_g} \tag{1.20}$$

The crystallinity, φ_c, of a sample can be determined by the heat of fusion from differential scanning calorimetry, or from the WAXD pattern, or by Fourier self deconvolution of the FTIR spectrum. If $\varphi_M + \varphi_c < 1$, besides the amorphous region and crystalline region, a rigid amorphous phase also exists in the polymer matrix, and it complies with the three phase model; If $\varphi_M + \varphi_c = 1$, only the amorphous region and crystalline region exists in the polymer, and it complies with the two phase model.

1.3 Protein as a Polymer

Proteins are large macromolecules which are essential in biological systems. They are either naturally occurring or biosynthesized linear biopolymers, and they

perform a vast array of functions within living organisms, such as replicating DNA, responding to stimuli, and transporting molecules from one location to another [34]. The monomeric units of proteins are amino acids, and they are linked together by peptide bonds between the amino and the carboxylic acid groups of adjacent amino acid residues to form the protein polymer. The general structure of the amino acid is shown in **Figure 1.11**.

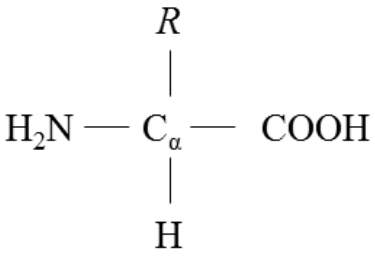

Figure 1.11 General structure of the amino acid. "R" represents a side-chain specific to each amino acid.

There are twenty standard amino acids that are used to make proteins, each distinguished by the identity of the "R" group (the side group). As can be seen, in an amino acid, one amino group, one carboxylic acid group, one "R" group (side chain group) and a hydrogen atom are connected to the center carbon, C_α. **Table 1.1** lists the twenty standard amino acids with their detailed information [5], such as their three-letter and one-letter abbreviations, their residue molecular weights (actual amino acid molecular weight minus water due to the formation of the peptide bond), and chemical structures. For the molar mass of the amino acid itself, the molar mass of the water molecule (18.0 D), needs to be added back to the residue molecular weight.

Table 1.1 Twenty Standard Amino Acids with Their Detailed Information [5]

Amino Acid	Abbreviations		Residue Mass* (D)	Structural Formula
Amino Acids with nonpolar side chains				
Glycine	Gly	G	57.0	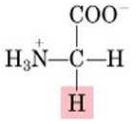
Alanine	Ala	A	71.1	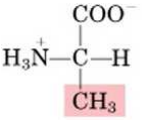
Valine	Val	V	99.1	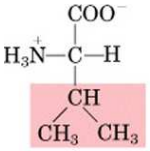
Leucine	Leu	L	113.2	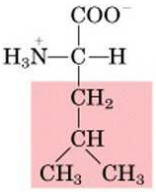
Isoleucine	Ile	I	113.2	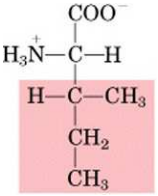
Methionine	Met	M	131.2	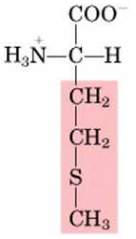
Proline	Pro	P	97.1	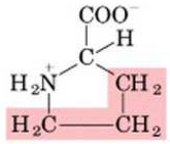
Phenylalanine	Phe	F	147.2	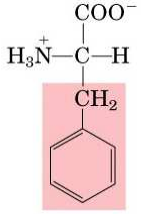

Table 1.1 Twenty Standard Amino Acids with Their Detailed Information [5] (continued)

Tryptophan	Trp	W	186.2	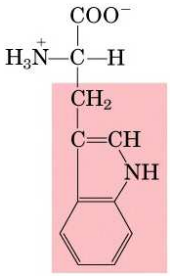
Amino Acids with uncharged polar side chains				
Serine	Ser	S	87.1	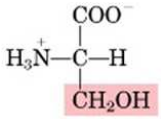
Threonine	Thr	T	101.1	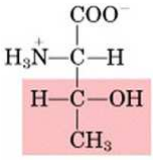
Asparagine	Asn	N	114.1	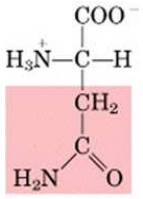
Glutamine	Gln	Q	128.1	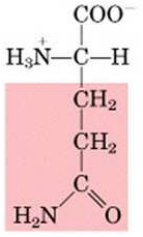
Tyrosine	Tyr	Y	163.2	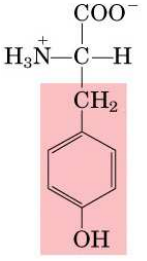
Cysteine	Cys	C	103.1	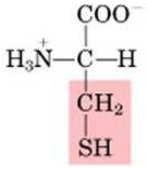

Table 1.1 Twenty Standard Amino Acids with Their Detailed Information [5] (continued)

Amino Acids with charged polar side chains				
Lysine	Lys	K	128.2	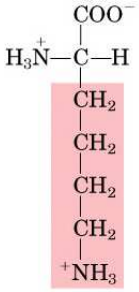
Arginine	Arg	R	156.2	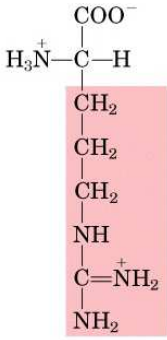
Histidine	His	H	137.1	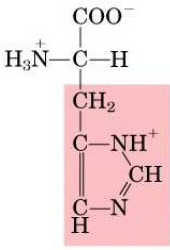
Aspartic acid	Asp	D	115.1	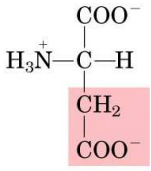
Glutamic acid	Glu	E	129.1	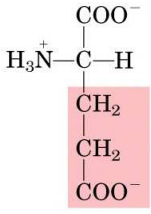

* For the molar mass of the amino acid itself, add 18.0 D, the molecular mass of H_2O.

Proteins differ from one another primarily in their sequence of amino acids, which is dictated by the nucleotide sequence of their genes (DNAs). The difference between the protein amino acid sequences usually results in folding of the proteins into a different three-dimensional structure that determines its activity [35]. In other words, the protein secondary structures, such as the α-helix, the β sheet and turns, are the specific geometric shape caused by intra-molecular and inter-molecular hydrogen bonding of amide groups, and they form motifs or supersecondary structures, which are responsible for the protein's function. The detailed information of protein secondary structures and motifs are discussed in Chapter II.

There are several types of proteins that exist in nature, such as: 1) spider silk in which GA/A_n motif forms β sheets and the $(GGX)_n$ motif forms α helices; or, 2) silk fibroins in which the $(GAGAGS)_n$ sequence forms β sheets; 3) collagen in which $(GPP)_n$ sequence forms triple helices; 4) keratins in which the 7-residue pseudo-repeat forms coil-coil structures; and, 5) elastin in which the $(GVGVP)_n$ sequence forms β spiral structures [5, 35]. By using recombinant DNA technology, the amino acid sequences that are related to different specific structural motifs can be selected and re-attached together to generate a new protein, one which does not exist in nature. By this method, new functionalized protein-based biomaterials can be generated and applied in biomedical applications [11, 36, 37].

In this thesis, we utilized the amino acid sequence in *Nephila Clavipes* spider dragline silk. By using the biosynthesized protein with well controlled sequences, we investigate the amino acid sequence in relation to physical properties and function of this new family of proteins.

1.3.1 Spider Silk

Silks are generally defined as externally spun fibrous protein secretions produced by some lepidoptera larvae such as silkworms, spiders, scorpions, and mites. Spider silks are synthesized in glands located in the abdomen of spiders, and spun out through a series of spinnerets [38]. The spider silk glands [39, 40] and a close up look at the spider spinnerets [41] are shown in **Figure 1.12**.

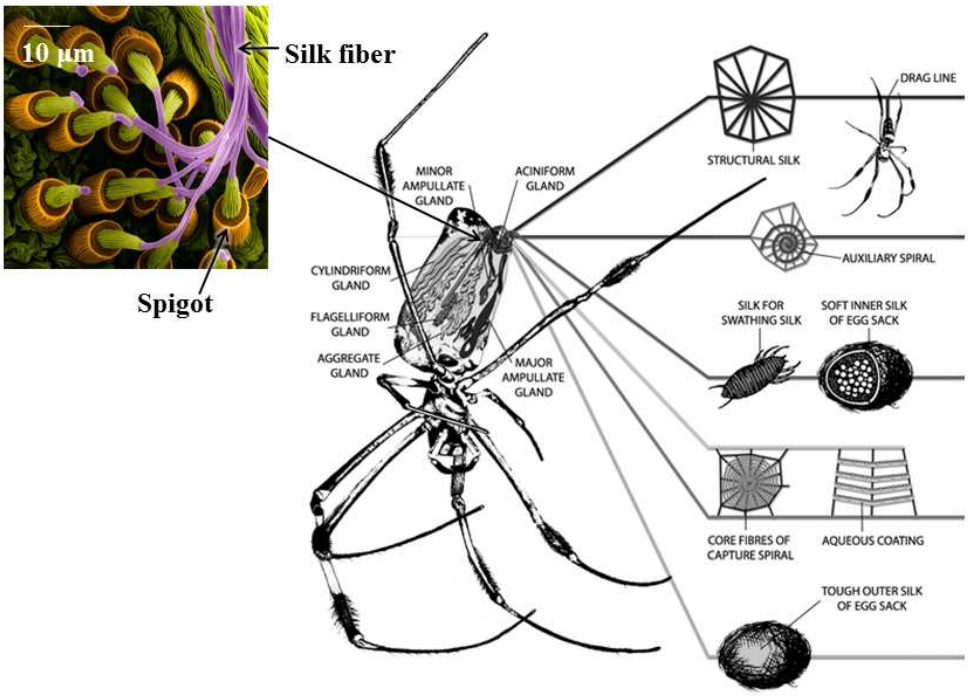

Figure 1.12 Silk glands, silk types and silk uses of *Nephila Clavipes*, taken from reference [40]. A close up look at the spider spinnerets, which consist of a number of spigots, is shown at the upper left corner, taken from reference [41].

Spider silks differ in properties, composition, morphologies and functions depending on their primary amino acid sequences and the type of silk gland through

which they are spun. For example, the spider dragline silk from the major ampullate gland is for orb web frame and radii construction; the spider viscid silk from the flagelliform gland is for prey capture; the spider wrapping silk from the aciniform gland is for wrapping captured prey; and the spider glue-like silk from the aggregate gland is for attachment [42]. **Table 1.2** summarizes the type of spider silk including the gland where the silks are synthesized, the spinnerets used for each type of silk, and the general function of each silk [43]. Among over 30,000 species of spiders (class *Arachnida*) [44], the orb-weaving spider, *Nephila clavipes*, has become the most well understood with its dragline silk the best characterized.

Table 1.2 Type of Spider Silks, Glands, Spinnerets, and Silk Functions [43].

Silk	**Gland**	**Spinneret**	**Function**	**Fiber Proteins**
Dragline	Major ampullate	Anterior/ Median	Orb web frame and radii construction, safety line	MaSp1; MaSp2
Viscid	Flagelliform	Posterior	Prey capture	Flag
Glue-like	Aggregate	Posterior	Prey capture, attachment	Unknown
Minor ampullate	Minor ampullate	Anterior/ Median	Orb web construction	MiSp1
Cocoon	Cylindrical (Tubuliform)	Median/ Posterior	Reproduction	TuSp1; ECP-1; ECP-2
Wrapping	Aciniform	Median/ Posterior	Wrapping captured prey	AcSp1
Attachment	Piriform	Median/ Posterior	Attachment to environmental substrates	PySp1

Spider silk fibers are remarkable materials when considering their low density, excellent mechanical properties, and thermal stability over a wide range of temperature. On a strength-to-weight basis, the elongation at break, the Young's modulus, and the average ultimate tensile strength of spider silks are close to, or even higher than, Kevlar and steel [45-47], as shown in **Table 1.3**. Spider dragline silk is thermally stable to about 230 °C according to thermogravimetric analysis (TGA) [48]. Due to these attractive properties, spider silks have received extensive research attention.

Table 1.3 Mechanical Properties of *Nephila Clavipes* Spider Silks in Comparison to other fibers [43].

Fiber	**Elongation (%)**	**Young's modulus (GPa)**	**Tensile strength (GPa)**	**Energy to break (J/kg)**
N. Clavipes dragline	9-11	22-60	1.1-2.9	3.7×10^4
B. mori fibroin	15-35	5	0.6	7×10^4
Kevlar	4	100	4	3×10^4
Steel	8	200	2	2×10^3

Spider silk is also an good example of a natural block copolymer, in which alanine-rich hydrophobic blocks and glycine-rich hydrophilic blocks are linked together generating a functional polymer used in biomedical applications such as guided tissue repair and drug delivery [49, 50]. The spider dragline silk of *Nephila clavipes* from the major ampullate gland contains at least two different proteins, major ampullate dragline

silk protein 1 (MaSp1) and major ampullate dragline silk protein 2 (MaSp2), which are held together by three to five disulphide bonds [51]. The amino acid sequences of *Nephila Clavipes* MaSp1 and MaSp2 repetitive region [52-54] are listed in **Figure 1.13**. MaSp1 and MaSp2 proteins are modular in nature. Both of them consist of three specific structural motifs with highly repetitive consensus sequences: (1) the poly-alanine GA/A_n motif, (2) the GG*X* motif in MaSp1 or GPGG*X* motif in MaSp2, and (3) the N-terminus and C-terminus. The main difference between MaSp1 and MaSp2 is that MaSp1 is a proline free protein, while the total amino acid content of MaSp2 contains 15% proline residues, which is known as a strong β-sheet breaker due to its unique pyrrolidine ring structure and the lack of one potential H-bond donor [55-57]. Biophysical studies have found evidence that different motifs are responsible to form various secondary structures corresponding to silk's mechanical properties. The GA/A_n motif forms beta sheets structures that correspond to the crystalline regions in the spun fibers, which provide the high tensile strength and stiffness [42, 58, 59]; the GG*X* motif forms alpha helices that give rise to a non-structured amorphous region [51, 60] to stabilize the fiber; and GPGG*X* motif has been hypothesized to form stackable type II beta turns structures, which provide the elasticity and extensibility of the threads [61]. In this thesis, we have studied as a model system, di-block copolymers based on MaSp1 motifs, GA/A_n and GG*X*, and mass produced a family of di-block copolymers, which possess these motifs as their blocks, using recombinant DNA technology bio-synthesized by Prof. Kaplan's group. These bioengineered spider silk block copolymers were then used to study the thermal properties, structural properties and morphological features with respect to the controlled amino acid sequences of proteins.

MaSp1

1	GQGGYGGLGGQGA -	13
14	GQGGYGGLGGQGA - - - - - - GQGAGAAAAAAAGGA	41
42	GQGGYGGLGSQGAGR - - - GGQGAGAAAAAA - GGA	71
72	GQGGYGGLGSQGAGRGGLGGQGAGAAAAAAAGGA	105
106	GQGGYGGLGNQGAGRG - - - GQG - - - AAAAAAGGA	133
134	GQGGYGGLGSQGAGRGGLGGQGAGAAAAAA - GGA	166
167	GQGGYGGLGGQGA - - - - - - - - - - - - - - - - - - -	179
180	GQGGYGGLGSQGAGRGGLGGQGAGAAAAAAAGGA	213
214	GQG - - - GLGGQGA - - - - - - GQGAGASAAAA - GGA	237
238	GQGGYGGLGSQGAGRGGE - - - GAGAAAAAA - GGA	267
268	GQGGYGGLGGQGA - - - - - - - - - - - - - - - - - - -	280
281	GQGGYGGLGSQGAGRGGLGGQGAGAAAA - - - GGA	311
312	GQG - - - GLGGQGA - - - - - - GQGAGAAAAAA - GGA	335
336	GQGGYGGLGSQGAGRGGLGGQGAGAVAAAAAGGA	369
370	GQGGYGGLGSQGAGR - - - GGQGAGAAAAAA - GGA	399
400	GQRGYGGLGNQGAGRGGLGGQGAGAAAAAAAGGA	433
434	GQGGYGGLGNQGAGR - - - GGQGA - - - - AAAAGGA	460
461	GQGGYGGLGSQGAGR - - - GGQGAGAAAAAAVG - A	490
491	GQE - - - - - - - - G I - R - - - - GQGA - - - - - - - - - -	500
501	GQGGYGGLGSQGSGRGGLGGQGAGAAAAAA - GGA	533
534	GQG - - - GLGGQGA - - - - - - GQGAGAAAAAA - GGV	557
558	RQGGYGGLGSQGAGR - - - GGQGAGAAAAAA - GGA	587
588	GQGGYGGLGGQGVGRGGLGGQGAGAAAA - - - GG -	617

Consensus Sequence

GQGGYGGLGGQGAGRGGLGGQGAGA$(A)_n$GGA

MaSp2

1	GPGGYGPGQQGPGGYGPGQQGP - - SGPGSAAAAAAAAAA - - - - - GPGGYGPGQQ	47
48	GPGCYCPCQQCPGRYGPGQQGP - - SGPGSAAAAAA - - - - - - - - - - - - - - GSGQQ	85
86	GPGGYGPRQQGPGGYGQGQQGP - - SGPGSAAAASAAASAESGQQGPGGYGPGQQ	137
138	GPGGYGPGQQGPGGYGPGQQGP - - SGPGSAAAAAAAAS - - - - - - - - - - - GPGQQ	178
179	GPGGYGPGQQGPGGYGPGQQGP - - SGPGSAAAAAAAAS - - - - - - - - - - - GPGQQ	219
220	GPGGYGPGQQGPGGYGPGQQGL - - SGPGSAAAAAAA - - - - - - - - - - - - - - - - - -	253
254	- - - - - GPGQQGPGGYGPGQQGP - - SGPGSAAAAAAAAA - - - - - - - - - - - - - - -	284
285	GPGGYGPGQQGPGGYGPGQQGP - - SGAGSAAAAAAA - - - - - - - - - - - - - GPGQQ	323
324	GLGGYGPGQQGPGGYGPGQQGPGGYGPGSASAAAAAA - - - - - - - - - - - - - - - - -	360
361	- - - - - GPGQQGPGGYGPGQQGP - - SGPGSASAAAAAAAA - - - - - - - - - - - - - -	392
393	GPGGYGPGQQGPGGYAPGQQGP - - SGPGSASAAAAAAAA - - - - - - - - - - - - - - -	429
430	GPGGYGPGQQGPGGYAPGQQGP - - SGPGSAAAAAAAAA - - - - - - - - - - - - - - - -	465
466	- - - - - - - - - - GPGGYGPAQQGP - - SGPGIAASAASA - - - - - - - - - - - - - - - - -	489
490	GPGGYGPAQQGPAGY - - - - - - - - - - GPGSAVAASAGA - - - - - - - - - - - - - - - -	516
517	- - - - - - - - - - GSAGY - - - - - - - - - - GPGSQASAAA - - - - - - - - - - - - - - - - - -	531

Consensus Sequence

GPGGYGPGQQGPGGYGPGQQGPSGPGS$(A)_n$

Figure 1.13 Amino acid sequences of the repetitive region of MaSp1 and MaSp2 from the dragline silk of *Nephila Clavipes* and the consensus sequences, taken from reference [52-54].

1.3.2 Spider Silk-like Block Copolymers

Block copolymer is a special kind of copolymer, which is made up of blocks of different polymerized monomers linked by covalent bonds [62]. In this thesis, to provide further insight into the relationships among protein amino acid sequence, block length, and physical properties, a family of synthetic proteins inspired by the genetic sequences found in MaSp1 of *Nephila Clavipes* dragline silk was produced using recombinant DNA technology in Prof. Kaplan's group. These spider silk-like block copolymers have *m* A-blocks and *n* B-blocks along with a His-tag, and are named as HA_mB_n or HB_nA_m. The A-block is a hydrophobic alanine-rich block based on MaSp1 motif GA/A_n. The amino acid sequence of A-block is GAGAAAAAGGAGTS (14 amino acids). The B-block is a hydrophilic glycine-rich block based on MaSp1 motif GG*X*, where *X* = Q, Y, or L. The amino acid sequence of B-block is QGGYGGLGSQGSGRGGLGGQTS (22 amino acids). The His-tag is for protein purification purposes. **Figure 1.14** shows a cartoon picture of HBA and HBA_6 spider silk-like block copolymers.

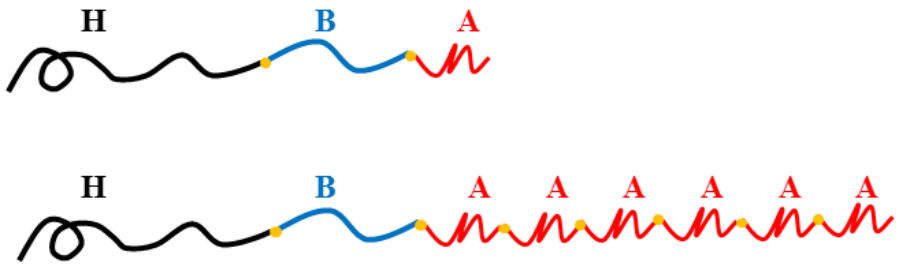

Figure 1.14 Cartoon picture of spider silk-like block copolymer, HBA and HBA_6.

Due to the hydrophobic/hydrophilic nature and the different motif structure formed by each block, the physical properties, such as the thermal properties, and structure, whether the tertiary or secondary, will be different among the spider silk-like block copolymers. These spider silk-like block copolymers also tend to self–assemble to form various microstructures [11, 63]. **Figure 1.15** illustrates a typical morphology formed by A-block rich spider silk-like block copolymer, HBA_4. Detailed discussion of the amino acid sequence dependent physical properties and morphological features of spider silk-like block copolymer are discussed in Chapter IV, V and VI.

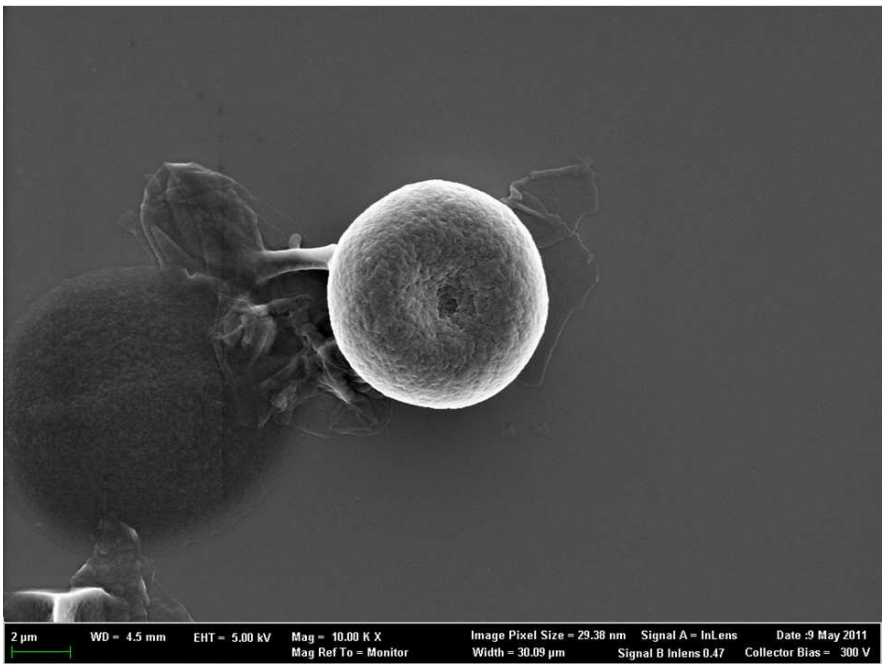

Figure 1.15 Vesicle structure formed by A-block rich spider silk-like block copolymer, HBA_4.

1.4 Motivations and Topics in This Thesis

Natural silk fibers have been discovered since ancient times, and some of them have been wildly used in textile industry for over 5,000 years [64, 65]. With the help of modern characterization techniques, the intrinsic properties of silks are beginning to be understood. Knowledge about the silk amino acid sequence, thermal properties and phase transitions, and silks' structural changes under various conditions facilitate the fabrication of silk products and leads to a variety of high-tech applications of silk.

The two most well studied naturally occurring silks are the *B. mori* silkworm silks and the dragline silk of *Nephila clavipes* spider. By knowing the physical properties of silks, the silks can be fabricated into different forms, such as film, scaffold, hydrogel, vesicle, fiber, particle and nanofibers or nanoparticles, and they can be further utilized in different high-tech applications. For example, a biosensor made of silk film is one of the interesting applications of silk protein [66]. By utilizing the biocompatibility of silks films, the sensor is implantable into the human body, and can be degraded *in-situ*, without making additional surgery to take it out. Silk is also wildly used in tissue engineering. Tissue scaffolds made of silk can be used to grow cells for the treatment of defective bone or skin [50].

Silk is also a remarkable material for loading with drugs for drug delivery. The hydrogel patch made of drug-loaded silk provides a controlled release of the drug into the human body [67]. The release rate of the drug from the silk depends upon the degree of crystallinity of the silk. Crystals are more dense than non-crystalline silk, and the crystal beta sheets of silk act as crosslinks and control the diffusion of the drug. So the physical properties of the silk affect its performance in the body. Besides the hydrogels, in other

forms, such as vesicle, microspheres, and nanoparticles, the silk also served as a drug carrier to deliver drug to cells [68].

There are also many other biological or industrial applications for silk, such as serving as a nerve guide for nerve regeneration [69] and making tough strings for musical instruments [70].

To make full use of silks, these remarkable materials and their intrinsic properties need to be studied in detail. Unfortunately, among tens of thousands types of silks, only a few types are well characterized. Moreover, with the development of recombinant DNA technology, more and more "man-made" silks with well-defined amino acid sequences have been synthesized, and these new materials need to be characterized as well. In this project, we want to improve our knowledge about silks, especially the recombinant silks, and also improve the methods used to characterize the silks by adopting the characterization techniques that have long been used for studies of synthetic polymers.

The goal of this thesis is to use a new family of silk-based block copolymers to understand and then control the thermal, structural, and morphological features of the recombinant proteins with specific motifs. By utilizing recombinant DNA technology, the volume ratio of each structural motif in the recombinant silks can be adjusted, and in this manner their self-assembly morphology, thermal and structural properties are adjusted accordingly. We anticipate that the results from our study will provide a roadmap for the design and synthesis of precise materials having some of the same properties of spider silks, or other valuable rare material, using well controlled protein sequences.

In this thesis, to achieve our goal, the following studies of spider silk-like block copolymer were discussed step by step.

a. Heat Capacity of Spider Silk-like Block Copolymers

Thermal property studies of protein-based material are very crucial because of the potential use of these materials in biomedical applications in drug delivery [43]. Therefore, we investigated the heat capacities of our spider silk-like block copolymer. The reversing heat capacities, $C_p(T)$, for temperatures below and above the glass transition, T_g, were measured by temperature modulated differential scanning calorimetry. For the solid state, we then calculated the heat capacities of spider silk-like block copolymers based on the vibrational motions of the constituent poly(amino acid)s, whose heat capacities are known or can be estimated from the ATHAS Data Bank. For the liquid state, the heat capacity was estimated by using the rotational and translational motions in the polymer chain. Excellent agreement was found between the measured and calculated values of the heat capacity, showing that this method can serve as a standard by which to assess the C_p for other biologically inspired block copolymers. The fraction of beta sheet crystallinity of spider silk block copolymers was also determined by using the predicted C_p, and was verified by wide angle X-ray diffraction and Fourier transform infrared spectroscopy. The glass transition temperatures of spider silk block copolymer were fitted by Kwei's equation. Results, which were published in Macromolecules [21], indicate that, in the solid state, attractive interaction exists between A-block and B-block, while intermolecular interactions exist between A-block and the His-tag.

b. Determining the Effect of Water on Spider Silk-like Block Copolymer Glass Transition

To obtain a fuller understanding of the protein−water interactions with respect to the protein amino acid sequence, advanced thermal analysis methods using temperature modulated differential scanning calorimetry (TMDSC) in combination with thermogravimetric analysis (TGA) were employed to capture the effect of bound water acting as a plasticizer in water cast protein films. A theoretical model, which was used to predict the specific reversing heat capacity of the protein-water system, $C_p(T)$, based on the vibrational, rotational and translational motions of protein amino acid residues and water molecules, along with the TMDSC measurements show that two glass transitions formed in all samples during heating. The low temperature glass transition, $T_g(1)$, is related to both the bound water removal induced conformational change and to the hydrophobicity of the protein sequences, while the high temperature glass transition, $T_g(2)$, above 130 °C is the now dry protein glass transition. Real-time Fourier transform infrared spectroscopy (FTIR) confirmed that conformational changes occurred during the two glass transitions, with a random coils to beta turns transition during $T_g(1)$ and alpha helices to beta turns transition during $T_g(2)$. This study provides a deeper understanding of the protein-water relationships and the conformational changes in protein-water system during heating with implications for the thermal induced structural transitions of other protein based materials. A portion of this work has been published in Journal of Thermal Analysis and Calorimetry [71], and Polymer Preprints [72].

c. Tunable Self-assembly, Crystallization and Degradation of Recombinant Spider Silk-like Block Copolymer

Due to the hydrophobic and hydrophilic nature of the blocks, the spider silk block copolymers tend to self–assemble into various microstructures. To investigate the morphological features formed by spider silk-like block copolymers, thin films were prepared either from solutions of hexafluoroisoprpanol (HFIP), or from methanol (MeOH) which served as a control. Secondary structure and crystallinity of the films were monitored by Fourier transform infrared spectroscopy during heating from 30 - 340 ^{o}C. Thermal properties were determined by differential scanning calorimetry. Using scanning electron microscopy, micelles were observed in thermally-treated HBA_6, HBA_3, HBA_2 and HBA films. Hollow vesicles and fibrillar networks were observed in methanol-cast HBA_6, HBA_3, HBA_2 and HBA sample films, while no micro-structures were formed in HFIP-cast films or in HAB_2 and HAB_3, indicating that morphology and crystallinity can be tuned by not only be the block length and also the thermal/chemical treatments. Results indicate when we increase the number of repeating units of A-block in the protein, sample films crystallize more easily. When the volume fraction of A-block is increased, the final crystallinity upon thermal treatment increases. Because beta sheets acted as a cross-link between protein chains, the crystalline sample films became more thermally stable. Moreover, when samples crystallize, the secondary structure of the A-block and B-block become different, thus it will be easier to form bilayer structures which could fold into vesicles and tube structures during drying. A portion of this work has been published in MRS Proceedings [73].

Side Projects

Two side projects: 1) Nanocomposites of poly(vinylidene fluoride) with multi-walled carbon nanotubes, and 2) PVDF-based polymer blend films for fuel cell membranes, which were completed during the summer internship at Tufts are also briefly summarized in Appendix I and J. The projects resulted in publication in Journal of Applied Polymer Science [74], PMSE Preprints [75] and MRS Proceedings [76].

1.5 References

1. Stevenson A. *Oxford dictionary of English*. Oxford: Oxford University Press, 2011; online resource.
2. Young RJ and Lovell PA. *Introduction to polymers, 2nd ed*. Cheltenham, England: Stanley Thorne (Publishers) Ltd, 2000: 241-300.
3. Strobl GR. *The physics of polymers: concepts for understanding their structures and behavior*. Berlin; New York: Springer, 2007: 1-11.
4. Odian GG. *Principles of polymerization, 4th ed*. Hoboken, N.J.: Wiley-Interscience, 2004: 1-22.
5. Voet D, Voet JG, and Pratt CW. *Fundamentals of biochemistry upgrade, Rev. ed*. New York: Wiley, 2002: 124-148.
6. Allcock HR, Mark JE, and Lampe FW. *Contemporary polymer chemistry, 3rd ed*. Upper Saddle River, N.J.: Prentice Hall, 2003: 335-484.
7. Wunderlich B. *Thermal analysis of polymeric materials*. Berlin: Springer, 2005: 304-404.

8. Kourtides DA. *Polymer-Plastics Technology and Engineering* 1978; 11(2): 159-198.
9. Gennes P-Gd. *Scaling concepts in polymer physics*. Ithaca, N.Y.: Cornell University Press, 1979: 59-88.
10. Rubinstein M and Colby RH. *Polymer physics. Oxford*; New York: Oxford University Press, 2003: online resource.
11. Rabotyagova OS, Cebe P, and Kaplan DL. *Biomacromolecules* 2009; 10(2): 229-236.
12. Wunderlich B. *Journal of Thermal Analysis and Calorimetry* 2008; 93(1):7-17.
13. Androsch R and Wunderlich B. *Polymer* 2005; 46(26): 12556-12566.
14. Chen HP and Cebe P. *Macromolecules* 2009; 42(1): 288-292.
15. Ma QA and Cebe P. *Journal of Thermal Analysis and Calorimetry* 2010; 102(2): 425-434.
16. Pyda M, Nowak-Pyda E, Heeg J, Huth H, Minakov AA, Di Lorenzo ML, Schick C, and Wunderlich B. *Journal of Polymer Science Part B-Polymer Physics* 2006; 44(9): 1364-1377.
17. Ma Q, Mao B, and Cebe P. *Polymer* 2011; 52(14): 3190-3200.
18. Wunderlich B. *Progress in Polymer Science* 2003; 28(3): 383-450.
19. Suzuki H, Grebowicz J, and Wunderlich B. *British Polymer Journal* 1985; 17(1): 1-3.
20. Menczel J and Wunderlich B. *Journal of Polymer Science Part C-Polymer Letters* 1981; 19(5): 261-264.
21. Huang WW, Krishnaji S, Hu X, Kaplan D, and Cebe P. *Macromolecules* 2011; 44(13): 5299-5309.

22. Ince-Gunduz BS, Alpern R, Amare D, Crawford J, Dolan B, Jones S, Kobylarz R, Reveley M, and Cebe P. *Polymer* 2010; 51(6): 1485-1493.

23. Ince-Gunduz BS, Burke K, Koplitz M, Meleski M, Sagiv A, and Cebe P. Journal of *Macromolecular Science Part a-Pure and Applied Chemistry* 2010; 47(12): 1208-1219.

24. Bassett DC. *Principles of Polymer Morphology*. Cambridge Univeristy Press, 1981: 5-26.

25. Hu X, Kaplan D, and Cebe P. *Macromolecules* 2006; 39(18): 6161-6170.

26. Hu X, Kaplan D, and Cebe P. *Macromolecules* 2008; 41(11): 3939-3948.

27. Hu X, Lu Q, Kaplan DL, and Cebe P. *Macromolecules* 2009; 42(6): 2079-2087.

28. Du BY, Liu JP, Zhang QL, and He TB. *Polymer* 2001; 42(13): 5901-5907.

29. Chen H. Ph.D. Thesis 2009: 7-10.

30. Hoffman JD. *Spe Transactions* 1964; 4(4): 315-362.

31. Huo PP and Cebe P. *Macromolecules* 1993; 26(12): 3127-3130.

32. Magill JH. *Makromolekulare Chemie* 1965;86(1): 232-288.

33. Pyda M, Hu X, and Cebe P. *Macromolecules* 2008; 41(13): 4786-4793.

34. Nelson PC, Radosavljeviâc M, and Bromberg S. *Biological physics: energy, information, life*. New York: W.H. Freeman and Co., 2004: 1-87.

35. Mathews CK, Van Holde KE, and Ahern KG. *Biochemistry*, 3rd ed. San Francisco, Calif.: Benjamin Cummings, 2000: 161-167.

36. Xia XX, Xu QB, Hu X, Qin GK, and Kaplan DL. *Biomacromolecules* 2011; 12(11): 3844-3850.

37. Rabotyagova OS, Cebe P, and Kaplan DL. *Biomacromolecules* 2011; 12(2):269-289.

38. McGrath K and Kaplan D. P*rotein-based materials*. Boston: Birkhäuser, 1997: 103-132.

39. Vollrath F and Knight DP. *Nature* 2001;410(6828): 541-548.

40. Vollrath F and Porter D. *Soft Matter* 2006; 2(5): 377-385.

41. Dennis Kunkel. http://www.astrographics.com/GalleryPrintsIndex/GP2017.html, 2002.

42. Gosline JM, Demont ME, and Denny MW. *Endeavour* 1986; 10(1): 37-43.

43. McGrath K and Kaplan D. *Protein-based polymers*. Boston: Birkhäuser, 1997: 100-132.

44. Foelix RF. *Biology of spiders, 2nd ed*. New York: Oxford University Press, 1996: 1-55.

45. Gosline JM, Guerette PA, Ortlepp CS, and Savage KN. *Journal of Experimental Biology* 1999; 202(23): 3295-3303.

46. Sponner A, Schlott B, Vollrath F, Unger E, Grosse F, and Weisshart K. *Biochemistry* 2005; 44(12): 4727-4736.

47. Kluge JA, Rabotyagova O, Leisk GG, and Kaplan DL. *Trends in Biotechnology* 2008; 26(5): 244-251.

48. Cunniff PM, Fossey SA, Auerbach MA, and Song JW. *Silk Polymers - Materials Science and Biotechnology*, 1994; 544: 234-251.

49. Vendrely C and Scheibel T. *Macromolecular Bioscience* 2007; 7(4): 401-409.

50. Sofia S, McCarthy MB, Gronowicz G, and Kaplan DL. *Journal of Biomedical Materials Research* 2001; 54(1): 139-148.

51. Rising A, Nimmervoll H, Grip S, Fernandez-Arias A, Storckenfeldt E, Knight DP, Vollrath F, and Engstrom W. *Zoological Science* 2005; 22(3): 273-281.

52. Foo CWP and Kaplan DL. *Advanced Drug Delivery Reviews* 2002; 54(8): 1131-1143.

53. Xu M and Lewis RV. *Proceedings of the National Academy of Sciences of the United States of America* 1990; 87(18): 7120-7124.

54. Kaplan D, Adams WW, Farmer B, and Viney C. *ACS (American Chemical Society) Symposium Series* 1994;544: 370.

55. Li SC, Goto NK, Williams KA, and Deber CM. *Proceedings of the National Academy of Sciences of the United States of America* 1996; 93(13): 6676-6681.

56. Liu Y, Sponner A, Porter D, and Vollrath F. *Biomacromolecules* 2008; 9(1): 116-121.

57. Hu X, Vasanthavada K, Kohler K, McNary S, Moore AMF, and Vierra CA. *Cellular and Molecular Life Sciences* 2006; 63(17): 1986-1999.

58. Simmons A, Ray E, and Jelinski LW. *Macromolecules* 1994; 27(18): 5235-5237.

59. Hayashi CY, Shipley NH, and Lewis RV. *International Journal of Biological Macromolecules* 1999; 24(2-3): 271-275.

60. Gosline J, Lillie M, Carrington E, Guerette P, Ortlepp C, and Savage K. *Philosophical Transactions of the Royal Society of London Series B-Biological Sciences* 2002; 357(1418): 121-132.

61. Hayashi CY and Lewis RV. *Journal of Molecular Biology* 1998; 275(5): 773-784.

62. Hamley IW. *The physics of block copolymers. Oxford*; New York: Oxford University Press, 1998: 1-98.

63. Krishnaji ST, Huang WW, Rabotyagova O, Kharlampieva E, Choi I, Tsukruk VV, Naik R, Cebe P, and Kaplan DL. *Langmuir* 2011; 27(3): 1000-1008.

64. Schoeser M. *Silk*. New Haven, Conn.; London: Yale University Press, 2007: 1-21.

65. Franck RR and Textile Institute (Manchester England). *Silk, mohair, cashmere and other luxury fibres*. Woodhead Publishing Limited series on fibres. Boca Raton, FL Cambridge, Eng.: CRC Press ; Woodhead Pub., 2001: 1-56, 247 p.

66. Hwang S-W, Tao H, Kim D-H, Cheng H, Song J-K, Rill E, Brenckle MA, Panilaitis B, Won SM, Kim Y-S, Song YM, Yu KJ, Ameen A, Li R, Su Y, Yang M, Kaplan DL, Zakin MR, Slepian MJ, Huang Y, Omenetto FG, and Rogers JA. *Science* 2012; 337(6102): 1640-1644.

67. Kim UJ, Park JY, Li CM, Jin HJ, Valluzzi R, and Kaplan DL. *Biomacromolecules* 2004; 5(3): 786-792.

68. Lammel A, Schwab M, Hofer M, Winter G, and Scheibel T. *Biomaterials* 2011; 32(8): 2233–2240.

69. Yang Y, Chen X, Ding F, Zhang P, Liu J, and Go X. *Biomaterials* 2007; 28(9): 1643-1652.

70. Osaki S. *Physical review letters* 2012; 108(15): 154301.

71. Huang W, Krishnaji S, Kaplan D, and Cebe P. *Journal of Thermal Analysis and Calorimetry* 2012;109:1193-1201.

72. Huang W, Krishnaji S, Hu H, Kaplan DL, and Cebe P. *Polymer Preprints* 2010; 51(2): 488-489.

73. Huang WW, Krishnaji S, Kaplan D, and Cebe P. *MRS Proceedings* 2012; 1417: kk01-05.

74. Huang WW, Edenzon K, Fernandez L, Razmpour S, Woodburn J, and Cebe P. *Journal of Applied Polymer Science* 2010; 115(6): 3238-3248.

75. Huang WW, Edenzon K, Fernandez L, Razmpour S, Woodburn J, and Cebe P. *PMSE Preprints* 2009; 101: 852-853.

76. Huang W, Zhao M, Yang F, Haghighi P, Farovitch L, Macisco LJ, Swob T, Smith T, and Cebe P. *MRS Proceedings* 2011; 1384: b05-02.

Chapter II. Theory of Characterization Methods

This chapter provides the theoretical background of the experimental approaches used in this thesis, which includes differential scanning calorimetry, thermogravimetric analysis, Fourier transform infrared spectroscopy, and X-ray diffraction. Other experimental approaches used in the side projects are also briefly introduced at the end of this chapter.

2.1 Differential Scanning Calorimetry

Differential scanning calorimetry (DSC) is a powerful analytical tool which has been widely used in polymer characterization [1] and biomedical research [2, 3]. DSC enables the determination of the glass transition, the characterization of crystallization and melting transition temperatures and the corresponding enthalpy and entropy changes, and other thermally induced effects which show either changes in heat capacity or latent heat. The invention and development of DSC can be traced all the way back to the early 1960s [4], and because of the quantitative features of calorimetry and ease of measurement of thermal properties during heating and cooling, DSC now becomes a well-accepted analysis technique. Traditional thermal analysis techniques include differential thermal analysis (DTA) and standard DSC. More advanced DSCs were also developed in recent decades such as temperature modulated DSC (TMDSC) [5-10], Nano-DSC [11, 12] and fast scanning chip calorimetry (FSC) [13-18]. The techniques used in this thesis are standard DSC and TMDSC.

2.1.1 Fundamental Principles of DSC

The basic principle underlying DSC measurements is that when the sample undergoes phase transitions or other thermally induced physical changes, more or less heat will need to be absorbed or released from the sample (which is encapsulated in aluminum pan for measurement) than from the reference (which is just an empty aluminum pan), to maintain both at the same temperature [19]. Therefore, by detecting the difference of heat needed to heat up or cool down a sample relative to a reference, enthalpy changes due to a change of state of the sample can be determined, and a number of thermal properties, such as the specific heat capacity, and important thermal transitions, such as glass transition, crystallization, melting and degradation, can be further quantified and analyzed by the enthalpy change.

There are two types of DSCs commonly used: heat flux DSC and power compensation DSC. In heat flux DSC, the heat flow (differential temperature) as a function of sample temperature is measured, while in power compensation DSC, the electrical energy provided to maintain the sample and the reference at the same temperature is measured. Because the heat flux DSC is used for the thesis project, it will be discussed in more detail.

Figure 2.1 shows a schematic representation of the heat flux differential scanning calorimeter, which consists of a twin DSC cell holder with sample platform and reference platform [4]. The reference (an empty pan) and the sample which is sealed in an identical aluminum pan are represented by rectangular boxes. In the DSC furnace, the sample and reference are heated by the furnace heating block and their temperatures are measured by the individual thermocouples. If a temperature difference between the sample and

reference ($\Delta T = T_r - T_s$) is detected, the heat is immediately supplied by the heaters until the temperature difference between the sample and reference is less than a predefined value (< 0.005 ºC). The temperature difference ΔT will lead to an electrical signal that is proportional to a heat flow-rate signal.

$$\Delta T = \Delta U / S \tag{2.1}$$

where ΔU is the adjusted voltage of thermocouple and S is the thermocouple response.

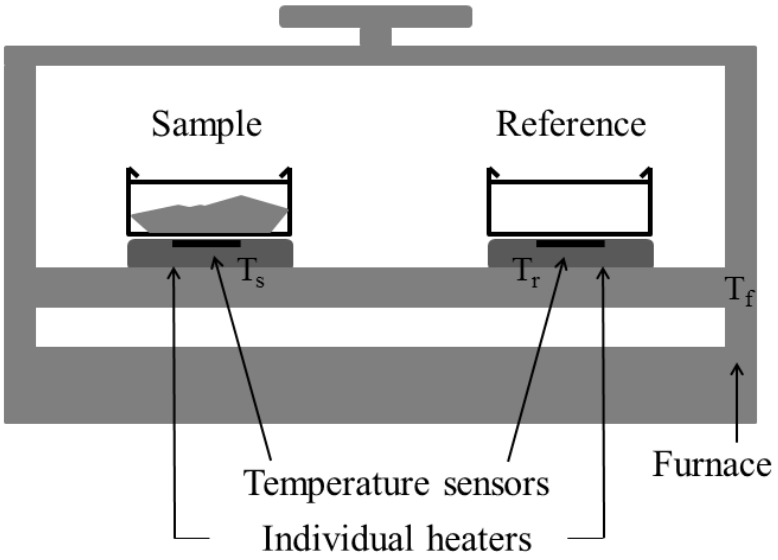

Figure 2.1 Schematic representation of the differential scanning calorimeter. Sample is sealed in an aluminum pan, and is heated together with an empty reference pan on two nearly identical platforms in a furnace.

In reporting of DSC data, the differential heat absorbed or released by the sample is usually examined. The sample heat absorption process is called an endothermic process, which typically can cause solvent evaporation, crystal melting, or the physical aging peak during glass transition, while the sample heat releasing process is called an

exothermic process, such as crystallization. To avoid confusion, the endotherm or exotherm direction must be marked on DSC heat flow traces. **Figure 2.2** illustrates a typical heat flow vs. temperature curve measured by DSC depicting several transition types [19]. A given sample may not show all of the features in Figure 2.2. The structure of the sample, set by its thermal history, will determine which features are seen.

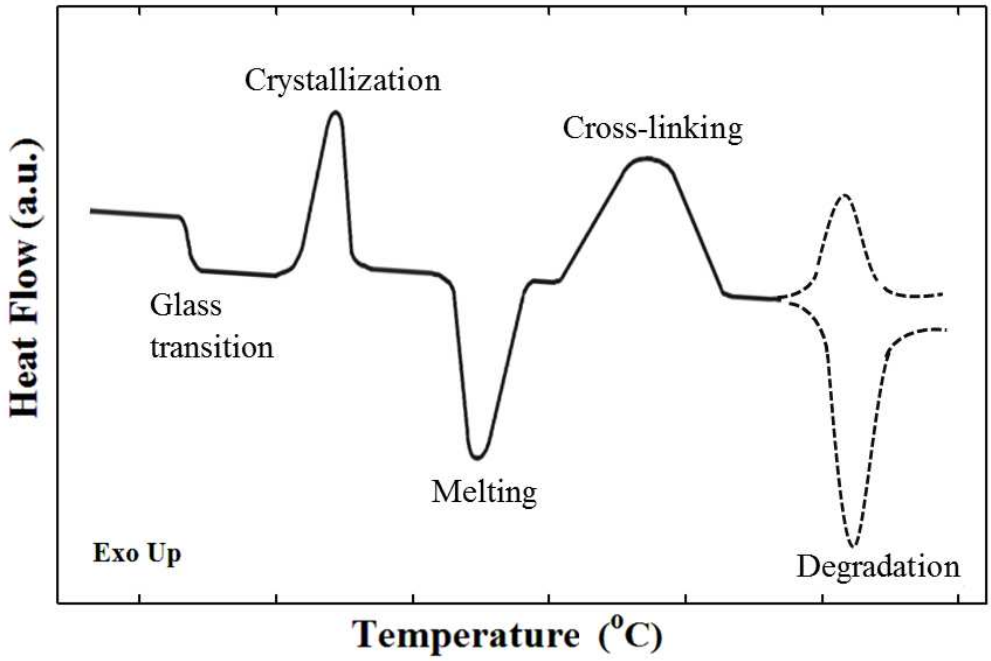

Figure 2.2 A typical heat flow vs. temperature curve by DSC during heating.

2.1.2 Standard DSC

The standard DSC is the conventional DSC which has been used since the 1960s. It is operated under a constant heating/cooling rate $q = dT/dt$ by the programmed heating/cooling furnace block. The block temperature can be expressed as a linear function of time with an initial temperature T_0 as

$$T_b = T_0 + qt \quad . \tag{2.2}$$

When the steady state [4, 19] is reached in standard DSC, the reference and sample temperatures, T_r and T_s, can be expressed as

$$dT_r/dt = q = dT_b/dt \tag{2.3a}$$

$$dT_s/dt = q\, dT_s/dT_r \tag{2.3b}$$

The data collected by standard DSC includes temperature, time and differential heat flow. With the approximation of a negligible temperature gradient within the sample, and under steady state conditions throughout the instrument, the heat flow rate into the reference and sample, dQ_r/dt and dQ_s/dt, in a standard DSC can be modeled by Newton's law of cooling [4, 20]:

$$dQ_r/dt = K(T_b - T_r) \tag{2.4a}$$

$$dQ_s/dt = K(T_b - T_s) \tag{2.4b}$$

where T_b is the furnace block temperature, T_s and T_r are the sample and reference temperatures, respectively, and K is the geometry and DSC cell-material dependent thermal conductivity which is independent of sample properties. When a sample passes a thermal transition, the heat absorbed or released from the sample, Q_s, within a short period of time can be calculated as

$$Q_s = C_s(T_s - T_0) \tag{2.5a}$$

$$dQ_s/dt = C_s dT_s/dt \tag{2.5b}$$

where C_s is the heat capacity of sample calorimeter (pan and sample), and it is assumed to be a constant over a short time (within 1s) during which the sample temperature is almost a constant. Therefore, by combining equations 2.2 – 2.5, we can conclude that

$$T_b - T_r = \frac{C_r}{K}(\frac{dT_r}{dt}) \tag{2.6a}$$

$$T_b - T_s = \frac{C_s}{K}(\frac{dT_s}{dt}) = \frac{mc_p + C_r}{K}(\frac{dT_s}{dt}) \tag{2.6b}$$

$$\Delta T = T_r - T_s = \frac{C_r + mc_p}{K}(\frac{dT_s}{dt}) - \frac{C_r}{K}(\frac{dT_r}{dt}) \approx \frac{mc_p}{K}q \tag{2.6c}$$

where the C_s and C_r are the heat capacities of the sample and reference calorimeters, respectively, and c_p is the specific heat capacity of the sample with mass m. So the heat capacity of sample can be then re-written as [4]

$$mc_p = K\frac{\Delta T}{q} + (K\frac{\Delta T}{q} + C_r)(\frac{d\Delta T}{dT_s}) \approx K\frac{\Delta T}{q} = K''\frac{HF}{q} \tag{2.7}$$

where K'' is the calibration constant obtained by running a standard material such as sapphire, and HF is the differential heat flow into or out of the sample. After the baseline subtraction and calibration of K'', the heat capacity of the sample material C_s can be obtained [21-23]. A detailed description about using this "three runs methods" to calibrate K'' for measuring sample heat capacity is given in Chapters III and IV.

Using the fact that the melting endotherm area is proportional to the crystallinity, the crystallinity of semicrystalline synthetic polymers can be calculated as a fraction of the enthalpy of fusion from the area of the DSC melting endotherm, $\Delta H(measured)$, in ratio to the heat of fusion of a fully crystalline sample, ΔH_f, as

$$\varphi_c = \Delta H(measured) / \Delta H_f \tag{2.8}$$

However, for biopolymers, usually no thermal melting peak can be observed because of their low thermal stability. Thus, usually it is not possible to determine the crystallinity of biopolymers by using heat of fusion from DSC.

2.1.3 Temperature Modulated DSC

Temperature Modulated DSC (TMDSC) can be considered as an extension of standard DSC. This technique, first reported in 1992 [4, 6], involves applying a super-imposed sinusoidal oscillation (modulation) on a DSC temperature and deconvoluting of the total heat flow rate into two parts: one part that follows the modulation in phase, the reversing heat flow; and one part that does not, the non-reversing heat flow. In general, TMDSC can be used to perform the same material characterization as the standard DSC, including determining the transition temperatures, the enthalpy of fusion during crystallization and melting, and the specific heat capacities. Moreover, TMDSC can also be used to solve more complicated thermal transitions and increase the amount of information that can be obtained from DSC measurements. For example, most protein samples contain bound water molecules which affect their structure and transition temperature. During heating, the bound water evaporation peak overlaps the glass transition of the bound water-protein system, and this complication cannot be well explained by standard DSC measurements. However, by using TMDSC, the non-reversing water evaporation peak can be separated from the reversing glass transition, which separates this complex transition into more easily interpreted components. The detailed description of the protein-water thermal transitions can be found in Chapter V.

TMDSC preserves the same DSC cell from the standard DSC as shown in Figure 2.1. It also measures the differential heat flow between the sample and the reference as a function of time and temperature. The only difference is, in TMDSC a sinusoidal temperature modulation with frequency of oscillation ω and amplitude A is added to the conventional constant heating rate ($q \neq 0$) or absolute isotherms ($q = 0$). Therefore the temperature of the programmed furnace heating/cooling block is

$$T_b = T_0 + qt + A_{T_b} \sin(\omega t) \tag{2.9}$$

where q is the underlining heating/cooling rate which is calculated by averaging over a full modulation cycle. **Figure 2.3** shows the temperature profile of TMDSC compared with standard DSC.

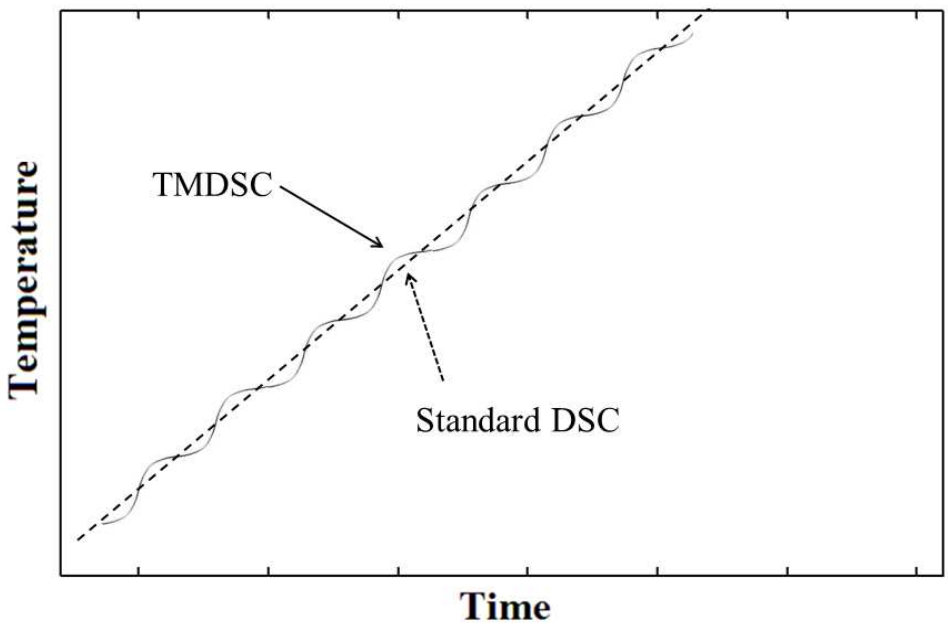

Figure 2.3 Illustration of the temperature profile of TMDSC (solid curve) using the "heat only" condition (sample temperature never decreases during heating). The linear temperature profile of standard DSC (dashed line) is also plotted for comparison.

When TMDSC reaches the steady state, the modulated reference and sample temperatures, T_r and T_s, can be separated into two components. One is in-phase with T_b which is described by a sine function of ωt, and the other is out-of-phase with T_b which is described by a cosine function of ωt [4].

$$\begin{aligned} T_r &= T_0 + qt - \frac{qC_r}{K} + A_{T_r}\sin(\omega t - \phi) \\ &= T_0 + qt - \frac{qC_r}{K} + A_{T_r}[\cos\phi\sin\omega t - \sin\phi\cos\omega t] \end{aligned} \tag{2.10a}$$

$$\begin{aligned} T_s &= T_0 + qt - \frac{qC_s}{K} + A_{T_s}\sin(\omega t - \varepsilon) \\ &= T_0 + qt - \frac{qC_s}{K} + A_{T_s}[\cos\varepsilon\sin\omega t - \sin\varepsilon\cos\omega t] \end{aligned} \tag{2.10b}$$

where ϕ and ε are the phase lag of reference and sample, respectively. Considering a quasi-isothermal TMDSC mode with the underlying heating rate $q = 0$ and using a common mathematical relation: $\sin\theta - i\cos\theta = -ie^{i\theta}$, the modulated reference and sample temperature can also be expressed in the complex plane as following

$$T_r - T_0 = A_{T_r} ie^{i(\omega t-\phi)} \tag{2.11a}$$

$$T_s - T_0 = A_{T_s} ie^{i(\omega t-\varepsilon)} \tag{2.11b}$$

$$\Delta T = T_r - T_s = A_\Delta ie^{i(\omega t-\delta)} \tag{2.11c}$$

where phase angle δ equals ($\varepsilon - \phi$), and A_Δ is the amplitude of temperature difference. Inserting equation 2.11 into equation 2.6 yields

$$\begin{aligned} A_\Delta e^{i(\omega t-\delta)} &= \frac{C_s - C_r}{K}\frac{dT_s}{dt} - \frac{C_r}{K}\frac{d(T_r - T_s)}{dt} \\ &= \frac{C_s - C_r}{K}A_{T_s} i\omega e^{i(\omega t-\varepsilon)} - \frac{C_r}{K}A_\Delta i\omega e^{i(\omega t-\delta)} \end{aligned} \tag{2.12}$$

which can be rearranged with an imaginary part and a real part

$$e^{-i(\varepsilon-\delta)} = -i\sin(\varepsilon-\delta)+\cos(\varepsilon-\delta) = -\frac{KA_{\Delta}i}{A_{T_s}\omega(C_s-C_r)}+\frac{A_{\Delta}C_r}{A_{T_s}(C_s-C_r)} \tag{2.13}$$

using $sin^2\theta + cos^2\theta = 1$, we have

$$1=\left[\frac{KA_{\Delta}}{A_{T_s}\omega(C_s-C_r)}\right]^2+\left[\frac{A_{\Delta}C_r}{A_{T_s}(C_s-C_r)}\right]^2 \tag{2.14}$$

Considering that the position of reference and sample are symmetric in the DSC cell, equation 2.14 can be rearranged to be an equation for the sample heat capacity [4, 22, 23]

$$\left|C_s-C_r\right| = \frac{A_{\Delta}}{A_{T_s}}\sqrt{\left(\frac{K}{\omega}\right)^2+C_r^2} = \frac{A_{HF}}{A}K' \tag{2.15}$$

where C_s and C_r are the heat capacity of the sample and pan, and reference, respectively; $A = A_{Ts}$ is the modulated temperature amplitude; A_{HF} is the modulated heat flow amplitude; K is Newton's law calibration constant; and K' is the calibration constant for the heat flow amplitude for a given empty reference pan and modulation frequency.

For most of the cases, the reference side and the sample side are not symmetric and not thermally balanced, even though two identical aluminum pans were used, because of the existence of cell asymmetry, ΔC_{cell}. Thus, equation 2.12 can be expressed as equation 2.16 by separating out the sample heat capacity, mc_p, from the heat capacity of its pan C_{sp}, written by substituting C_s with $mc_p + C_{sp} \pm \Delta C_{cell}$ [4, 22, 23], we obtain:

$$\left|mc_p+C_{sp}-C_r\pm\Delta C_{cell}\right| = \frac{A_{\Delta}}{A}\sqrt{\left(\frac{K}{\omega}\right)^2+C_r^2} = \frac{A_{HF}}{A}K' \tag{2.16}$$

where mc_p is the heat capacity of a sample of mass, m, and specific heat capacity, c_p; C_{sp} is the heat capacity of the empty sample pan; ΔC_{cell} is the cell asymmetry correction [24]; A_Δ is the amplitude of temperature difference between sample and reference; A is the sample temperature modulation amplitude; K is Newton's law calibration constant; A_{HF} is the heat flow amplitude and K' is a calibration constant [23] related to the experimental conditions.

The specific heat capacity, c_p, of a sample measured by TMDSC is called "reversing heat capacity", because it is a modulation-induced signal. Since thermodynamic equilibrium has not been assured during scanning, the term "reversing" is used rather than "reversible." Using the sample specific heat capacity, the reversing heat flow, *RHF(t)*, can be expressed as

$$RHF(t) = mc_p \cdot q \tag{2.17}$$

The reversing heat flow refers to that component which is reversing within the time scale of the temperature oscillation. The glass transition phenomenon is an example of a transition which is reversing. The non-reversing heat flow, *NHF(t)*, is computed as the difference between the total heat flow, *HF(t)*, and the reversing heat flow, *RHF(t)*:

$$NHF(t) = HF(t) - RHF(t) \tag{2.18}$$

Nonreversing processes include solvent or water removal, melting and crystallization, or degradation. As discussed above, TMDSC can be used to separate the reversible process from non-reversible process. Therefore, it was extensively used for the thermal analysis of protein and protein-solvent system in this thesis because of this advantage.

2.2 Thermogravimetric Analysis

Thermogravimetric analysis (TGA) is an extensively used technique in which sample mass is measured as a function of time or temperature [19] in a controlled atmosphere. TGA measurements are primarily used to characterize materials that exhibit weight loss or gain due to dehydration, degradation, or oxidation either with time or at an elevated temperature up to 1000 °C. For example, TGA was used to calibrate the sample weight of biological samples when the bound water molecules escaped from the material during heating [25]. The operational details are discussed in Chapter IV. A typical TGA curve is shown in **Figure 2.4**.

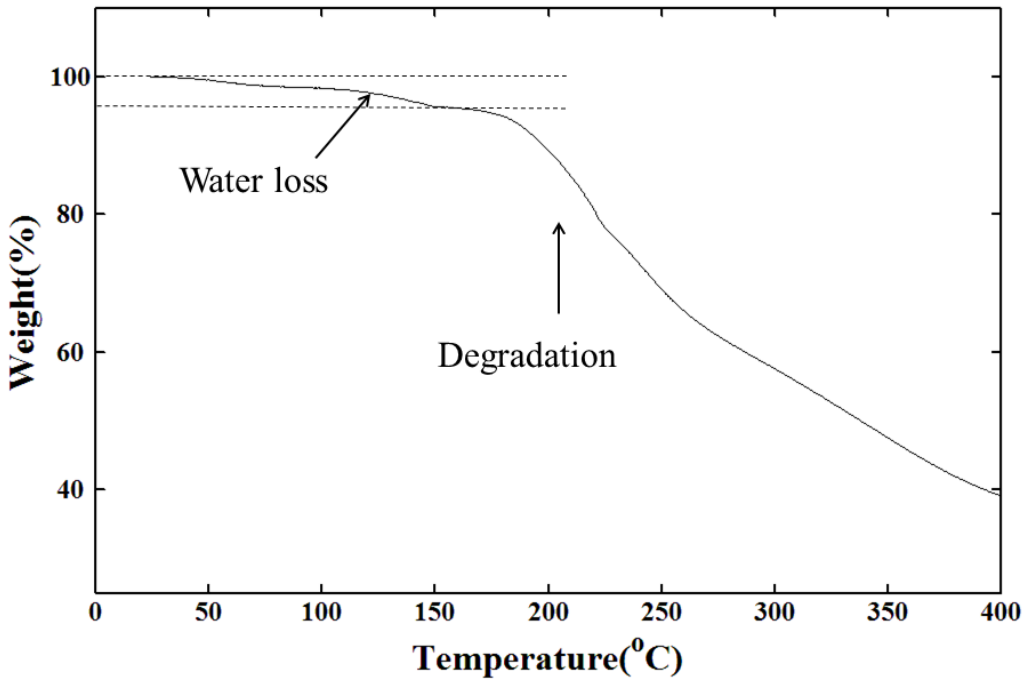

Figure 2.4 A typical TGA curve of recombinant spider silk-like block copolymer, illustrated by B-block.

A TGA curve usually has limited ability to identify the sample thermal transitions, but in combination with DSC, it provides a fuller profile of the sample thermal properties during heating or cooling. It is especially useful for determining the change of sample mass with temperature, allowing correction to be made in the mass of sample used to normalize the DSC heat flow data following the method provided in our previous publications [26, 27]. For example, the total sample mass of a protein-water system is decreasing during a TMDSC heating scan, but the weight loss of samples due to water evaporation during heating can be estimated by running the same experiment using TGA. Thus, the TGA profile, *wt%(T)*, can be used to calibrate the temperature dependent sample mass in TMDSC, *M(T)*, by:

$$M(T) = M_{DSC} \times wt\%(T) \tag{2.19}$$

where M_{DSC} is the initial sample mass in the DSC, and *wt%(T)* is the percent residual weight at temperature *T* measured by TGA. Therefore, the total heat flow, *HF(T)*, and the reversing heat flow, *RHF(T)*, are normalized at each temperature by *M(T)* using:

$$HF(T) = HF_{DSC} \times M_{DSC} / M(T) = HF_{DSC} / wt\% \tag{2.20a}$$

$$RHF(T) = RHF_{DSC} \times M_{DSC} / M(T) = RHF_{DSC} / wt\% \tag{2.20b}$$

2.3 Fourier Transform Infrared Spectroscopy

Fourier transform infrared spectroscopy (FTIR) has emerged as a powerful tool for the investigation of polymer structures and the analysis of functional groups [19, 28]. It is also widely used to study the protein secondary structures [29-31]. The infrared light (IR) is an electromagnetic wave with longer wavelengths than those of visible light, and

its electric part of light, called electric vector, interacts with molecules [32]. IR can usually be divided into three different spectral regions [32] depending on their wavenumber: the near infrared (14000 – 4000 cm^{-1}), the mid infrared (4000 – 400 cm^{-1}) and the far infrared (400 – 10 cm^{-1}). The wavenumber, *v*, is defined as the reciprocal of the wavelength, λ, and it is directly proportional to energy, *E*, as follows

$$\nu = 1/\lambda \tag{2.21a}$$

$$E = hc/\lambda = hc\nu \tag{2.21b}$$

where *c* is the speed of light (3 x 10^8 m/s) and *h* is Planck's constant (6.63 x 10^{-34} Js).

The basic principle of FTIR is that at temperature above absolute zero, all atoms in molecules are in continuous vibration with respect to each other [19, 22]. When IR interacts with polymer or biopolymer functional groups, a portion of the incident IR is absorbed which excites the vibration of the chemical bonds inside the molecules from the ground state to an excited state. In a heteronuclear diatomic molecule, the dipole moments can be described as uneven distribution of electron density between the atoms, while in a homonuclear diatomic molecule, the dipole moments in the molecule is evenly distributed. In order for a molecule to be IR active, the electric dipole moment of the molecule must change as a result of the vibration that occurs when IR radiation is absorbed [33]. Therefore, for a heteronuclear diatomic molecule, the vibration of the molecule due to the IR absorption can be detected by FTIR. However, the homonuclear diatomic molecule shows zero dipole moment no matter how long the bond length is, and thus the vibration cannot be detected by FTIR. The FTIR absorption intensity, *Abs*, increases with the change of the dipole moment in the molecules, and the larger the dipole moment change, the strong the absorption intensity will be. *Abs* is given by:

$$Abs \propto \left(\frac{d\mu}{dQ} \right)^2 \tag{2.22}$$

where μ is the dipole moment and Q is the vibrational coordinate.

The vibrational modes of chemical bonds of molecules include stretching and bending which are the major types of molecular vibrations. To be more detailed, the stretching includes symmetrical stretching and asymmetrical stretching, as shown in **Figure 2.5 (a)**, and the bending includes twisting bending, wagging bending, scissoring bending and rocking bending, as shown in **Figure 2.5 (b)**. The IR radiation energy absorbed by the molecules is generally converted into these types of motions. Because the IR absorption of individual functional group tends to be in the same wavenumber range regardless of the structure of the rest of the molecules, by correlating the IR absorption band wavenumbers with sample chemical structure, IR can be used to provide qualitative identification of polymer and biopolymer structures and functional groups [19, 32]. **Figure 2.6** shows infrared absorption bands of interest for polymers grouped by approximate wavenumber [19]. IR can also be used to perform the quantitative measurement of each structural component [23, 30, 32] as well, and the basis of all quantitative analysis in FTIR is Beer's law [19], which has the following form

$$A = \log_{10}(I_0/I) = \varepsilon lc \tag{2.23}$$

where I_0 is the incident IR intensity, I is the transmitted IR intensity, ε is the molar absorptivity, l is the cell path length and c is the molar concentration of the absorbing substance. In this thesis, FTIR is extensively used to characterize the change of the secondary structures of recombinant spider silk-like block copolymers and the details are discussed in Chapter IV, V and VI.

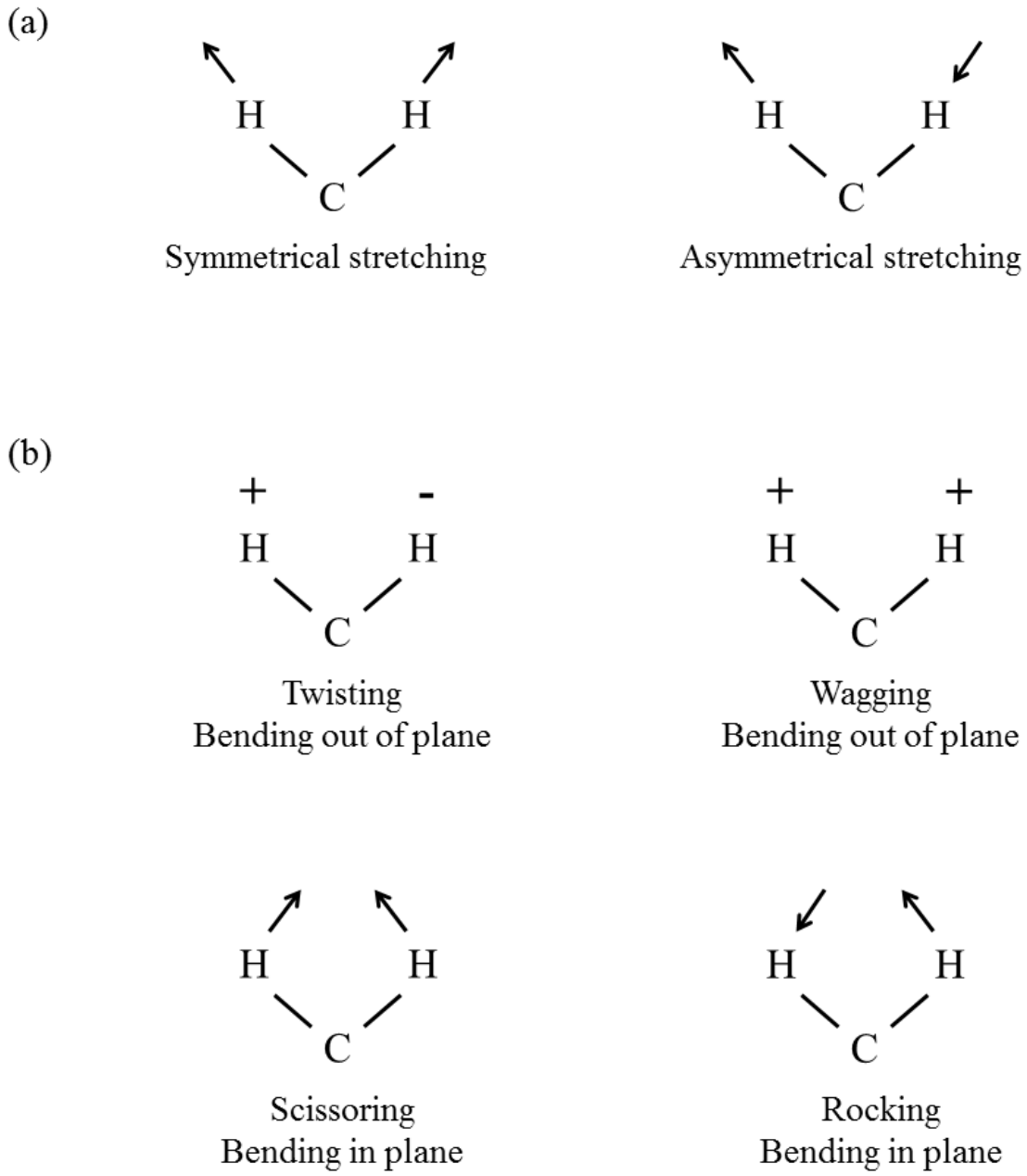

Figure 2.5 Vibrational modes of chemical bond illustrated by a CH_2 group. The arrows indicate the atom moving direction in plane. The "+" and "-" signs denote the atom moving in directions out of, or into, the plane respectively.

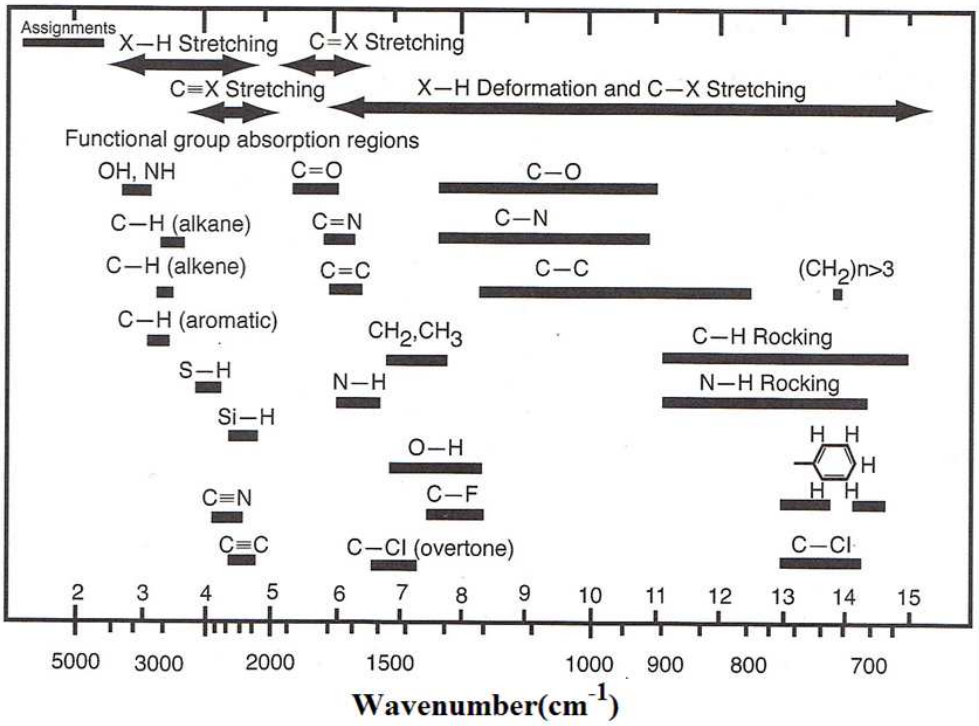

Figure 2.6 Infrared absorption bands of interest of polymer by approximte wavenumber taken from reference [19].

2.3.1 FTIR for Protein Secondary Structure Identification

An important problem in biomaterials research is the determination of protein secondary structure and structural changes under various conditions [34-38]. FTIR spectroscopy provides information about the secondary structure content of proteins [23, 30, 35, 39, 40], and because it is nondestructive and simple to perform, it has become a well-established method for the protein analysis. When the frequencies of incident IR and vibration frequencies of the chemical bonds in protein sample coincide, the IR light can be absorbed. The FTIR absorption spectra are usually used to determine the secondary structures in the protein.

The common secondary structures in proteins include helices, beta sheets and turns. The random coil is not a true secondary structure, but is the class of conformations that indicate an absence of regular secondary structure. The chemistry of amino acid side chains is critical to protein structure. Charged amino acid side chains can form ionic bonds, polar amino acids are capable of forming hydrogen bonds, and hydrophobic side chains interact with each other via weak van der Waals interactions. The majority of bonds formed by the amino acid side chains are non-covalent. In fact, cysteine is the only amino acid capable of forming covalent bonds, the disulfide bond. Because of side chain interactions, the sequence and location of amino acids in a particular protein guide where the bends and folds occur in that protein.

α helix

The α helix, as shown in **Figure 2.7 (a)**, is the most common type of helical secondary structure of proteins, and it was proposed by Linus Pauling and Robert Corey in the 1950s [41]. In theory, an α helix can be either right handed or left handed, however, the α helices found in proteins are almost always right handed [42, 43]. The α helix repeats after 18 amino acid residues, which amounts to 5 complete turns, with a residue per turn number of 3.6. Each carbonyl oxygen in the α helix is hydrogen-bonded to the amido proton on the fourth residue toward the C-terminus and forms a loop of 13 atoms (11 backbone atoms, one carbonyl oxygen and one amido hydrogen). Thus, an α helix is also called an 3.6_{13} helix. The hydrogen bonds, as shown in Figure 2.7 by the red dotted lines, are near parallel to the helix axis and stabilize the structure. The amino acid side chains in an α helix are pointing outward from the helix axis, as shown in Figure 2.7 by the R group.

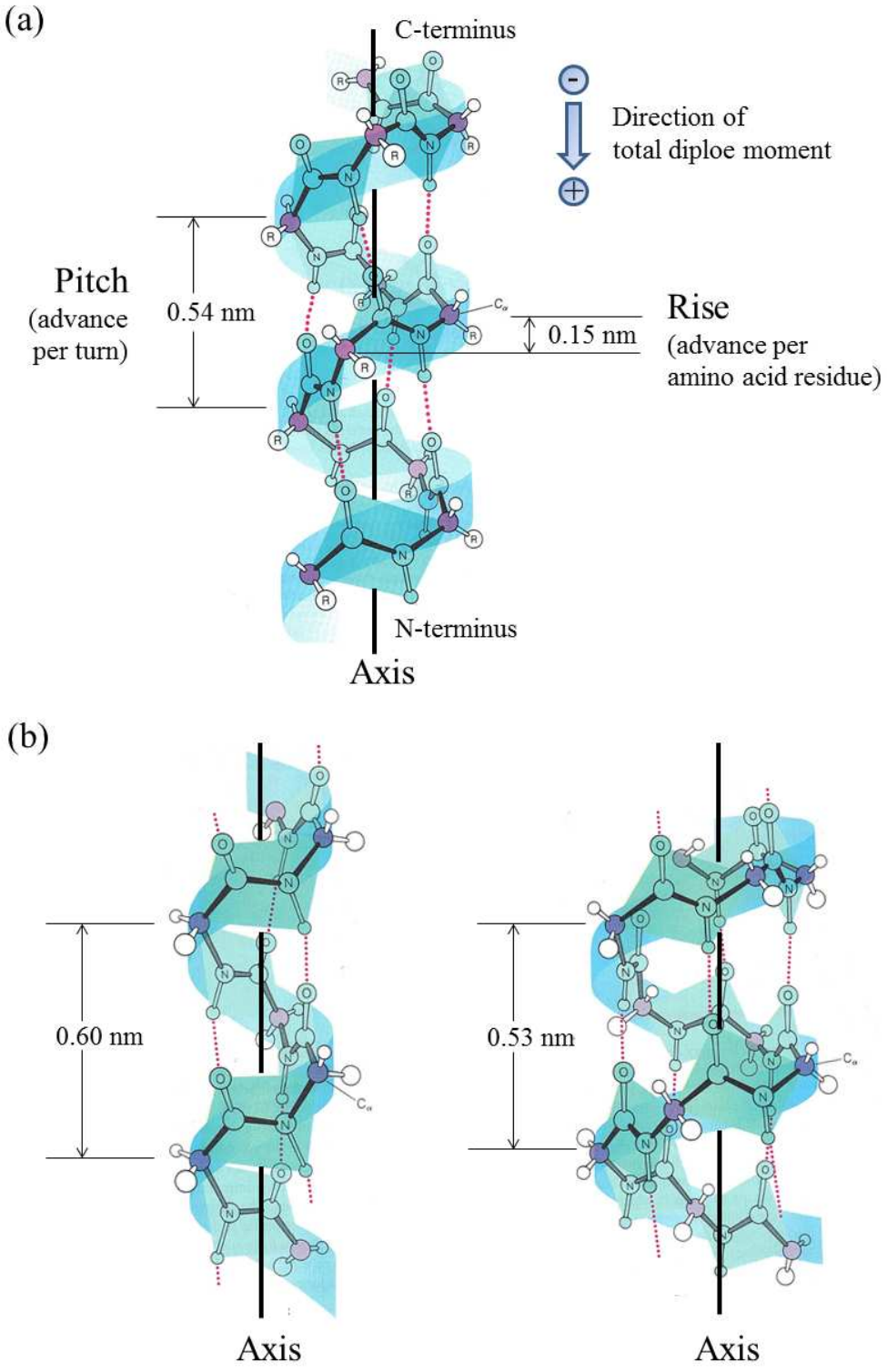

Figure 2.7 Ball-and-stick model of (a) α (3.6_{13}) helix, (b) 3_{10} helix (left) and π (4.4_{16}) helix (right) based on reference [42]. The hydrogen bonds are shown by red dotted lines.

The pitch of an α helix, which is defined as the distance the helix rises per turn, is 0.54 nm with a rise of 0.15 nm/residue [42, 43]. The length of an α helix of proteins can range from 4 residues to more than 40 residues, but the average length is about 12 residues corresponding to about 3 turns with a length of 1.8 nm [42, 43]. The dipole moment in an α helix is due to individual dipoles of the C=O groups involved in hydrogen bonding and the total dipole moment of the entire helix is a dipole with a positive N-terminus and negative C-terminus. The α helix content in a protein is about 26% on average [42, 43]. Some proteins also contain a few short regions of 3_{10} helices, as shown in **Figure 2.7 (b)** on the left. The π (4.4_{16}) helix, as shown in Figure 2.7 (b) on the right, is sterically possible but has not been observed in proteins yet [42, 43].

β sheet

The β sheet, as shown in **Figure 2.8 (a)**, is another common type of secondary structure of proteins, and it was also proposed by Linus Pauling and Robert Corey in the 1950s [44]. The structural unit of β sheets is called β strand, and a β sheet is composed of multiple (usually from 2 to 15) β strands which are arranged side-by-side. The β strand is an almost fully extended polypeptide chain with a length of 0.32 to 0.34 nm per residue [43], in contrast to the compact coil of α helix (0.15 nm per residue), and a β strand is usually from 5 to 10 residues long [45]. Isolated β strands rarely exist in the proteins because the structure by itself is not as stable as other secondary structures. However, when β strands stack together and form β sheets, the β sheet structures are stabilized by hydrogen bonds.

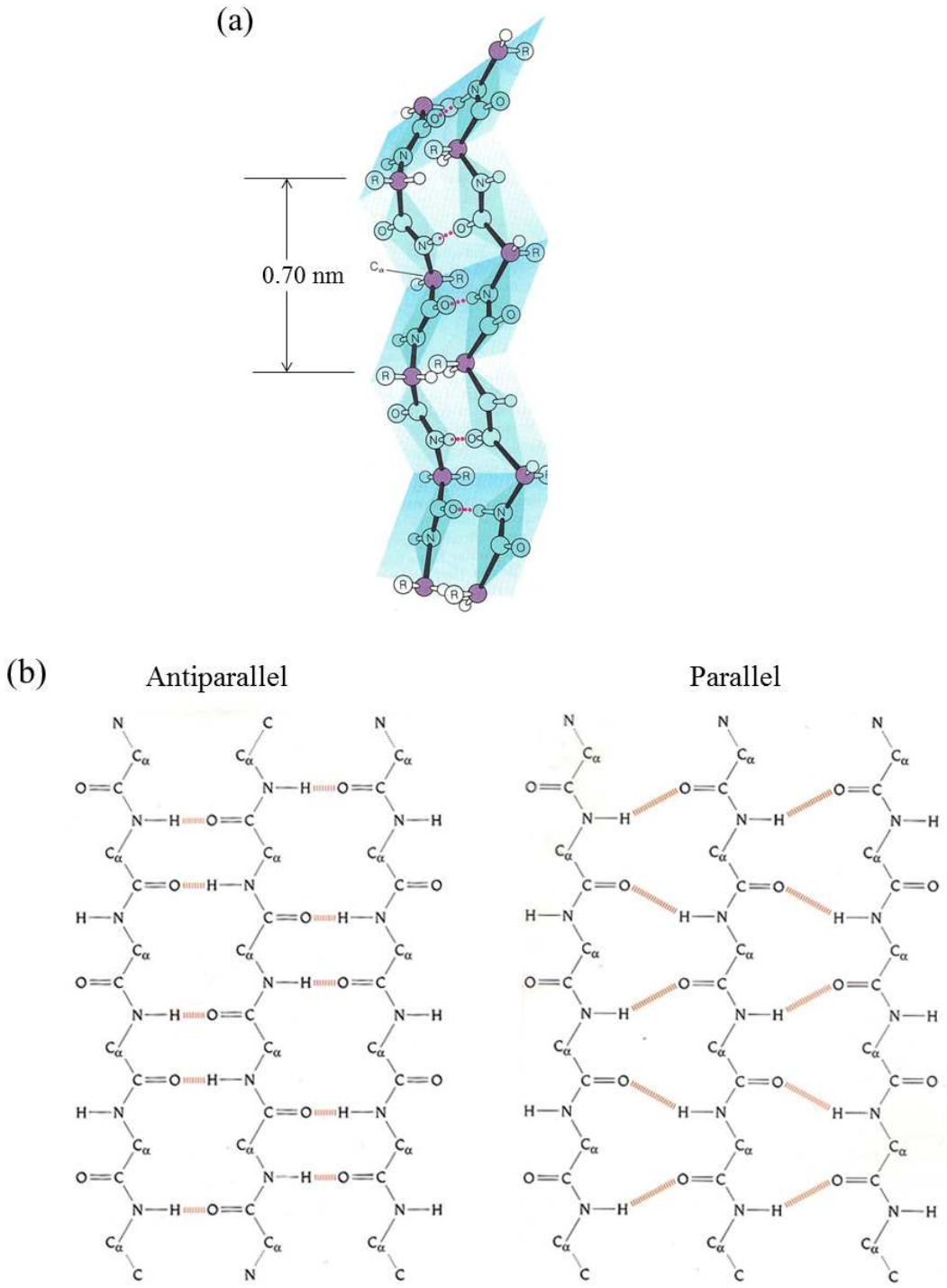

Figure 2.8 (a) Ball-and-stick model of β sheet, and (b) chemical structures of antiparallel β sheet (left) and parallel β sheet (right) based on reference [42, 45]. The hydrogen bonds are shown by red dotted lines.

There are two types of β sheets: the antiparallel β sheet, as shown in **Figure 2.8 (b)** on the left, in which neighboring hydrogen bonded β strands running in the opposite N- to C-terminus directions, and the parallel β sheet, as shown in **Figure 2.8 (b)** on the right, in which neighboring hydrogen bonded β strands running in the same N- to C-terminus directions. Hydrogen bonds in antiparallel β sheet are nearly perpendicular to the extended polypeptide chains, while hydrogen bonds in parallel β sheet are not. Thus, parallel β sheets are less stable than antiparallel β sheets because of the distortion of the hydrogen bond alignment [42, 43]. The dipole moment in a β sheet is also due to individual dipoles of the C=O groups involved in hydrogen bonding, and parallel β sheet have a significant dipole moment, in contrast to antiparallel β sheets with a direction from C-terminal (partially negative) to N-terminal (partially positive) [46]. The β sheet content in a protein is defined as the crystallinity of the protein, found from Fourier self deconvolution of the FTIR spectrum in the Amide I region. It can range from 0% to more than 60%, such as in cocoon silk fibroin or recombinant proteins [23].

β turns

The β turns are usually involved in connecting regular secondary structures such as α helices or β sheets, since they cause direction changes in the polypeptide backbone. A β turn consists of 4 amino acid residues, which arranges in one of the two ways: Type I β turn, as shown in **Figure 2.9 (a)**, or Type II β turn, as shown in **Figure 2.9 (b)**. The β turns are also stabilized by hydrogen bonds.

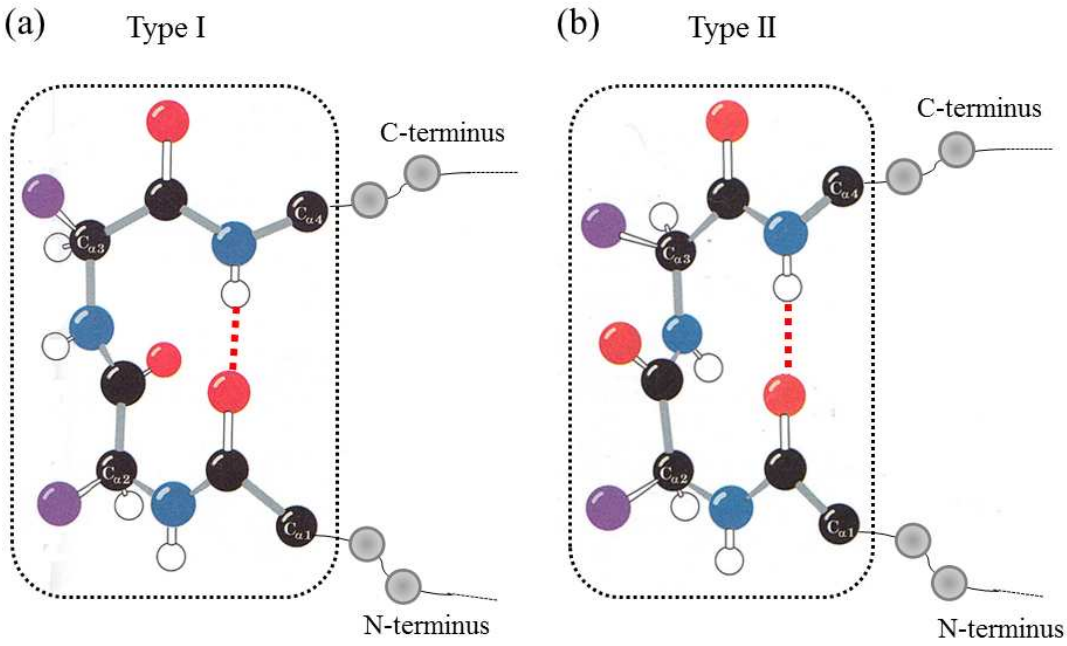

Figure 2.9 Ball-and-stick model of (a) type I β turn, and (b) type II β turn based on reference [47]. The hydrogen bonds are shown by red dotted lines.

The combination of a few secondary structures with specific geometric arrangement is often called a motif or supersecondary structure. Some of these motifs can be associated with particular protein functions [45]. For example, different motifs are responsible to form various secondary structures corresponding to silk's mechanical properties; for example, the GA/A_n motif provides the high tensile strength and stiffness [48-50] to silks.

When characterizing the secondary structures of proteins and polypeptides by FTIR, there are several characteristic bands which can be found in the infrared spectra including Amide I, Amide II, Amide III, Amide A and Amide B vibrations. Amide I vibration is centered near 1650 cm^{-1} and usually ranges from 1690 – 1600 cm^{-1}. It arises

mainly from the C=O stretching vibration with minor contributions from the out-of-phase C-N stretching vibration, the CCN deformation and the N-H in-plane bending [30, 40]. The Amide I vibration is hardly affected by the side-chains, and mainly depends on the secondary structure of the backbone [30, 40]. Therefore the Amide I vibration is most commonly used region for secondary-structure analysis. The Amide II vibration is centered near 1550 cm^{-1} and usually ranges from 1575 – 1480 cm^{-1}. It is the combination of the out-of-phase N-H in-plane bending and the C-N stretching vibration with smaller contributions from the C=O in-plane bending and the C-C and N-C stretching [30, 40]. The Amide II vibration overlaps some of the side-chain vibrations, such as the 1515 cm^{-1} peak of the tyrosine side chain which arises from C-C stretching and C-H bending mode in the 6-carbon aromatic ring [38]. Therefore the Amide II vibration is less straightforward than Amide I vibration for the secondary structure analysis. Amide III ranges from 1400 – 1200 cm^{-1}. In protein or polypeptide, the composition of this mode involves amino acid side chain vibrations as well as vibrations from backbones [30, 40]. Due to these complications, Amide III vibration is less suitable for the secondary structure analysis. Amide A and B are centered at 3300 and 3170 cm^{-1}. They arise from the NH stretching vibrations and are thus insensitive to the conformation of the polypeptide backbone, but strongly depend on the strength of the hydrogen bond [30, 40]. Therefore, Amide A and B are not suitable for secondary structure analysis either, but could be used to study the change of the hydrogen bonding during the environmental changes of protein or polypeptide samples. General FTIR absorption band assignments of recombinant spider silks of Amide I and II are summarized in **Table 2.1**.

Table 2.1 General FTIR Absorption Band Assignments for Recombinant Spider Silk-like Block Copolymer

Amide I [22, 30, 40]		**Amide II** [35, 39]	
Wavenumber Range (cm^{-1})	**Peak Assignment**	**Wavenumber Range (cm^{-1})**	**Peak Assignment**
1595-1605	(Try) side chains		
1605-1615	(Try) side chains, aggregated strands	1498-1518	(Tyr) side chains
1618-1629	Beta sheet (strong)	1520-1530	Beta sheet
1630-1642	Random coils, extended chain structures	1520-1545	Random coils
1643-1657	Random coils	1526-1527	(Lys) side chains
1658-1667	Alpha helices	1545-1551	Alpha helices
1668-1678	Turns	1556-1560	(Glu) side chains
1679-1685	Turns	1574-1579	(Asp) side chains
1686-1696	Turns	1575, 1594	(His) side chains
1697-1703	High-frequency antiparallel beta sheets (weak)		

2.3.2 Fourier Self Deconvolution

Fourier self deconvolution (FSD) is a mathematical approach for reducing bandwidths, so that overlapped bands can be resolved from one another and hence improving the information content [51, 52]. To analyze protein secondary structures and determine the crystallinity with FSD, FTIR absorbance spectrum in the Amide I region are usually deconvoluted, because the Amide I region mainly depends on the secondary structure of the backbone and it is hardly affected by the side-chains. The general principle of FSD is to consider the original FTIR spectrum, *E(ν)*, as the convolution of a Dirac delta function that has area *A* located with the center of the band at ν_0, following the method of Lorenz-Fonfria [53-55]. Two spreading functions, the band shape function *L(ν)*, which broaden the band homogeneously and inhomogenously, and the instrumental broadening function *R(ν)*, are used to describe the delta function [23] as

$$E(\nu) = A\delta(\nu - \nu_0) \otimes L(\nu) \otimes R(\nu) \tag{2.24}$$

where $\otimes$ is the convolution operator. Generally, *R(ν)* is insignificant compared to *L(ν)*.

The original FTIR spectrum can also be expressed as the Fourier transformation, $\Im$, of interferogram *I(x)*, as

$$E(\nu) = \Im\{I(x)\} \tag{2.25}$$

Thus, *I(x)* can also be expressed as

$$\begin{aligned} I(x) &= \Im^{-1}\{E(\nu)\} = \Im^{-1}\{A\delta(\nu - \nu_0) \otimes L(\nu) \otimes R(\nu)\} \\ &= \Im^{-1}\{A\delta(\nu - \nu_0)\} \cdot \Im^{-1}\{L(\nu)\} \cdot \Im^{-1}\{R(\nu)\} \end{aligned} \tag{2.26}$$

Resolution enhanced deconvoluted spectrum, *E'(ν)*, is obtain by dividing *I(x)* by $\Im^{-1}\{L(\nu)\}$, which is typically a Lorentzian function [23], and Fourier transforming the

result. In this thesis, the FSD was performed by commercial FTIR analysis software Opus 5.0. An example of the FSD of the FTIR absorbance spectrum is shown in **Figure 2.10 (a)**. After FSD, the crystallinity, ϕ_{c_FTIR}, of the sample can be determined by fitting *E'(v)* with a series of Gaussian functions, as shown in **Figure 2.10 (b)**, and ϕ_{c_FTIR} is the ratio of the area of the beta sheet peak, Q_B, over the total area under *E'(v)*, *Q*.

$$\phi_{c\_FTIR} = Q_B / Q \tag{2.27}$$

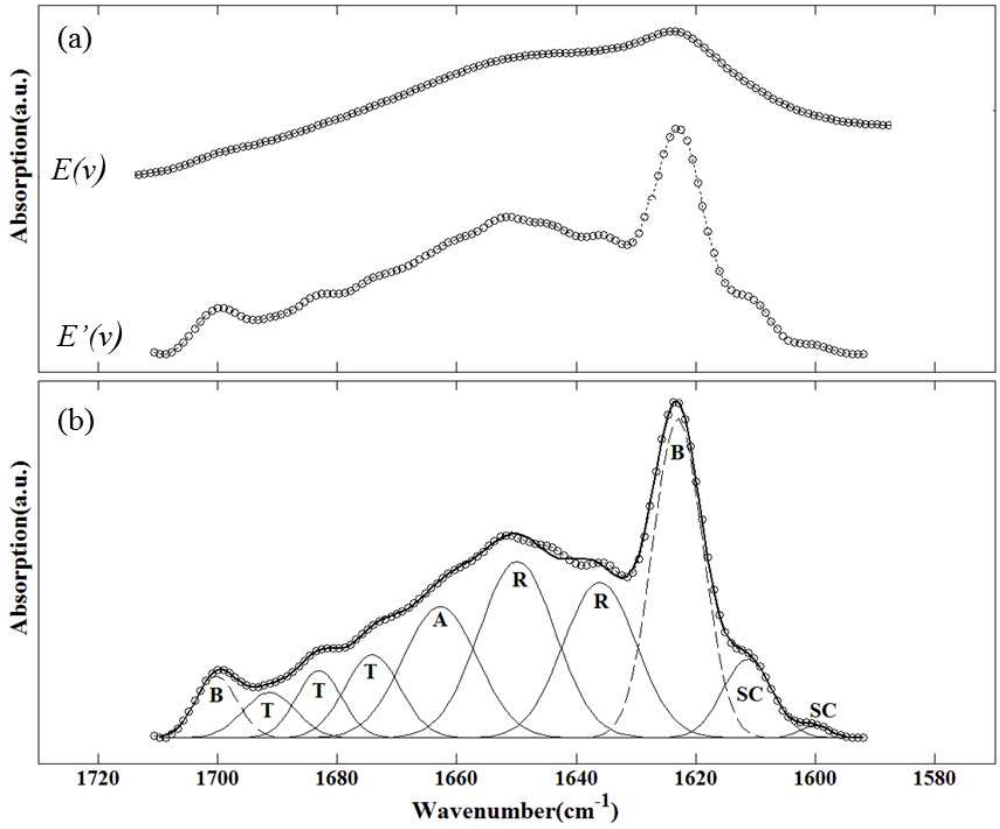

Figure 2.10 (a) FSD of Amide I spectra for spider silk-like block copolymer, HBA_3. *E(v)* is the raw data; *E'(v)* is spectrum after FSD. (b) The curve fitting of the deconvoluted spectrum, showing bands related to random coils (R), β sheets (B), α helices (A), turns (T), and side chains (SC). Symbols represent *E'(v)* data, and the solid heavy line is the summation of the individual deconvoluted peaks.

2.4 X-ray Diffraction

X-ray diffraction is one of the primary techniques used to determine the macromolecular structure, because the wavelengths generally used for X-ray crystallography are in the range from 0.05 to 0.25 nm [56], which is comparable to the C-C covalent bond (about 0.15 nm) and interatomic distance of the polymer crystals. For biological materials, the mean distance of amino acid residues in the crystalline β sheet region is about 0.33 nm [57], thus the protein tertiary structure is generally determined by X-ray diffraction. In the late 1950s, the structures of hemoglobin and myoglobin at an atomic resolution were solved by Max Perutz [58] and John Kendrew [59] using X-ray diffraction which marked the beginning of protein crystallography and they were awarded the Nobel Prize for Chemistry in 1962. Since that success, over 39,000 X-ray crystal structures of proteins, nucleic acids, and other biological molecules have been determined. The atomic coordinates of most of these structures are stored in the Protein Data Bank (http://www.rcsb.org) now, and this allows the tertiary structures of a variety of proteins to be analyzed and compared.

To explain X-ray diffraction, we use the properties of light as an electromagnetic wave with a wavelength, λ, and energy, E, that is related by

$$E = \frac{hc}{\lambda} \tag{2.28}$$

where h is Planck's constant (h = 6.63x10^{-34} Js) and c is the speed of electromagnetic wave propagation in a vacuum (c = 3x10^{8} m/s). One of the fundamental properties of electromagnetic waves is that two waves can interfere with each other. If we consider two identical waves with intensity $I_1=I_2=I_0$ and wavelength λ interfering with each other, the total intensity can be expressed as [60]

$$I = I_1 + I_2 + 2\sqrt{I_1 I_2}\cos\varphi = 2I_0(1+\cos\varphi) \tag{2.29}$$

where φ is the phase difference. In two extreme cases, when $\varphi = 2n\pi$ *(*for *n* an integer*)*, the two waves are in phase, and they will constructively interfere; while if $\varphi = (2n+1)\pi$ the two waves are out of phase, and they will destructively interfere (zero amplitude).

The basic principle of X-ray diffraction follows Bragg's Law:

$$n\lambda = 2d_{hkl}\sin\theta \tag{2.30}$$

where n is an integer indicating the order of the reflection, λ is the wavelength of the X-ray, d_{hkl} is the distance between the planes in the atomic lattice (h, k, and l are Miller indices as illustrated by **Figure 2.11**), and θ is the scattering angle. Bragg's Law describes the condition for constructive interference from successive crystallographic planes and the representation of Bragg's Law is shown in **Figure 2.12**. In one variation of an X-ray diffraction measurement, the sample with a microscopic three dimensional structure is gradually rotated which leads to a series of different scattering angles, θ, and the diffraction pattern in reciprocal space is produced following the mathematical method of Fourier transforms [56]. In reciprocal space, equation 2.30 is usually rearranged into

$$s = \frac{q}{2\pi} = \frac{1}{d_{hkl}} = \frac{2\sin\theta}{\lambda} \tag{2.31}$$

where s (or q) is called the scattering vector in reciprocal space. The X-ray scattering intensity, I_s, by one single electron can be obtained by Thomson's formula [56]:

$$I_s(2\theta) = \left(\frac{e^2}{mc^2}\right)^2 \frac{I_o}{r^2}\frac{1+\cos^2 2\theta}{2} \tag{2.32}$$

where I_0 is the incident beam intensity; r is the sample-to-detector distance; e is the charge on the electron; m is the mass of the electron; and c is the speed of light.

(a)

Cubic

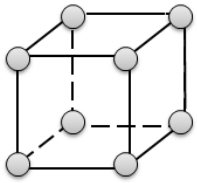

$$\frac{1}{{d_{hkl}}^2} = \frac{h^2 + k^2 + l^2}{a^2}$$

Orthorhombic

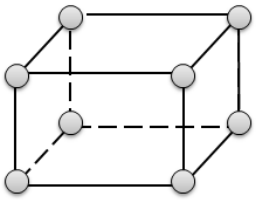

$$\frac{1}{{d_{hkl}}^2} = \frac{h^2}{a^2} + \frac{k^2}{b^2} + \frac{l^2}{c^2}$$

Hexagonal

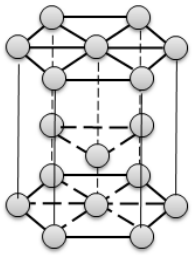

$$\frac{1}{{d_{hkl}}^2} = \frac{4}{3}\left(\frac{h^2 + hk + k^2}{a^2}\right) + \frac{l^2}{c^2}$$

(b)

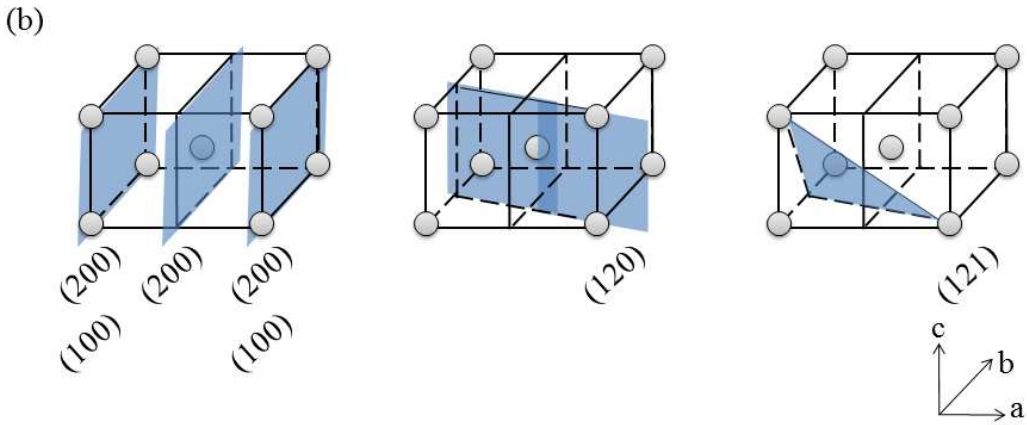

Figure 2.11 (a) Atom positions in a cubic, orthorhombic and hexagonal unit cell, and their calculated d-spacing, d_{hkl}, based on the lattice information. *a*, *b*, *c* are the lattice constants [61], and *h*, *k*, *l* are the miller indices of the unit cell in *x*, *y* and *z* directions, respectively. (b) Miller indices of some important crystal planes in body-centered orthorhombic unit cells.

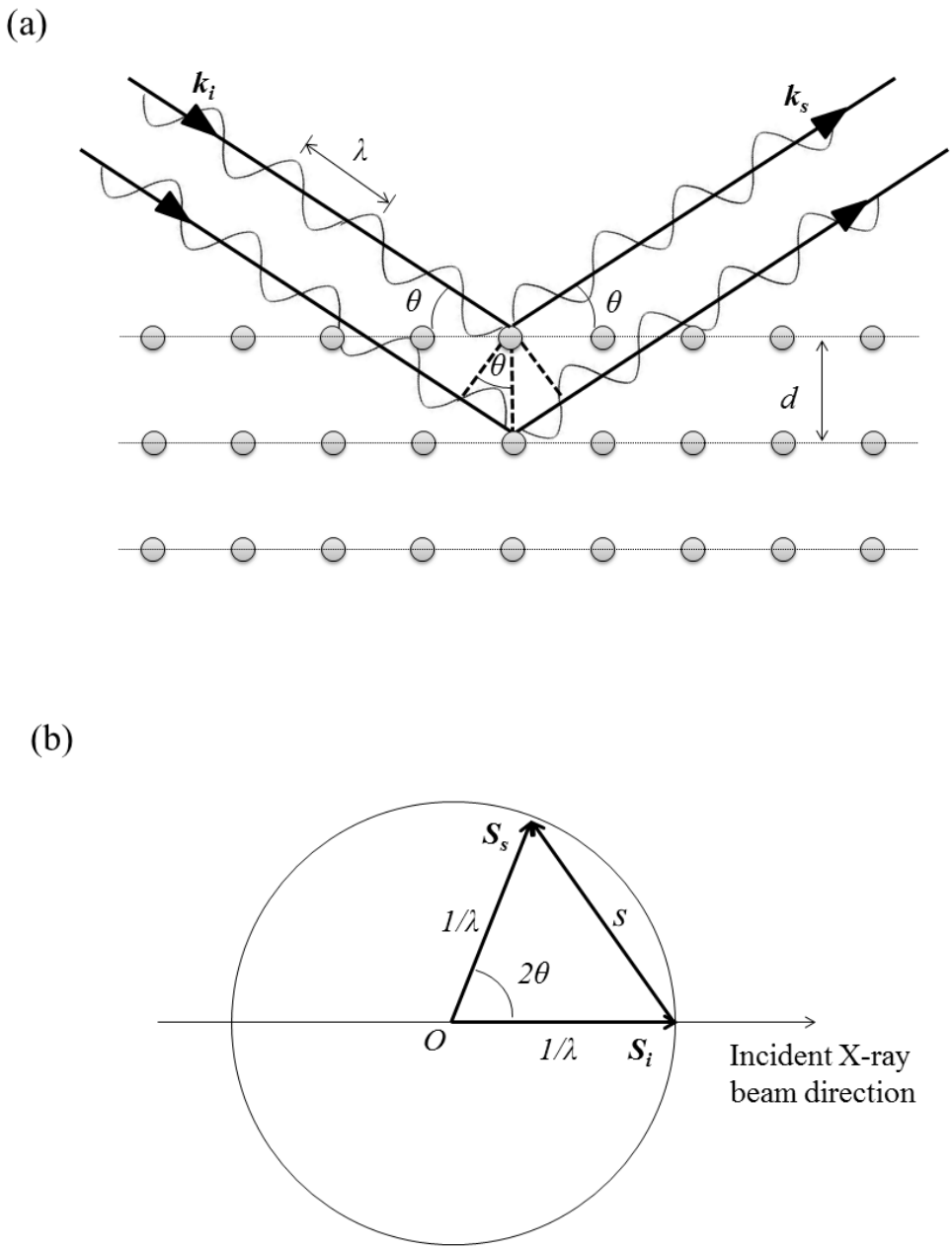

Figure 2.12 (a) Bragg's Law in real space. Two X-ray beam plane waves with identical incident angle, θ, wavelength, λ, and phase, approach parallel planes of crystalline solid and are scattered off two different atoms within it. (b) Bragg's Law in reciprocal space by the Ewald sphere construction. S_i and S_s are the wave vectors of the incident and diffracted beams, respectively; and S is the scattering vector.

There are two types of X-ray diffraction methods used to study polymers and biopolymers: wide angle X-ray diffraction (WAXD) and small angle X-ray scattering (SAXS). WAXD has a scattering angle 2θ usually greater than 3º dependent on the beam stop size, and it provides information of crystal size, crystal structure, crystallinity of the sample and degree of orientation within the sample. For example, WAXD was used to determine the crystal structures and crystallinities of proteins [22, 25, 62], and it was also used to observe the orientation induced by electrospinning or zone-drawing of polymer nanofibers [63] or drawn polymer strips [28]. SAXS has a scattering angle 2θ usually smaller than 3º, and it useful in detecting larger periodicities in a structure. For example, SAXS was used to determine the microphase separation of block copolymers [64, 65].

In this thesis, WAXD is extensively used to characterize the spider silk-like block copolymers. Two phases (amorphous phase and crystalline phase) are considered to contribute to the protein's WAXD diffraction intensities [22, 23]: the β-sheet crystalline region in proteins gives rise to the diffraction peaks, while the amorphous matrix causes an isotropic and broad scattering halo. To determine the crystalline structure and the lattice parameters for polymers and biopolymers, the diffraction peak position in a diffraction intensity vs. scattering angle 2θ plot is usually evaluated by Bragg's Law following equation 2.30 at a given X-ray wavelength λ. Thus, the d-spacing and lattice constants can be calculated. The Miller indices, scattering peak positions, and correspondent d-spacing for the pseudo orthorhombic unit cell of the β sheet crystals of recombinant spider silk-like block copolymer measured by WAXD (λ= 0.154 nm) [22, 66] are summarized in **Table 2.2**.

Table 2.2 Miller Indices and Correspondent *2θ*, d-spacing and q-vector for the Scattering Peaks of Recombinant Spider Silk-like Block Copolymer [22, 66].

Miller index (*hkl*)	**Scattering Angle, *2θ* (º) (*λ*= 0.154 nm)**	**d-spacing (nm)**	**q-vector (nm^{-1})**
200	17.09	0.520	12.08
120	20.54	0.433	14.51
121	24.20	0.371	16.96

WAXD intensity can also be used to calculate the crystallinity index of semi-crystalline samples [22, 28, 67]. Prior to data analysis to find the crystallinity index, the raw intensity data must undergo a few corrections. First, the background scattering profile due to the air scattering and the effect of the sample holder must be subtracted from the sample scattering data. The scattering angle and the sample-to-detector distance should be calibrated by standards, such as S_i and Al_2O_3. Then, the scattering intensity needs to be further corrected by a Lorentz weighting factor, $4\pi s^2$, which leads to $I_{corr} \propto Iq^2$. After raw intensity data corrections, the crystallinity index of the sample can be determined by fitting the Lorentz-corrected scattered intensity Iq^2 vs. q with a sum of Gaussian functions and a quadratic baseline as

$$I(q)q^2 = \sum \left\{ A_i \exp\left(\frac{(q - q_{0i})^2}{2\sigma_i^2} \right) \right\} + Bq + Cq^2 \qquad (2.33)$$

where A_i is the amplitude, q_{0i} is the mean q-vector, σ_i is the standard deviation of the Gaussian functions, and B and C are the q and q^2 coefficients of the quadratic baseline,

respectively. The crystallinity index, ϕ_{C_Xray}, can be calculated using area of crystal peaks, Q_c, divided by total area, Q, as

$$\phi_{c\_Xray} = \frac{Q_c}{Q} = \frac{\int I_c q^2 dq}{\int I_{corr} q^2 dq} \tag{2.34}$$

An example of this procedure is illustrated by the WAXD profile of recombinant spider silk-like block copolymer, HBA_3, shown in **Figure 13**.

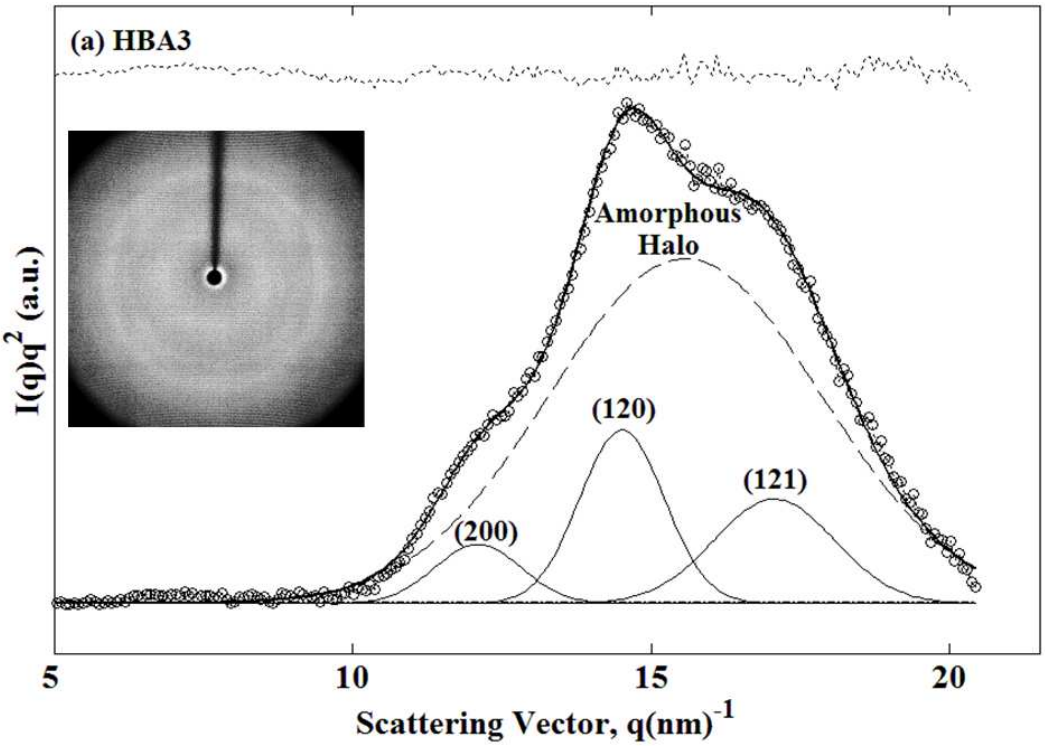

Figure 2.13 Deconvolution of the Lorentz-corrected WAXD intensity, $I(q)q^2$ vs. q, using Gaussian wave functions for spider silk like block copolymers HBA_3 (Open circles - measured data; heavy curve - summation of Gaussian peaks; thin solid curves - individual crystalline Gaussian peaks; dashed curves - amorphous Gaussian peaks; dotted lines at the top - the residual between the fitted curve and measured curve) shown on the same intensity scale. The insert is the 2-D X-ray diffraction pattern.

2.5 Other Experimental Approaches

The mechanical tests used in nanocomposite and polymer blend side projects are briefly introduce in this session.

2.5.1 Tensile Testing

Tensile testing is a fundamental material science experimental technique to test the mechanical properties of a sample, in which a sample is subjected to uniaxial tension until failure. The sample specimens used for tensile testing are of a standardized shape, the "dog bone" shape, with a fixed width, *d*, as shown in **Figure 2.14**. The basic terminologies used in tensile test, such as stress and strain, are also described in Figure 2.14. During the test, one end of the sample is fixed in a static grip while the other end of the specimen is pulled at a constant velocity, thus the specimen is deformed by applying a uniaxial force. The mechanical properties that are directly measured via a tensile test including the ultimate tensile strength (UTS), which is the maximum load the specimen sustains during the test when there is no strain hardening, and the maximum elongation of the sample. The Young's modulus *E*, which describes the stiffness of the material, can be calculated from a stress-strain curve in the elastic region as shown in **Figure 2.15** by the following equation:

$$E = \frac{\sigma}{\varepsilon} \tag{2.35}$$

where σ is the uniaxial stress and ε is the uniaxial strain. The higher Young's modulus indicates a stiffer material, while the lower Young's modulus indicates a more elastic material.

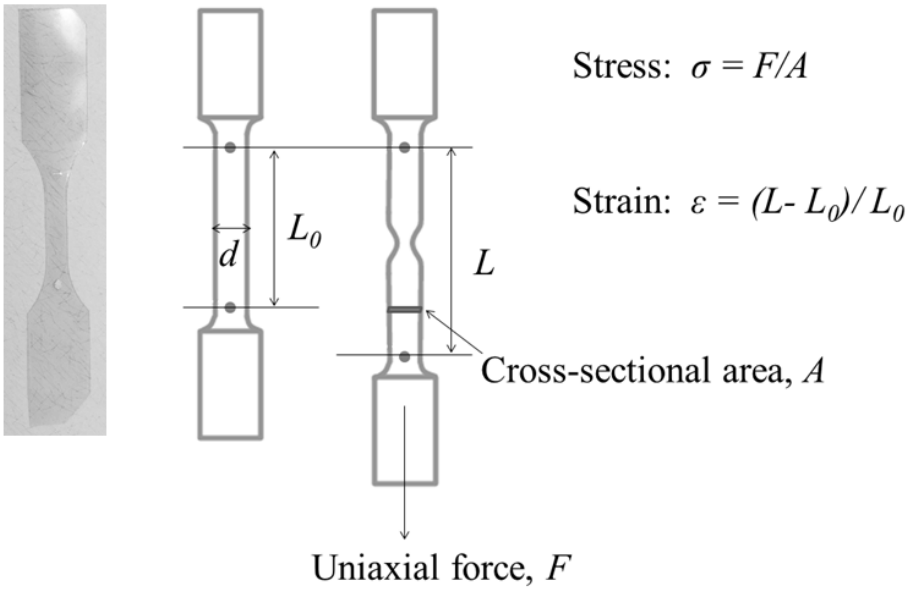

Figure 2.14 The "dog bone" shape sample specimen commonly used for tensile testing, which was also used in the nanocomposite side project.

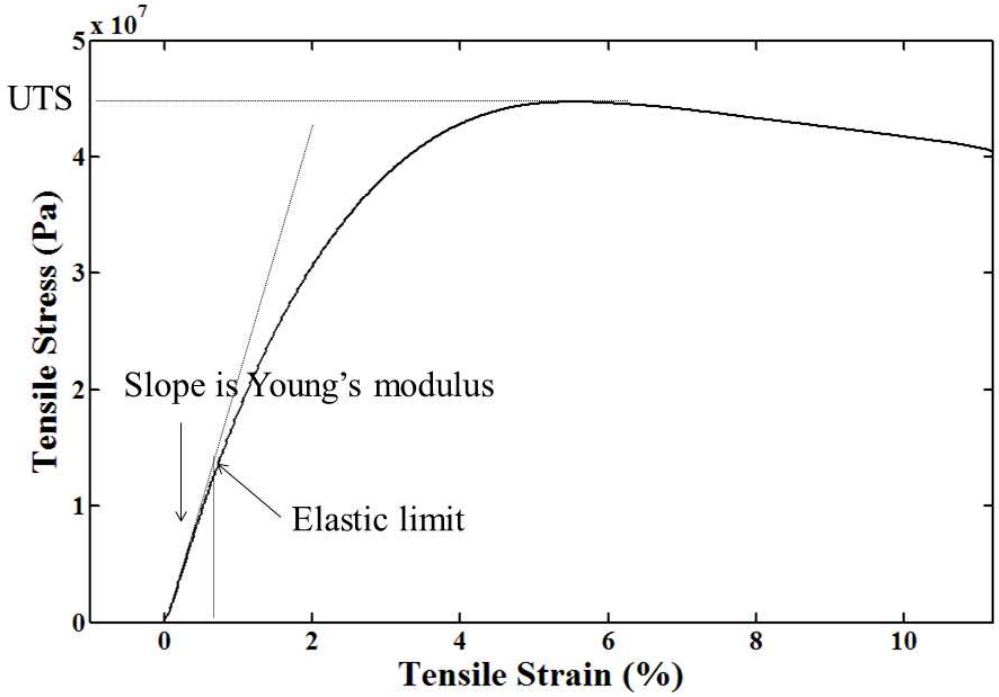

Figure 2.15 A typical stress-strain curve from the tensile test.

2.5.2 Dynamic Mechanical Analysis

Dynamic Mechanical Analysis (DMA) is a technique used to measure the mechanical properties of a wide range of materials, especially the viscoelastic properties of polymers, such as the frequency and temperature dependent complex modulus, $E^* = E' + iE''$. During a DMA measurement, a small sinusoidal stress is applied to a sample of known geometry, and a sinusoidal strain (deformation) is measured. As shown in **Figure 2.16**, the stress, σ, and the strain, ε, from DMA measurements can be expressed as

$$\sigma(t) = \sigma_0 \cos(2\pi ft) \tag{2.36a}$$

$$\begin{aligned} \varepsilon(t) &= \varepsilon_1 \cos(2\pi ft) + \varepsilon_2 \sin(2\pi ft) \\ &= \varepsilon_0 \cos(2\pi ft + \delta) \end{aligned} \tag{2.36b}$$

where σ_0 is the stress amplitude, ε_1 is the strain amplitude of the elastic part, in which strain responds to the stress instantaneously, ε_2 is the strain amplitude of the viscous part, in which strain responds to the stress shifted with respect to time, ε_0 is the strain amplitude calculated by $\varepsilon_0^2 = \varepsilon_1^2 + \varepsilon_2^2$, f is the frequency and δ is the phase difference between the two waves. Many polymers exhibit viscoelasticity properties, which contains both viscous and elastic characteristics. The storage modulus is the elastic component, and it is related to the sample's stiffness. The loss modulus is the viscous component, and it is related to the sample's ability to dissipate mechanical energy through molecular motion. The storage modulus, E', and loss modulus, E'', can be calculated as

$$E' = \frac{\sigma_0}{\varepsilon_0} \cos\delta \tag{2.37a}$$

$$E'' = \frac{\sigma_0}{\varepsilon_0} \sin\delta \tag{2.37b}$$

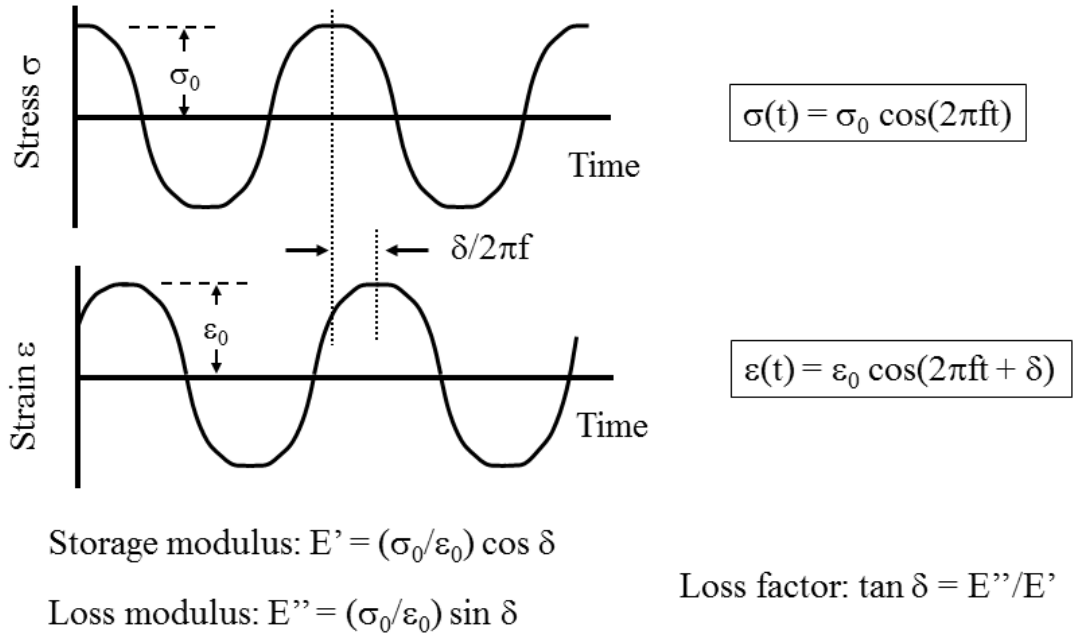

Figure 2.16 The storage modulus, *E'*, and loss modulus, *E''*, calculated by DMA at test frequency, *f*.

The tangent of the phase difference, *tan δ = E''/E'*, is a common parameter that provides information on the relationship between the elastic and inelastic components. For elastic materials, *tan δ* is negligible. For viscoelastic materials, the stress and strain are related as a function of time with a phase difference, *δ*, between the two, and the *tan δ* is high when samples exhibit a more viscous characteristics. As the material goes through its glass transition, the sample absorbs energy and its storage modulus reduces. At the same time, the *tan δ* goes through a peak, because the sample becomes less stiff and molecular reorganization of the relaxation induces less elastic behavior [68]. The major peak of *tan δ* in amorphous polymer usually relates to the glass transition, called

the alpha relaxation, in which the polymer chains transform from a glassy state to a rubbery state during heating [19, 28]. In semicrystalline PVDF, *tan δ* is related to the segmental motions of PVDF polymer chains in the amorphous regions [69, 70], and it is usually used to determine the glass transition temperature of a polymer during frequency/temperature sweep test [28]. There are also other relaxations relating to other movements, such as side chain motion [71]. An example of using *tan δ* by a frequency/temperature sweep test using DMA is shown in **Figure 2.17**.

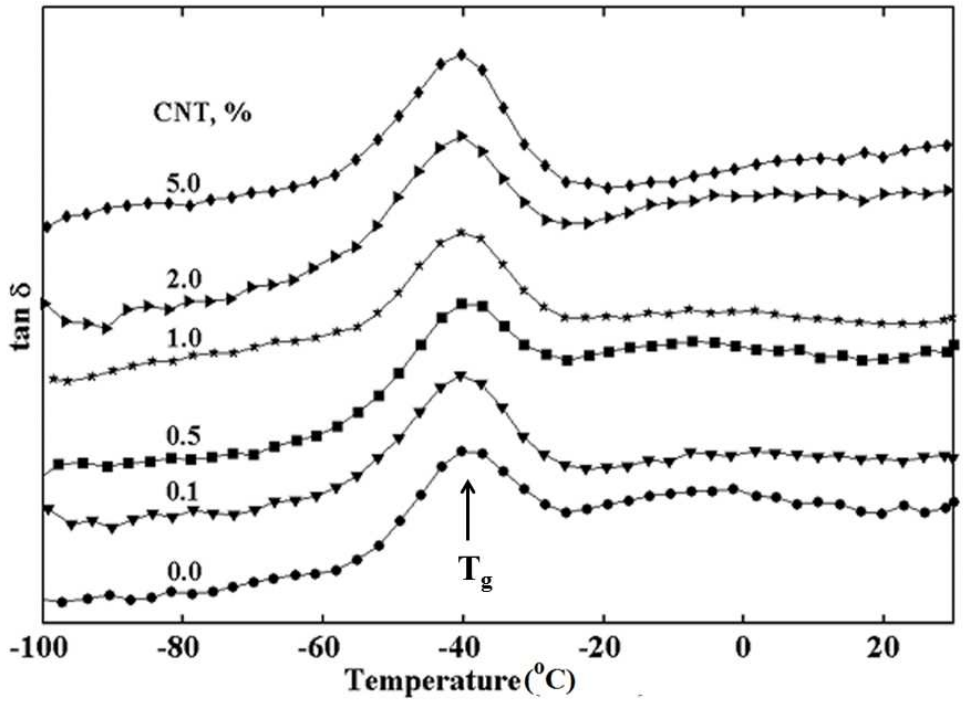

Figure 2.17 Loss factor, *tan δ*, versus temperature for nanocomposites of PVDF with MWCNT indicating the glass transition temperature of the samples at frequency of 1.0 Hz.

DMA is used to study primarily the linear viscoelastic range and therefore it is more sensitive to structure, while tensile testing is used primarily outside the linear viscoelastic range.

2.6 References

1. Schick C. *Analytical and Bioanalytical Chemistry* 2009; 395(6): 1589-1611.
2. Sturtevant JM. *Annual Review of Physical Chemistry* 1987; 38: 463-488.
3. Sanchez-Ruiz JM. *Sub-cellular biochemistry* 1995; 24: 133-176.
4. Wunderlich B. *Thermal analysis of polymeric materials*. Berlin: Springer, 2005: 304-404.
5. Reading M, Elliott D, and Hill VL. *Journal of Thermal Analysis* 1993; 40(3): 945-955.
6. Gill PS, Sauerbrunn SR, and Reading M. *Journal of Thermal Analysis* 1993; 40(3): 931-939.
7. Reading M, Luget A, and Wilson R. *Thermochimica Acta* 1994; 238: 295-307.
8. Hensel A, Dobbertin J, Schawe JEK, Boller A, and Schick C. *Journal of Thermal Analysis* 1996; 46(3-4): 935-954.
9. Pyda M and Wunderlich B. *Macromolecules* 2005;38(25):10472-10479.
10. Pyda M, Nowak-Pyda E, Heeg J, Huth H, Minakov AA, Di Lorenzo ML, Schick C, and Wunderlich B. *Journal of Polymer Science Part B-Polymer Physics* 2006; 44(9): 1364-1377.

11. Gill P, Moghadam TT, and Ranjbar B. *Journal of biomolecular techniques* 2010; 21(4): 167-193.
12. Xia XX, Xu QB, Hu X, Qin GK, and Kaplan DL. *Biomacromolecules* 2011; 12(11): 3844-3850.
13. Lai SL, Ramanath G, Allen LH, Infante P, and Ma Z. *Applied Physics Letters* 1995; 67(9): 1229-1231.
14. Cassel RB and Wiese M. *American Laboratory* 2003; 35(1): 13-16.
15. Efremov MY, Warren JT, Olson EA, Zhang M, Kwan AT, and Allen LH. *Macromolecules* 2002; 35(5): 1481-1483.
16. Efremov MY, Olson EA, Zhang M, Schiettekatte F, Zhang ZS, and Allen LH. *Review of Scientific Instruments* 2004; 75(1): 179-191.
17. Minakov AA, Mordvintsev DA, and Schick C. *Polymer* 2004; 45(11): 3755-3763.
18. Mileva D, Androsch R, Zhuravlev E, and Schick C. *Polymer* 2012; 53(18): 3994-4001.
19. Sandler SR. *Polymer synthesis and characterization: a laboratory manual*. San Diego: Academic Press, 1998: 98-206.
20. Hèohne G, Hemminger W, and Flammersheim HJ. *Differential scanning calorimetry : an introduction for practitioners, 2nd rev. and enl. ed*. Berlin; New York: Springer, 2003: 1-65.
21. Pyda M, Hu X, and Cebe P. *Macromolecules* 2008; 41(13): 4786-4793.
22. Huang WW, Krishnaji S, Hu X, Kaplan D, and Cebe P. *Macromolecules* 2011; 44(13): 5299-5309.
23. Hu X, Kaplan D, and Cebe P. *Macromolecules* 2006; 39(18): 6161-6170.

24. Xu H and Cebe P. *Macromolecules* 2004; 37(8): 2797-2806.

25. Huang W, Krishnaji S, Kaplan D, and Cebe P. *Journal of Thermal Analysis and Calorimetry* 2012; 109(3): 1193-1201.

26. Hu X, Kaplan D, and Cebe P. *Thermochimica Acta* 2007; 461(1-2): 137-144.

27. Huang WW, Krishnaji S, Kaplan D, and Cebe P. in prep for *Macromolecules* 2012.

28. Huang WW, Edenzon K, Fernandez L, Razmpour S, Woodburn J, and Cebe P. *Journal of Applied Polymer Science* 2010; 115(6): 3238-3248.

29. Jackson M and Mantsch HH. *Critical Reviews in Biochemistry and Molecular Biology* 1995; 30(2): 95-120.

30. Barth A. *Biochimica Et Biophysica Acta-Bioenergetics* 2007; 1767(9): 1073-1101.

31. Xie J, Riley C, Kumar M, and Chittur K. *Biomaterials* 2002; 23(17):3609-3616

32. Smith BC. *Fundamentals of Fourier transform infrared spectroscopy*. Boca Raton, Fla.: CRC Press, 1996:1-85.

33. Alexandre M and Dubois P. *Materials Science & Engineering R-Reports* 2000; 28(1-2): 1-63.

34. Vanstokkum IHM, Linsdell H, Hadden JM, Haris PI, Chapman D, and Bloemendal M. *Biochemistry* 1995; 34(33): 10508-10518.

35. Tamm LK and Tatulian SA. *Quarterly Reviews of Biophysics* 1997; 30(4): 365-429.

36. Remmele RL, Stushnoff C, and Carpenter JF. *Pharmaceutical Research* 1997; 14(11):1548-1555.

37. Hienerwadel R, Boussac A, Breton J, Diner BA, and Berthomieu C. *Biochemistry* 1997; 36(48): 14712-14723.

38. Hu X, Kaplan D, and Cebe P. *Macromolecules* 2008; 41(11): 3939-3948.

39. Barth A. *Progress in Biophysics & Molecular Biology* 2000; 74(3-5): 141-173.

40. Barth A and Zscherp C. *Quarterly Reviews of Biophysics* 2002; 35(4): 369-430.

41. Pauling L, Corey RB, and Branson HR. *Proceedings of the National Academy of Sciences of the United States of America* 1951; 37(4): 205-211.

42. Mathews CK, Van Holde KE, and Ahern KG. *Biochemistry, 3rd ed*. San Francisco, Calif.: Benjamin Cummings, 2000:161-167.

43. Horton HR. *Principles of biochemistry, 4th ed*. Upper Saddle River, NJ: Pearson Prentice Hall, 2006: 92-98.

44. Pauling L and Corey RB. *Proceedings of the National Academy of Sciences of the United States of America* 1951; 37(5): 251-256.

45. Branden C and Tooze J. *Introduction to protein structure*. New York: Garland Pub., 1991: 11-56.

46. Vanduijnen PT, Dejager JC, and Thole BT. *Biopolymers* 1985; 24(5): 735-745.

47. Voet D, Voet JG, and Pratt CW. *Fundamentals of biochemistry, upgrade, Rev. ed*. New York: Wiley, 2002: 124-148.

48. Gosline JM, Demont ME, and Denny MW. *Endeavour* 1986; 10(1): 37-43.

49. Simmons A, Ray E, and Jelinski LW. *Macromolecules* 1994; 27(18): 5235-5237.

50. Hayashi CY, Shipley NH, and Lewis RV. *International Journal of Biological Macromolecules* 1999; 24(2-3): 271-275.

51. Kauppinen JK, Moffatt DJ, Mantsch HH, and Cameron DG. *Applied Spectroscopy* 1981; 35(3): 271-276.

52. Tooke PB. *Trac-Trends in Analytical Chemistry* 1988; 7(4): 130-136.

53. Lorenz-Fonfria VA, Villaverde J, and Padros E. *Applied Spectroscopy* 2002; 56(2): 232-242.

54. Lorenz-Fonfria VA and Padros E. *Spectrochimica Acta Part a-Molecular and Biomolecular Spectroscopy* 2004; 60(12): 2703-2710.

55. Lorenz-Fonfria VA and Padros E. *Analyst* 2004; 129(12): 1243-1250.

56. Guinier A. *X-ray diffraction in crystals, imperfect crystals, and amorphous bodies*. San Francisco: W. H. Freeman, 1963: 1-27.

57. Glisovic A, Vehoff T, Davies RJ, and Salditt T. *Macromolecules* 2008; 41(2): 390-398.

58. Perutz MF, Rossmann MG, Cullis AF, Muirhead H, Will G, and North AC. *Nature* 1960; 185(4711): 416-422.

59. Kendrew JC, Bodo G, Dintzis HM, Parrish RG, Wyckoff H, and Phillips DC. *Nature* 1958; 181(4610): 662-666.

60. Saleh BEA and Teich MC. *Fundamentals of photonics, 2nd ed*. Hoboken, N.J.: Wiley-Interscience, 2007: 58-60.

61. Ashcroft NW and Mermin ND. *Solid state physics*. New York,: Holt, 1976: 1-98.

62. Hu X, Lu Q, Kaplan DL, and Cebe P. *Macromolecules* 2009; 42(6): 2079-2087.

63. Ma Q, Mao B, and Cebe P. *Polymer* 2011; 52(14): 3190-3200.

64. Caillol S, Lecommandoux S, Mingotaud AF, Schappacher M, Soum A, Bryson N, and Meyrueix R. *Macromolecules* 2003; 36(4): 1118-1124.

65. Babin J, Rodriguez-Hernandez J, Lecommandoux S, Klok HA, and Achard MF. *Faraday Discussions* 2005; 128: 179-192.

66. Warwicker JO. *Journal of Molecular Biology* 1960; 2(6): 350-362.

67. Buckley J, Cebe P, Cherdack D, Crawford J, Ince BS, Jenkins M, Pan JJ, Reveley M, Washington N, and Wolchover N. *Polymer* 2006; 47(7): 2411-2422.

68. Kang P-H, Jeon Y-K, Jeun J-P, Shin J-W, and Nho Y-C. *Journal of Industrial and Engineering Chemistry* 2008; 14(5): 672-675.

69. Liu ZH, Marechal P, and Jerome R. *Polymer* 1997; 38(19): 4925-4929.

70. Mano JF, Sencadas V, Costa AM, and Lanceros-Mendez S. *Materials Science and Engineering a - Structural Materials Properties Microstructure and Processing* 2004; 370(1-2): 336-340.

71. Yu L and Cebe P. *Journal of Polymer Science Part B-Polymer Physics* 2009; 47(24): 2520-2532.

Chapter III. Experimental Approaches

This chapter provides the background information of the materials preparation process, as well as the experimental details of temperature modulated differential scanning calorimetry (TMDSC), thermogravimetric analysis (TGA), Fourier transform infrared spectroscopy (FTIR), wide angle X-ray diffraction (WAXD) and scanning electron microscopy (SEM). The thermal analysis using TMDSC and TGA, and the structural analysis using FTIR and WAXD were performed in our lab at Science and Technology Center, Tufts University. The morphology studies using SEM are performed at the Center for Nanoscale Systems (CNS), Harvard University.

3.1 Preparation of Spider Silk-like Block Copolymer Films

Recombinant DNA technology [1] was applied in this thesis to prepare a new family of spider silk-like block copolymers. Two spider silk amino acid sequences, named A-block (hydrophobic) and B-block (hydrophilic), based on the major ampullate spidroins 1 proteins (MaSp1) in the dragline of *Nephila Clavipes* were picked as the building blocks of our block copolymers. The poly(alanine) A-block, which is similar to the 'crystalline module' in natural spider silks, is composed of 14 amino acid residues; and the glycine rich B-block, which is similar to the 'elastic module' in natural spider silks, is composed of 22 amino acid residues. The amino acid sequences for A-block and B-block are shown in **Figure 3.1**.

A block (Hydrophobic, 14 amino acids):
G A G A A A A A G G A G T S

B block (Hydrophilic, 22 amino acids):
Q G G Y G G L G S Q G S G R G G L G G Q T S

Figure 3.1 Amino acid sequences of A-block and B-block.

The process of obtaining spider silk-like block copolymers with his-tag is shown in **Figure 3.2**. This process is describe in detail in the previous publication [2]. In brief, a spacer region of pET30a(+) plasmid was modified with an adaptor sequence to generate a cloning vector pET30L. After constructing the cloning vector, the hydrophilic B-block and hydrophobic A-block were ligated into the adaptor sequence utilizing *SpeI* and *NheI* restriction sites, and all the internal *SpeI* and *NheI* restriction sites were destroyed during ligation. Then the successfully constructed plasmid with desired number of A-blocks and B-blocks is transformed into an expression host, *E.coli* RY-3041 strain, and were grown at 37 ºC in LB medium to an OD_{600} of 0.6 at which point protein expression was induced with 1mM isopropylthio-β-galactoside (IPTG). The cells were harvested 4 hours after induction and were lyzed for purification. Protein purification was performed by immobilized metal affinity chromatography using a Ni-NTA resin, followed by dialysis with DI water for 3 days. Centrifugation and filtration were performed to remove insoluble residues after dialysis, and the spider silk-like block copolymer aqueous solution was obtained after the whole process. To obtain the protein in solid form, the dialysed solution were frozen and lyophilized. After obtaining the material, they were stored in desiccators to prevent absorbing moisture from the air. The synthetic peptides

were run on SDS-PAGE gel electrophoresis to confirm purity. Protein identification was confirmed by matrix-assisted laser desorption/ionization time of flight (MALDI-TOF) mass spectrometry. Another set of proteins, A, BA and B without histidine tags were purchased from the Tufts University Protein Core Facility (TUCF) for comparison. In order to prevent cyclization of the peptides, the C-terminus was modified to an amide. These samples were also checked and stored in the same fashion as the his-tag containing proteins. The number of residues, the amino acid sequences, and the calculated molecular weight of all the samples are list in **Table 3.1**.

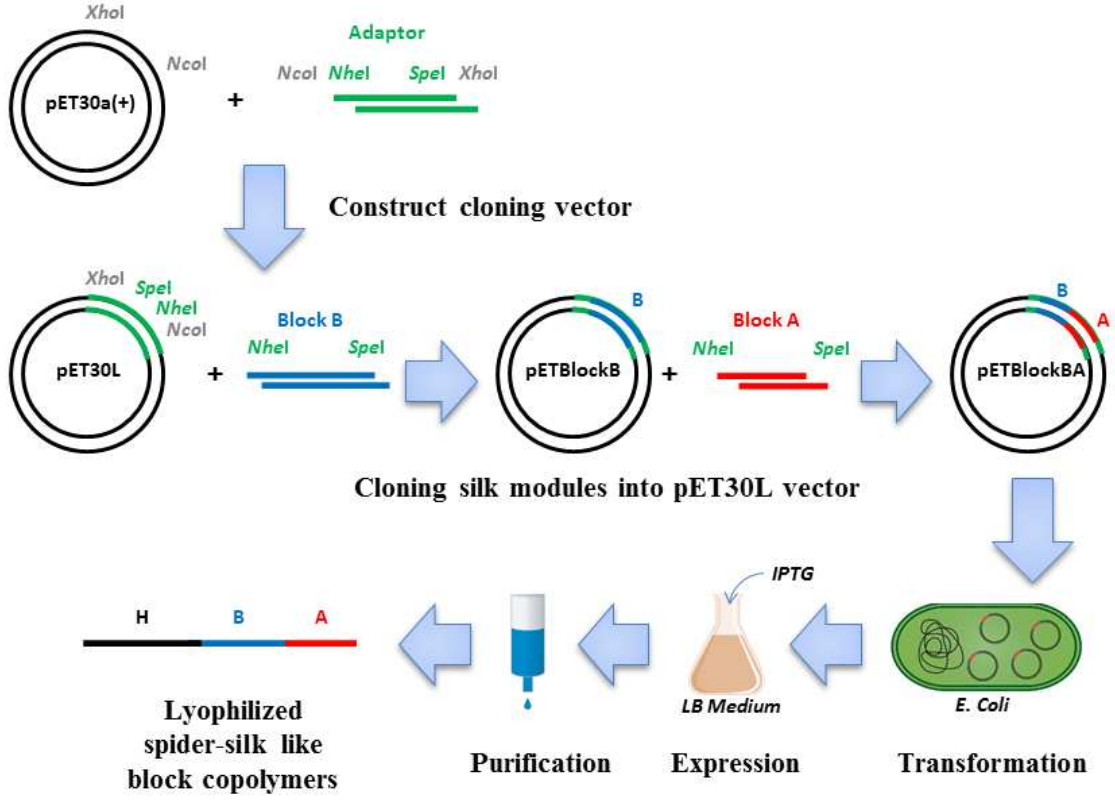

Figure 3.2 The process of obtaining spider silk-like block copolymers using recombinant DNA technology [2].

Table 3.1 Number of Residues, Amino Acid Sequence and Molecular Weight of Recombinant Spider Silk-like Block Copolymers

Sample	# Residues	Sequence*	M_w (Da)
HBA_6	154	M H H H H H H S S G L V P R G S G M K E T A A A K F E R Q H M D S P D L G T D D D D K A M A A S Q G G Y G G L G S Q G S G R G G L G G Q T S G A G A A A A A A G G A G T S G A G A A A A A A G G A G T S G A G A A A A A A G G A G T S G A G A A A A A A G G A G T S G A G A A A A A A G G A G T S	12 982
HBA_3	112	M H H H H H H S S G L V P R G S G M K E T A A A K F E R Q H M D S P D L G T D D D D K A M A A S Q G G Y G G L G S Q G S G R G G L G G Q T S G A G A A A A A A G G A G T S G A G A A A A A A G G A G T S	10 069
HBA_2	98	M H H H H H H S S G L V P R G S G M K E T A A A K F E R Q H M D S P D L G T D D D D K A M A A S Q G G Y G G L G S Q G S G R G G L G G Q T S G A G A A A A A A G G A G T S G A G A A A A A A G G A G T S	9 098
HBA	84	M H H H H H H S S G L V P R G S G M K E T A A A K F E R Q H M D S P D L G T D D D D K A M A A S Q G G Y G G L G S Q G S G R G G L G G Q T S G A G A A A A A G G A G T S	8 127
HAB_2	106	M H H H H H H S S G L V P R G S G M K E T A A A K F E R Q H M D S P D L G T D D D D K A M A A S G A G A A A A A G G A G T S Q G G Y G G L G S Q G S G R G G L G G Q T S Q G G Y G G L G S Q G S G R G G L G G Q T S	10 047
HAB_3	128	M H H H H H H S S G L V P R G S G M K E T A A A K F E R Q H M D S P D L G T D D D D K A M A A S G A G A A A A A G G A G T S Q G G Y G G L G S Q G S G R G G L G G Q T S Q G G Y G G L G S Q G S G R G G L G G Q T S Q G G Y G G L G S Q G S G R G G L G G Q T S	11 967
A	17	MASGAGAAAAAGGAGTS	1 278
B	25	MASQGGYGGLGSQGSGRGGLGGQTS	2 227
BA	39	MASQGGYGGLGSQGSGRGGLGGQTSGAGAAAAA GGAGTS	3 198

*End group or His-tag shown in black; B-block in blue; A-block in red.

The lyophilized spider silk-like block copolymers were dissolved into DI water, hexafluoroisopropanol (HFIP), or methanol (MeOH) at a concentration of 2 mg/mL, and cast into films for further measurements. Free standing films about 300 μm thick were also cast on Teflon substrates for DSC, TGA, and WAXD. Films about 10 μm thick were cast on a IR transparent calcium fluoride (CaF_2) substrates for FTIR. Free standing films about 10 μm thick, which were peeled off from PDMS substrates, were also used for real-time FTIR. Sample solution was also drop cast on a pre-cleaned Si wafer; after drying the sample was coated with Pt/Pd for SEM. Films were placed into a vacuum oven at 25 °C for 24 h to remove the surface water. Examples of the sample films from CaF_2 and PDMS substrate, used for real time-FTIR analysis, are shown in **Figure 3.3**.

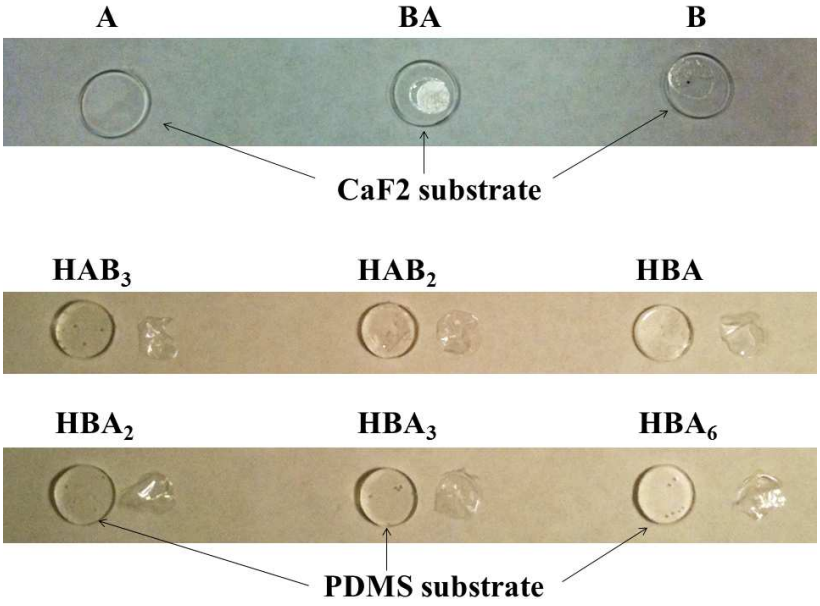

Figure 3.3 A, BA and B sample films on CaF_2 substrates and HBA_6, HBA_3, HBA_2, HBA, HAB_2 and HAB_3 free standing films from PDMS substrates. The diameter of the CaF_2 and PDMS substrates is 10 mm.

3.2 Thermal Analysis

Thermal analysis is conducted on a TA Instruments DSC Q100 and TGA Q500 in room 219, Science and Technology Center, Tufts University.

3.2.1 Temperature Modulated Differential Scanning Calorimetry

Differential Scanning Calorimetry (DSC) studies were carried out using a TA Instruments DSC Q100. This instrument can be operated in two modes: one is the conventional standard DSC mode and the other is the temperature modulated DSC (TMDSC) mode. The theoretical backgrounds of both standard DSC mode and TMDSC mode have been given in Chapter II.

Figure 3.4 shows the setup of the TA Instrument Q100 DSC. Our DSC system includes a main DSC Q100 unit, a refrigerated cooling system, a nitrogen gas purge system and a computer which is used to set up the experiment and collect data. The DSC cell which is located on the main DSC unit is used to measure the differential heat flow that is needed to heat up or cool down a sample relative to a reference [3, 4]. The inside view of the DSC cell is also shown at the upper right corner with the reference platform (marked as R), which is located farther away from the user, and the sample platform (marked as S), which is located nearer to the user. The DSC cell is covered with the AutoLid during the measurement as well as during the standby conditions. The AutoLid is controlled by the touch screen on the main DSC unit and it is only opened during loading and removing the sample and reference when the DSC cell temperature is close to room temperature. Opening the AutoLid below 0 ºC is strictly forbidden because the moisture condensation from air will damage the cell.

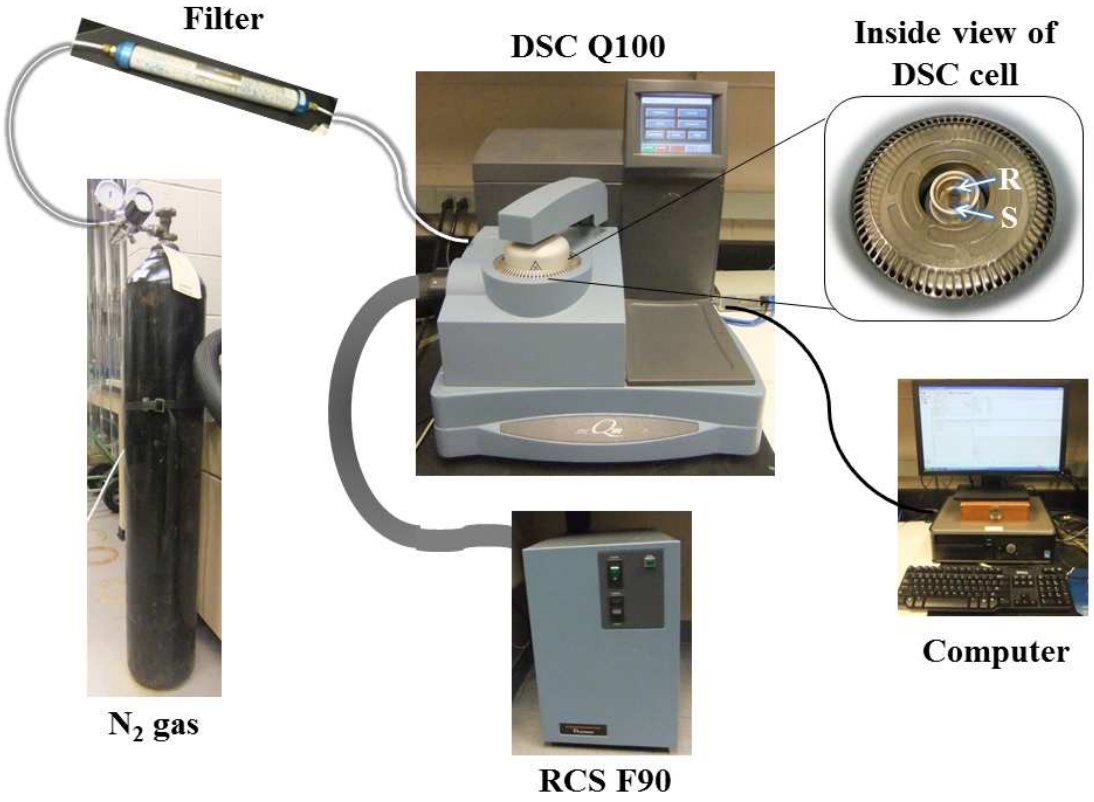

Figure 3.4 Experimental setup of the TA Instruments DSC Q100. The inside view of the DSC cell is shown at the upper right corner with the reference platform (marked as R) and sample platform (marked as S).

The main DSC unit is used in conjunction with a cooling accessory, the refrigerated cooling system (RCS) F90. RCS F90 is used to control the temperature in DSC cell for performing cooling experiments, and it has an operating range of -90°C to 550°C [5]. Another important accessory of our DSC is the gas purge system. The purge gas used in our experiments is nitrogen gas, but it could also be helium or other inert gas with high thermal conductivity. The purge gas is delivered from the gas storage tank to a gas filter to remove moisture before it comes into the DSC cell. The flow rate of nitrogen

gas is controlled by a regulator, which is located on the top of the gas tank and always left at 18 psi. The flow rate of the purge gas in the DSC is 50 mL/min.

To prepare DSC sample and reference for measurement, two pairs of aluminum pan and lid having identical total weights are selected. One pair of pan and lid is compressed without any sample inside by a mechanical press to make the reference pan, and the other pair is compressed with the sample in-between the pan and lid to make the sample pan. A picture of the TA mechanical press for DSC and the Mettler AE240 digital balance (with an uncertainty of ± 0.01mg) that is used to measure the weight of the pan and lid are shown in **Figure 3.5**.

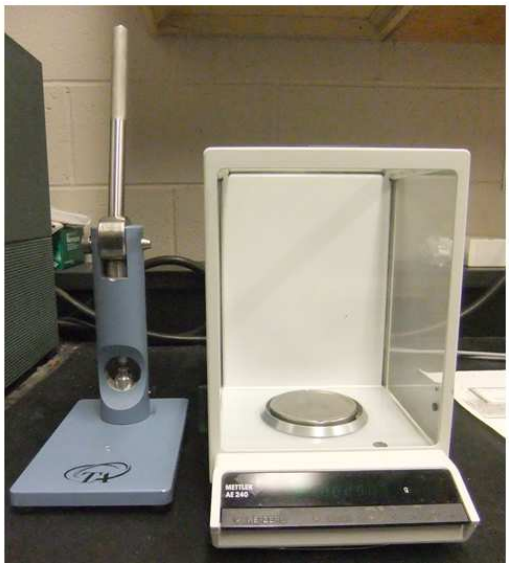

Figure 3.5 TA mechanical press for DSC (at the left) and the digital balance that is used to measure the weight of the pan and lid (at the right).

To calibrate the temperature and heat flow, indium standard is usually used. To calibrate the heat capacity, sapphire standard is usually used following a “three run”

method. In the "three run" method, the first run is empty aluminum sample pan vs. empty aluminum reference pan to obtain the cell asymmetry and baseline correction. The second run is sapphire standard in aluminum pan vs. empty aluminum reference pan to calibrate heat flow amplitude according to standard equations [6, 7]. The third run is sample in aluminum pan vs. empty aluminum reference pan. The same empty aluminum reference pan is used in all the runs, and all the aluminum sample pans are kept the same in weight within ± 0.01 mg.

The heat capacity measured by standard DSC is given in Chapter II as

$$mc_p = K'' \frac{HF}{q} \tag{3.1}$$

where *K''* is the calibration constant obtained by running a standard material such as sapphire, and *HF* is the differential heat flow into or out of the sample. The heat capacity measured by TMDSC from Chapter II is given by

$$\left| mc_p + C_{sp} - C_r \pm \Delta C_{cell} \right| = \frac{A_{HF}}{A} K' \tag{3.2}$$

where mc_p is the heat capacity of a sample of mass, m, and specific heat capacity, c_p; C_{sp} and C_r are the heat capacities of the sample pan and empty reference pan, respectively; ΔC_{cell} is the cell asymmetry correction [8]. A_{HF} is the modulated heat flow amplitude, and *K'* is the calibration constant for the heat flow amplitude for a given empty reference pan and modulation frequency.

When setting up a TMDSC measurement, at least 4 complete modulation cycles need to be ensured in one thermal transition to guarantee resolution of the transition, thus the appropriate heating/cooling rates need to be carefully considered. An example of

modulated heat flow vs. temperature curve is shown in **Figure 3.6**. The heat flow envelope boundaries correspond to the heat flow at the slowest and fastest heating rate during each modulation cycle. When the slowest heating rate is zero, the upper boundary should be equal to the non-reversing heat flow because only the kinetic component exists under this condition. The amplitude of the temperature modulation is ±0.318 ºC/min in Figure 3.6, which was chosen based on both the heat/cooling rate and the oscillation period. **Table 3.2** gives the suggested parameters under "heat only" conditions (i.e., sample temperature never decreases during heating) for TMDSC [5]. The oscillation period used in this thesis is 60 s for all the measurements.

Table 3.2 Maximum Modulation Amplitude for TMDSC under "Heat Only" Conditions

Period (s)	**Heating Rate (ºC/min)**						
	0.1	**0.2**	**0.5**	**1**	**2**	**5**	**10**
10	0.003	0.005	0.013	0.027	0.053	0.133	0.265
20	0.005	0.011	0.027	0.053	0.106	0.265	0.531
30	0.008	0.016	0.040	0.080	0.159	0.398	0.796
40	0.011	0.021	0.053	0.106	0.212	0.531	1.062
50	0.013	0.027	0.066	0.133	0.265	0.663	1.327
60	0.016	0.032	0.080	0.159	0.318	0.796	1.592
70	0.019	0.037	0.093	0.186	0.372	0.929	1.858
80	0.021	0.042	0.106	0.212	0.425	1.062	2.123
90	0.024	0.048	0.119	0.239	0.478	1.194	2.389
100	0.027	0.053	0.133	0.265	0.531	1.327	2.654

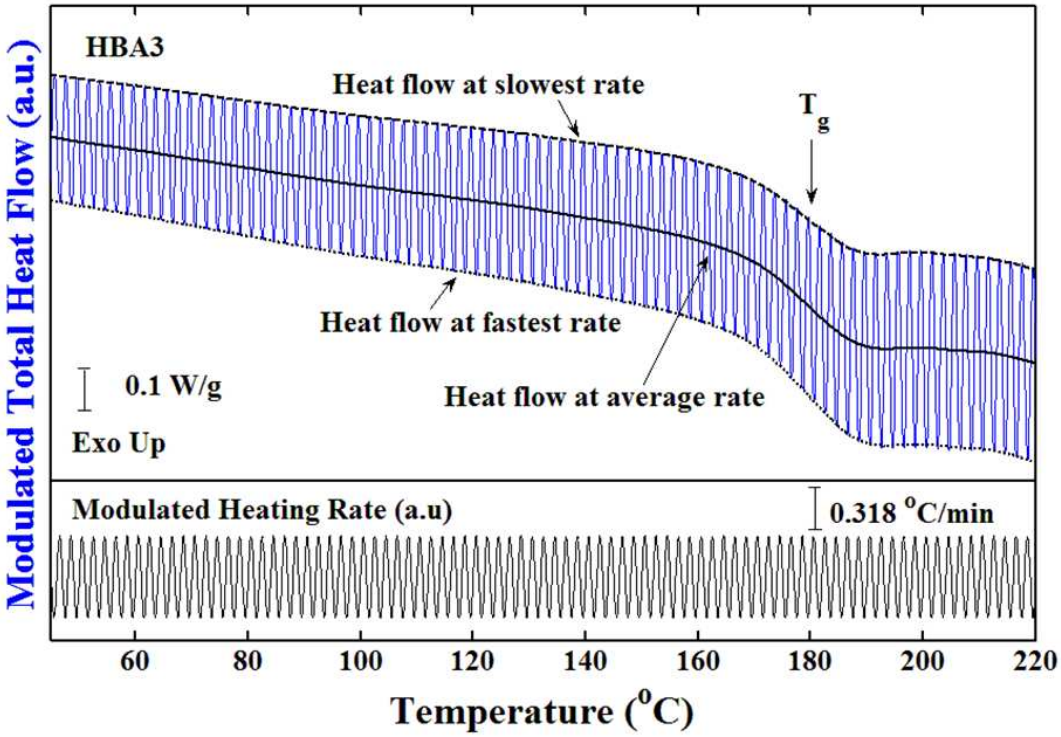

Figure 3.6 Modulated heat flow vs. temperature curve (in blue) of recombinant spider silk-like block copolymer HBA_3 after annealing at 120 ºC. The heat flow at the slowest, average, and the fastest rate, vs. temperature curve with the modulated heating rate vs. temperature curve are also shown as a reference.

The standard operating procedure for TA Q100 DSC is listed below.

1. Sign up time for DSC experiments in Room 219 (at the back of the door).
   (TGA scan must be accomplished before you can sign up for DSC.)
2. Sign the Log book.
3. Turn on the gas, adjust regulator and turn on the cooling system.

a) The DSC requires purge gas to run properly. Turn the knob on top of the cylinder first counter clockwise to open the tank, then adjust the regulator, to make sure the reading on the second (low pressure) gauge is at 18 psi.

b) Turn on the cooling system (Green button).

4. Encapsulate the sample.

a) Measure the weight of pan+lid for sample pan on the Mettler balance.

b) Find a similarly weighted reference in the DSC reference book. Make a new one if necessary. The weight difference must be less than 0.01mg.

c) Place the sample into the bottom pan, and put the lid on gently.

d) Compress the sample pan and lid using the blue TA mechanical press.

e) Measure the total weight of pan+lid+sample.

5. Put pan and lid inside DSC cell compartment.

a) Go to Control Menu on the DSC screen, press *lid* to open the lid automatically.

b) Put the reference at the farther side, and put the sample closer to operator.

c) Press *lid* again to close the lid automatically.

6. Open TA Instruments data collection software, set up program and GO.

a) Double click *TA Instrument Explorer*, then double click *Q100-0974*.

b) Input sample information. Use only the sample's weight as the entered weight in the DSC set up software.

c) Select the directory where your data will be stored. This should be a subdirectory in the TA Instruments >> Data >> DSC directory path.

d) Change the measuring method if needed. Be sure to select the correct operation, such as "Calibration", "Standard" or "Modulated" DSC.

e) Start the run.

7. During data collection, double click *TA Universal Analysis* to see a real time DSC graph.

8. When finished, close the software, then close the cooling system and the gas.

To measure the reversing heat capacity of the dry recombinant spider silk-like block copolymer using a “three run method” by TMDSC, the method used is listed as following:

1. Equilibrate at 120.00 °C
2. Isothermal for 60.00 min
3. Equilibrate at -30.00 °C
4. Isothermal for 3.00 min
5. Modulate +/- 0.318 °C every 60 seconds
6. Ramp 2.00 °C/min to 350.00 °C
7. End of method

To measure the reversing heat capacity of the protein-water system, step 1 and 2 are skipped. The same method was used for all the three runs in the “three run method”, which is described in Chapter II.

After data collection using TMDSC, the data can be viewed and exported as a text file using *TA Universal Analysis* software. The TMDSC data text file is then imported into Matlab to plot heat flow vs. temperature plots or to calculate the reversing heat capacity based on equation 3.2 using the “three run method”. The Matlab program for calculating the reversing heat capacity is attached as Appendix II (a). During that calculation, a text file called SapphireLiter.txt is used as the heat capacity literature value of the sapphire standard [9] for calibration, and this file is attached as Appendix II (b).

3.2.2 Thermogravimetric Analysis

Thermogravimetric analysis (TGA) studies were carried out using a TA Instruments Q500 thermogravimetric analyzer. It is a type of thermal analysis instrument that is used to determine the change of sample weight with respect to the change in temperature during a heating ramp or time during isothermal holding. The TGA is used to characterize any material that exhibits a weight change and to detect phase changes due to decomposition, oxidation, or dehydration.

Figure 3.7 shows the setup of the TA Instruments Q500 TGA. Our TGA system includes a main TGA Q500 unit, a heat exchanger, a nitrogen gas purge system and a computer which is used to set up the experiment and collect data. The main TGA unit has 3 major components: the balance, the furnace and the sample platform as shown in the insert picture of Figure 3.7. The balance is the key to the TGA, which provides precise measurement of the sample weight. The sample is loaded into the platinum basket at the sample platform first then automatically transferred onto the hook of the high-precision balance. The sample platform is controlled by the touch screen on TGA and used to load and unload the samples. The furnace in the main Q500 TGA unit is used to control the temperature and it can perform measurements in the temperature range from room temperature to 1000 °C [10]. The main TGA unit is used in conjunction with a water-based cooling accessory, the heat exchanger. Another important accessory of our TGA is the gas purge system. The inert nitrogen purge gas flow rate in the TGA is 60 mL/min. The purge gas is used to prevent oxidation and undesired reactions in air.

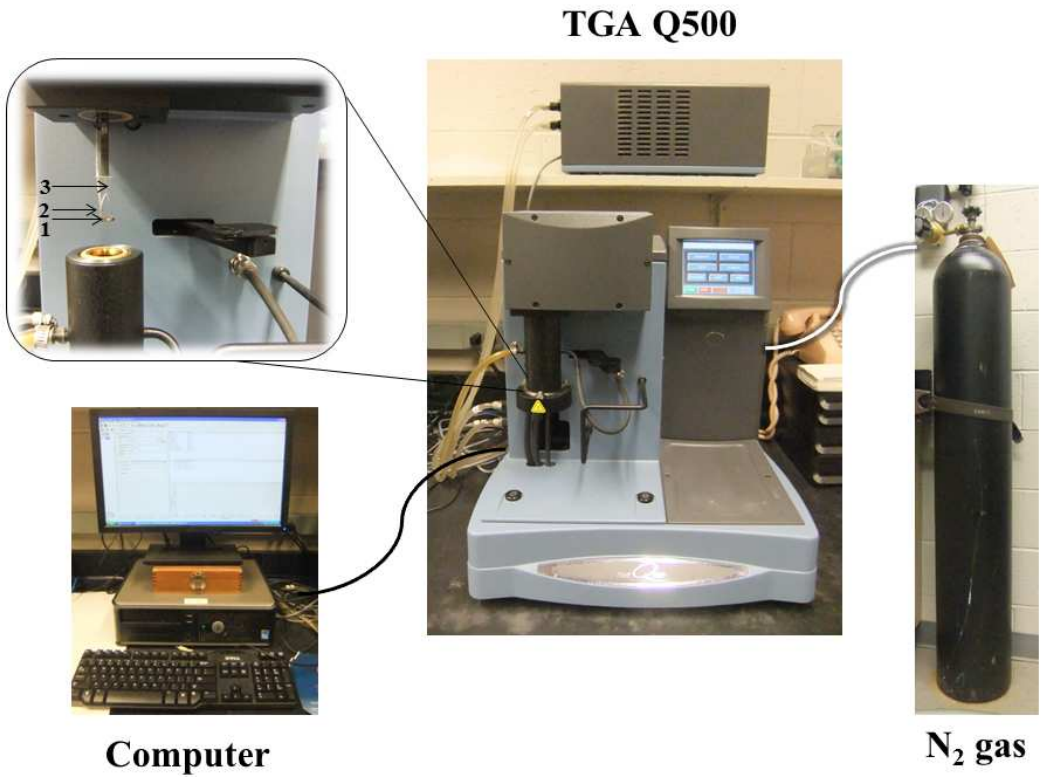

Figure 3.7 The setup of the TA Instruments Q500 TGA. The inset picture at upper left shows the platinum sample basket (1), the temperature sensor (2) and the force sensor (3) seen while opening the furnace.

In this thesis, the TGA was used for determining the change of sample mass with temperature, allowing correction to be made in the mass of sample used to normalize the DSC heat flow data [11, 12]. For example, to obtain the true glass transition temperature of dry spider silk-like block copolymers, the samples at 120 °C were annealed to eliminate the effect of bound water. During annealing, the water molecules escaped, and the total weight of sample changed. To avoid absorbing surface water from air again, we kept the sample in the DSC and estimated the sample weight after annealing by running the same experiment with the TGA. To obtain the reversing heat capacity of a protein-

water system, the sample was run directly in TMDSC without annealing. The total sample mass is decreasing during the TMDSC heating scan, and the temperature dependent mass *M(T)* of the sample due to water evaporation during heating is obtained by running the same experiment using TGA. Therefore, the total heat flow, *HF(T)*, and the reversing heat flow, *RHF(T)*, for a protein-water system during heating are normalized at each temperature by the TGA profile, *wt%*, and can be expressed as

$$HF(T) = HF_{DSC} / wt\% \tag{3.3a}$$

$$RHF(T) = RHF_{DSC} / wt\% \tag{3.3b}$$

The standard operating procedure for TA Q500 TGA is listed below.

1. Sign up time for TGA experiments in Room 219 (at the back of the door).
2. Sign the Log book.
3. Turn on the gas, and adjust regulator.

   The TGA requires purge gas to run properly. Turn the knob on top of the cylinder first counter clock wise to open the tank, then adjust the regulator, to make sure the reading is between 0 and 1 psi.
4. Zero the balance.

   a) Go to Control Menu on the TGA screen, press *load/unload* to open the furnace and transfer the platinum basket from the balance to the sample platform automatically.

   b) Clean the basket with acetone and Q-tips and put it back to the sample platform.

   c) Wait until the basket is completely dry.

   d) Go to Control Menu on the TGA screen, press *Tare* to zero the balance.

(By pressing *Tare*, the empty platinum basket will be transferred from the sample platform to the balance and the furnace will be closed automatically. After taring the basket, which takes about 5 min, the platinum basket will be transferred back from the balance to the sample platform and the furnace will be open automatically.)

5. Loading sample.

   a) Load sample carefully into the platinum basket on the sample platform.

   b) Go to Control Menu on the TGA screen, press *load/unload* again to transfer the full basket from the sample platform to the balance and close the furnace automatically.

6. Open TA Instruments data collection software, set up program and GO.

   a) Double click *TA Instrument Explorer*, then double click *Q500-0698.*

   b) Select the directory where the data will be stored. This should be a subdirectory in the TA Instruments >> Data >> TGA directory path.

   c) Change the measuring method if needed.

   d) Wait for a minute for a steady weight, and then start the run.

7. During data collection, double click *TA Universal Analysis* to see a real time TGA graph.

8. When finished, close the software, then close the gas.

After data collection using TGA, the data can be viewed and exported as a text file using *TA Universal Analysis* software. The TGA data text file is then imported into Matlab to plot residual weight % vs. temperature plots or to calibrate the mass of the DSC data using equation 3.3. Because the DSC data, such as total heat flow and reversing heat flow, are collected at a different temperature interval than the TGA data, a

Matlab command is used to interpolate the TGA residual weight % at a temperature *T* in DSC data file. This Matlab command [13] has a general form of

>> $y = \text{interp1}(X, Y, x)$

which used linear interpolation to find the values of *y* at *x* by using the underlying function *Y(X)*. In particular, the following Matlab command is used for converting the original TGA data, named *TGA*, to a new TGA file, named TGA_{DSC}, which has the same temperature profile as the DSC data:

>> $TGA_{DSC}(:, Temperature) = DSC(:, Temperature)$

>> $TGA_{DSC}(:, wt\%) = \text{interp1}(TGA(:, Temperature), TGA(:, wt\%), TGA_{DSC}(:, Temperature))$

3.3 Structural Analysis

Structural analysis is conducted on a Jasco FT/IR-6200, Jasco infrared microscope IRT-5000 and Bruker GADDS D8 X-ray diffractometer in room 221, Science and Technology Center, Tufts University.

3.3.1 Fourier Transform Infrared Spectroscopy

Fourier transform infrared spectroscopy (FTIR) studies were carried out using a Jasco FT/IR-6200, and the real-time FTIR studies were carried out using a Jasco infrared microscope IRT-5000 in conjunction with a Mettler optical microscopy hot stage FP90. FTIR is a type of characterization technique that is used to analyze the chemical components in a sample by IR absorption caused by molecular vibration [14-16]. The intensity of the IR absorption is proportional to the square of the rate of change in dipole

moment with respect to the displacement of the atoms [15]. The theoretical background of FTIR and its application to biopolymers can be found in Chapter II.

The major components of the FTIR system including a Jasco FT/IR-6200 spectrometer, a Jasco infrared microscope IRT-5000 spectrometer, and a computer which is used to set up the experiment and collect data. **Figure 3.8** shows the setup of the Jasco FTIR instrument.

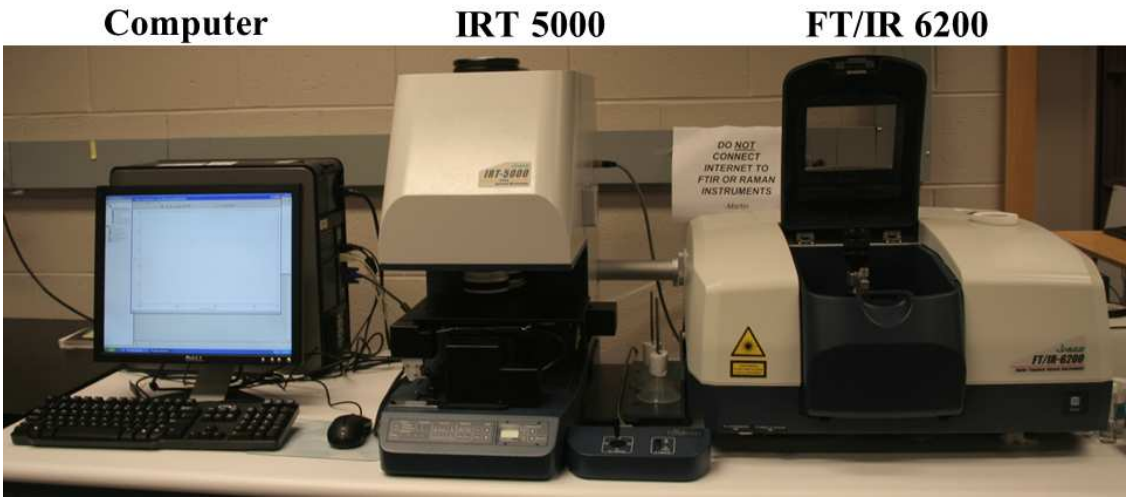

Figure 3.8 Jasco FTIR instrument, including computer, microscope spectrometer (IRT-5000), and ATR (FT/IR-6200) compartment.

The most important part of FTIR instrument is the Michelson interferometer inside of the spectrometer. An optical diagram of the Michelson interferometer is shown in **Figure 3.9**. The function of the interferometer is to modulate the intensity of the incident beam with time according to each frequency [14, 17, 18]. When the polychromatic light in the IR region passes through the semitransparent beam splitter with a calibration monochromatic laser beam, the total beam is split into two beams. One

beam is reflected back to the beam splitter by a fixed mirror, and the other is reflected back by a moving mirror which creates a time dependent optical path difference with the first beam. The two beams will interfere with each other when they recombine at the beam splitter, which leads to an intensity-modulated IR beam with an intensity-modulated laser calibration beam. Then the total modulated beam will travel through the sample and reach the detector.

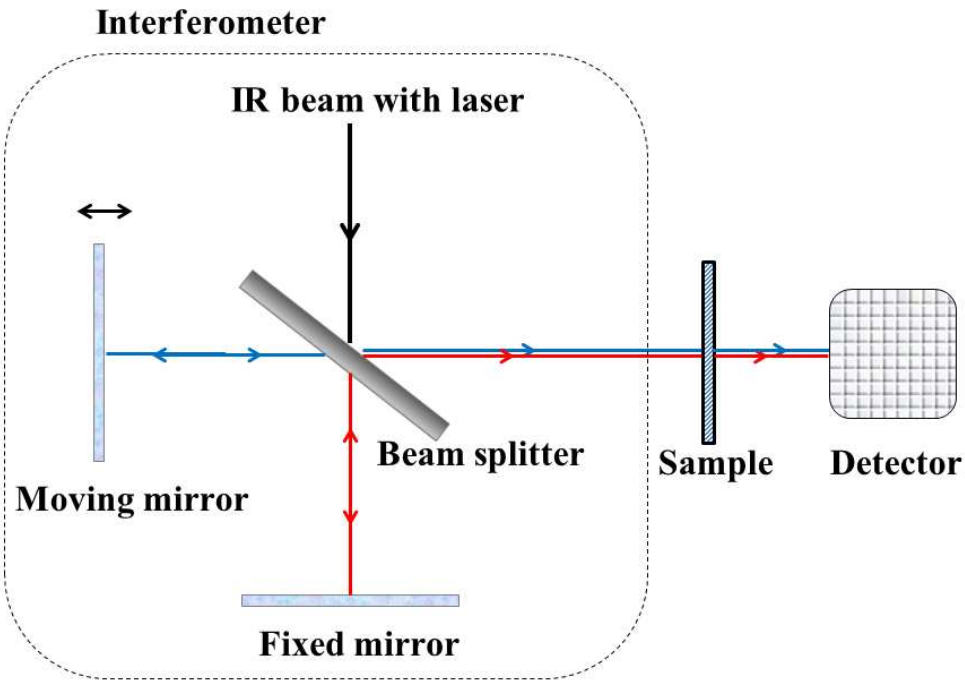

Figure 3.9 An optical diagram of the Michelson interferometer.

The signal measured by the detector is called an interferogram which is provided as an intensity vs. optical path difference plot. A mathematical Fourier transform is performed after IR light passes through the sample to convert the interferograms into a spectrum. When an interferogram is Fourier transformed, the resulting spectrum is called

a single beam spectrum, which is a plot of the raw detector response vs. wavenumber. The transmittance spectrum can be calculated by the following equation [14]:

$$T = \frac{I}{I_0} \tag{3.4}$$

where T is the transmittance, I is the IR intensity measured with a sample in the beam from the sample single beam spectrum, and I_0 is the intensity measured with no sample in the beam from the background single beam spectrum. The absorbance spectrum can then be calculated from the transmittance spectrum by [14]

$$A = -\log_{10} T \tag{3.5}$$

There are two commonly used sample stage setups for the FTIR instrument: the transmission sample stage and the attenuated total reflectance (ATR) sample stage as shown in **Figure 3.10**. Transmission spectroscopy, as shown in Figure 3.10 (a), is the most commonly used technique and it has a high signal-to-noise ratio, because the transmitted IR beam directly reaches the detector after interacting with the sample. The effective path length of transmission spectroscopy is just the thickness of the sample. For the transmission spectroscopy, free standing films and thin films which are cast on IR transparent substrates can be measured. The common materials used as an IR transparent substrate include potassium bromide (KBr), which is soluble in water, and calcium fluoride (CaF_2), which is insoluble in water. In this thesis, we used free standing films and thin films on CaF_2 substrate to perform transmission spectroscopy. The attenuated total reflectance sample stage, as shown in Figure 3.10 (b), is another stage setup for FTIR measurement which is used when the sample is thick and therefore has a low transmission. The advantage of the ATR stage setup is that it requires almost no sample

preparation, and it can also be easily used to take measurement of liquid. The ATR technique is based on a contact sampling technique which utilizes the property of total internal reflection, and it only takes measurement on the surface layer of the samples. The most important component of the ATR stage setup is the ATR crystal, which has a high refractive index and low IR absorption in the IR region of interest. The refractive indices of the common materials that are usually used for the ATR crystal are listed in **Table 3.3**. In the ATR crystal, at least one total internal reflection happens at the interface between the ATR crystal and sample. When total internal reflection happens, an evanescent wave is formed at the interface and extends into the sample. The depth of penetration of the evanescent wave, d_p, is typically about 1 μm, which can be expressed as [19]

$$d_p = \frac{\lambda}{2\pi(n_c^2 \sin^2\theta - n_s^2)^{1/2}} \tag{3.6}$$

where λ is the wavelength of the IR light, n_c is the refractive index of the ATR crystal, n_s is the refractive index of the sample, and θ is the incident angle of IR at the ATR/sample interface, which is greater than the critical angle. The evanescent effect can only be observed if $n_c > n_s$. After interacting with the sample, the IR is sent back to the detector to form an ATR spectrum. The signal-to-noise ratio of the ATR spectrum depends on the number of reflections, the contact between the crystal and the sample, and also the total length of the optical light path. During the ATR measurement, the optical path is pre-determined and the operator needs to make sure the sample is tightly attached to the surface of the ATR crystal.

(a)

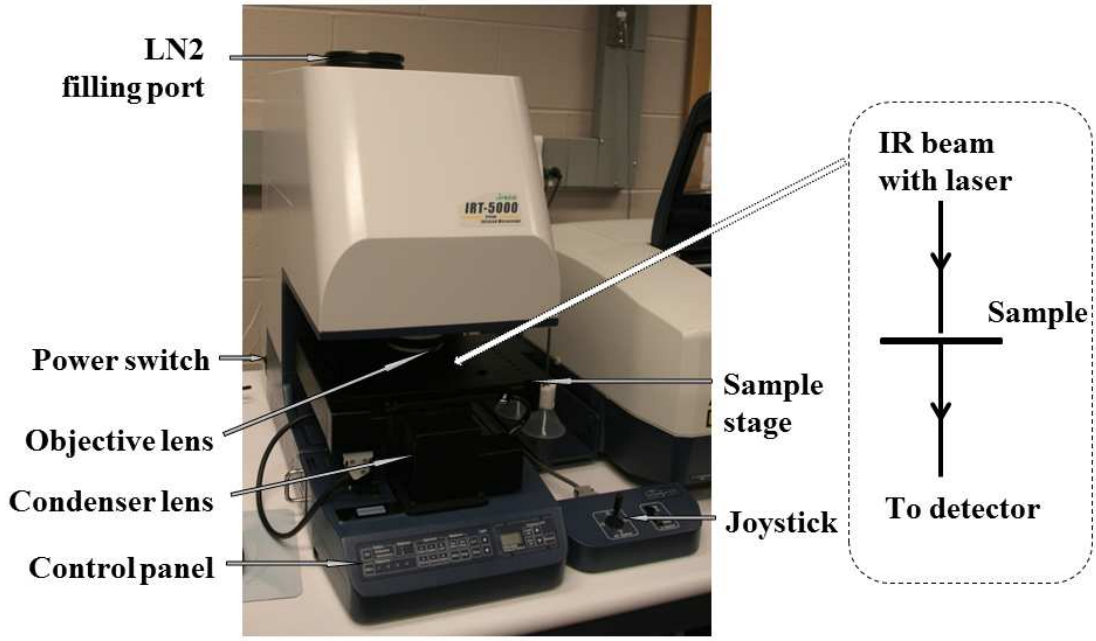

(b)

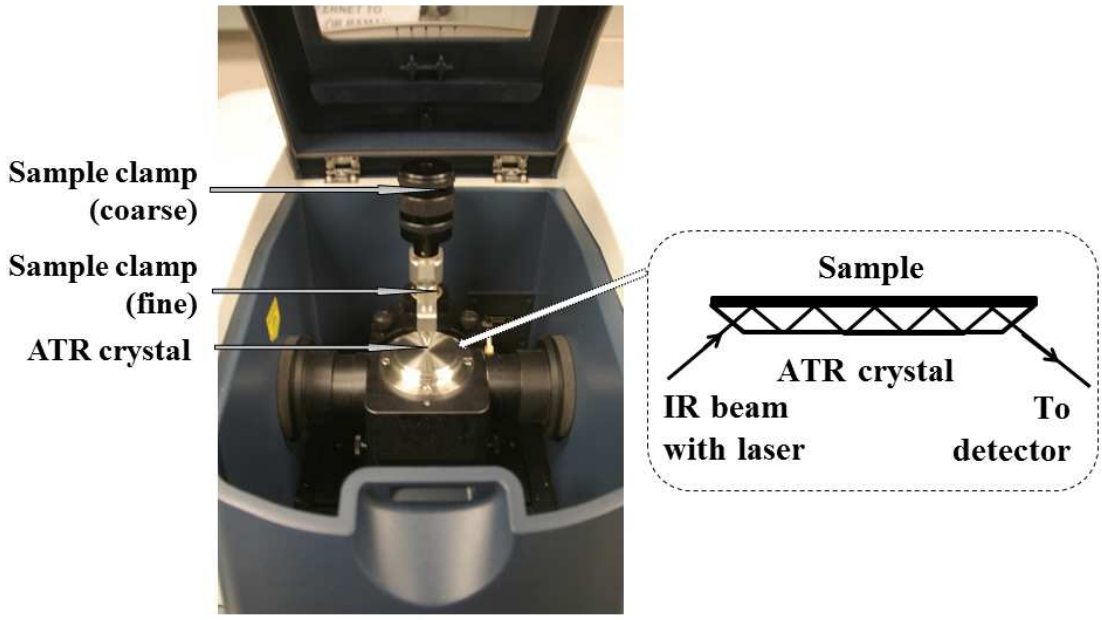

Figure 3.10 Two commonly used sample stage setups for the FTIR instrument: (a) the transmission sample stage and (b) the attenuated total reflectance sample stage.

Table 3.3 Common Materials Used for the ATR Crystal

Material	**Refractive Index at 1000 cm^{-1}**	**Spectral Range (cm^{-1})**
ZnSe	2.4	15,000 - 630
AMTIR	2.5	11,000 - 630
Ge	4.0	5,500 - 780
Si	3.4	8,300 - 1,500
Diamond/ZnSe	2.4	17,900 - 525
Diamond/KRS-5	2.4	17,900 - 250

The standard operating procedure for the Jasco FTIR instrument is listed below.

Operation procedure for Jasco 6200

1. Sign up time for Jasco instrument from online google calendar.
2. Turn on Power
   a) Make sure the *Resume* light (top of Jasco 6200) is green.
   b) Turn on the power switch (top of Jasco 6200), and wait until the *End of initialization* beep sound (3 beeps).
3. Open software
   a) Double-click *Spectra Manager* icon on PC desktop.
   b) Double-click *Spectra Measurement* under *Instrument – Jasco IR Microscope*
   c) Wait for the instrument initialization
4. Background measurement
   a) Clean the ATR crystal gently with Lens paper. Clean with solvent if necessary.

      For most cases, the preferred solvent is DI water or isopropyl alcohol. If a

stronger solvent is required, acetone may be used.

b) Click *Monitor Background* from the *Measure* menu. *Monitor Background Advanced* window pops out, with a real-time background spectrum is displayed on the left.

c) Setting parameter in the *Monitor Background Advanced* window on the *Standard* tab. You may choose your desired value according to your sample. A typical value for solid form material is:

Number of scan: 32

Resolution: 4.0 cm^{-1}

Range: 4000-600 cm^{-1}

View range: 4000-600 cm^{-1}

Vertical axis: Sample - Abs; Background - Single

d) Observed the background spectrum. Make sure it looks similar to **Figure 3.11**. Then wait until the spectrum is stable during time.

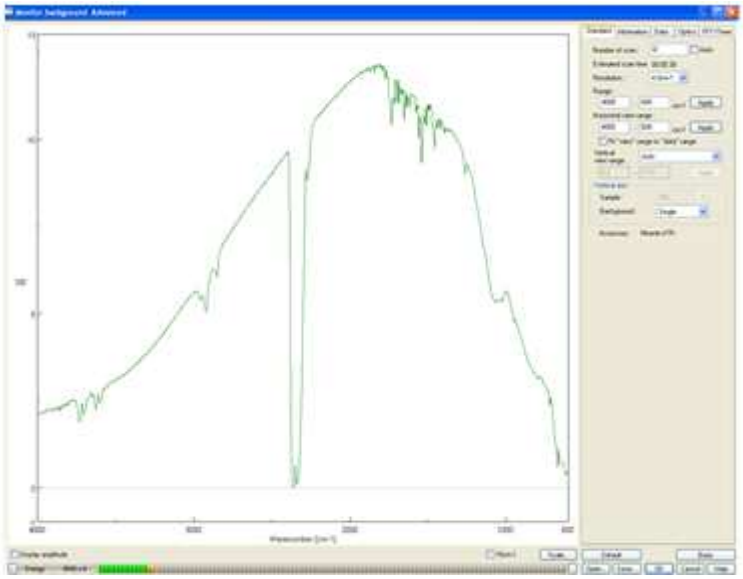

Figure 3.11 Single beam background spectrum for air background

e) Click *ok* at lower right to start the actual measurement. A progress bar is displayed at lower left during data measurement.

5. Sample measurement

a) Place sample onto the ATR crystal, turn the sample clamp knob (coarse) clockwise to increase the pressure exerted on sample until your material is firmly touching the ATR crystal (1 click sounds). Use sample clamp knob (fine) to apply extra pressure if necessary.

b) Click *Monitor Sample* from the *Measure* menu. *Monitor Sample Advanced* window pops out, with a real-time sample spectrum displayed on the left.

c) Make sure the parameters in the *Monitor Sample Advanced* window on the *Standard* tab are the same as those for the background.

d) Wait until the spectrum is stable during time. Then click *ok* at lower right to start the actual measurement. A progress bar is displayed at lower left during data measurement.

6. Save the spectrum

Measured spectrum is automatically sent to *Spectra Analysis* software.

a) Select *Save* from *File* menu.

b) Ensure that the file type is set to *. *jws*. Then put in File name and select the right directory.

c) Click *save* at lower right to save the spectrum.

d) To save file as a *. *txt* file, use *Export* from *File* menu, and make sure the file type is change to *. *txt*.

7. Shut down

a) After measurement, turn the sample clamp knob (coarse) counter-clockwise to release the sample.

b) Clean the ATR crystal with Lens paper.

c) Close Spectra Manager software.

d) Turn off the power switch on top of Jasco 6200.

Operation procedure for Jasco5000

1. Sign up time for Jasco instrument from online google calendar.
2. Turning on Power
   a) Pour liquid nitrogen for the MCT detector
      i. Wear goggle and cold protection gloves, and fill the liquid nitrogen Dewar from the tank in Room 221.
      ii. Remove the lid from the filling port and insert a funnel.
      iii. Pour liquid nitrogen into the funnel slowly till a small amount of liquid nitrogen overflows from the filling port.
      iv. Remove the funnel and replace the lid.
      v. Wait for at least 5 min to let the detector temperature stablize.
   b) Turn on Jasco 6200 (as above).
   c) Turn on the power switch (rear left) of Jasco 5000. Make sure that the LED on the control panel has changed from blinking to lighting. This initialization takes about 1 minute.
3. Open software

Do not open software before initialization*

a) Double-click *Spectra manager* icon on PC desktop.

b) Double-click *MicroScope measurement* under *Instrument – Jasco IR Microscope*

c) Wait for the instrument initialization

4. Observe sample using the microscope on Jasco 5000

a) Adjust the *Brightness* on *Illumination/Zoom* tab in *MicroScope Parameter* window. Start with a low brightness.

b) Adjust the sample stage position with Joystick.

5. Background measurement

a) Make sure to use the transmission sample holder. Confirm that the shutter on the sample stage is open.

b) Select X16 Cassegrain objective lens on *Objective Lens* tab in *MicroScope Parameter* window.

c) Select Transmission mode in *Ref/Trans* tab in *MicroScope Parameter* window. Then click *Auto Correct* in *Trans Focus* tab.

d) Adjust the sample stage position in x-y direction to let IR light go completely through the sample holder.

e) Setting parameter in the *Measurement parameter* window.

f) Click *Monitor Background* from *Measure* menu. A spectrum displays on center top of the window.

g) Observed the real-time background spectrum. Make sure it looks similar to Figure 3.11. Then wait until the spectrum is stable and click *Ok* to start the actual measurement.

6. Sample measurement

a) Place sample onto the sample stage under IR light.

(Uneven sample surface, such as a convex surface at the edge of a drop cast film, redirects the IR beam and distorts the FTIR spectrum, thus it should be avoided during FTIR measurement.)

b) Click *Monitor Sample* from *Measure* menu.

c) Make sure the parameters in the *Monitor Sample Advanced* window on the *Standard* tab are the same as those for the background.

d) Wait until the spectrum is stable during time. Then click *ok* at lower right to start the actual measurement. A progress bar is displayed at lower left during data collection.

7. Save the spectrum (same as Jasco 6200)

a) Click *Send Data to Analysis App* in *File* menu to send the spectrum to *Spectra Analysis* software.

b) Select *Save* from *File* menu in *Spectra Analysis* software.

c) Ensure that the file type is set to **. jws*. Then input file name and select the right directory.

d) Click *save* at lower right to save the spectrum.

e) To save file as a **. txt* file, use *Export* from *File* menu, and make sure the file type is change to **. txt*.

8. Shut down

a) After measurement, remove the sample from sample stage.

b) Close Spectra Manager software.

c) Turn off the power switch on the rear left of Jasco 5000.

d) Turn off the power switch on top of Jasco 6200.

In this thesis, the Jasco IRT-5000 is used in transmission mode in conjunction with a Mettler optical microscopy hot stage FP90 which controls the sample temperature to perform the real-time FTIR studies. The experimental setup for the real-time FTIR studies is shown in **Figure 3.12**. The Jasco IRT-500 can also be operated in the ATR mode with an ATR objective.

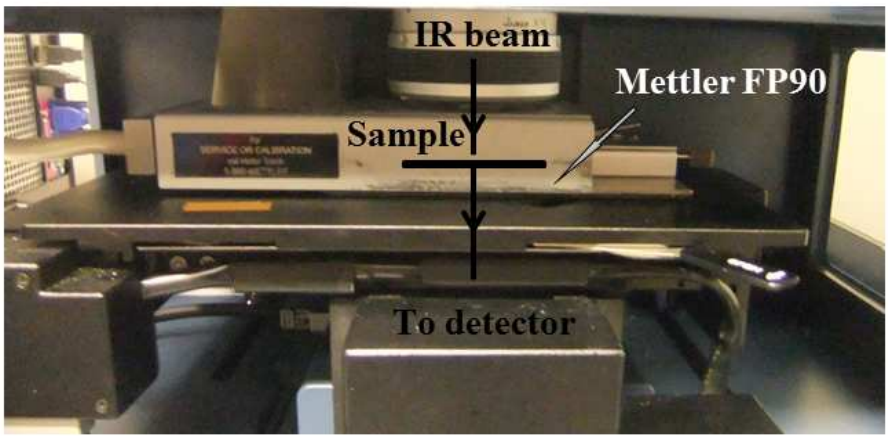

Figure 3.12 Experimental setup for the real-time FTIR studies.

After data collection using Jasco, the data can be viewed and corrected using *Spectra Analysis* software in *Spectra Manager*. The standard data correction procedures include: ATR correction (for ATR mode), baseline correction, extraneous peak elimination and smoothing (optional). When an ATR spectrum needs to be compared with a transmission spectrum in literature, ATR correction must be performed on the ATR spectrum. As shown in equation 3.6, the depth of penetration, d_p, of the evanescent wave is proportional to the wavelength of the incident IR light. The effect of this varying depth of penetration is to change the relative peak heights compared to a transmission spectrum, which gives lower peak intensity at the higher wavenumber range (where the

wavelength is shorter). The ATR correction is to correct the spectrum intensity with a normalized d_p and it is done by the ATR correction in *Spectra Analysis* software, as shown in **Figure 3.13 (a)**. For the transmission mode spectrum, no ATR correction needs to be performed. The baseline correction is used to fix the non-zero baseline or curved baseline. The non-zero baseline is caused by the incomplete subtraction of the air background spectrum from the sample spectrum, and this can be fixed by adding a linear baseline to bring the baselines to zero. The curved baseline is caused by both the incomplete subtraction and Rayleigh scattering. Most ATR crystals have large noise in the low wavenumber range, and this will be amplified by the ATR technique due to the longer d_p in that range. By superimposing the noise onto the sample spectrum, it generally induces baseline drifting in the low wavenumber range. The Rayleigh scattering, on the other hand, generally induces baseline drifting in the high wavenumber range, because the scattering intensity of Rayleigh scattering is proportional to the fourth power of the wavenumber, ν^4 [20]. The curved baseline can be fixed by adding a concave baseline which follows the drifting trend of the sample spectrum, as shown in Figure 3.13 (b). The extraneous peak elimination correction cuts absorption peaks for atmospheric carbon dioxide gas (CO_2), as shown in Figure 3.13 (c). The smooth function is generally used to reduce noise in the spectrum by a mathematical method when the signal to noise ratio is low, and it was not used in this thesis. After data collection using Jasco, the data can be viewed and exported as a text file using *Spectra Analysis* software in *Spectra Manager*. The FTIR data text file is then imported into Matlab to plot Absorption vs. wavenumber plots to get the structural information, especially the secondary structure information of protein samples [11, 12, 21-24].

(a)

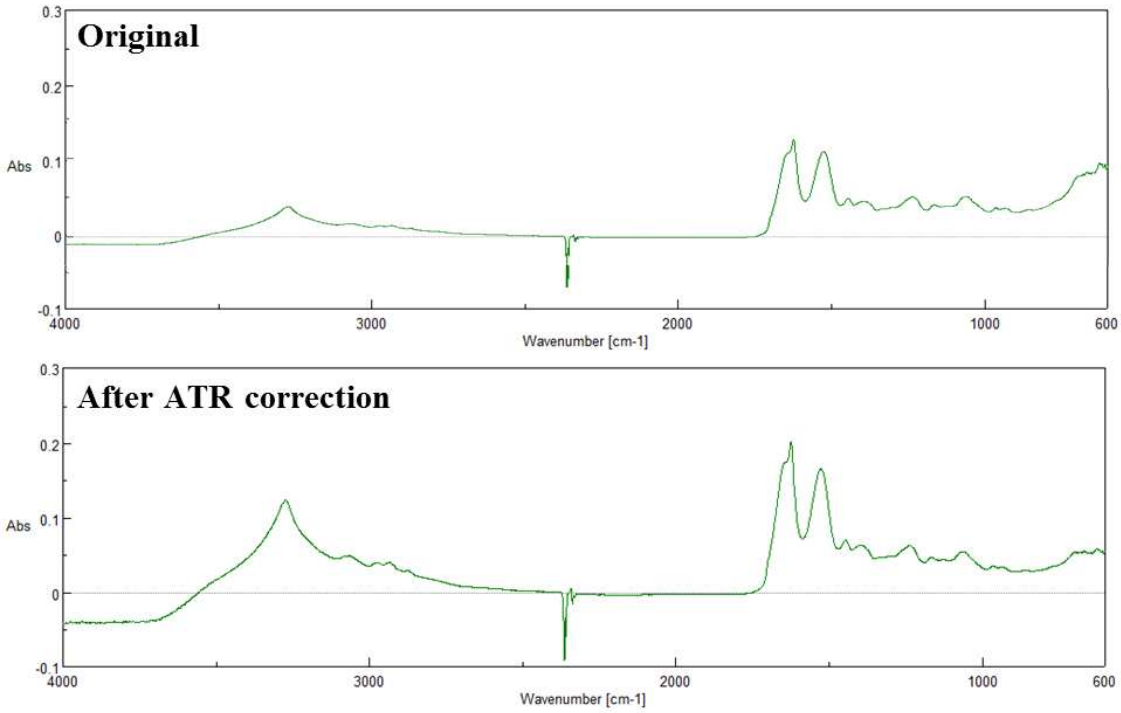
Original
Abs
0.3
0.2
0.1
0
-0.1
4000
3000
2000
1000
600
Wavenumber [cm-1]
After ATR correction
Abs
0.3
0.2
0.1
0
-0.1
4000
3000
2000
1000
600
Wavenumber [cm-1]

(b)

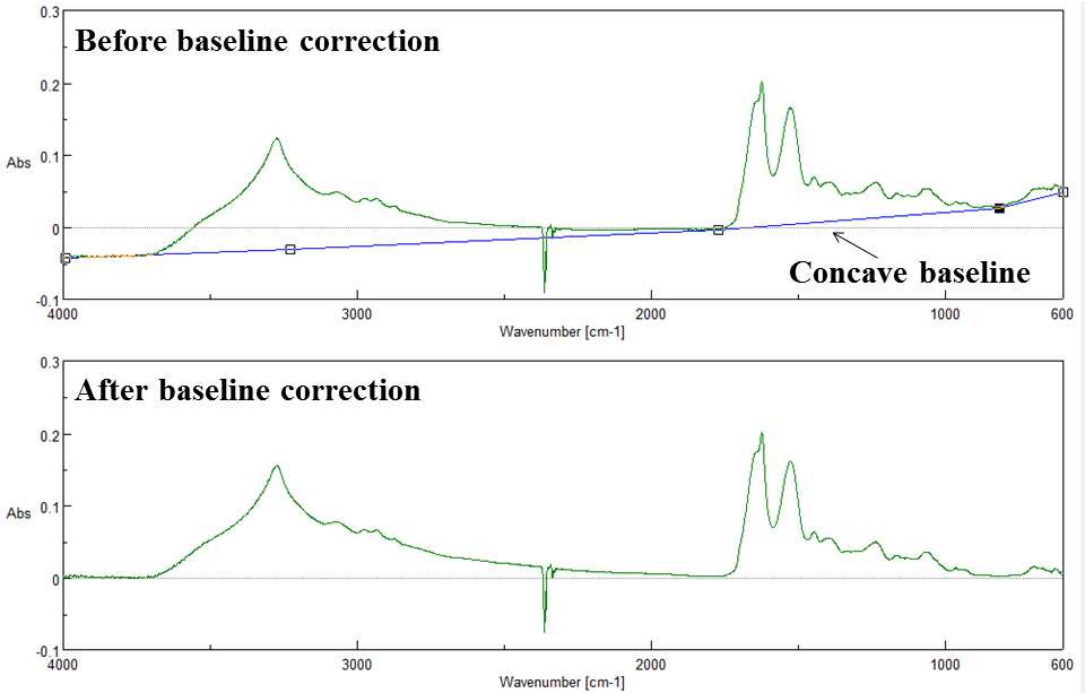
Before baseline correction
Concave baseline
Abs
0.3
0.2
0.1
0
-0.1
4000
3000
2000
1000
600
Wavenumber [cm-1]
After baseline correction
Abs
0.3
0.2
0.1
0
-0.1
4000
3000
2000
1000
600
Wavenumber [cm-1]

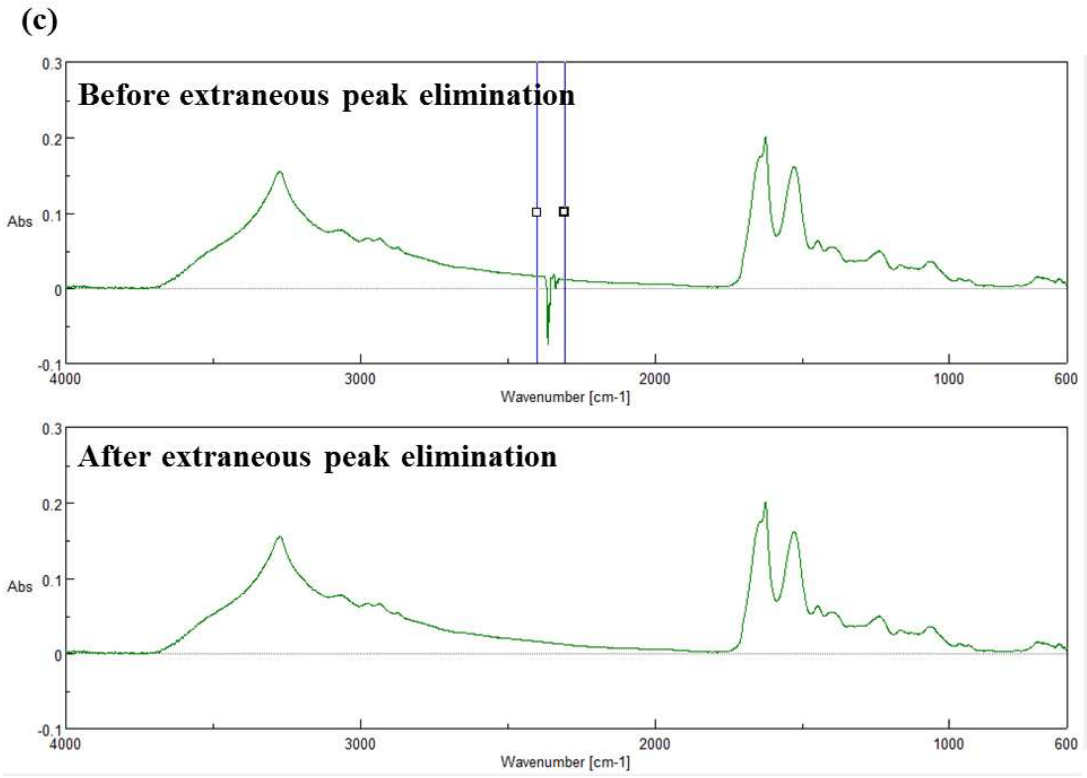

Figure 3.13 (a) ATR correction, (b) baseline correction, and (c) extraneous peak elimination of FTIR absorption spectrum.

The FTIR absorption spectrum in the Amide I region can be used to determine the secondary structure content and the crystallinity, ϕ_{c_FTIR}, of proteins [11, 21]. The theoretical background has been introduced in Chapter II. To calculate ϕ_{c_FTIR}, FTIR spectrum will first be deconvoluted, and then fitted with a series of Gaussian functions. ϕ_{c_FTIR} is the ratio of the area of the beta sheet peak, Q_B, over the total area under the deconvoluted spectrum, Q.

$$\phi_{c\_FTIR} = Q_B / Q \tag{3.7}$$

An FTIR spectrum with low signal-to-noise ratio or containing bound water cannot be

used to do the FSD and curve fitting for proteins.

The standard operating procedure for using Opus to calculate ϕ_{c_FTIR} is listed below.

1. Perform baseline correction in the wavenumber range 1830 – 1330 cm^{-1}.
2. Perform smoothing if needed (5 or 9 point smoothing).
3. Perform Fourier self deconvolution in the wavenumber range 1750 – 1550 cm^{-1}
   a) Choose deconvolution parameters using Lorentzian function:

      Bandwidth: 23-27;

      Noise reduction: 0.30.

   b) Perform the baseline correction and cut the spectrum out for curve fitting in that wavenumber range
4. Fit the deconvoluted curve by a series of Gaussian functions. The peak position is determined by literature and the shape of the curve.
5. Calculate the crystallinity using equation 3.7.

3.3.2 Wide Angle X-ray Diffraction

Wide Angle X-ray Diffraction (WAXD) studies were carried out using a Bruker GADDS D8 X-ray diffractometer (Cu-Kα, wavelength λ = 0.154 nm) operated at 40 kV and 20 mA. X-ray diffraction is a type of characterization technique that is used to analyze the macromolecular structure of polymer and protein tertiary structures [25, 26]. The theoretical background of X-ray diffraction and its application to biopolymers is presented in Chapter II.

Figure 3.14 shows the setup of the Bruker GADDS D8 X-ray diffractometer. The major components of the WAXD system including a GADDS D8 X-ray diffractometer, a Haskris water cooling system, and a computer which is used to set up the experiment and collect data. The main X-ray diffraction unit is used to generate the two dimensional wide angle X-ray diffraction patterns of samples. It is used in conjunction with a cooling accessory, the Haskris water cooling system that is used to cool down the X-ray generator. The water flow rate of Haskris should be at 3 ~ 4 liter/min (about 1.2 gallon/min), and the temperature should be set at 68 ~ 70 F [27, 28].

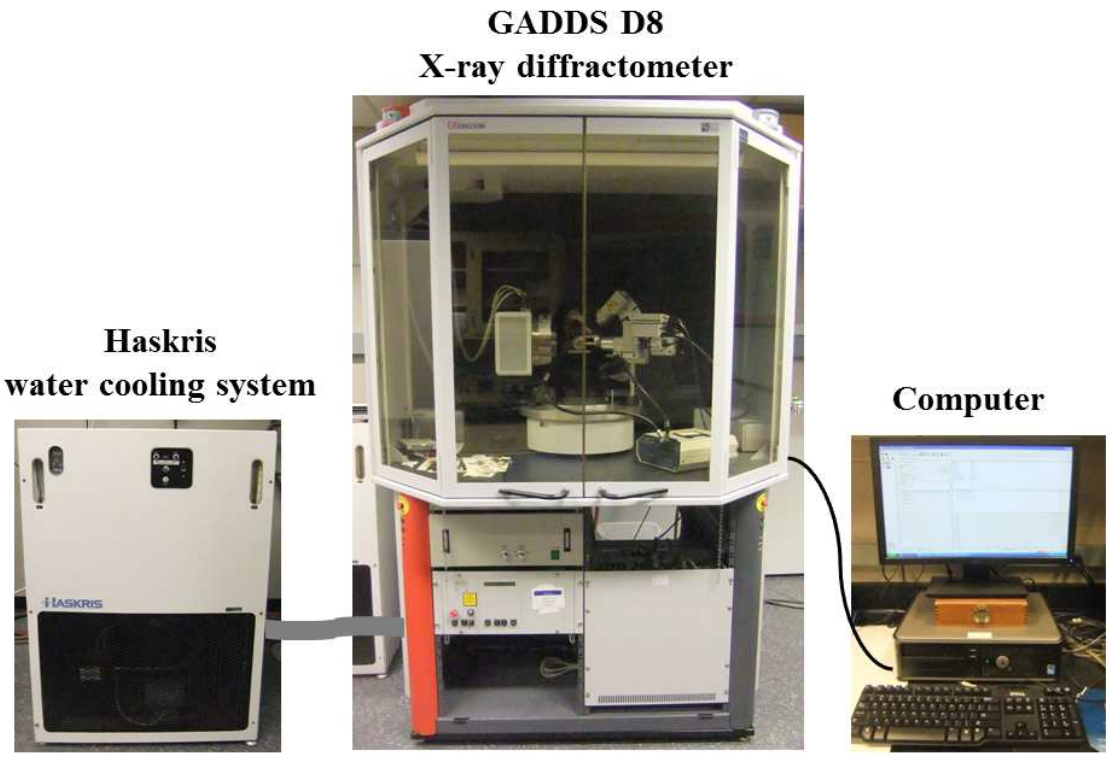

Figure 3.14 Experimental setup of the Bruker GADDS D8 X-ray diffractometer.

The inside view of the GADDS D8 X-ray diffractometer is also shown in **Figure 3.15**. The incident X-ray is generated by the Bruker AXS X-ray tube with copper target, then diffracted by the sample which is mounted on the sample stage that is connected to the goniometer, and finally reaches the detector to form a two dimensional X-ray diffraction pattern.

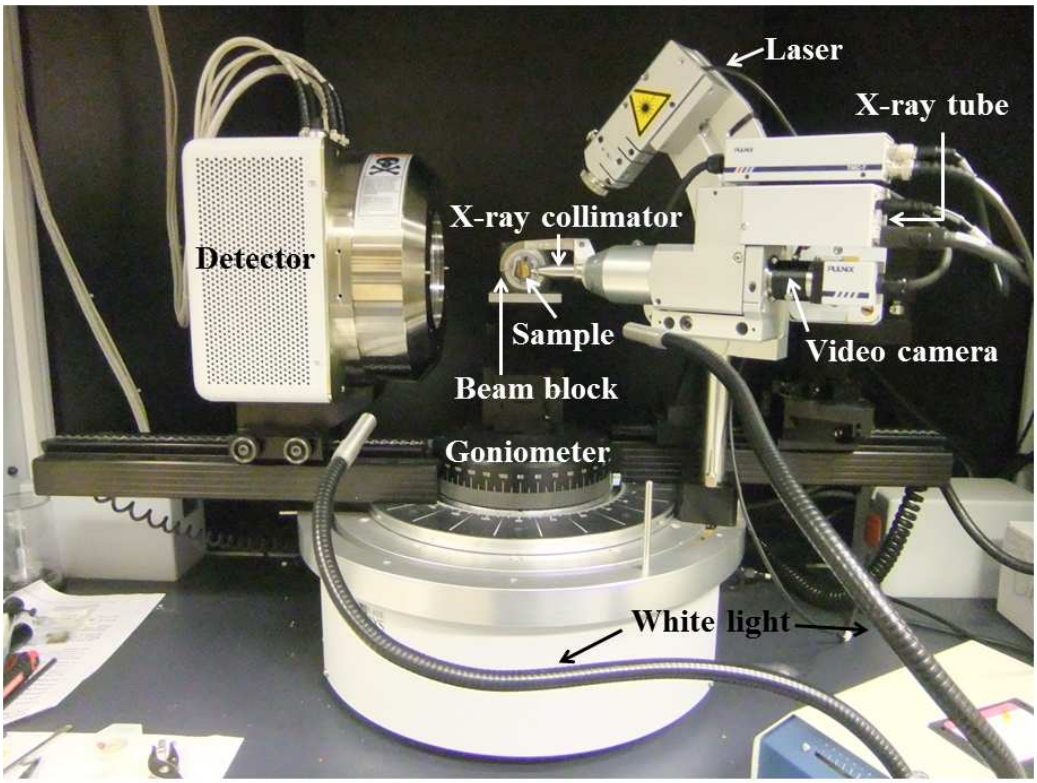

Figure 3.15 The inside view of X-ray diffractometer, showing X-ray generator, sample stage, goniometer and the detector; laser, video camera and white light illumination for sample positioning.

The standard operating procedure for the Bruker GADDS D8 X-ray diffractometer is listed below.

1. Before starting the generator, make sure the Haskris cooling water supply is running properly. (Water flow is about 1.2 gallon/min, and temperature is in the range from 68 to 70 F.)

2. Switch on external power switch (green button on the right of Bruker).

3. Set key switch to the “I” position.

4. Hold the “Heater” key for about 2 seconds.

5. Press the “ON” key. The “X-ray on” signal lamp and the radiation warning lamp of Bruker light up. The X-ray generator is switched on now, and it is at the standby condition: kV=20, mA=5.

(The Bruker is always left at the standby condition, thus user usually starts from here.)

6. Load the sample to the sample stage.

7. Open GADDS software: Desktop -> Shortcut to Bruker AXS -> Gadds

8. Choose yes to change the setup to 40kV and 20 mA.

9. Open the laser: Collect -> Goniometer -> Laser

10. Use the goniometer head tool to adjust the stage until the laser goes through the sample.

11. Close the door, and make sure the “alarm” lamp is off.

12. Set up working directory for data saving: Project -> New -> Working directory.

13. Data collection: Collect -> Scan -> Single run. Set up the running time, 2 theta, file name and click “ok” to start. Wait for data collection and do not open the door when X-ray shutter is open.

14. When finished, save the file as the *.raw* file.

(Repeat step 10-14 for air (or Kapton) background and Si standard reference.)

15. After data collection, convert two-dimensional pattern to a one-dimensional pattern by integrating over azimuthal angle (**Figure 3.16**) avoiding beam block area: Peak -> Integrate -> Chi. Save the X-ray data file (intensity vs. 2θ) as the *.plt* file.

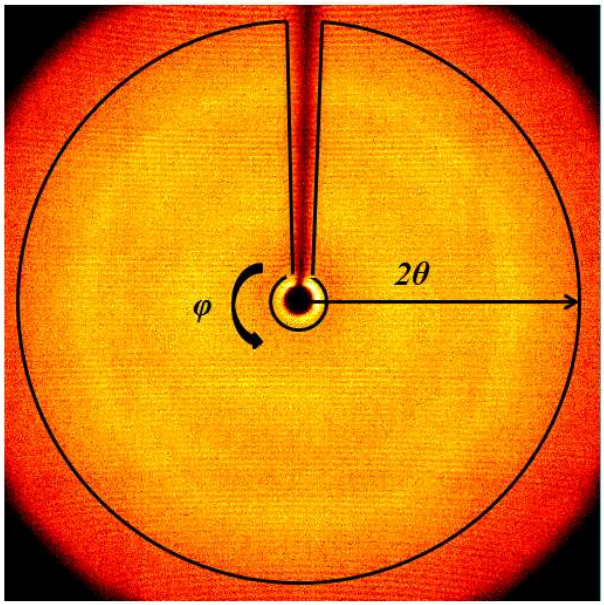

Figure 3.16 Two dimensional X-ray diffraction pattern of spider silk-like block copolymer, HBA_3, showing the integrated area, the direction of azimuthal angle, φ, and scattering angle, 2θ.

16. After test: Project -> exit. Choose "yes" to set generator to standby setting "20kV, 5mA".

After data collection using the Bruker, the two dimensional X-ray diffraction patterns can be viewed using Gadds online or Gadds offline software, and the one dimensional X-ray data, intensity vs. 2θ, can be plotted by Matlab after corrections. The

X-ray intensity will be corrected by subtracting the air (or Kapton) background from the original sample which was taken under the same condition. The 2θ angle is calibrated by using silicon powder reference standard with silicon (111) peak at 28.444° [11].

The corrected WAXD intensity can then be used to calculate the crystallinity index of proteins as discussed in Chapter II. First, the scattering intensity needs to be further corrected by a Lorentz weighting factor [29]. Then, the crystallinity index of the sample can be determined by fitting the Lorentz-corrected scattered intensity Iq^2 vs. q with a sum of Gaussian functions and a quadratic baseline [11, 25, 26]. The crystallinity index, ϕ_{C_Xray}, can be calculated using area of crystal peaks, Q_c, divided by total area, Q, as

$$\phi_{c\_Xray} = \frac{Q_c}{Q} = \frac{\int I_c q^2 dq}{\int I_{corr} q^2 dq} \tag{3.8}$$

A master Matlab program, XRayFitGUI.m, along with four slave programs, XRAYFITCALC.m, XRAYFITGUI.fig, XRAYFITLOOP.m, and XRAYFITPLOT.m, written by Matt Reveley, are used to perform the curve fitting and calculate ϕ_{C_Xray} using equation 3.8.

3.4 Morphology Analysis

Morphology analysis using SEM is conducted at the Center for Nanoscale Systems (CNS), Harvard University.

Scanning electron microscopy (SEM) studies were carried out using Zeiss Ultra55 and Supra55VP scanning electron microscopes. SEM is a type of electron microscope that uses electrons instead of light to form an image. It uses a focused beam of high-

energy electrons to generate a variety of signals at the surface of solid specimens under vacuum to study the surface morphology of samples.

Figure 3.17 shows the setup of Zeiss Ultra55 SEM. Our SEM system includes a main SEM unit, and a computer which is used to set up the experiment and get pictures. As shown in the insert of Figure 3.17, the electron beam is generated by the electron gun and accelerated to an energy in the range of 0.1 - 30 keV, in the vacuum chamber of the main SEM unit [30]. The electron wavelength, λ_{el}, can be expressed by the de Broglie relations as

$$\lambda_{el} = \frac{h}{p} = \frac{h}{mv} = \frac{h}{\sqrt{2meV}} \tag{3.8}$$

where h is Planck's constant, $p = mv$ are the momentum, mass and velocity of the electron, respectively; and e is electron charge. For example, the generated electron has an electron wavelength of 0.018 nm under 5 keV acceleration voltage. Because the electron beam diameter produced directly by the conventional electron gun is too large to generate a sharp image at high magnification, the electron beam is then condensed by the magnetic lens and focused on the sample surface by the scanning coil. Once the focused electron beam hits the sample, the accelerated electrons, which carry significant amounts of kinetic energy, are decelerated in the solid sample, and generate a variety of signals produced by electron-sample interactions. Two major types of electron signals are used to produce SEM images: secondary electrons and backscattered electrons. Secondary electrons are generated when the incident electron excites an electron in the sample and loses most of its energy in the process. The excited electron of the sample moves towards the sample surface undergoing elastic and inelastic collisions, and only the

secondary electron that are very near the surface (<10 nm) can exit the sample surface and be examined [31]. Therefore, secondary electrons are most valuable for showing morphology and topography of samples. Backscattered electrons consist of high-energy electrons originating from the electron beam, which are produced by elastic interactions of beam electrons with nuclei of atoms in the specimen [31]. The production rate of backscattered electrons varies directly with the specimen's atomic number: higher atomic number elements appear brighter than lower atomic number elements. Therefore, backscattered electrons are most valuable for illustrating contrasts in composition in multiphase samples. Because most of the polymer and protein samples are non-conductive, they need to be sputter-coated with gold or platinum before being observed in SEM to prevent the accumulation of surface charge. The resolution of our SEM is about 1 nm at 15 keV and 1.7 nm at 1 keV.

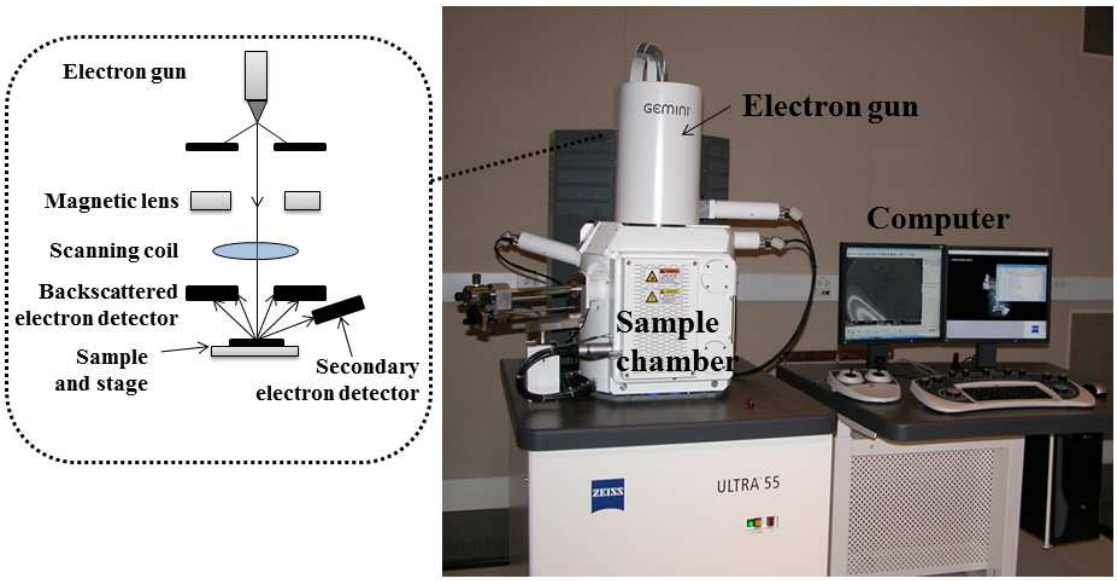

Figure 3.17 The setup of Zeiss Ultra55 SEM at CNS, Harvard University.

The standard operating procedure for Zeiss Ultra55 and Supra55VP SEM is listed below.

1. Sputter-coat samples with Pt/Pd for 60 seconds at 40 mA with Cressington 208HR sputter coater at CNS.
2. Sign up time for SEM experiments at CNS website.
3. Sign the Log book.
4. Start the SEM software by double-clicking on the SmartSEM logo icon on the desktop, and vent the chamber (it takes about 5 min).
5. Load samples onto the sample holder. Once the sample chamber has been vented, open the sample chamber and insert the sample holder onto the sample stage.
6. Pump down the sample chamber by clicking: Vac -> pump.
7. Switch on the beam by clicking: EHT -> ON. (EHT = 5 kV for our case.)
8. Adjust Z position by joy stick first to lift the sample stage close to the detector (WD ~ 7 mm).
9. Adjust magnification, focus, brightness and contrast to get the SEM picture. Start with low magnification first.
10. Correct for any observed astigmatism using the X and Y stig knobs alternately with the focusing knobs to improve picture quality.
11. Select a suitable scanning/noise reduction mode to remove any noise from the image (Pixel average noise reduction mode in our case), click “Freeze” to freeze the image, and then take a picture under the option of “scanning” with a slow scanning speed (scanning speed 8 to 10 in our case).
12. Save the picture by clicking “save”. Input the directory and name for the file.

13. To end the SEM session: the operator should turn off the EHT, vent the chamber, take out the sample holder with samples, pump down the chamber again, and log off the software.

After taking sample pictures with SEM, the pictures are used directly without any further altering.

3.5 References

1. Old RW and Primrose SB. *Principles of gene manipulation: an introduction to genetic engineering, 5th ed*. Oxford England; Boston: Blackwell Scientific, 1994: 1-73.
2. Rabotyagova OS, Cebe P, and Kaplan DL. *Biomacromolecules* 2009; 10(2): 229-236.
3. Wunderlich B. *Thermal analysis of polymeric materials*. Berlin: Springer, 2005: 304-404.
4. Hoèhne G, Hemminger W, and Flammersheim HJ. *Differential scanning calorimetry: an introduction for practitioners, 2nd rev. and enl. ed*. Berlin ; New York: Springer, 2003: 1-65.
5. TA Instrument. *Online DSC operation manual*, 2012.
6. Boller A, Okazaki I, Ishikiriyama K, Zhang G, and Wunderlich B. *Journal of Thermal Analysis* 1997; 49(2): 1081-1088.
7. Ishikiriyama K and Wunderlich B. *Journal of Thermal Analysis* 1997; 50(3): 337-346.

8. Xu H and Cebe P. *Macromolecules* 2004; 37(8): 2797-2806.

9. Ditmars DA, Ishihara S, Chang SS, Bernstein G, and West ED. *Journal of Research of the National Bureau of Standards* 1982; 87(2): 159-163.

10. TA Instrument. *Online TGA operation manual,* 2012.

11. Huang WW, Krishnaji S, Hu X, Kaplan D, and Cebe P. *Macromolecules* 2011; 44(13): 5299-5309.

12. Huang WW, Krishnaji S, Kaplan D, and Cebe P. in prep for *Macromolecules* 2012.

13. Matlab 7.0.1. *Online help*, 2012.

14. Smith BC. *Fundamentals of Fourier transform infrared spectroscopy*. Boca Raton, Fla.: CRC Press, 1996: 1-85.

15. Sandler SR. *Polymer synthesis and characterization a laboratory manua*l. San Diego: Academic Press, 1998: 98-206.

16. Barth A. *Biochimica Et Biophysica Acta-Bioenergetics* 2007; 1767(9): 1073-1101.

17. Ferraro JR and Basile LJ. *Fourier transform infrared spectroscopy: applications to chemical systems*. New York: Academic Press, 1978: 1-98.

18. Theophanides TM and Spectroscopy Society of Canada. *Fourier transform infrared spectroscopy: industrial chemical and biochemical applications*. Dordrecht, Holland ; Boston Hingham, MA, U.S.A.: D. Reidel; Sold and distributed in the U.S.A. and Canada by Kluwer Academic Publishers, 1984: 1-30.

19. Kazarian SG and Chan KLA. *Biochimica Et Biophysica Acta-Biomembranes* 2006; 1758(7): 858-867.

20. Saleh BEA and Teich MC. *Fundamentals of photonics, 2nd ed*. Hoboken, N.J.: Wiley-Interscience, 2007: 58-60.

21. Hu X, Kaplan D, and Cebe P. *Macromolecules* 2006; 39(18): 6161-6170.

22. Hu X, Kaplan D, and Cebe P. *Macromolecules* 2008; 41(11): 3939-3948.

23. Hu X, Lu Q, Kaplan DL, and Cebe P. *Macromolecules* 2009; 42(6): 2079-2087.

24. Huang WW, Krishnaji S, Kaplan D, and Cebe P. in prep for *Biomacromolecules* 2012.

25. Buckley J, Cebe P, Cherdack D, Crawford J, Ince BS, Jenkins M, Pan JJ, Reveley M, Washington N, and Wolchover N. *Polymer* 2006; 47(7): 2411-2422.

26. Huang WW, Edenzon K, Fernandez L, Razmpour S, Woodburn J, and Cebe P. *Journal of Applied Polymer Science* 2010; 115(6): 3238-3248.

27. Haskris. *Standard manual*, 2012.

28. Bruker. *GADDS D8 X-ray diffractometer online help manual*, 2012.

29. Fava RA. *Methods of experimental physics: polymers*. New York: Academic Press, 1980, 16(B), 125.

30. CNS Harvard University. *Guide to Ultra and Supra FESEMs*. 2012.

31. Reimer L. *Scanning electron microscopy: physics of image formation and microanalysis, 2nd completely rev. and updated ed*. Berlin; New York: Springer, 1998: 1-12.

Chapter IV. Heat Capacity of Spider Silk-like Block Copolymers

This chapter studied the thermodynamic properties of spider silk-like block copolymers with respect to protein amino acid sequence. The heat capacities of spider silk-like block copolymers were interpreted by the underlying molecular motion of the constituent amino acids in proteins.

4.1 Introduction

The dragline of *Nephila Clavipes* has been widely studied because of its potential application in tissue engineering and drug delivery [1-3]. Recent studies suggest that at least two proteins, the major ampullate spidroins 1 (MaSp1) and major ampullate spidroins 2 (MaSp2), comprise the spider dragline silk fiber [4]. MaSp1 and MaSp2 proteins are modular in nature. Both of them consist of three specific structural motifs with highly repetitive consensus sequences [4]: (1) the poly-alanine GA/A_n motif, (2) the GGX motif in MaSp1 or GPGG*X* motif in MaSp2, and (3) the N-terminus and C-terminus. Hayashi and co-workers extensively studied the correlation between the sequence, structure, and mechanical properties of spider silk proteins [5, 6]. They associated these motifs with its impact on the mechanical properties of a silk fiber. In particular, alanine-rich 'crystalline module' gives the fiber tensile strength and toughness, and the GG*X* and GPGG*X* 'elasticity module' stabilized the fiber and provide the elasticity and extensibility.

Thermal property studies of spider silk proteins are also very crucial especially for the application in drug delivery [1-3]. To draw a correlation between the sequence, structure, and thermodynamic properties of biomacromolecules, in our work, we synthesize a family of protein block copolymers based on the genetic sequences found in spider dragline silks, and use a model to calculate the heat capacity of spider silk block copolymer in the solid or liquid state, below or above the glass transition temperature, respectively. We characterize the thermal phase transitions and other thermal properties by temperature modulated differential scanning calorimetry (TMDSC) and thermogravimetric analysis (TGA). We also assess the crystal structure and secondary structure by Fourier transform infrared spectroscopy (FTIR) and wide angle X-ray diffraction (WAXD). The methods used here can serve as a standard way to assess the structural features and crystallinity of biological di-block copolymers.

4.2 Experimental Section

4.2.1 Materials

Two spider silk amino acid sequences were picked as the blocks, named A-block (hydrophobic) and B-block (hydrophilic), respectively. A-block and B-block polypeptides were purchased from Tufts Protein Synthesis Laboratory in powder form, and then purified. The di-block copolymers containing a His-tag H were bio-synthesized in our labs. The synthesis method of these block copolymers was described in our previous paper [7]. In brief, after constructing cloning vector, cloning silk modules into a pET30L vector, expressing and purifying spider silk block copolymers, bio-synthesized block copolymers with His-tag H, HAB_3, HBA, HBA_2, and HBA_3, were obtained in solid

form. Protein identification was confirmed by Matrix Assisted Laser Desorption Ionization Mass Spectrometer (MALDI-TOF; Chemistry Department, Tufts University, Medford, MA).

The spider silk block copolymers were dissolved into water at a concentration of 2 mg/ml, and cast into films about 10 microns thick on a Calcium Fluoride (CaF_2) substrate for FTIR. Free standing films about 300 microns thick were also cast from the same solution on Teflon substrate for DSC, TGA and WAXD. Films were placed into a vacuum oven at 25 °C for 24 hours to remove the surface water.

4.2.2 Thermal Analysis

Temperature Modulated Differential Scanning Calorimetry (TMDSC)

Samples with mass about 2 or 3 mg were encapsulated into aluminum pans and heated in a TA Instruments Q100 DSC, which was purged with dry nitrogen gas at a flow rate of 50 mL/min. The temperature and heat flow of the DSC were carefully calibrated using indium standard before experiments. The samples were annealed in the DSC at 120 °C for 60 min to eliminate the surface water absorbed during handling before each run. The total weight of pan and lid for sample encapsulation and reference were kept the same in all runs.

TMDSC was performed at a heating rate of 2 °C/min from -30 °C to 350 °C with oscillation amplitude of 0.318 °C and a modulation period of 60s. To measure the reversing heat capacity, we used a “three run method”, as described in our earlier work [8]. The first run is empty aluminum sample pan versus empty aluminum reference pan to obtain the cell asymmetry and baseline correction. The second run is sapphire

standard in aluminum pan versus empty aluminum reference pan to calibrate heat flow amplitude according to standard equations [9, 10]. The third run is sample in aluminum pan versus empty aluminum reference pan. The same empty aluminum reference pan was used in all the runs, and all the aluminum sample pans were kept the same in weight.

The basic mechanism of quantitative TMDSC involves adding a sinusoidal temperature modulation to the conventional linear temperature ramp to separate reversing and non-reversing heat effects within the temperature range of the modulation. The time dependence of sample temperature is expressed as:

$$T_s(t) = T_0 + qt + A_T \sin(\omega t - \varepsilon) \tag{4.1}$$

where T_0 is the initial temperature, q is the underlying linear heating rate, A_T is the corresponding modulation amplitude, ω is the modulation frequency, and ε is the phase shift with respect to the reference.

In TMDSC, the signal deconvolution is accomplished by a mathematical technique known as Discrete Fourier Transformation (DFT) [11]. As the first step in the deconvolution process, the raw data are averaged over one complete period to remove the modulation. This gives the total heat flow and the deconvoluted temperature, which is equivalent to information obtained by standard DSC. Then the averaged signal is subtracted from the raw data and DTF procedure is applied with a sliding transform window to obtain the amplitude and phase difference of the heat flow response at modulation frequency ω so as to obtain the reversing heat capacity [12]. The heat capacity in TMDSC can be expressed as:

$$\left| mc_p + C_{sp} - C_r \pm \Delta C_{cell} \right| = \frac{A_\Delta}{A} \sqrt{(\frac{K}{\omega})^2 + C_r^{\,2}} \tag{4.2a}$$

$$= \frac{A_{HF}}{A} K' \qquad (4.2b)$$

where mc_p is the heat capacity of a sample of mass, m, and specific heat capacity, c_p; C_{sp} and C_r are the heat capacities of the sample pan and empty reference pan, respectively; ΔC_{cell} is the cell asymmetry correction [8]. On the right hand side of Equation 4.2a, A_Δ is the amplitude of temperature difference between sample and reference; A is the sample temperature modulation amplitude; K is Newton's law calibration constant. In Equation 4.2b, A_{HF} is the heat flow amplitude and K' is a calibration constant [13] related to the experimental conditions.

Using the sample specific heat capacity c_p, determined by the "three run method" and Equation 4.2b, we obtain the reversing heat flow, *RHF(t)* as:

$$RHF(t) = mc_p \cdot q \qquad (4.3)$$

The non- reversing heat flow, *NHF(t)*, is computed as the difference between the total heat flow, *HF(t)*, and the reversing heat flow, *RHF(t)*:

$$NHF(t) = HF(t) - RHF(t) \qquad (4.4)$$

Since thermodynamic equilibrium has not been assured during scanning, the term "reversing" is used rather than "reversible". The reversing heat flow refers to that component which is reversing within the time scale of the temperature oscillation. The glass transition phenomenon is an example of a transition which is reversing. Non-reversing processes include melting and crystallization, or degradation.

Thermogravimetric Analysis (TGA)

Samples with masses about 4.0 mg or 5.0 mg were encapsulated in aluminum DSC pans to prevent powder sample from being blown out of the pan by nitrogen gas flow. Several holes (d ~ 1mm) were made on DSC lids to let the sample surface be exposed to the atmosphere to let degradation products escape. Samples were heated in a TA Instruments Q500 thermogravimetic analyzer, which was purged with a dry nitrogen gas at a flow rate of 60 mL/min. Before each run, the empty pan was used to calibrate the zero point of the total weight. The experiments were performed at a heating rate of 2°C/min from 25 °C to 400 °C.

4.2.3 Wide Angle X-ray Diffraction (WAXD)

Water cast sample films about 300 microns in thickness were mounted in a Bruker GADDS D8 X-ray diffractometer (wavelength λ = 0.154 nm) operated at 40 kV and 20 mA. Scattering angle, 2θ, was calibrated by using silicon powder reference standard with silicon (111) peak at 28.444º. The scan time used was 1800 s per sample. The scattering angle, 2θ, ranged from 4º to 28°. The air background was subtracted from the original scan for each sample. To compare the peak position and identify the crystalline content, the 2-D WAXS patterns were converted to a one-dimensional pattern by integrating with χ over all sectors (the beam stop region is avoided). The baseline was determined by subtracting air background and fitted using quadratic baseline. The crystallinity index, ϕ_{c_Xray}, was calculated using the ratio of the area of crystal peaks to the total scattered intensity by fitting the Lorentz-corrected WAXS peak intensity using Gaussian wavefunctions as described previously [14, 15].

4.2.4 Fourier Transform Infrared Spectroscopy (FTIR)

Water cast sample film about 10 microns in thickness was cast onto CaF_2 substrate for FTIR measurements. Fourier transform infrared spectroscopy was carried out on a Jasco FT/IR-6200 with a TGS detector. The absorbance spectra were obtained by averaging 128 scans with a resolution of 4.0 cm^{-1}. The background spectra were collected under the same conditions and subtracted from the scan for each sample.

4.3 Theoretical Basis

4.3.1 Calculation of Solid State Heat Capacity of Dry Block Copolymers

The heat capacity in the solid state of the genetically engineered spider silk block copolymers is determined based on the assumption that at sufficiently low temperature, the major part of the total heat capacity comes from vibrational motion. This common assumption has been successfully applied to calculate the heat capacity of synthetic polymers [16] as well as bio-polymers, *Bombyx mori* silk fibroin [17, 18], from 0 K to the glass transition temperature.

The total solid vibrational heat capacity of dry spider silk block copolymer film, $C_{p,vib}^{Block\ copolymer}$, can be estimated as a linear combination of the vibrational heat capacities of each block through [16]:

$$C_{p,\,vib}^{Block\ copolymer} = n_A C_{p,\,vib}^{Block\ A} + n_B C_{p,\,vib}^{Block\ B} + n_H C_{p,\,vib}^{Block\ H} \qquad (4.5)$$

where $C_{p,vib}^{Block\ A}$, $C_{p,vib}^{Block\ B}$, and $C_{p,vib}^{Block\ H}$ are the solid vibrational heat capacity of each block, A, B and H; while n_A, n_B and n_H are the molar ratios of each block in the block

copolymers. For example, in 1 mol block copolymer HBA_3, the molar ratios are $n_A = 3$, $n_B = 1$ and $n_H = 1$.

Following the method of Pyda, *et al*. [16] the solid vibrational heat capacity of each block, $C_{p,\,vib}^{block\ I}$ *(I = A, B* or *H)*, is constructed as a sum of products of the vibrational heat capacities of the individual poly(amino acid) residues, $C_p(i)$, by Equation 4.6 using the Advanced Thermal Analysis System (ATHAS) data bank [19].

$$C_{p,\,vib}^{Block\ I} = N_{Ala}C_p(Ala) + N_{Gly}C_p(Gly) + N_{Ser}C_p(Ser) + \cdots + N_{Thr}C_p(Thr)$$

$$= \sum_i N_i C_p(i) \qquad (4.6)$$

where N_i is the total number of each kind of amino acid present in the amino acid sequence of an individual block. For example, in block A, $N_{Ala} = 7$, $N_{Gly} = 5$ *and* $N_{Ser} = N_{Thr} = 1$. Among 20 amino acids, the solid vibrational heat capacity data of 12 of them, alanine, asparagine, glycine, histidine, leucine, methionine, phenylalanine, proline, serine, tryptophan, tyrosine, and valine, are recorded in ATHAS data bank. But for other amino acids, such as arginine, aspartic acid, cysteine, glutamic acid, glutamine, isoleucine, lysine, and threonine, the solid vibrational heat capacity data are not available in the ATHAS data bank. Therefore, we present a strategy [20] to estimate the unknown ones by the following method. (a) Because the side chain difference between threonine and serine is the same as the difference between alanine and glycine (**Figure 4.1a**), $C_p(Thr)$ can by estimated by using the solid vibrational heat capacities of other amino acids, which can be found in ATHAS data bank [21]. To estimate $C_p(Thr)$, we used:

$$C_p(Thr) - C_p(Ser) = C_p(Ala) - C_p(Gly) \qquad (4.7a)$$

For the same reason $C_p(Gln)$ can also be estimated by using $C_p(Asn)$, $C_p(Leu)$ and $C_p(Val)$ (**Figure 4.1a**). (b) For arginine, which has a relatively more complicated side chain, no amino acid with a similar structure can be found. But in the ATHAS data bank we find heat capacity data for poly(arginine) hydrogen chloride, poly(histidine) hydrogen chloride, and poly(histidine). Assuming the influence of HCl is the same for both poly(arginine) and poly(histidine) (**Figure 4.1b**), we estimate $C_p(Arg)$ from:

$$C_p(Arg-HCl) - C_p(Arg) = C_p(His-HCl) - C_p(His) \quad (4.7b)$$

$C_p(Lys)$ can also be estimate by this method (**Figure 4.1b**). The total solid vibrational heat capacity of spider silk block copolymers from the glass transition up to 1000 K were calculated using the strategy outlined above.

In TMDSC or DSC, the heating rates are not fast enough to prevent degradation of the biopolymers just above T_g. However, faster scanning rates are possible using thin-film (chip) calorimetry, which provides scanning rates as high as several thousand Kelvin per second [22]. For these fast scanning rates, the sample degradation could be deferred to a much higher temperature. Thus, extension of the calculated total solid vibrational heat capacity to temperatures above the TMDSC-determined glass transition could serve as a baseline for the fast heating techniques.

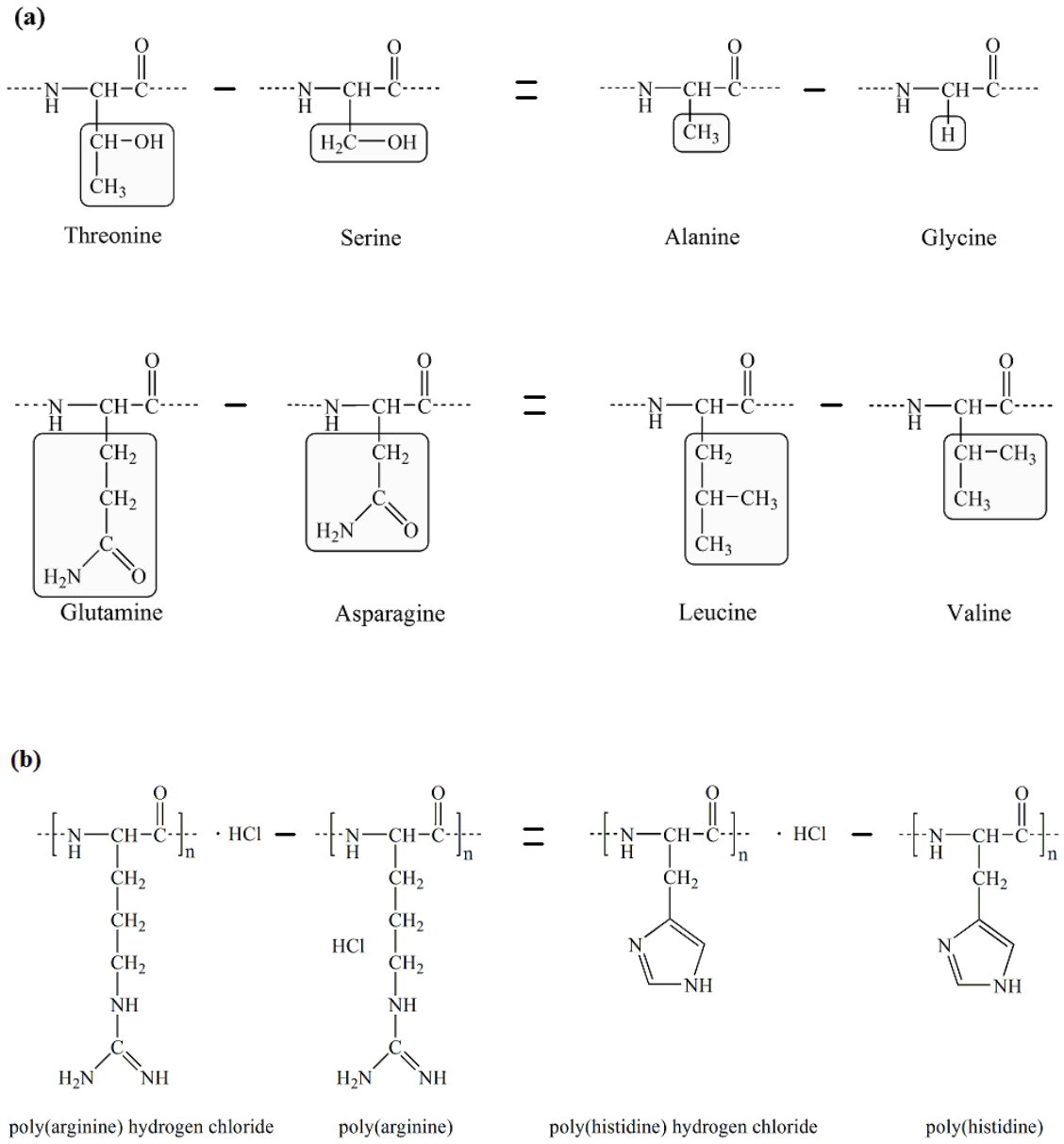

Figure 4.1 General scheme to estimate the vibrational heat capacity of an amino acid using an equation format for the chemical structure, illustrated by: (a) threonine and glutamine, with side chain of each amino acid highlighted by a rectangle, and (b) poly(arginine).

4.3.2 Calculation of Liquid State Heat Capacity of Dry Block Copolymers

The heat capacity in the liquid state (*i.e.*, viscous liquid, or rubbery state, of the polymer above T_g) is more complicated to estimate. Because the contribution comes not only from the vibrational motion, but also from the rotational and the translational degrees of freedom, all of them should be taken into consideration. According to Wunderlich [23], each mobile unit in the polymer chain on average contributes 11 J/(mol K) to the change of heat capacity at the glass transition temperature, T_g. The number of mobile units of each kind of amino acid residue in our block copolymers can be determined from their chemical structure, shown in **Figure 4.2**.

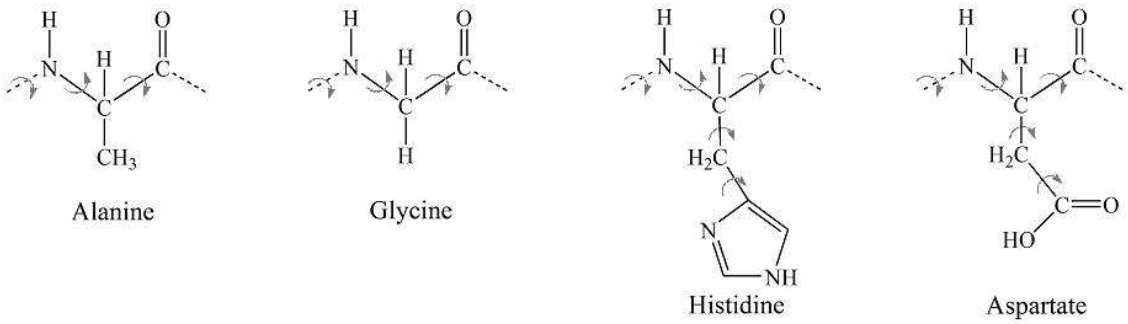

Figure 4.2 Mobile units in the amino acid residues, exemplified by alanine, glycine, histidine and aspartic acid. The arrows represent one rotational bond in each type of amino acid residue that changes the conformation of the chain at T_g. Alanine and glycine have 3 mobile units, while aspartate and histidine have 5 mobile units.

By adding up the rotational bonds in the individual amino acid residues, the total number of mobile units that start to mobilize at T_g can be calculated. According to Pyda

[17], this rotational degree of freedom contributes approximately 91% of the heat capacity increment, ΔC_p, at the temperature T_g in dry *Bombyx mori* silk fibroin. Though the sequence of the amino acid residues is different in a spider silk block copolymers, we assume this approximation should still be valid in our bio-material, because genetically engineered spider silk block copolymers also consists of similar amino acid sequences to *Bombyx mori* silk. Thus, the total degrees of freedom contributing to the change in heat capacity can be estimated as the sum of the contribution from each mobile unit divided by 91%. For example, there are 44 rotational bonds in one A-block, thus the heat capacity increment of A-block at the glass transition temperature is ΔC_p*(A-block)* = 44 x 11 J/(mol K) / 91% = 537.8 J/(mol K).

4.4 Results and Discussion

4.4.1 Modeling the Heat Capacity of Spider Silk Block Copolymer in the Solid and Liquid States

Determination of the heat capacity in the solid state of spider silk block copolymer from 0 K to the glass transition region is based on the assumption that contributions to the heat capacity come only from vibrational motions, C_p*(solid)* = C_p*(vibrational)*. It has been extensively studied that water in polymeric systems can affect the total heat capacity and the glass transition temperature [18, 24-26]. To obtain the true glass transition temperature of dry spider silk block copolymers, we anneal the samples at 120 °C to eliminate the effect of bound water. During annealing, the water molecules escaped, and the total weight of sample changed. To avoid absorbing surface water from air again, we kept the sample in the DSC and estimate the sample weight after

annealing by running the same experiment with TGA. After annealing, the spider silk block copolymers are free of bound water, and their true experimental reversing heat capacity was measured by TMDSC. Figure 4.3 a–d shows a comparison of the calculated vibrational heat capacity (solid lines), C_p*(vibrational)*, with the experimental heat capacity (thick solid lines), C_p*(experimental)*, of spider silk block copolymers, HAB_3, HBA, HBA_2 and HBA_3, respectively. C_p*(experimental)* was displayed only in the region (from -30 ºC up to about 200 ºC) for which region we are confident no degradation occurred in the samples. The vibrational heat capacity was constructed using the vibrational motion spectra of the individual amino acids (found in the ATHAS data bank [21] or estimated from the procedure of Figure 4.1) using Equations 4.5, 4.6 and 4.7, following the scheme discussed above.

The vibrational heat capacity of individual poly amino acids in ATHAS were first calculated by Wunderlich and co-workers [27, 28], and developed by Pyda to apply them to the other biopolymers, such as *Bombyx mori* silk fibroin [16]. In the present work, we further applied this calculation to a bio-block copolymer system. The detailed amino acid compositions and their properties in A-block, B-block, and H-block are summarized in Table 4.1a, 4.1b, and 4.1c, respectively. Note that $M_w(i)$ is the molecular weight mass of the repeating unit of the poly(amino acids). For example, we used the molecular weight mass of the repeating unit of poly(glycine), 75.97 – 18.02 = 57.05 g/mol, rather than the molecular weight of glycine, 75.97 g/mol, to calculate the molar mass of A-block and B-block. The numbers, N_i, are the total numbers of each type of amino acid existing in the block copolymer, e.g. N_{gly} = 5 in the A-block. Knowing the numbers N_i and their corresponding poly(amino acid)s' vibrational heat capacities as a function of temperature

(from the ATHAS data bank or estimated), the calculated solid state heat capacity of spider silk block copolymers from 0.1 K to 600K can be constructed by a linear combination of the vibrational heat capacity of each amino acid component. Excellent agreement was found between the measured and calculated values of the heat capacity between 250 K and the glass transition temperature T_g with an error of ±1%. This agreement supports the conclusion that only the vibrational motion of the amino acid components contributes to the heat capacity below T_g and also shows that this can serve as a standard method to predict the solid state heat capacity for other biologically inspired block copolymers.

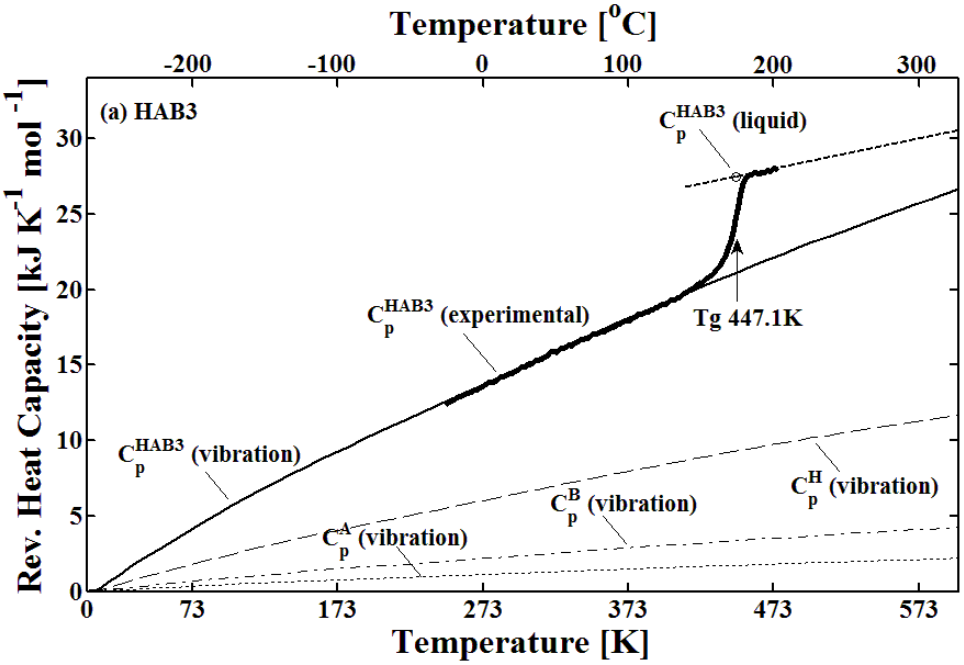

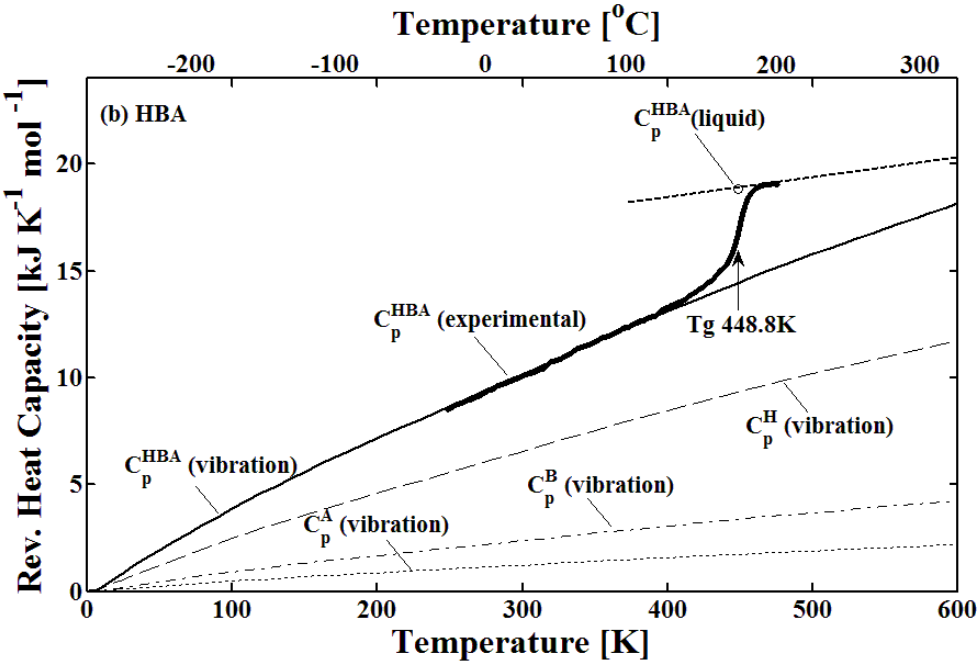
Temperature [^{0}C]
-200
-100
0
100
200
300
(b) HBA
C_p^{HBA}(liquid)
C_p^{HBA} (experimental)
Tg 448.8K
C_p^{H} (vibration)
C_p^{HBA} (vibration)
C_p^{B} (vibration)
C_p^{A} (vibration)
Rev. Heat Capacity [kJ K^{-1} mol^{-1}]
0
5
10
15
20
0
100
200
300
400
500
600
Temperature [K]

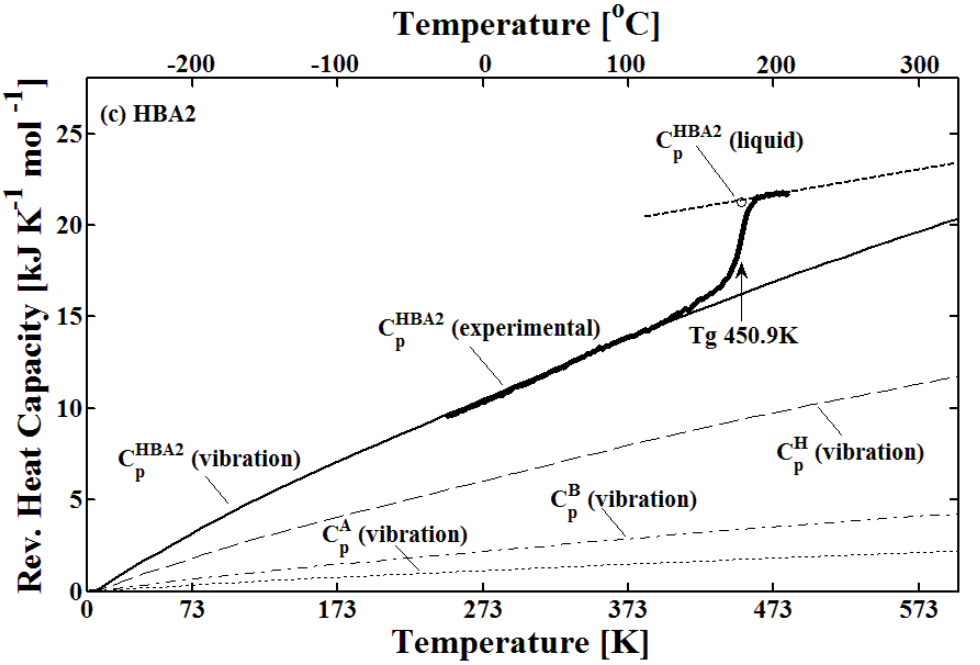
Temperature [^{0}C]
-200
-100
0
100
200
300
(c) HBA2
C_p^{HBA2} (liquid)
C_p^{HBA2} (experimental)
Tg 450.9K
C_p^{H} (vibration)
C_p^{HBA2} (vibration)
C_p^{B} (vibration)
C_p^{A} (vibration)
Rev. Heat Capacity [kJ K^{-1} mol^{-1}]
0
5
10
15
20
25
0
73
173
273
373
473
573
Temperature [K]

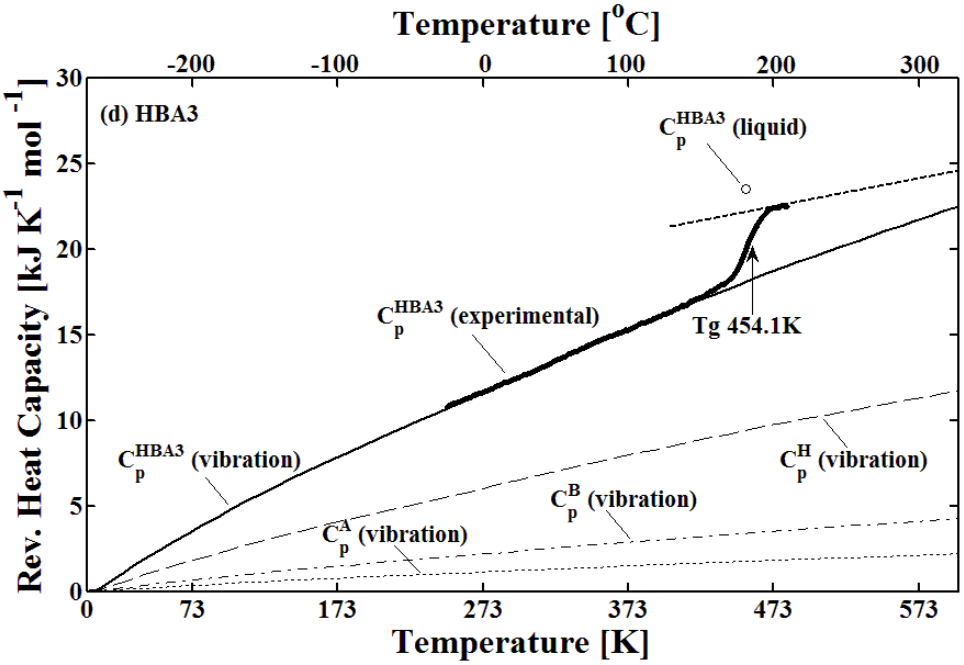

Figure 4.3 The experimentally measured and calculated apparent reversing heat capacity vs. temperature, after annealing at 120 °C, for dry films of: (a) HAB_3, (b) HBA, (c) HBA_2, and (d) HBA_3. Heavy curve -- *C_p(experimental)*; thin solid curve -- *C_p(vibrational)*; open circles -- *C_p(liquid)* calculated at T_g. The individual solid state heat capacities of A-block (dotted curve), B-block (dash-dot curve), and His-tag (dashed curve) are shown for reference. Heavy dashed lines are extrapolated best fits to experimental curve above T_g.

The heat capacity in the liquid state (viscous liquid, or rubbery state, of the polymer above T_g), *C_p(liquid)*, of spider silk block copolymer above the glass transition can be estimated by the considering the contribution comes not only from the vibrational motion, but also from the rotational and translation motion in polymer side chains and backbone. Calculations of the liquid heat capacity for synthetic polymers [29] and a few experimental liquid heat capacity data for biopolymers [13, 18] are available but only for

a limited temperature range above the glass transition. Empirically, it was found that the liquid state heat capacity is often a linear function of temperature with a smaller slope than that of the solid state heat capacity [17, 29, 30]. In **Table 4.1a-c**, we summarize the number of rotational bonds of the individual amino acids, RB_i, in each block. Knowing the RB_i, the heat capacity increment at the glass transition temperature can be estimated by assuming each rotational bond on average contributes 11 J/(mol K) to the change of heat capacity at the glass transition temperature[33]. Figure 4.3 a-d shows a comparison of the calculated liquid state heat capacity (open circles) of 100% non-crystalline spider silk block copolymers, C_p*(liquid)* evaluated at T_g, along with the best fit line of the experimental liquid state heat capacity (heavy dashed line). In the case of wholly amorphous copolymers, HAB_3, HBA, and HBA_2, good agreement exist between the best fit line of the experimental values and the calculated value of the heat capacity (Figure 4.3 a-c, open circles) at the glass transition temperature T_g within ±3%. HBA_3 is an exception - the extrapolated line of best fit to the data does not pass through the calculated value of C_p*(liquid)* because this sample is partially crystalline (crystallinity reduces the heat capacity increment at T_g). The good agreement for amorphous samples supports the conclusion that the vibrational, rotational, and translational motions of the amino acid components all contribute to the liquid state heat capacity above T_g. This agreement also demonstrates the utility of this model to serve as a standard method for predicting the liquid state heat capacity at T_g for other biologically inspired block copolymers.

Table 4.1a Amino Acids in the A-Block and Their Parameters

Amino Acid	M_w **(g/mol)**	***Number***	***Rotatable Bonds***
alanine (Ala) - A	71.082	7	3
glycine (Gly) - G	57.05	5	3
serine(ser) -S	87.078	1	4
threonine(thr) - T	101.10	1	4
A-block Totals	**970.99** [a]	**14**	**44**

[a] Sum of: M_w x Number

Table 4.1b Amino Acids in the B-Block and Their Parameters

Amino Acid	M_w **(g/mol)**	***Number***	***Rotatable Bonds***
glycine(gly) – G	57.05	11	3
leucine(leu) - L	113.16	2	4
glutamine(gln) – Q	128.13	3	6
arginine(arg) – R	156.19	1	8
serine(ser) – S	87.08	3	4
threonine(thr) – T	101.10	1	4
tyrosine(tyr) – Y	163.17	1	4
B-block Totals	**1919.97** [a]	**22**	**87**

[a] Sum of: M_w x Number

Table 4.1c Amino Acids in the His-Tag and Their Parameters

Amino Acid	M_w **(g/mol)**	***Number***	***Rotatable Bonds***
histidine (His) – H	137.14	7	5
alanine (Ala) – A	71.08	6	3
aspartate(Asp) – D	115.09	6	5
glutamate(Glu) – E	129.11	2	6
phenylalanine (Phe) – F	147.17	1	4
glycine (Gly) – G	57.05	4	3
lysine (Lys) – K	128.17	3	7
leucine (Leu) – L	113.16	2	4
methionine (Met) M-	131.20	4	6
proline (Pro) – P	97.12	2	4
glutamine (Gln) -Q	128.13	1	6
arginine (Arg) – R	156.19	2	8
serine(Ser) – S	87.08	5	4
threonine(thr) – T	101.10	2	4
valine(Val) - V	99.13	1	3
His-tag Totals	**5217.67** [a]	**48**	**225**

[a] Sum of: M_w x Number

4.4.2 Determining the Crystallinity of Spider Silk Block Copolymer by TMDSC

The crystallinity of semicrystalline synthetic polymers is conventionally determined by the enthalpy of fusion from the area of the DSC melting endotherm using $\varphi_C = \Delta H(measured)/\Delta H_f$ where $\Delta H(measured)$ is the heat of fusion obtained from the area of melting peak and ΔH_f is the heat of fusion of 100% crystalline polymer. But, for bio-polymers, usually no thermal melting peak can be observed because of their low thermal stability (bio-polymers degraded before melting). Thus, usually it is not possible to determine the crystallinity of bio-polymers by DSC. However, if we know the theoretical value of the solid state heat capacity and the liquid state heat capacity using the vibrational heat capacity model, we can use an alternate method to calculate the crystallinity by DSC.

The crystallinity of spider silk block copolymers can be determined from their calculated solid state heat capacity, $C_p(vibrational)$, liquid state heat capacity, $C_p(liquid)$, and experimental heat capacity curves, $C_p(experimental)$. By analogy to semicrystalline synthetic polymers [8, 31-33], spider silk block copolymers will be modeled as comprising three phases: (1) the mobile fraction, ϕ_M, (2) the crystalline beta-sheet fraction, ϕ_C, and (3) the immobilized non-crystalline fraction, ϕ_{IMM}. The immobilized non-crystalline fraction, $\phi_{IMM,}$ is an analogue to the rigid amorphous fraction (RAF) in semicrystalline synthetic polymers, which is amorphous material assumed not to participate in the conventional glass transition process [34]. The beta-sheet crystals fraction, ϕ_C, and the immobilized non-crystalline portions, ϕ_{IMM}, remained solid-like above the T_g and constitute the rigid fraction, ϕ_{RIGID}, in spider silk block copolymer. The

amorphous region (turns, random coils, alpha helices, etc.) of spider silk block copolymer constitutes the mobile fraction, $\phi_{M.}$ Therefore, a three-phase model can be used to describe the phase structure of spider silk block copolymer by:

$$\phi_{RIGID} + \phi_M = (\phi_C + \phi_{IMM}) + \phi_M = 1 \tag{4.8}$$

Because the crystalline beta-sheet fraction and the immobilized noncrystalline fraction have less molecular mobility, they do not contribute to the glass transition [34]. The heat capacity increment at T_g, ΔC_p, can be used to deduce the mobile fraction, ϕ_M, from:

$$\phi_M = \Delta C_p / \Delta C_{p0} = [\Delta C_p / (C_p(vibrational) - C_p(liquid))]\Big|_{T_g} \tag{4.9}$$

where ΔC_p is the heat capacity increment at T_g; ΔC_{p0} is the calculated heat capacity increment for the 100% noncrystalline spider silk block copolymers, which is the difference between $C_p(vibrational)$ and $C_p(liquid)$ at T_g.

Table 4.2 lists the measured heat capacity increment, ΔC_p, calculated heat capacity increment for the 100% noncrystalline samples, ΔC_{p0}, and mobile fraction, ϕ_M, calculated from Equation 4.9. The rigid fraction, ϕ_{RIGID}, is deduced by subtracting ϕ_M from unity as discussed in Equation 4.8. The error ranges listed in the table show sample-to-sample variations in the heat capacity as well as experimental error, such as the cell asymmetry within ± 0.01 J/g K during measurements. To validate our model, we also used two alternate methods to determine the crystallinity.

Table 4.2. Heat Capacity Increment, Mobile, Rigid, and Crystalline Fractions of Spider Silk Block Copolymers

Sample	ΔC_p (kJ/mol K) [a] (±0.02)	ΔC_{p0} (kJ/mol K) [b]	ϕ_M [c] (±0.02)	ϕ_{RIGID} [c] (±0.02)	ϕ_{C_Xray} (±0.03)	ϕ_{C_FTIR} (±0.03)
B	1.06	1.05	1.0	0	0.03	0
HAB_3	6.39	6.41	1.0	0	0.03	0
HBA	4.31	4.30	1.0	0	0.02	0
HBA_2	4.80	4.84	1.0	0	0.02	0.03
HBA_3	4.05	5.37	0.74	0.26	0.26	0.28
A	0.38	0.53	0.70	0.30	0.31	0.33

[a] Measured data

[b] Calculated heat capacity step at T_g using RB_i from Table 4.1

c The mobile fraction ϕ_M and rigid fraction ϕ_{RIGID} determined by TMDSC using Equations 4.8 and 4.9

WAXD has been used as a conventional method to determine the crystallinity index in both semicrystalline synthetic polymers [14, 15, 35] and biopolymers [36-38] in Nature. From early studies by Warwicker [36], beta sheet crystal structure of *Nephila* species can be classified into the Warwicker system group 3b using X-ray diffraction analysis. This type of beta sheet has a pseudo orthorhombic unit cell [36, 39] with dimensions of a = 1.06 nm in the direction of the amino acid side chains, b = 0.944 nm along the direction of the hydrogen bond, and c = 0.695 nm along the main polymer chain

[36, 38, 39]. **Figure 4.4** shows 1-D WAXD patterns of water cast film of the spider silk block copolymers. The X-ray diffraction patterns for A-block and B-block are also included for reference. In Figure 4.4, three major crystalline peaks were observed for HBA_3 and the A-block at 2θ = 17.09°, 20.54° and 24.20° corresponding to lattice distances d_{200} (beta sheet) = 0.520 nm, d_{120} (beta sheet) = 0.433 nm and d_{121} (beta sheet) = 0.371 nm, respectively [36, 38]. A broad peak of the amorphous halo centered at 2θ = 22.06° was also observed for all samples. Results indicate that a minimum of 3 A-blocks are required to form beta sheet crystalline regions at room temperature in water cast spider silk block copolymer films.

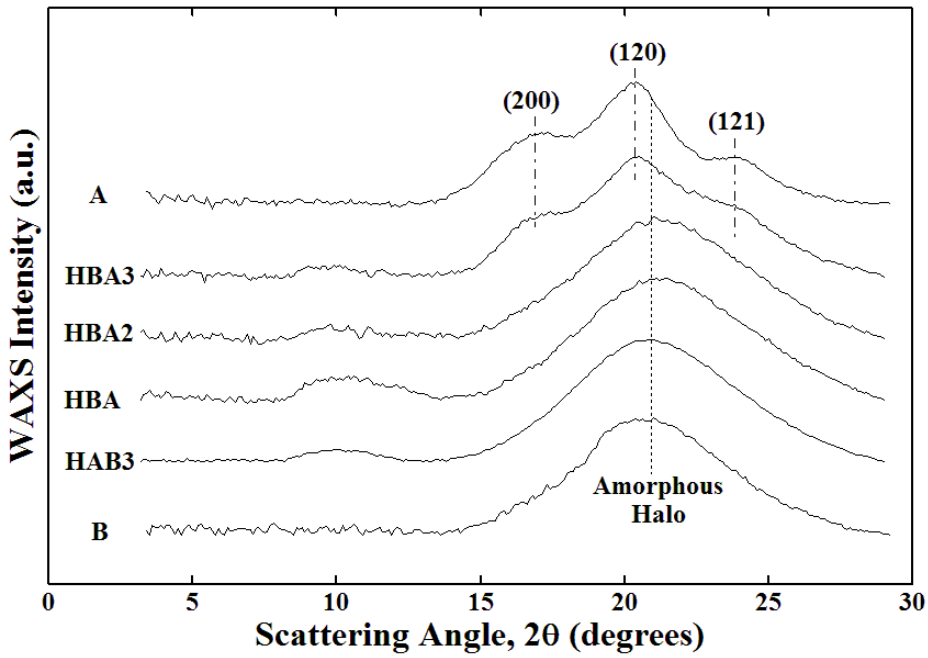

Figure 4.4 1-D WAXD patterns for spider silk block copolymers, HBA_3, HBA_2, HBA and HAB_3. The WAXD patterns for A-block and B-block are also included for reference.

As described in our previous work [14, 15], the crystallinity index can be calculated using the area of crystal peaks and the area of the amorphous halo by fitting the Lorentz-corrected WAXD peak intensity with Gaussian wavefunctions using a Nelder–Mead simplex direct search routine [14]. The crystalline beta sheet fraction gives rise to relatively sharp diffraction peaks, and the amorphous fraction causes a broad scattering halo. The ratio of the area of crystal peaks to the total area gives the crystallinity index, ϕ_{C_Xray}. Examples of this procedure are shown in **Figure 4.5 a,b** for HBA_3 (semicrystalline sample) and HAB_3 (nearly amorphous sample), respectively. The amorphous area, Q_a, and the crystalline area, Q_c, were determined by Equations 4.10(a) and (b), and thus the crystallinity index can be determined by Equation 4.10(c).

$$Q_a = \int I_a q^2 dq \tag{4.10a}$$

$$Q_c = Q - Q_a = \int I_{corr} q^2 dq - \int I_a q^2 dq \tag{4.10b}$$

$$\phi_{c\_Xray} = Q_c / Q \tag{4.10c}$$

where I_a is the intensity of the amorphous peak, I_{corr} is the scattered intensity after all corrections have been applied and q is the scattering vector. The crystallinity indices, ϕ_{C_Xray}, are listed in the sixth column of **Table 4.2**.

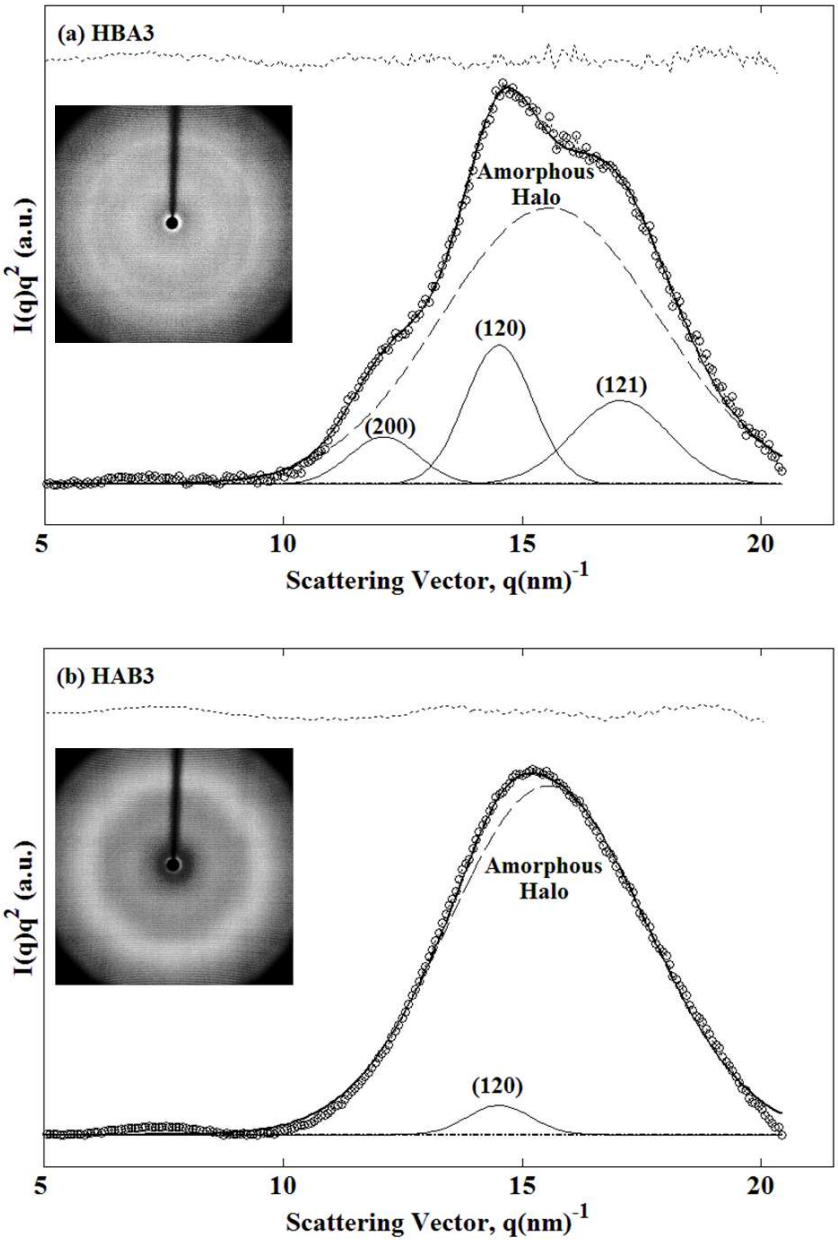

Figure 4.5. Deconvolution of the Lorentz-corrected WAXD intensity, $I(q)q^2$ vs. q, using Gaussian wavefunctions for (a) HBA_3 (semicrystalline sample) and (b) HAB_3 (nearly amorphous sample). Open circles -- measured data; heavy line -- summation of Gaussian peaks; thin solid lines -- individual crystalline Gaussian peaks; dashed lines – amorphous Gaussian peaks; dash-dot lines – baseline; dotted lines -- the residual between the fitted curve and measured curve. The inserts shows the 2-D WAXD raw data.

Fourier Transform Infrared Spectroscopy (FTIR) has been used to provide information on the secondary structure of polypeptide and proteins since 1950 by Elliot and Ambrose [40, 41]. The amide I (1690-1600 cm^{-1}) and amide II (1575-1480 cm^{-1}) vibrations are sensitive to the secondary structure of the backbone and hardly affected by the nature of the side chain [42, 43]; therefore they are most commonly used for secondary structure analysis [43, 44]. Water cast films of the spider silk block copolymers on calcium fluoride (CaF_2) substrate were examined. **Figure 4.6** depicts the FTIR absorbance spectra for spider silk block copolymers with the spectra of A-block and B-block as references in amide I and amide II region. The baseline was fixed for each scan and the air background was also subtracted.

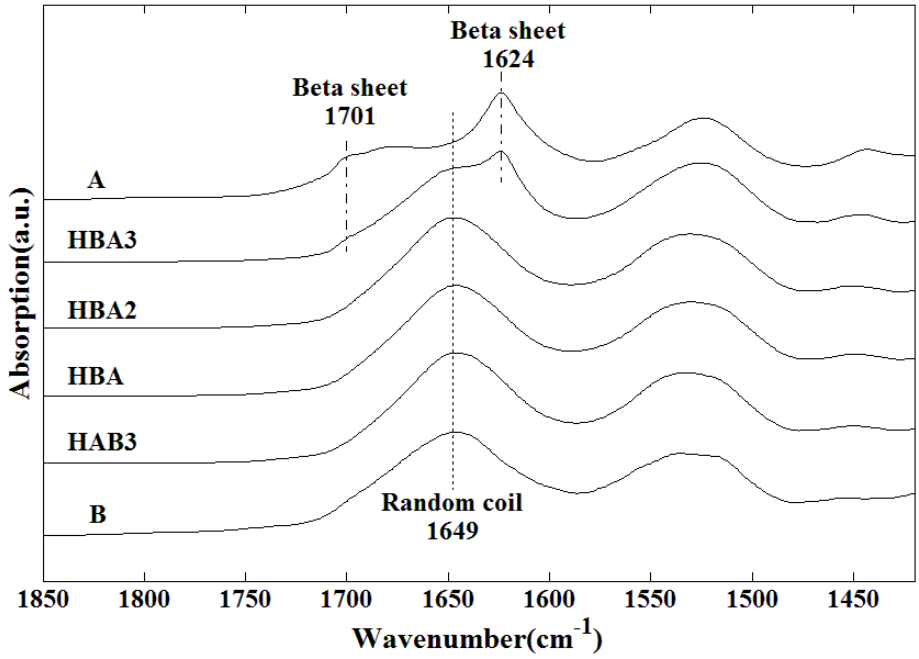

Figure 4.6 FTIR absorbance spectra for spider silk block copolymers. Prominent bands are marked with vertical lines.

Because the amide I vibration has a more straightforward correlation with secondary structure than the amide II vibration [43, 44], we performed Fourier self-deconvolution (FSD) over the amide I peaks on the spectra in Figure 4.6, using Opus 5.0 software with Lorentzian peak profile (half-bandwidth of 25 cm^{-1} and a noise reduction factor of 0.3). In this process, the broad and indistinct amide I band is transformed to a set of distinct self-deconvoluted bands. The details of this method were discussed in our previous work [13]. After FSD, we fitted the deconvoluted spectra with 10 Gaussian peaks. The peak positions and assignments of the amide I region vibration bands of spider silk block copolymer were determined by reference to the literature, and listed in **Table 4.3**. Generally we classify the components between 1620–1630 cm^{-1} to intermolecular beta sheets, 1630-1667 cm^{-1} to random coils and alpha helices, and 1670–1695 cm^{-1} to turns. As shown in **Figure 4.7**, the band between 1595 and 1615 cm^{-1} (centered at 1597 and 1612 cm^{-1} in Figure 4.6 and marked SC in Figure 4.7) comes from the side chains or aggregated strands [7, 45, 46]; the band between 1618 and 1629 cm^{-1} (centered at 1624 cm^{-1} in Figure 4.6 and marked B in Figure 4.7) and the band between 1697 and 1703 cm^{-1} (centered at 1701 cm^{-1} in Figure 4.6, and in also marked B Figure 4.7) comes from the beta sheets [7, 13, 47]; the band between 1630-1642 cm^{-1} and the band between 1643-1657 cm^{-1} (centered at 1633 and 1649 cm^{-1} in Figure 4.6 and marked R in Figure 4.7) comes from random coils [7, 44, 45]; the band between 1658 and 1667 cm^{-1} (centered at 1662 cm^{-1} in Figure 4.6 and marked A in Figure 4.7) comes from helices structure [7, 48]; and the band in the range of 1668-1696 cm-1 (centered at 1674, 1684 and 1693 cm^{-1} in Figure 4.6 and marked T in Figure 4.7) usually is contributed by the turns [13, 43, 48]. Examples of fitted FSD spectra are shown in Figure 4.7 (a) and (b),

for HBA_3 (semicrystalline sample) and HAB_3 (nearly amorphous sample), respectively. FTIR results confirm that a minimum of 3 A-blocks are required to form beta sheet crystalline regions. It should be pointed out that *Bombyx mori* silk fibroins contain a band centered around 1630 cm^{-1}, which is believed to come from the formation of the intramolecular beta-sheets [13]. The band centered at similar wavenumber, 1635 cm^{-1} - 1640 cm^{-1}, was observed in other proteins, such as Elastase and Trypsin, in the less ordered state, which most authors believe comes from the low wave number components of a "turns"-like extended chain structure [49-51]. In our spider silk block copolymers, we also observed a peak at 1634 cm^{-1} after FSD. We classified this peak as a random coil contribution, consistent with our WAXD result and the crystallinity determined by heat capacity modeling.

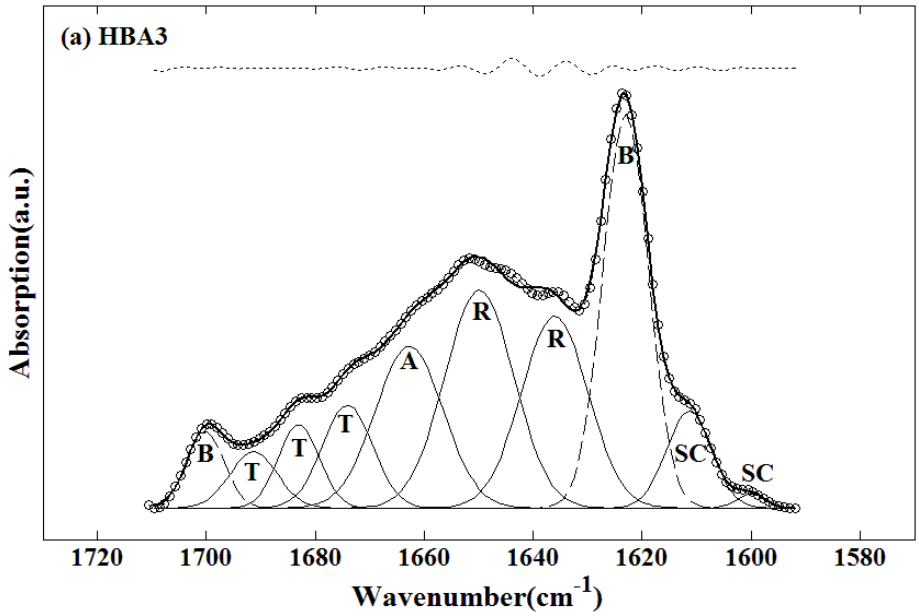

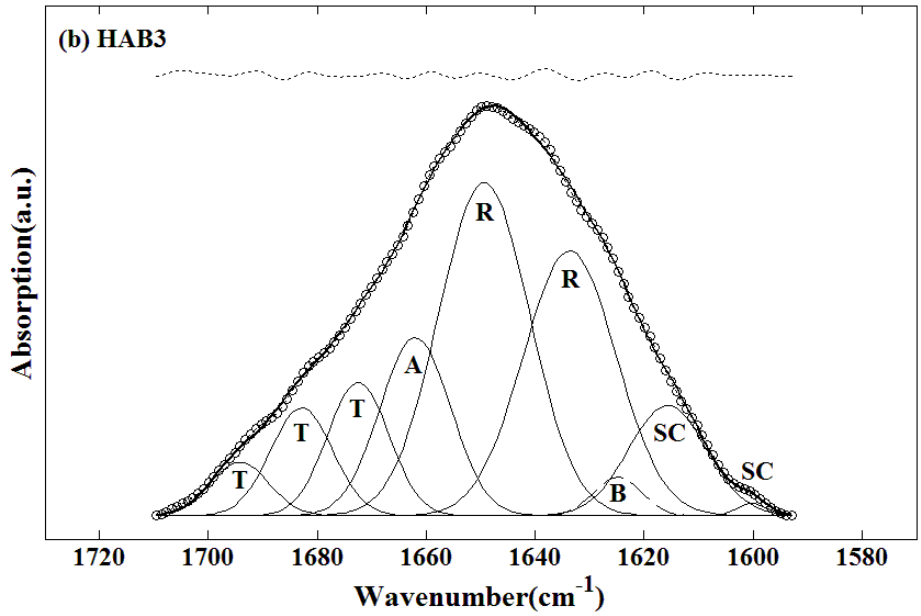

Figure 4.7 Fourier self-deconvolution of amide I spectra for (a) HBA_3 (semicrystalline sample) and (b) HAB_3 (nearly amorphous sample). Open circles -- measured data; heavy line -- summation of Gaussian peaks; thin solid lines -- individual amorphous Gaussian peaks; dashed lines -- individual Gaussian peaks from beta sheets; dotted lines -- the residual between the fitted curve and measured curve. The assignment of amide I bands is taken from the literature [7, 13, 43-51] and bands are marked as random coil (R), beta-sheets (B), alpha-helices (A), turns (T), and side chains (SC).

The close agreement between the total rigid fraction, ϕ_{RIGID}, calculated from heat capacity modeling and the crystalline fraction from WAXD and FSD of the infrared spectra, ϕ_{C_Xray} and ϕ_{C_FTIR}, suggests that the immobilized non-crystalline fraction, ϕ_{IMM}, is negligible. This result is similar to what we found in the *Bombyx mori* silk fibroin [13]. The crystal fraction accounts for the rigid fraction almost entirely. Therefore, the two phase model is also a more suitable one for these bio-block copolymers.

Table 4.3 Peak Positions and Assignments of the Amide I Region Vibrational Bands of Spider Silk-like Block Copolymer

Wavenumber Range (cm^{-1})	Peak Position (cm^{-1}) (±2)	Peak Assignment	References
1595-1605	1597	(Try) side chains	[7, 45, 46]
1605-1615	1612	(Try) side chains, aggregated strands	[7, 45, 46]
1618-1629	1624	Beta sheet (strong)	[7, 13, 47]
1630-1642	1634	Random coils, extended chain structures	[7, 44, 45, 49-51]
1643-1657	1649	Random coils	[7, 44, 45], [47]
1658-1667	1662	Alpha helices	[7, 48]
1668-1678	1674	Turns	[13, 43, 48]
1679-1685	1684	Turns	[13, 43, 48]
1686-1696	1693	Turns	[13, 43, 48]
1697-1703	1701	High-frequency antiparallel beta sheets (weak)	[7, 13, 47]

4.4.3 Interaction of Blocks in Spider Silk Block Copolymer

The glass transition is an important intrinsic property in a block copolymer or a binary polymer blend. The T_g value as a function of volume fraction reveals the interaction between different components. Generally, it is believed that a single T_g can be observed for all compositions when components of the block polymers are miscible, while two T_g values can be observed in a compatible system where the components of the

block polymers are partially miscible [52]. T_g values for pure components do not change with composition in immiscible polymers [52]. In our spider silk block copolymers, we observed a single step change in heat capacity as spider silk block copolymers undergo their glass transition during heating for all compositions (Figure 4.3). The data in Figure 4.3 show His-tag, A-block and B-block are miscible. The T_g values are determined by the inflection point and are summarized in **Table 4.4**.

Table 4.4 The Glass Transition Temperature and Theoretical Isoelectric Point (pI) of Spider Silk Block Copolymers

Sample	**T_g Onset (°C) ±0.8**	**T_g Inflection (I) (°C) ±0.8**	**T_g End (°C) ±0.8**	**ΔC_p J/(mol °C) ±2**	**pI**
A	131	140.5	145.7	537.8	5.2
B	131.8	137.7	141.7	1063.3	8.8
BA	117.1	132.6	142.7	1601.1	8.5
HAB_3	167.9	173.9	179	6406.6	7.1
HBA	170.5	175.6	181.3	4303.3	6.3
HBA_2	170.7	177.7	183.8	4835.2	6.3
HBA_3	172.3	180.9	189.8	5367.0	6.3

Several models have been proposed to predict block copolymer and polymer blend glass transition temperatures, such as the Fox equation [53], Gordon−Taylor

equation [54], and Couchman equations [55]. Although these equations have been successfully applied to certain blends and copolymers, for di-block copolymers and miscible blends, when specific interactions exist between components, these equations do not actually coincide with the experimental T_g [56]. Kwei's equation [57] adds in a term to the Gordon−Taylor equation corresponding to the strength of polymer chain interaction, which may include hydrogen bonding, in the block copolymer [58, 59] or blend [59, 60]. Therefore is the most popular equation applicable for systems with specific interactions:

$$T_g = \frac{(W_1 T_{g1} + W_2 T_{g2})}{(W_1 + kW_2)} + qW_1W_2 \tag{4.11}$$

where W_1 and W_2 are weight fractions of pure components, T_{g1} and T_{g2} represent the corresponding glass transition temperatures, and k and q are fitting constants.

The T_g values determined by the inflection point as a function of weight fraction of A-block is plotted in **Figure 4.8**. The T_g value of the block copolymer without His-tag (BA) and with His-tag (HAB_3, HBA, HBA_2, and HBA_3) were fitted separately by Kwei's equation (4.11) and are shown in Figure 4.8 by dashed line and dash-dot line, respectively. For simplicity, we adopt k = 1 in both cases [58, 59, 61]. For non-His polymer, q = -27. For polymers with His-tag, because the His-tag and B have a similar secondary structure, we treated them as one block, which leads to q = 90. According to Lin [62], when k = 1, q < 0, the enthalpy of mixing must be negative for the two polymers to be compatible, and the overall interaction between the polymers must therefore be attractive. The energy barrier to backbone movement decreases, which leads to a lower T_g. On the other hand, when k = 1, q > 0, the energy barrier to backbone movement increases, which leads to a higher T_g [74]. Thus, we can conclude that in the

dry, condensed state, an attractive interaction exists between A-block and B-block, and intermolecular interactions also exist between HB-block and A-block.

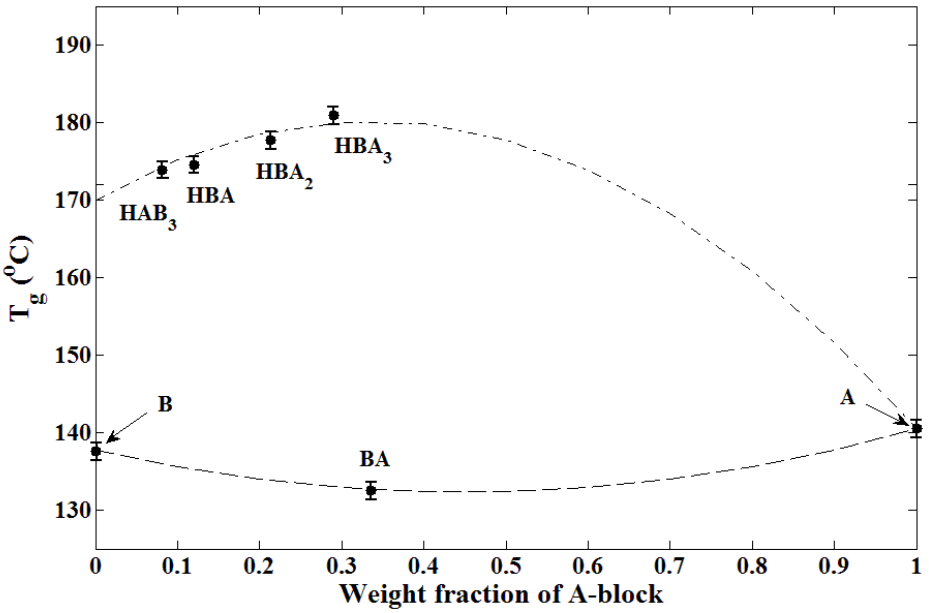

Figure 4.8 Glass transition temperature vs. weight fraction of A-block. Filled circles – T_g value for each composition (as marked); dashed line – best fit line of spider silk block copolymer without His-tag using Kwei's equation (4.11) with k = 1 and q = −27; dash-dot line – best fit line of spider silk block copolymer with a His-tag using Kwei's equation (4.11) with k = 1 and q = 90.

To further investigate the origin of the interaction between blocks, the theoretical isoelectric point (pI) of all compositions was calculated by using the Compute pI/M_w tool from Expert Protein Analysis System (ExPASy) [63] based on their amino acid sequences. From the Compute pI/Mw tool, we have PI (A-block) = 5.2, PI (B-block) = 8.8, PI (His-tag) = 6.1 and PI (HB) = 6.3, which means A-block, His-tag and HB-block

are slightly negatively charged, and B-block is positively charged in a neutral (pH = 7) environment. This is the reason for the attractive force between A-block and B-block, but repulsive force exists between HB-block and A-block. The PI values of spider silk block copolymers are summarized in the last column of Table 4.4.

4.5 Conclusions

We have characterized the thermal properties of our newly-synthesized family of di-block copolymers inspired by *Nephila clavipes* major ampulate dragline spider silk, comprising an alanine-rich hydrophobic A-block, a glycine-rich hydrophilic B-block, and a histidine tag, H. The secondary structure and crystal fraction can be controlled by the volume fraction of each block. By WAXD and FTIR studies, we conclude that a minimum of 3 A-blocks is required to form beta sheet crystals in the spider silk block copolymer.

In this work, we also successfully predicted the solid state heat capacities of our novel block copolymers based on the vibrational motions of the constituent poly(amino acid)s using heat capacity data from the ATHAS Data Bank. The liquid state heat capacity was estimated by the sum of rotational and translational motions of individual amino acid residues in spider silk block copolymers. Excellent agreement was found between the measured and predicted values of the heat capacity. From our prediction of heat capacity, we provide an alternate method to estimate the crystallinity from DSC for biological polymers, whose melting peak is usually unobservable because of relatively low thermal stability. Our result is confirmed by both WAXD and FTIR. The close agreement between the total rigid fraction, calculated from heat capacity modeling, and

the crystalline fraction, from WAXD and FSD of the infrared spectra, suggests that the immobilized non-crystalline fraction is negligible. A two phase model is therefore more suitable for the bio-block copolymers. Interaction of blocks in spider silk block copolymer was studied by Kwei's equation applied to the glass transition temperatures of spider silk block copolymer. Results indicate that attractive interaction exists between A-block and B-block, while intermolecular interaction also exists between A-block and His-tag.

4.6 References

1. Altman GH, Diaz F, Jakuba C, Calabro T, Horan RL, Chen JS, Lu H, Richmond J, and Kaplan DL. *Biomaterials* 2003; 24(3): 401-416.
2. Kluge JA, Rabotyagova U, Leisk GG, and Kaplan DL. *Trends in Biotechnology* 2008; 26(5): 244-251.
3. Krishnaji ST, Huang WW, Rabotyagova O, Kharlampieva E, Choi I, Tsukruk VV, Naik R, Cebe P, and Kaplan DL. *Langmuir* 2011; 27(3): 1000-1008.
4. McGrath K and Kaplan D. *Protein-based materials*. Boston: Birkhäuser, 1997: 103-132.
5. Hayashi CY, Shipley NH, and Lewis RV. *International Journal of Biological Macromolecules* 1999; 24(2-3): 271-275.
6. Hayashi CY and Lewis RV. *Science* 2000; 287(5457): 1477-1479.
7. Rabotyagova OS, Cebe P, and Kaplan DL. *Biomacromolecules* 2009; 10(2): 229-236.

8. Xu H and Cebe P. *Macromolecules* 2004; 37(8): 2797-2806.
9. Boller A, Okazaki I, Ishikiriyama K, Zhang G, and Wunderlich B. *Journal of Thermal Analysis* 1997; 49(2): 1081-1088.
10. Ishikiriyama K and Wunderlich B. *Journal of Thermal Analysis* 1997; 50(3): 337-346.
11. Press WH. *Numerical recipes: the art of scientific computing, 3rd ed*. Cambridge, UK ; New York: Cambridge University Press, 2007: 23-50.
12. Xu SX, Li Y, and Feng YP. *Thermochimica Acta* 2000; 343(1-2): 81-88.
13. Hu X, Kaplan D, and Cebe P. *Macromolecules* 2006; 39(18): 6161-6170.
14. Buckley J, Cebe P, Cherdack D, Crawford J, Ince BS, Jenkins M, Pan JJ, Reveley M, Washington N, and Wolchover N. *Polymer* 2006; 47(7): 2411-2422.
15. Huang WW, Edenzon K, Fernandez L, Razmpour S, Woodburn J, and Cebe P. *Journal of Applied Polymer Science* 2010; 115(6): 3238-3248.
16. Wunderlich B. *Thermochimica Acta* 1997; 300(1-2): 43-65.
17. Pyda M, Hu X, and Cebe P. *Macromolecules* 2008; 41(13): 4786-4793.
18. Hu X, Kaplan D, and Cebe P. *Thermochimica Acta* 2007; 461(1-2): 137-144.
19. Wunderlich B. *Pure and Applied Chemistry* 1995; 67(6): 1019-1026.
20. Pyda M. private communication, 2007.
21. Pyda M. The Advanced THermal Analysis System (ATHAS) Data Bank. http://athas.prz.rzeszow.pl/Default.aspx?op=db.
22. Minakov AA, Mordvintsev DA, and Schick C. *Polymer* 2004; 45(11): 3755-3763.
23. Wunderlich B. *Thermal analysis of polymeric materials*. Berlin: Springer, 2005: 304-404.

24. Hodge RM, Bastow TJ, Edward GH, Simon GP, and Hill AJ. *Macromolecules* 1996; 29(25): 8137-8143.

25. Kim YS, Dong LM, Hickner MA, Glass TE, Webb V, and McGrath JE. *Macromolecules* 2003; 36(17): 6281-6285.

26. Lee KY and Ha WS. *Polymer* 1999; 40(14): 4131-4134.

27. Roles KA and Wunderlich B. *Biopolymer*s 1991; 31(5): 477-487.

28. Roles KA, Xenopoulos A, and Wunderlich B. *Biopolymers* 1993; 33(5): 753-768.

29. Pyda M. *Journal of Polymer Science Part B-Polymer Physics* 2001; 39(23): 3038-3054.

30. Pyda M and Wunderlich B. *Macromolecules* 2005; 38(25): 10472-10479.

31. Chen HP and Cebe P. *Macromolecules* 2009; 42(1): 288-292.

32. Pak J, Pyda M, and Wunderlich B. *Macromolecules* 2003; 36(2): 495-499.

33. Schick C, Wurm A, and Mohammed A. *Thermochimica Acta* 2003; 396(1-2): 119-132.

34. Menczel J and Wunderlich B. *Journal of Polymer Science Part C-Polymer Letters* 1981; 19(5): 261-264.

35. Decher G. *Science* 1997; 277(5330): 1232-1237.

36. Warwicker JO. *Journal of Molecular Biology* 1960; 2(6): 350-360.

37. Krejchi MT, Cooper SJ, Deguchi Y, Atkins EDT, Fournier MJ, Mason TL, and Tirrell DA. *Macromolecules* 1997; 30(17): 5012-5024.

38. Glisovic A, Vehoff T, Davies RJ, and Salditt T. *Macromolecules* 2008; 41(2): 390-398.

39. Marsh RE, Corey RB, and Pauling L. *Biochimica Et Biophysica Acta* 1955; 16(1): 1-34.

40. Ambrose EJ and Elliott A. *Proceedings of the Royal Society of London Series a-Mathematical and Physical Sciences* 1951; 206(1085): 206-219.

41. Ambrose EJ and Elliott A. *Proceedings of the Royal Society of London Series a-Mathematical and Physical Sciences* 1951; 208(1092): 75-90.

42. Barth A. *Progress in Biophysics: Molecular Biology* 2000; 74(3-5): 141-173.

43. Barth A. *Biochimica Et Biophysica Acta-Bioenergetics* 2007; 1767(9): 1073-1101.

44. Barth A and Zscherp C. *Quarterly Reviews of Biophysics* 2002; 35(4): 369-430.

45. Jackson M and Mantsch HH. *Critical Reviews in Biochemistry and Molecular Biology* 1995; 30(2): 95-120.

46. Jung C. *Journal of Molecular Recognition* 2000; 13(6) :325-351.

47. Chen X, Knight DP, Shao ZZ, and Vollrath F. *Biochemistry* 2002; 41(50): 14944-14950.

48. Dicko C, Knight D, Kenney JM, and Vollrath F. *Biomacromolecules* 2004; 5(6): 2105-2115.

49. Byler DM and Susi H. *Biopolymers* 1986; 25(3): 469-487.

50. Susi H and Byler DM. *Methods in Enzymology* 1986; 130: 290-311.

51. Arrondo JLR, Muga A, Castresana J, and Goni FM. *Progress in Biophysics & Molecular Biology* 1993; 59(1): 23-56.

52. Brostow W, Chiu R, Kalogeras IM, and Vassilikou-Dova A. *Materials Letters* 2008; 62(17-18): 3152-3155.

53. Fox TG. *Bulletin of the American Physical Society*, 1956: 123.

54. Gordon M and Taylor JS. *Journal of Applied Chemistry* 1952; 2(9): 493-500.

55. Couchman PR. *Macromolecules* 1991; 24(21): 5772-5774.

56. Widmaier JM and Meyer GC. *Journal of Thermal Analysis* 1982; 23(1-2): 193-199.

57. Kwei TK. *Journal of Polymer Science Part C-Polymer Letters* 1984; 22(6): 307-313.

58. Kuo SW, Tung PH, and Chang FC. *Macromolecules* 2006; 39(26): 9388-9395.

59. Chen WC, Kuo SW, Jeng US, and Chang FC. *Macromolecules* 2008; 41(4): 1401-1410.

60. Chen HP, Pyda M, and Cebe P. *Thermochimica Acta* 2009; 492(1-2): 61-66.

61. Kuo SW, Liu WP, and Chang FC. *Macromolecules* 2003; 36(14): 5165-5173.

62. Lin AA, Kwei TK, and Reiser A. *Macromolecules* 1989; 22(10): 4112-4119.

63. **Ex**pert **P**rotein **A**nalysis **Sy**stem (ExPASy) proteomics server, http://expasy.org/, 2012.

Chapter V. Determining the Effect of Water on Spider Silk-like Block Copolymer Glass Transition

This chapter reports a study of the thermodynamic properties, and structural changes of protein-water system with respect to protein amino acid sequence. The heat capacities of protein-water systems were also interpreted by using the underlying molecular motion of both the constituent amino acids in proteins and the water molecules.

5.1 Introduction

Protein-water interactions are considered one of the most important topics in bio-macromolecule studies [1-5], protein science [6, 7] and food science [8, 9]. Generally, water in polymeric systems can be classified into three types [3, 10]: free water, freezable loosely bound water, and non-freezing bound water. In the protein-food systems, the classification of the type of water in protein-water interactions is described in more detail [8], and includes: structural, monolayers, unfreezable, hydrophobic hydration, imbibition or capillary condensation, and hydrodynamic hydration water. The character of protein-water interactions will determine not only the protein functional properties [8], such as solubility, wettability, swelling, gelation, colloidal dispersion, and water holding capacity, but also it will affect the stability of the proteins [11], the process of phase transition [12] and the kinetics of crystallization [4].

To further understand the relation between the protein-water interactions and their effects on the functional, structural, and physical properties of the proteins, researchers have attempted to determine the specific binding sites of water in the protein molecules. Kuntz *et al.* [1, 2] used nuclear magnetic resonance (NMR) to investigate the degree of hydration of synthetic polypeptides. According to their findings, water binding depends on the composition and conformation of the protein molecules: nonpolar amino acid side chains, such as those of alanine and valine, bind one water molecule; polar side chains bind two or three water molecules; and ionic side chains, such as those of aspartic and glutamic acids and lysine, bind four to seven water molecules per amino acid. Researchers also studied the plasticization effect of bound water molecules on silk crystallization and the thermodynamic properties of the polymer-small molecule system. Hu *et al.* [3, 4] using differential scanning calorimetry (DSC) suggested that the crystallization process of silk fibroin proceeds through an intermediate precursor stage associated with water removal. Pyda *et al.* [5, 12, 13] also found in DSC studies that water plasticizes the glass transition step in the starch-water system. The water-protein interaction is also widely investigated and used for controlled thermal treatment of silk samples. Jin *et al.* and Hu *et al.* used water vapor annealing to thermally treat regenerated silk fibroin and obtain transparent silk films with various beta sheet contents [14, 15]. However, few works have been focused on the nature of the influence of bound water to the glass transition and the relation with the proteins' amino acid sequences. Thus, in-depth investigations are still needed.

Spider silks are one of the most interesting biomaterials which can provide remarkable insights into protein−water interactions [16-18]. In addition to light weight

and extraordinary mechanical properties [19], the spider dragline silk of *Nephila clavipes* also displays an intriguing behavior when exposed to water: it will contract to about half of its original length and swell in diameter [20, 21]. This phenomenon is called supercontraction [21]. The spider dragline silk contains an alanine rich GA/A_n motif which forms β sheets structures that correspond to the crystalline regions, a glycine rich GG*X* motif that forms α helices giving rise to a non-structured amorphous region, and an N-terminus and C terminus [22, 23]. The supercontraction has been shown to result from the dissolution of the hydrogen-bonding network that holds the non-crystalline glycine-rich parts of the spider silk together [24, 25]. This knowledge about spider silk-water interactions is very valuable in the development of applications for silks. Studies of silk-water interactions are most widely applied in the biomedical area, such as in producing biodegradable protein membranes and micelles as potential drug delivery systems [26, 27]. It is also used in other areas, such as producing high-performance fibers and for tissue repair [19].

To obtain a fuller understanding about silk-water interactions and the relationship between the amino acid sequences, we characterized a new family of recombinant spider silk-like block copolymers inspired by the genetic sequences found in spider dragline silk. We used these biopolymers with well controlled amino acid sequences to further understand the morphological features, the thermodynamic properties, crystallization kinetics, and the plasticization effect of water molecules. We have chosen di-block copolymers as the model system based on MaSp1 motifs, hydrophobic GA/A_n and hydrophilic GG*X*, and produced the spider silk-like block copolymers using recombinant

DNA technology [27]. The self-assembly morphology was observed by scanning electron microscopy (SEM).

In Chapter IV, we used a model [28] to calculate the heat capacity of recombinant spider silk-like block copolymers in the solid or liquid state, below or above the glass transition temperature, respectively, based on their protein amino acid sequences. In this study, we apply this model to the synthetic protein-water system, using it with temperature modulated differential scanning calorimetry (TMDSC) and thermogravimetric analysis (TGA) to study the effect of water on the protein glass transition. We are able to quantify the water content in proteins as well. Fourier transform infrared spectroscopy (FTIR) has long been a sensitive tool for the characterization of the protein secondary structures [29, 30]. In this study, we used real-time FTIR during heating as a structure specific probe to monitor the secondary structural changes during water removal. With this approach, combined with quantitative heat capacity analysis, we can further understand the protein-water interactions and their relationship to specific amino acid sequence.

Aside from the fundamental perspective, we also anticipate that these results will inspire the design and control of water mediated biodegradable materials for drug delivery systems and smart silk-based materials, which will self-assemble into various structures as a function of processing conditions and thermal history [31].

5.2 Experimental Section

5.2.1 Materials

Two sets of recombinant spider silk-like block copolymers were used in this study. The first set of proteins, A, BA and B consists of genetic variants of MaSp1 from the dragline of the spider *Nephila clavipes*, where the A block (hydrophobic) is composed of GA/A_n poly-alanine repeat, and the B block (hydrophilic) is composed of GG*X* repeats. In order to prevent cyclization of the peptides, the C-terminus was modified to an amide. These proteins were purchased from Tufts University protein core facility (TUCF) in powder form, and then purified. The second set of proteins, HBA_3, HBA_2, HBA, HAB_2, and HAB_3, consists of the same genetic variants as those of the first set, but with a His-tag consisting of six histidine residues and a short linker sequence[27] instead of the C-terminus. These di-block copolymers with a His-tag were bio-synthesized in Prof. Kaplan's labs using recombinant DNA technology. The synthesis method was described in a previous paper [27]. Protein identification was confirmed by matrix-assisted laser desorption/ionization time of flight (MALDI-TOF) mass spectrometry. All the experimental measurements were performed with solid form material.

5.2.2 Thermal Analysis

Temperature Modulated Differential Scanning Calorimetry (TMDSC)

Temperature Modulated Differential Scanning Calorimetry (TMDSC) measurements were performed on a TA Instruments Q100 DSC equipped with a refrigerated cooling system. The samples with mass about 2 mg were encapsulated into aluminum pans and heated in the DSC cell at a heating rate of 2 °C/min with oscillation

amplitude of 0.318 °C and a modulation period of 60 s. The empty aluminum reference pan with the same weight as the sample pan was used in all the runs. The DSC cell was continuously purged with dry nitrogen gas at a flow rate of 50 mL/min. The temperature and heat flow of the DSC were carefully calibrated using indium standard before experiments.

Thermogravimetric Analysis (TGA)

Thermogravimetry (TGA) measurements were performed on a TA Instruments Q500 thermogravimetric analyzer. Samples with masses about 4.0 mg or 5.0 mg were heated in the TGA furnace at a heating rate of 2 °C/min from 25 °C to 400 °C. A nitrogen purge gas was used at a flow rate of 50 mL/min. To prevent light density samples from being blown out of the basket by nitrogen gas flow, samples were encapsulated in aluminum DSC pans during heating. Small pin holes were made on the DSC lids to let the sample surface be exposed to the atmosphere and to let degradation products escape. Before each run, the empty platinum basket and empty DSC pan were used together to calibrate the zero point of the total weight.

5.2.3 Real-time Fourier Transform Infrared Spectroscopy (FTIR)

Real-time Fourier transform infrared spectroscopy (FTIR) was carried out on a Jasco infrared microscope IRT-5000 in transmission mode with a liquid nitrogen cooled Mercury-Cadmium-Telluride (MCT) detector, in combination with a Mettler optical microscopy hot stage FP90. Sample films cast on calcium fluoride (CaF_2) discs with thickness about 10 microns were first stored in a vacuum oven for 1 hour and then

inserted into the hot stage for FTIR measurements. Holes in the hot stage platens permitted the IR beam to pass through the samples directly to the MCT detector. The real-time FTIR scans were performed at a heating rate of 2°C/min from 30 to 220 °C. The absorbance spectra were obtained by averaging 128 scans with a resolution of 4.0 cm^{-1}. The frequency ranged from 400 to 4000 cm^{-1}. The background spectra were collected under the same conditions and subtracted from the sample scans. Before the experiments, the temperature of the hot stage was calibrated with a thermocouple.

5.2.4 Scanning Electron Microscopy (SEM)

The surface morphologies of the water cast recombinant spider silk-like block copolymers films were imaged using a Zeiss Supra55VP SEM and a Zeiss Ultra55 SEM in the Center for Nanoscale Systems at Harvard University. Lyophilized samples were dissolved in water to a final concentration of 1 mg/mL, and then cast on a silicon wafer and air dried in vacuum oven for 1 hour at room temperature. After drying, samples were sputter coated with platinum- palladium. Images were taken using SE2 and InLens detectors at 5.00 kV.

5.3 Results and Discussion

5.3.1 Thermal Analysis

The state of water absorbed in polymeric systems can be classified into three types [3, 10]: (i) free water, (ii) freezable loosely bound water, and (iii) non-freezing bound water. Free water is not intimately bound to polymer chain and behaves like bulk water. A sharp melting endothermic peak at 0 °C should be observed by DSC if free water exists in the polymer matrix [32]. The freezable loosely bound water is weakly bound to the polymer chain or interacts weakly with non-freezing water and displays relatively broad melting endotherms at temperatures greater than 0 °C on heating due to these weak bonding interactions [10, 33]. The non-freezing bound water is strongly bound to the polymer chain and has no detectable phase transition [32, 33], but it can affect the glass transition by plasticization [3]. In our study, the influence of water on protein thermal properties was determined by TMDSC. Because the total sample mass is decreasing during the TMDSC heating scan, the weight loss of samples due to water evaporation during heating was measured by TGA and used to calibrate the temperature dependent sample mass in TMDSC, *M(T)*, by:

$$M(T) = M_{DSC} \times wt\%(T) \tag{5.1}$$

where M_{DSC} is the initial sample mass in the DSC, and *wt%(T)* is the percent residual weight (in the range from 1 to 0) at temperature *T* measured by TGA.

Figure 5.1 shows TMDSC total heat flow of recombinant spider silk-like block copolymers films: (a) A, BA, B and (b) HBA_3, HBA_2, HBA, HAB_2, and HAB_3, with

heating rate 2 °C/min from -60 to 220 °C. The total heat flow, *HF(T)*, and the reversing heat flow, *RHF(T)*, are normalized at each temperature by *M(T)* using:

$$HF(T) = HF_{DSC} \times M_{DSC} / M(T) = HF_{DSC} / wt\% \quad (5.2a)$$

$$RHF(T) = RHF_{DSC} \times M_{DSC} / M(T) = RHF_{DSC} / wt\% \quad (5.2b)$$

In these recombinant spider silk-like block copolymers, the free water was removed by storing samples in desiccators and keeping samples in a vacuum oven at room temperature for 1 hour before measurements. Thus, no endothermic peak at 0 °C could be observed in Figure 5.1, and the major influence of water on proteins comes from bound water. A series of wide endothermic peaks centered at about 65 °C were observed in all samples, and marked on the total heat flow with a dashed circle (on the left) in Figure 5.1(a) and 5.1(b). These endotherms can be attributed to the heat absorbed by the evaporated water molecules [34, 35]. As suggested by Hu *et al.*[36], the beta sheet crystal formation in silk fibroin-water system also involved a stage in which a disordered non-crystalline protein (state 1) containing bound water transformed into a precursor state (state 2) of higher molecular chain order following removal of bound water. Thus, if a crystallization process exists in the silk-water system, an exotherm should also be observed close to the endothermic water peak due to the protein chain rearrangement into a precursor state.

In our recombinant spider silk-water system, for A and BA, a sharp endotherm was observed before the wide endotherm. The wide endothermic water peak contains contributions from bound water removal as well as from exothermic heat flow from formation of a more ordered precursor state. For B, HBA_3, HBA_2, HBA, HAB_2, and

HAB_3, only one broad endotherm was observed because no precursor state is formed during the heating process, and the wide endotherm only comes from the bound water removal. The position of the endothermic peak was determined by the minimum of the total heat flow curve in the range from 50 to 100 °C and summarized **Table 5.1** column 2. Interestingly, as the volume fraction of hydrophilic B block increases from HBA_3 to HAB_3 in His-tag containing spider silk-block copolymers, the peak position continuously shifts to a higher temperature. This is as expected, since when the more hydrophilic B blocks were added into the block copolymer, due to the water-protein affinities, higher average activation energy is needed to partition water molecules from the protein chains which leads to a higher transition temperature. Therefore, we can confirm that this endothermic peak relates to the vaporization of the bound water molecules from protein, and the transition temperature is strongly related to the hydrophobicity of the protein amino acid sequence.

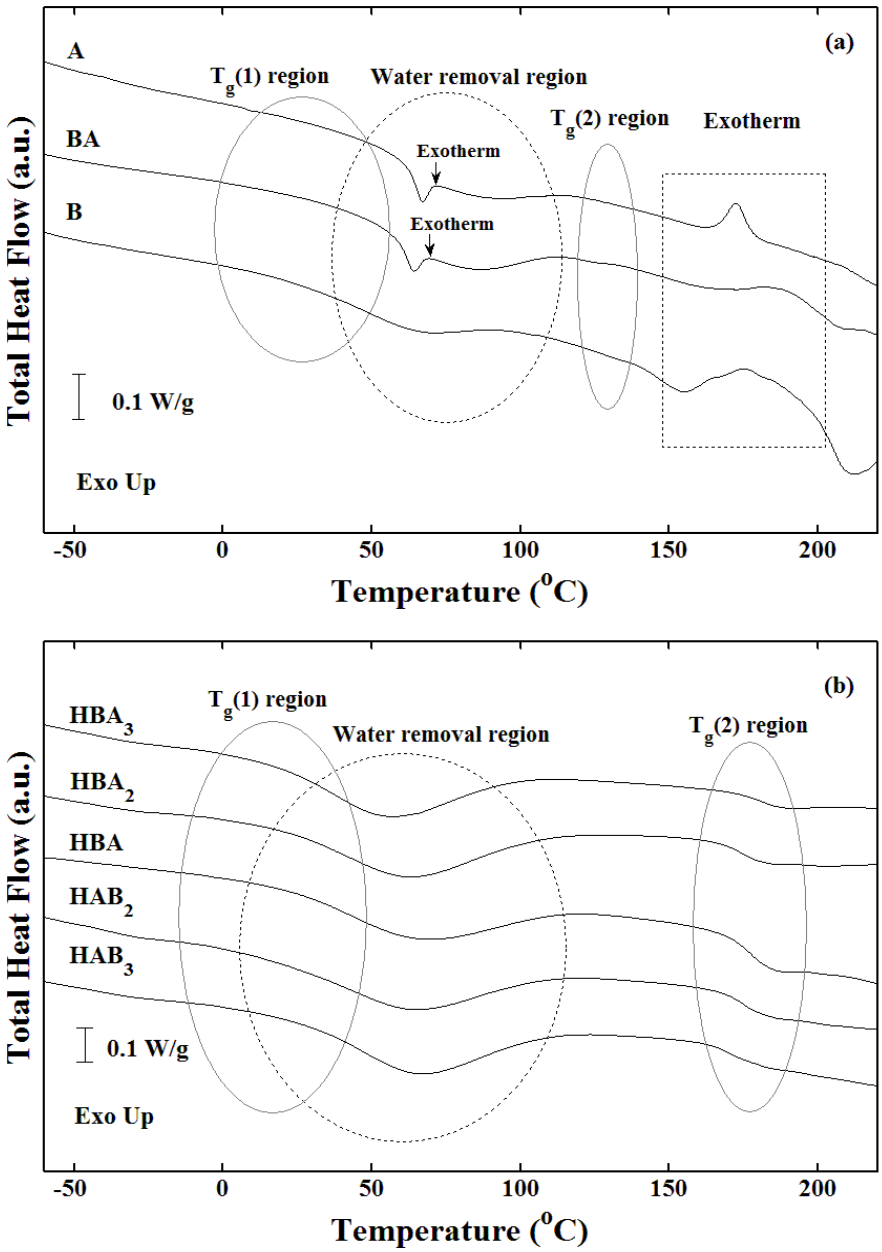

Figure 5.1 TMDSC total heat flow of recombinant spider silk-like block copolymers films: (a) A, BA, B and (b) HBA_3, HBA_2, HBA, HAB_2, and HAB_3, during heating at 2 °C/min from -60 to 220 °C. The endothermic water removal peaks are marked with dashed circles, the exotherms due to formation of a precursor state are marked with arrows, and the exotherms due to crystallization or cross-linking are marked with dashed square.

Table 5.1 Thermal Properties of Recombinant Spider Silk-like Block Copolymers

Sample	**Water Peak[a] (°C) ± 1**	**$T_g(1)$ [b] (°C) ± 2**	**$T_g(2)$ [b] (°C) ± 1**	**$T_g(2)_{Dry}$ [c] (°C) ± 1**	**ΔH[d] (J/g) ± 1**	**ΔE[e] (kcal/mol) ± 0.1**
A	67	67	140	141	38	/[f]
BA	65	63	128	133	41	/[f]
B	72	36	131	138	36	3.8
HBA_3	58	17	181	181	36	2.3
HBA_2	64	18	176	178	39	2.3
HBA	66	25	176	176	33	3.3
HAB_2	66	25	174	175	47	3.3
HAB_3	67	27	171	174	47	3.4

[a] From TMDSC total heat flow (Figure 5.1) at 2.0 ºC/min.

[b] From TMDSC reversing heat flow (Figure 5.2) at 2.0 ºC/min.

[c] The glass transition temperature of dry protein after annealing at 120 °C as reported in our previous study [28].

[d] Enthalpy calculated per gram of sample, from isothermal holding (Figure 5.4) at 50 ºC for 10 min.

[e] Binding energy per mole of bound water, from isothermal holding (Figure 5.4) at 50 ºC for 10 min.

[f] Cannot determined since precursor state is also forming.

Exothermic peaks were also formed above $T_g(2)$ in A, BA and B, and marked in the total heat flow with a dashed square in Figure 5.1(a). The exothermic peaks in A and BA are the non-isothermal crystallization peaks, attributed to the random coil to beta sheet conformational transition [4, 34, 36]. As shown in Figure 5.1(a), BA has a slightly higher and broader crystallization temperature than A, which indicates that BA needs larger enthalpy to self-assemble into different chain conformation due to its longer chain length and non-crystalline B-block [37]. Because B does not crystallize during heating, as shown by our previous studies [28, 38], its exotherm could be attributed only to the protein chain aggregation and crosslinking [39, 40], but not to crystallization of protein. Since HBA_3 had already crystallized during lyophilization, and HBA_2, HBA, HAB_2, and HAB_3 do not crystallize during heating, no exothermic peak was observed in His-tag containing recombinant spider silk-like block copolymers, as shown in Figure 5.1(b). When the temperature is above 230 °C, all samples start to degrade.

The glass transitions of protein-water systems, especially the bound water induced glass transitions of the protein−water system, are buried in the large endothermic peak related to the water loss in the total heat flow curves. Therefore, the reserving heat flow, as shown in **Figure 5.2**, is analyzed to separate the glass transition, a reversing process, from the water loss, a non-reversing process. Two glass transitions can be clearly observed in Figure 5.2 for all of the samples: the lower glass transitions of the protein−water system which are marked as $T_g(1)$, and the glass transitions of proteins after water evaporation which are marked as $T_g(2)$. The positions of the $T_g(1)$s and the $T_g(2)$s are marked by short lines at the midpoint of the glass transition step with two dotted lines that show the extrapolated baselines of the glass transitions in Figure 5.2.

The glass transition temperatures are summarized in Table 5.1 columns 3 and 4. For A and BA, a precursor state (state 2) [36] for beta sheet crystallization is formed during heating, and therefore a higher energy is needed for the protein chain to transform from a non-crystalline state to the more ordered precursor state, which leads to $T_g(1)$s occurring at about 65 ºC. The formation of the precursor state facilitates the beta sheet crystallization at high temperature, and they possess similar characteristics. When the protein chains form the precursor state, the process is exothermal, and due to the reduction of the molecular vibration induced by a more ordered structure, the reversing heat capacity decreases [41, 42], which leads to an increase of the reversing heat flow. After the precursor state, the water molecules are removed quickly in A and BA, due to the hydrophobic nature of the A-block, and this leads to a bound water removal peak at 65 ºC, which is very close to their $T_g(1)$s. On the other hand, for B, HBA_3, HBA_2, HBA, HAB_2, and HAB_3, the protein chains, which are hydrogen bonded to water molecules, only transform from a glassy state to a rubbery state, but not into a precursor state (as A and BA do). These samples have $T_g(1)$s at about 25 ºC. When the protein chains reach the rubbery state, the mobility of both the polymer and water molecules are considerably enhanced [43], the water molecules are removed more slowly in B, HBA_3, HBA_2, HBA, HAB_2, and HAB_3, due to the hydrophilic nature of the B-block and His-tag, and this leads to a bound water removal peak at 65 ºC, which is much higher than their $T_g(1)$s.

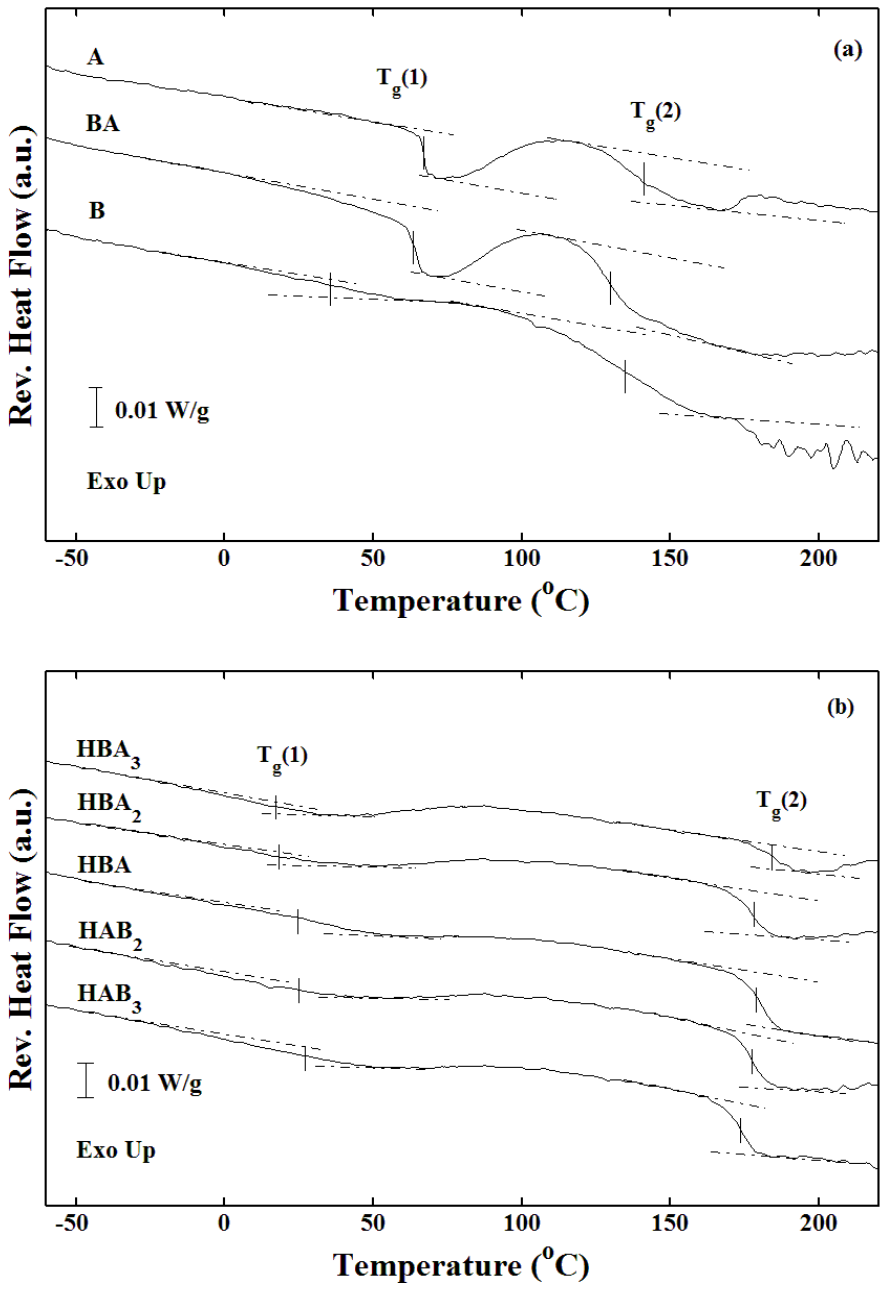

Figure 5.2 TMDSC reversing heat flow of recombinant spider silk-like block copolymers films: (a) A, BA, B and (b) HBA_3, HBA_2, HBA, HAB_2, and HAB_3, during heating at 2 °C/min from -60 to 220 °C. The positions of the $T_g(1)$s and the $T_g(2)$s are marked by short lines at the midpoint of the glass transition step with two dotted lines that extrapolate the baselines used to determine the glass transitions.

To further analyze the glass transitions of the protein-water system, the reversing heat capacity was calculated from TMDSC reversing heat flow measurements. To obtain the mass-normalized specific reversing heat capacities of recombinant spider silk-like block copolymers films, and account for water loss, specific reversing heat capacities, C_p, were first calculated. Because the DSC sample pan was not completely sealed, the sample mass was decreasing during heating due to the evaporation and removal of water molecules from the sample. Thus, the specific reversing heat capacities, C_p, need to be normalized by *M(T)*, and the mass normalized specific reversing heat capacities can be expressed as:

$$Mass\ Normalized\ C_p = C_p \times M_{DSC} / M(T) = C_p / wt\% \tag{5.3}$$

The heat capacity of polymer-small molecule systems has been studied in our previous works [4, 5, 44]. To calculate the theoretical heat capacity baselines for the protein-water system, we adopted a similar approach:

$$C_p(protein^{solid} - water^{glassy}) = \chi_{protein}(T)C_p^{\ solid}(protein) + \chi_{water}(T)C_p^{\ glassy}(water) \tag{5.4a}$$

$$C_p(protein^{liquid} - water^{liquid}) = \chi_{protein}(T)C_p^{\ liquid}(protein) + \chi_{water}(T)C_p^{\ liquid}(water) \tag{5.4b}$$

where $C_p(protein^{solid} - water^{glassy})$ and $C_p(protein^{liquid} - water^{liquid})$ are the calculated solid and liquid specific heat capacity of the protein−water system. $C_p^{\ solid}(protein)$ is the calculated solid state protein specific heat capacity based on the vibrational heat capacity of each amino acid in the protein sequences [28], $C_p^{\ liquid}(protein)$ is the calculated liquid state specific heat capacity based on the number of the mobile units of each amino acid in the protein sequences [28], $C_p^{\ glassy}(water)$ is the vibrational heat capacity of glassy water

[5, 13], $C_p^{liquid}(water)$ is the liquid heat capacity of water [13], and $X_{protein}(T)$ and $X_{water}(T)$ are the weight fractions of protein and water, respectively, at temperature T in the system determined by TGA with the relationship $X_{protein}(T) = 1 - X_{water}(T)$.

Figure 5.3 shows the mass normalized apparent specific reversing heat capacities (heavy curves) of all the samples based on the "three run method" [28] along with the theoretical baselines in the glass transition region. In our previous work [28], when the temperature is below the protein glass transition temperature, the specific heat capacity of dry protein is calculated based on the vibrational motion of each amino acid residue in the protein sequence. When the temperature is at or above the protein glass transition temperature, C_p is based on the vibrational, rotational, and translational motion. In our present study, we extended our calculation to a protein-water system through equations 5.4a and 5.4b using the glassy and liquid heat capacity of water listed in Pyda's work [5, 13], and employed these calculations to evaluate the four baselines in Figure 5.3. As can be observed in Figure 5.3, the mass normalized C_p overlaps $C_p(protein^{solid} - water^{glassy})$ at low temperature, and when the temperature increased, the deviation between them gradually increases due to the glass transition relaxation process, $T_g(1)$, in the protein-water system. After the glass transition of the protein−water system was completed, the reversing heat capacity decreases to the specific heat capacity of a dry protein, $C_p^{solid}(protein)$, due to evaporation of water during the TMDSC heating scan. This indicates the formation of the precursor state though decreases the C_p of the protein-water system, but has negligible effect on the C_p of the now dry proteins. Finally, as temperature increases, the mass normalized C_p increases again due to the second glass transition relaxation process, $T_g(2)$, in the now dry protein.

By analyzing the reversing heat capacity with the four baselines derived from the heat capacity model based on our previous paper [28] and equation 5.4, quantitative information was revealed from the glass transition steps. The heat capacity step changes at the glass transition temperature are due to the rotational or translational motion of the protein backbone [5, 28]. As shown in Figure 5.3, the heat capacity steps of $T_g(1)$, are much larger and more distinct in A and BA, than in B, HBA_3, HBA_2, HBA, HAB_2, and HAB_3. This result indicates more rotational or translational motion due to the formation of the precursor state exist in A and BA. Moreover, because A-block is a hydrophobic block while B-block and His-tag are hydrophilic blocks, more hydrogen-bonds are formed between the protein chains and water molecules in B, HBA_3, HBA_2, HBA, HAB_2, and HAB_3 than in A and BA. Thus, in A and BA, water only acts as plasticizer to increase the free volume which reduces the "friction" between protein chains during the conformational change at $T_g(1)$. In B, HBA_3, HBA_2, HBA, HAB_2, and HAB_3, water molecules not only act as plasticizers but also stabilized the protein chain conformation at $T_g(1)$ by inter-chain hydrogen-bonding, therefore in these proteins, the $T_g(1)$s are broadened. The second glass transition relaxation processes, $T_g(2)$s, in the now dry protein, are summarized in Table 5.1 column 4, and compared with the glass transitions of the annealed dry proteins, $T_g(2)_{Dry}$, reported in our previous study [28] and shown in Table 5.1 column 5. The T_g values in columns 4 and 5 are very close in most cases, which indicates the proteins are almost dried during heating, and $T_g(2)$ is just the glass transition of the protein-only system. For some of the hydrophilic proteins, such as B or HAB_3, $T_g(2)$ is slightly lower than the $T_g(2)_{Dry}$, which indicates an incomplete removal of non-freezing bound water which plasticizes the protein chains and reduces the glass

transition temperature. The heat capacity step size at $T_g(2)$ can also be used to determine if the sample is amorphous or semicrystalline below or a little above $T_g(2)$ during heating. As shown in Figure 5.3 (a) and (d), the heat capacity steps at $T_g(2)$ are smaller than the predicted values for amorphous sample, thus A and HBA_3 are semicrystalline samples with both amorphous phase and crystalline phase, while in Figure 5.3 (b), (c), (e) - (h), the heat capacity steps at $T_g(2)$ are equal to the predicted values for amorphous sample, thus B, BA, HBA_2, HBA, HAB_2, and HAB_3 are amorphous samples in the temperature region below $T_g(2)$.

In addition to the quantitative analysis of the protein-water system glass transition steps, this model can also be used to determine the water content inside the protein, by fitting the apparent specific heat capacity below $T_g(1)$ with equation 5.4a with a constant $X_{water}(T)$. The value of $X_{water}(T)$ indicates the percent of water inside the protein matrix. The bound water content determined by the heat capacity model agrees with the value that is determined from TGA measurement, and in all samples there was about 5 wt% of bound water.

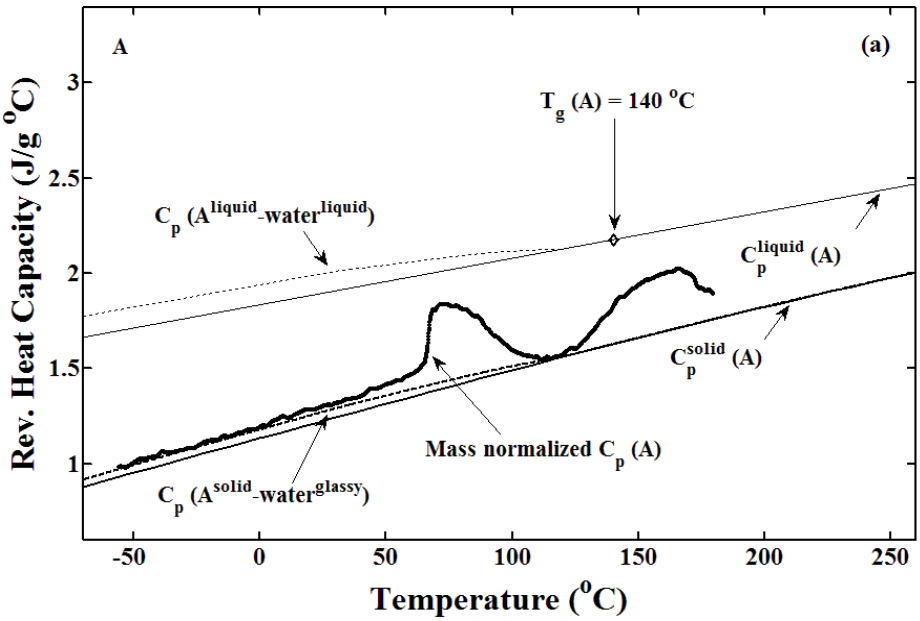
A
(a)
T_g (A) = 140 °C
C_p (A^{liquid}-$water^{liquid}$)
C_p^{liquid} (A)
C_p^{solid} (A)
Mass normalized C_p (A)
C_p (A^{solid}-$water^{glassy}$)
Rev. Heat Capacity (J/g °C)
Temperature (°C)

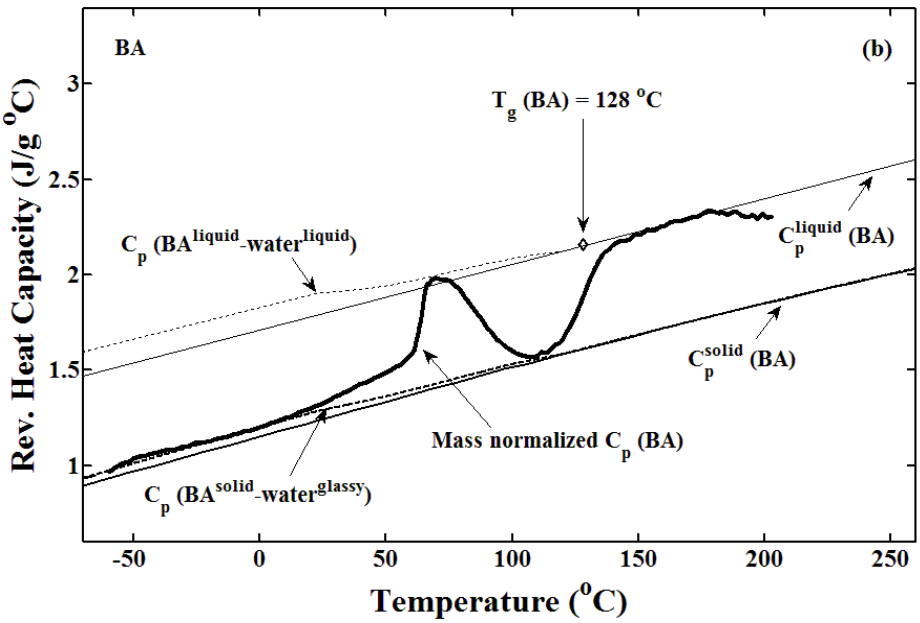
BA
(b)
T_g (BA) = 128 °C
C_p (BA^{liquid}-$water^{liquid}$)
C_p^{liquid} (BA)
C_p^{solid} (BA)
Mass normalized C_p (BA)
C_p (BA^{solid}-$water^{glassy}$)
Rev. Heat Capacity (J/g °C)
Temperature (°C)

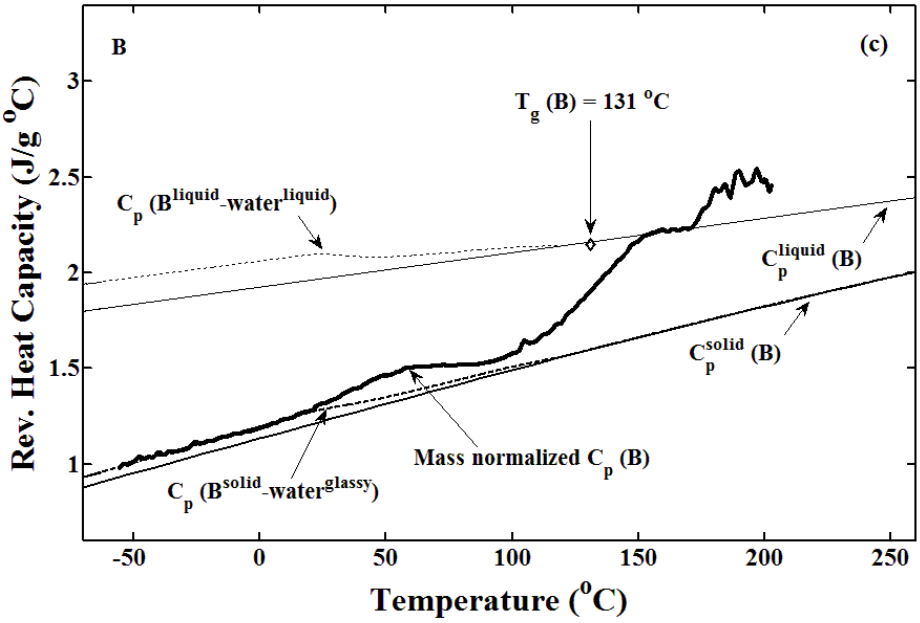
B
(c)
T_g (B) = 131 °C
C_p (B^{liquid}-$water^{liquid}$)
C_p^{liquid} (B)
C_p^{solid} (B)
Mass normalized C_p (B)
C_p (B^{solid}-$water^{glassy}$)
Rev. Heat Capacity (J/g °C)
Temperature (°C)
3
2.5
2
1.5
1
-50
0
50
100
150
200
250

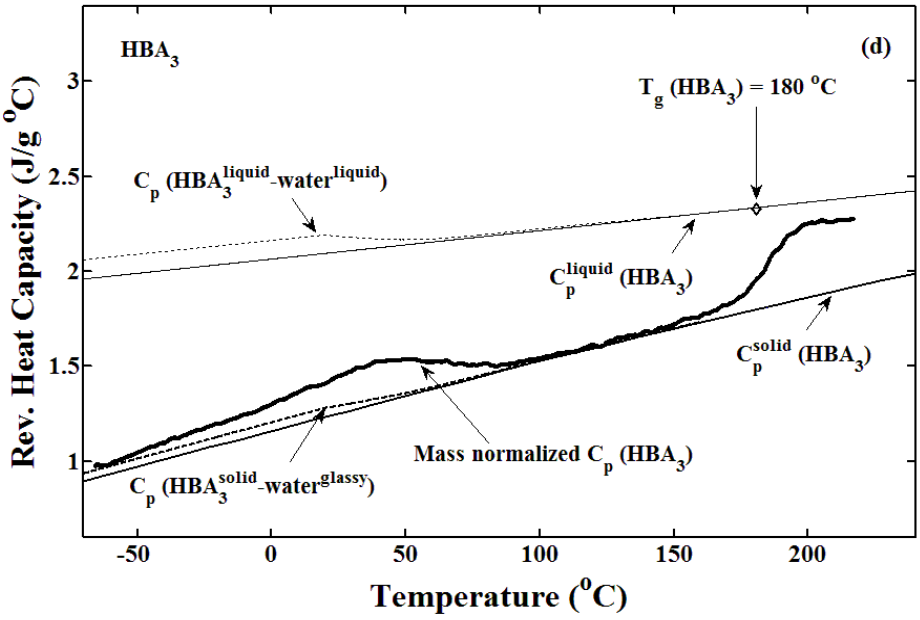
HBA_3
(d)
T_g (HBA_3) = 180 °C
C_p (HBA_3^{liquid}-$water^{liquid}$)
C_p^{liquid} (HBA_3)
C_p^{solid} (HBA_3)
Mass normalized C_p (HBA_3)
C_p (HBA_3^{solid}-$water^{glassy}$)
Rev. Heat Capacity (J/g °C)
Temperature (°C)
3
2.5
2
1.5
1
-50
0
50
100
150
200

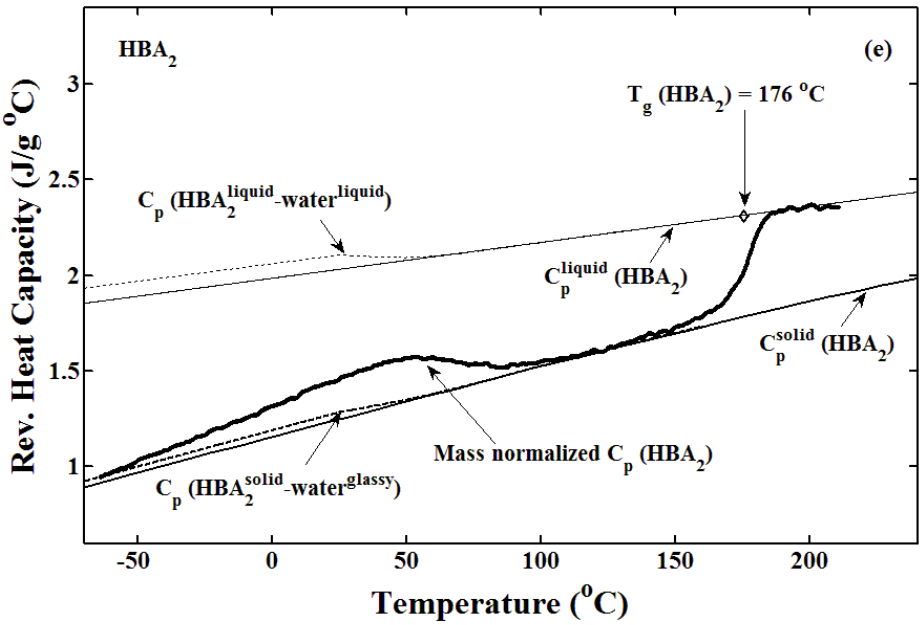
HBA2
(e)
Tg (HBA2) = 176 °C
Cp (HBA2liquid-waterliquid)
Cpliquid (HBA2)
Cpsolid (HBA2)
Mass normalized Cp (HBA2)
Cp (HBA2solid-waterglassy)
Rev. Heat Capacity (J/g °C)
Temperature (°C)

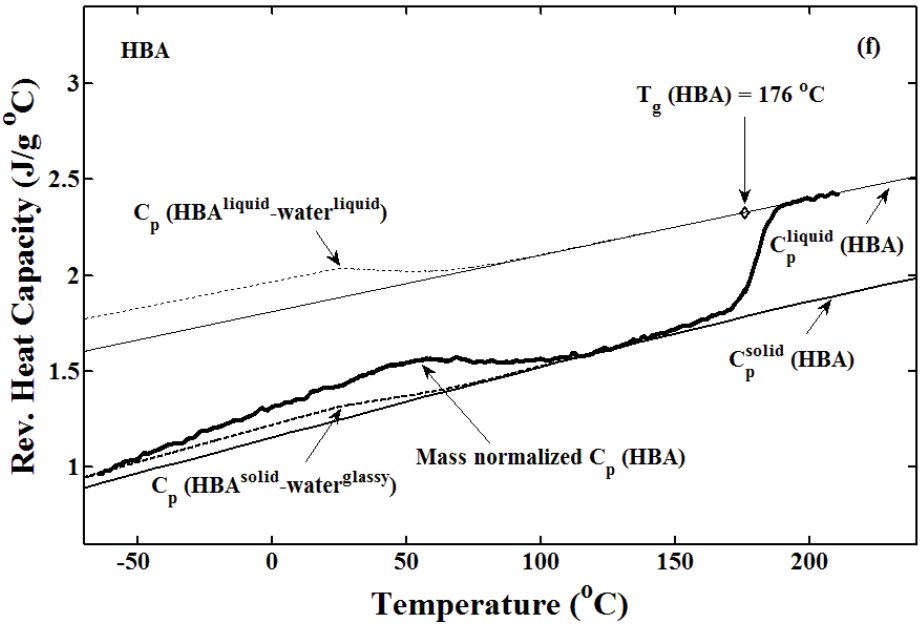
HBA
(f)
Tg (HBA) = 176 °C
Cp (HBAliquid-waterliquid)
Cpliquid (HBA)
Cpsolid (HBA)
Mass normalized Cp (HBA)
Cp (HBAsolid-waterglassy)
Rev. Heat Capacity (J/g °C)
Temperature (°C)

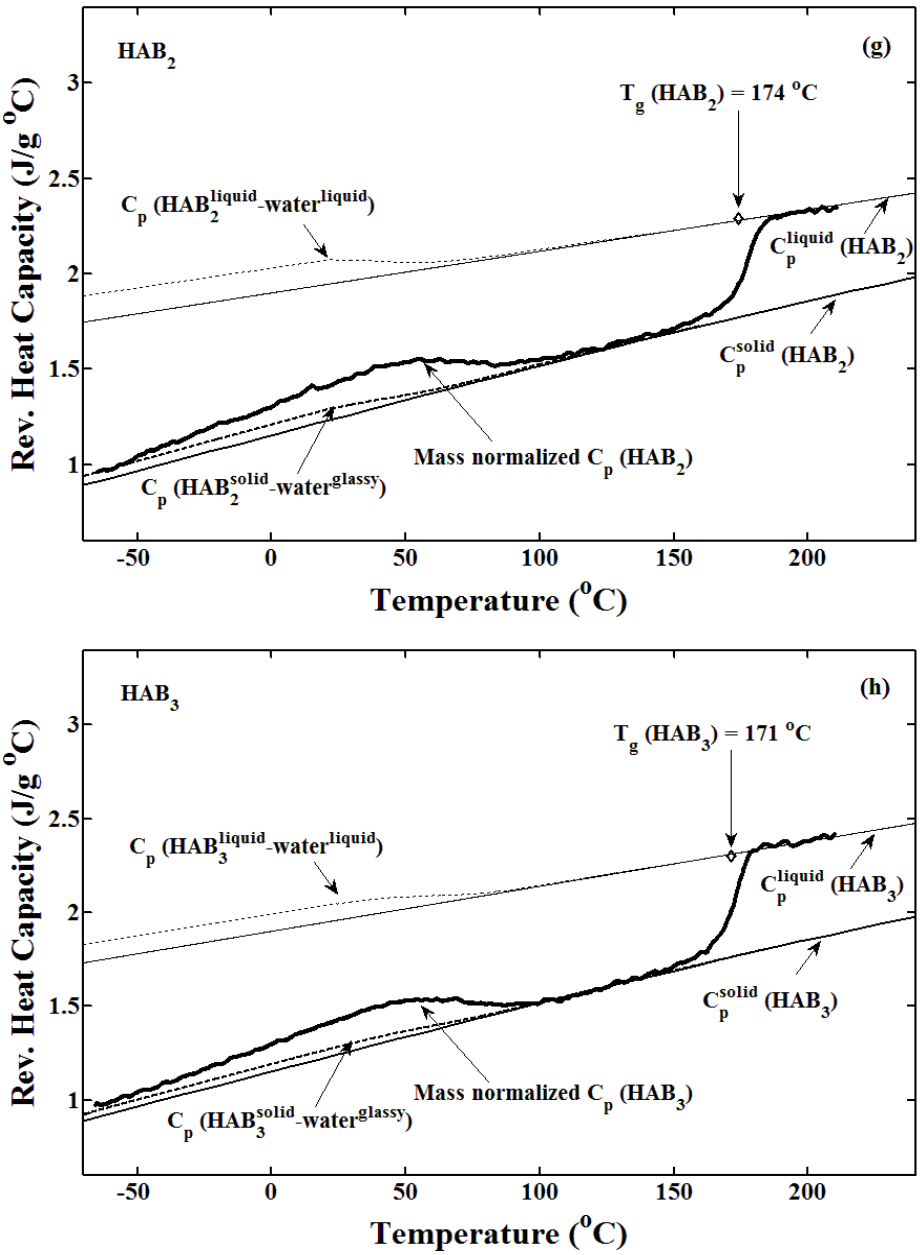

Figure 5.3. TMDSC apparent specific reversing heat capacity curves of recombinant spider silk-like block copolymers films: (a) A, (b) BA, (c) B, (d) HBA_3, (e) HBA_2, (f) HBA, (g) HAB_2, and (h) HAB_3, during heating at 2 °C/min from -60 to 220 °C. Key: heavy curve, mass normalized C_p*(protein)*; thick solid line, C_p^{solid}*(protein)*; thick dashed line, C_p *(protein*^{solid} - *water*^{glassy}*)*; thin solid line, C_p^{liquid}*(protein)*; thin dashed line, C_p*(protein*^{liquid} – *water*^{liquid}*)*; open diamond, C_p^{liquid}*(protein)* calculated at T_g.

Isothermal experiments were also performed to investigate the binding and conformational transition in the $T_g(1)$ region. **Figure 5.4** shows the endothermic total heat flow as a function of time when holding isothermally at 50 °C, and the endothermic behaviors ended at about 10 min for all samples. To calculate the protein-water binding energy and the conformational relaxation energy, the total heat flow was integrated with respect to time. The enthalpy, ΔH, which is determined by the endothermic peak area, is summarized in Table 5.1 column 5. The water-protein binding energy, ΔE, which is calculated as the heat absorbed to remove the water molecule from the protein chain per mole of bound water during the isothermal holding, is also summarized in Table 5.1 column 6. The calculated ΔE for our spider silk-like block copolymers is in the range from 2.3 to 3.8 kcal/mol, and the value is comparable to the prediction of ligand (water) binding affinities of 3.5 kcal/mol [45]. The result indicates that the energy absorbed by the evaporated water molecules is strongly dependent on the volume fraction of the hydrophilic block in the protein. As illustrated by HBA_3, HBA_2, HBA, HAB_2, and HAB_3, the water-protein binding energy, ΔE, increases with increased volume fraction of hydrophilic B-block. For A and BA, as we suggested previously, the endothermic peaks can be attributed to two phenomena: the water loss during heating and the protein chain rearrangement into a precursor state. Thus, the enthalpy that is determined by the endothermic peak area is the summation of the enthalpy needed for these two phenomena for A and BA at the fixed temperature, 50 °C, and these enthalpy values cannot be used to calculate the water-protein binding energy, ΔE, for A and BA.

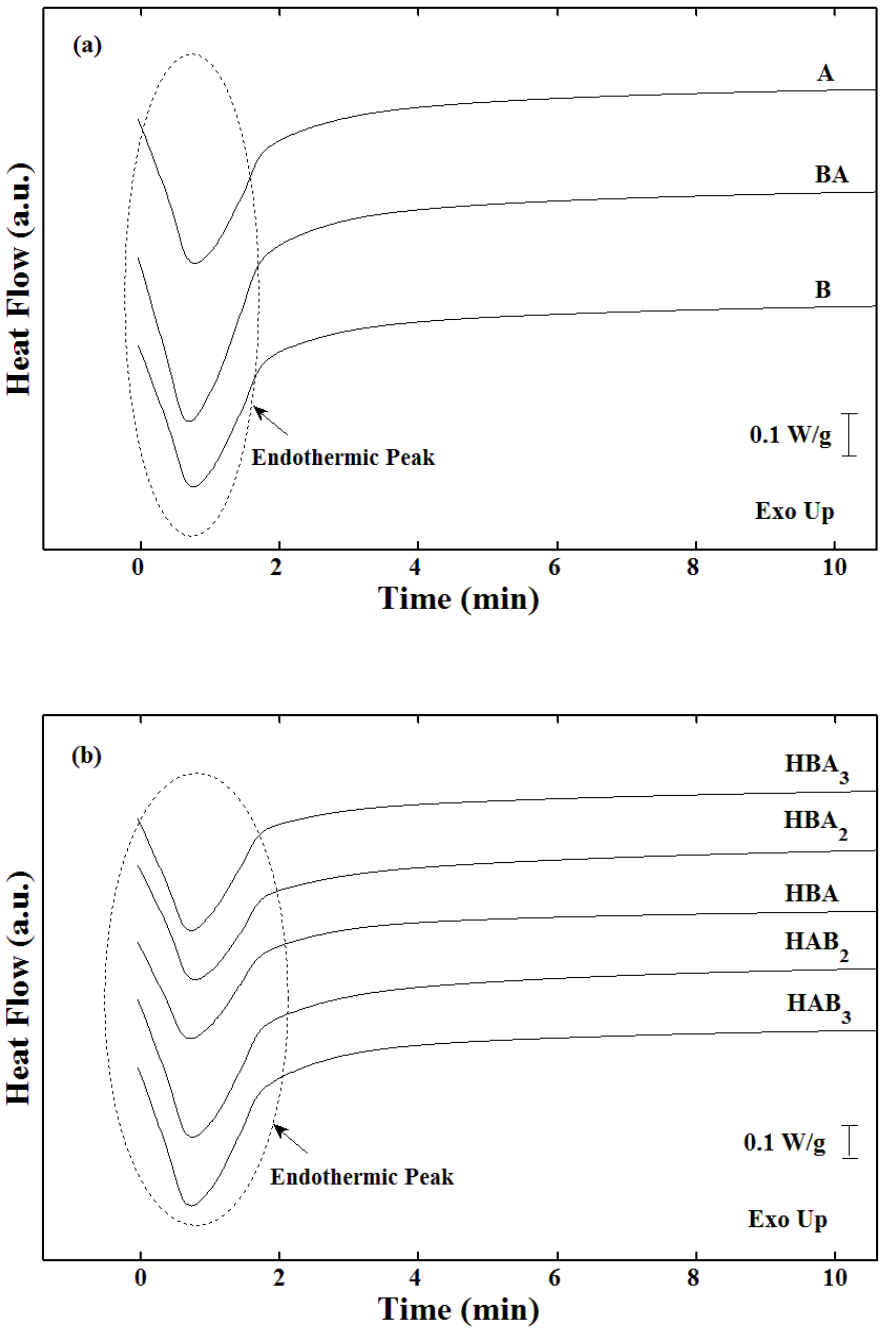

Figure 5.4. TMDSC total heat flow curves versus time of recombinant spider silk-like block copolymers films: (a) A, BA, B and (b) HBA_3, HBA_2, HBA, HAB_2, and HAB_3, during isothermal holding at 50 °C. The total heat flow is normalized by the initial weight, M_0.

5.3.2 Secondary Structure Analysis

Though TMDSC provides us a detailed picture about thermal transitions in the protein-water system, it does not provide any insight about what type of structure is formed or diminished during that transition. Thus, further investigation using a structure-specific probe to monitor the structural changes during heating is needed. Fourier transform infrared spectroscopy (FTIR) has been an established tool for the secondary structure characterization of polypeptide and proteins [29, 30, 46]. In this study, we carried out FTIR analysis to assess secondary structural changes of recombinant spider silk-like block copolymer during heating in the amide I region (1700–1600 cm–1), which contains contributions from the C=O stretching vibration of the amide group (about 80%) with a minor contribution from the C-N stretching vibration [30], and the amide II region (1575–1480 cm–1), which arises from N-H bending (60%) and C-N stretching (40%) vibrations [29].

Figure 5.5 shows the real-time FTIR spectra of recombinant spider silk-like block copolymers during heating at 2 °C/min from 30 to 220 °C. The spectra are collected *in situ* with the use of a hotstage. Compared to the traditional heat treatment method in which the samples are heated to varying elevated temperatures, and then measured at room temperature, more accurate kinetic information can be obtained using an *in situ* method by avoiding additional structural changes induced by cooling after the actual heat treatment. To separate the role of the temperature alone on the IR absorbance intensity, a Boltzmann calculation is performed for our spider silk-like block copolymers. Following the theoretical calculation by Snyder *et al.* [47], the ratio of the absorbance of an infrared band at two temperatures, T_1 and T_2, at wavenumber, $\bar{\upsilon}$, can be expressed as [47]

$$\frac{A_{T_2}}{A_{T_1}} = \frac{\exp(-hc\bar{\nu}/kT_1)+1}{\exp(-hc\bar{\nu}/kT_2)+1} \tag{5.5}$$

where *h* is the Planck's constant, *c* is the speed of light, and *k* is the Boltzmann constant, with the value of *hc/k* = 1.439 cm K. By equation 5.5, we can conclude that, in the Amide I and the Amide II regions (1700-1480 cm^{-1}), the ratio of the absorbances of an infrared band at 220 ºC and 30 ºC, A_{220}/A_{30}, is about 0.99, which means only about 1% of the decrease of IR absorbance at the highest temperature in our *in situ* measurement, 220 ºC, is due to the thermal effect. Other factors decrease the IR absorbance as well, such as the reduction of the free volume of the water plasticized sample film induced by annealing. Polymer chain conformational changes also influence the IR absorbance intensity. Hu *et al.* performed a similar *in situ* FTIR measurement for the water plasticized silk fibroin films [3, 4] with a methanol treated film as the reference. From their result the thermal effect from the Boltzmann calculation along with the reduction of free volume by annealing leads to no more than a 20% decrease of the IR absorbance intensity in the Amide I and the Amide II regions [3, 4], and the major influence on the IR absorbance comes from the conformational changes, such as the formation of the beta sheet secondary structure.

To investigate the structural changes during heating of our spider silk-like block copolymer, we correlate the IR wavenumber with secondary structures. The band assignments are summarized in **Table 5.2**. In general, we classify the components between 1620–1630 cm^{-1} and 1520-1530 cm^{-1} to intermolecular beta sheets; 1630–1667 cm^{-1} and 1520-1551 cm^{-1} to random coils and α helices; and 1670–1695 cm^{-1} to turns [28, 48]. Because HBA_2, HBA, HAB_2, and HAB_3 shows a similar structure to B at room

temperature, and exhibit a similar structural change during heating, in Figure 5.5, we only show A, BA, B, HBA_3 and HAB_2 as examples. As observed from the FTIR spectra, beta sheets dominated in A and HBA_3, while random coils and alpha helices dominated in BA, B, HBA_2, HBA, HAB_2, and HAB_3 at 30 °C. When temperature increases from 30 °C to 220 °C, we observed an increase of beta sheets structure in A and BA, as well as an increase of beta turns structures and a decrease of random coils and alpha helices in all samples. Results indicate that A, consisting of only the hydrophobic alanine rich block, is the most easily crystallized sample. It was crystallized at room temperature during the lyophilization process, and it can also by crystallized by thermal treatment. BA and HBA_3 have a relatively higher volume fraction of the hydrophobic alanine rich block, and they form beta sheets either by thermal treatment or by lyophilization, respectively. B, HBA_2, HBA, HAB_2, and HAB_3 have a relatively low volume fraction of hydrophobic alanine rich blocks, therefore they do not form any beta sheets in the protein matrix. Hydrogen-bonding also influences the wavenumber of the absorption peaks. In general, hydrogen-bonding lowers the frequency of stretching vibrations, but increases the frequency of bending vibrations [46]. By destroying the hydrogen-bonding between protein and water molecules during heating, the C=O stretching vibration of the amide group should shift to a higher frequency in the Amide I region, and the N-H bending vibration of the amide group should shift to a lower frequency in the Amide II region. As shown in Figure 5.5, the beta sheet peak, in the Amide I region, slightly shifted to a higher frequency (from 1624 cm^{-1} to 1629 cm^{-1} within the resolution), and in the Amide II region, it also slightly shifted to a lower frequency (from 1526 cm^{-1} to 1521 cm^{-1} within the resolution) in semicrystalline A and HBA_3 samples. Results indicate that

hydrogen-bonds in the protein-water system broke during heating in the *in situ* measurements.

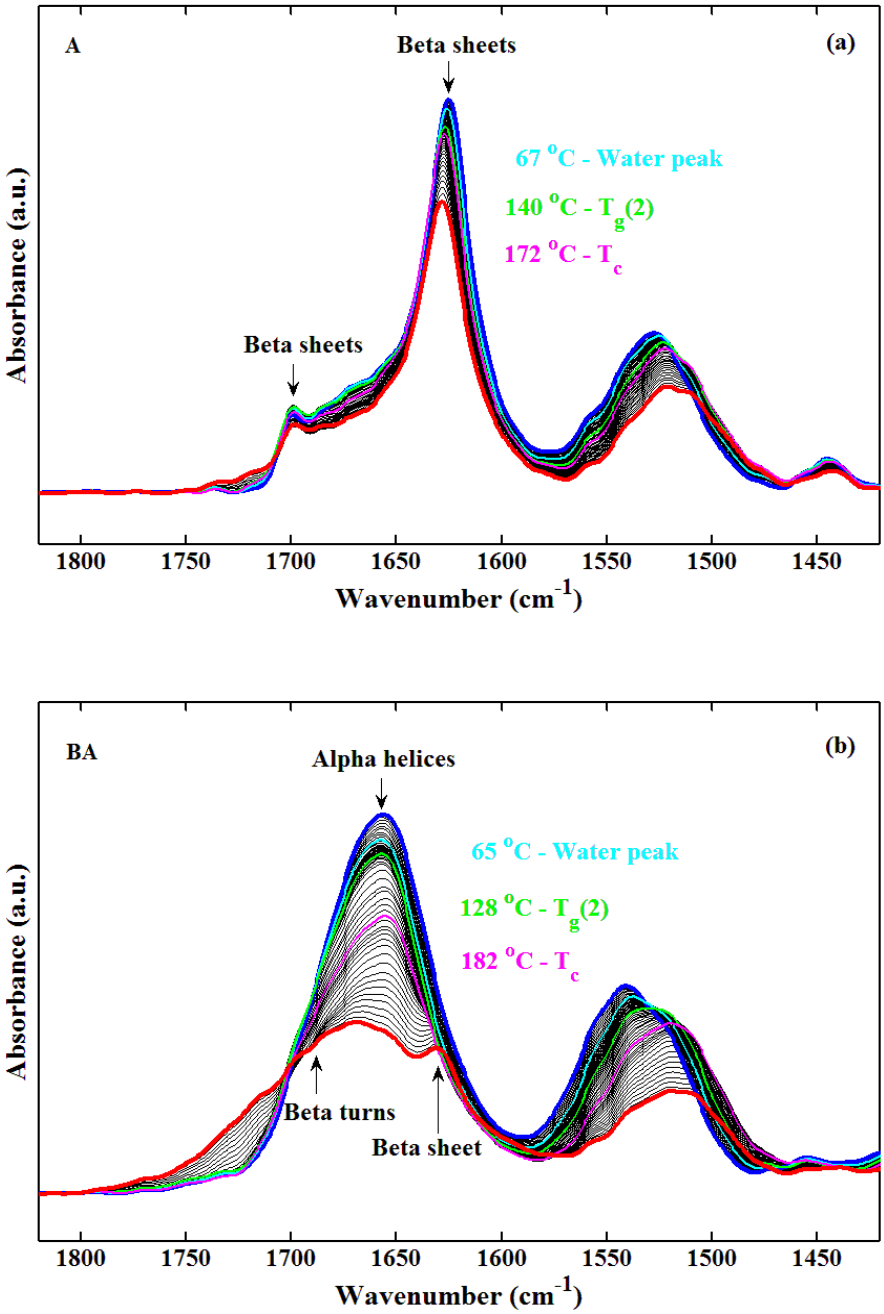

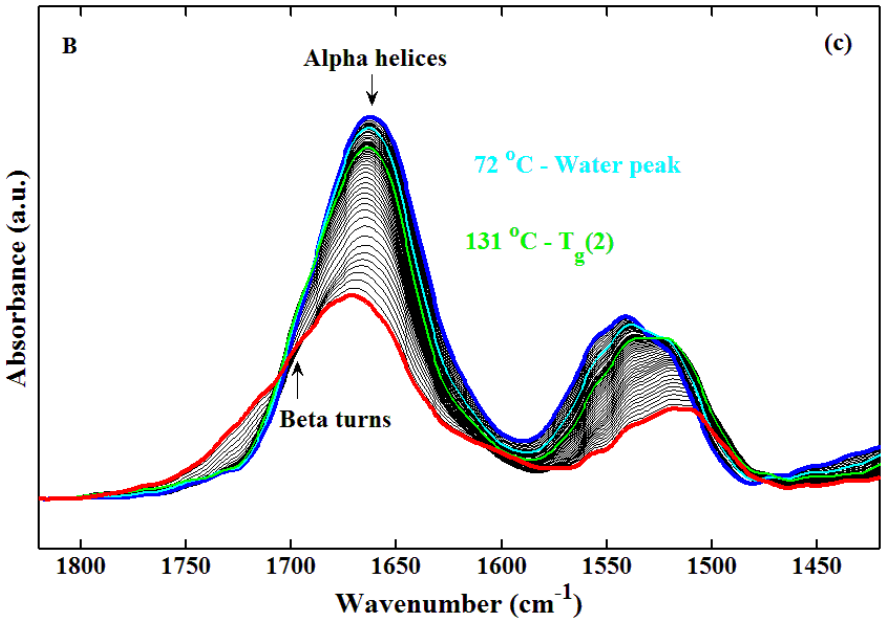
B
(c)
Alpha helices
72 °C - Water peak
131 °C - Tg(2)
Beta turns
Absorbance (a.u.)
1800
1750
1700
1650
1600
1550
1500
1450
Wavenumber (cm-1)

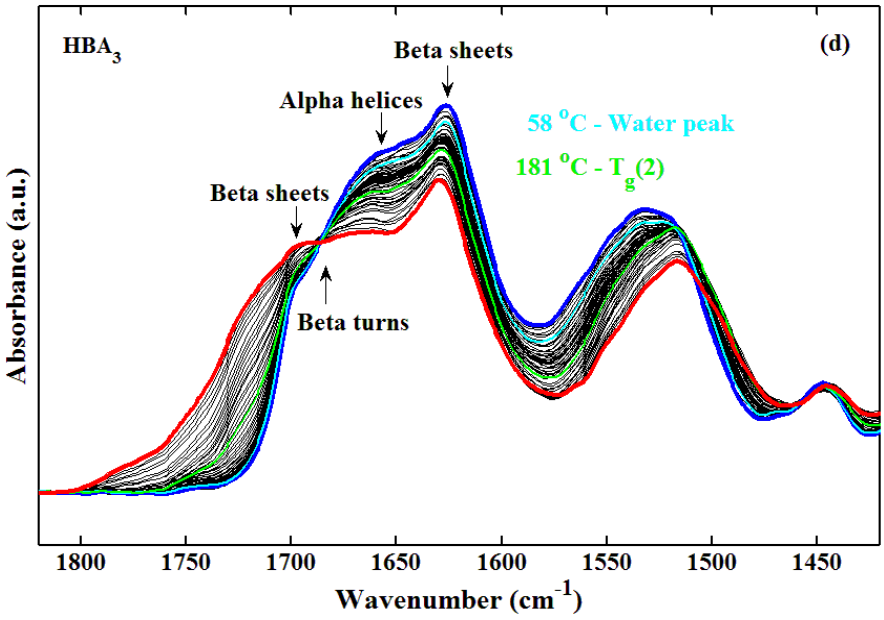
HBA3
(d)
Beta sheets
Alpha helices
58 °C - Water peak
181 °C - Tg(2)
Beta sheets
Beta turns
Absorbance (a.u.)
1800
1750
1700
1650
1600
1550
1500
1450
Wavenumber (cm-1)

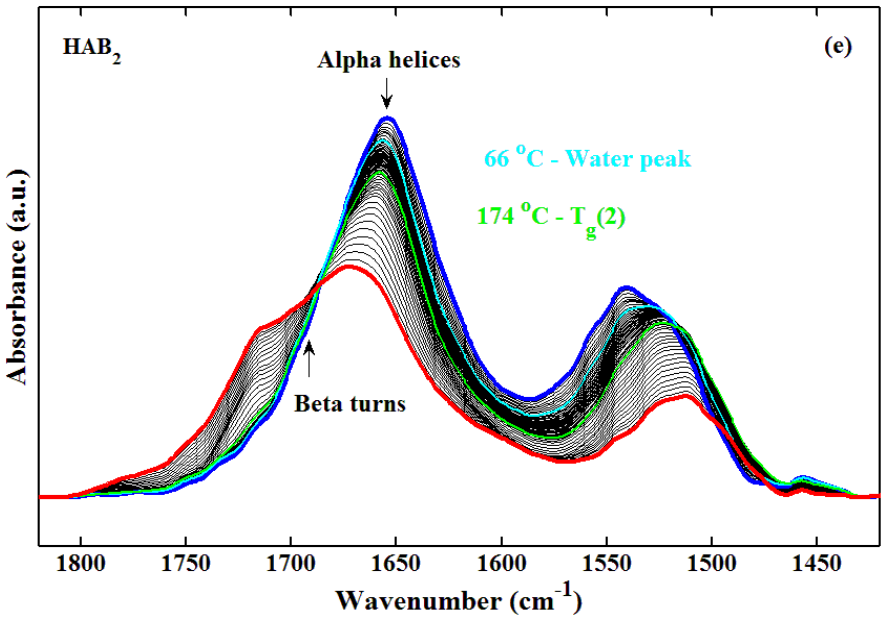

Figure 5.5 Real-time FTIR spectra of recombinant spider silk-like block copolymers films: a) A, (b) BA, (c) B, (d) HBA_3, and (e) HAB_2 during heating at 2 °C/min. HBA_2, HBA, HAB_2, and HAB_3 show a similar trend as B. Keys: Blue curve – 30 ºC; turquoise curve – water peak; green curve - T_g (2); and red curve - 220 ºC.

Table 5.2 FTIR Vibrational Band Assignments of Recombinant Spider Silk-like Block Copolymers in the Amide I and Amide II Regions

Amide I		**Amide II**	
Wavenumber Range (cm^{-1})	**Peak Assignment[a]**	**Wavenumber Range (cm^{-1})**	**Peak Assignment[b]**
1595-1605	Side chains		
1605-1615	Side chains, aggregated strands	1498-1518	(Tyr) side chains
1618-1629	Beta sheet (strong)	1520-1530	Beta sheet
1630-1642	Random coils, extended chain structures	1520-1545	Random coils
1643-1657	Random coils	1526-1527	(Lys) side chains
1658-1667	Alpha helices	1545-1551	Alpha helices
1668-1678	Turns	1556-1560	(Glu) side chains
1679-1685	Turns	1574-1579	(Asp) side chains
1686-1696	Turns	1575, 1594	(His) side chains
1697-1703	High-frequency antiparallel beta sheets (weak)		

[a] Reference [28, 30, 46]

[b] Reference [48, 49]

To further understand the conformational transition during heating, the changes in the absorption spectra are visualized and examined using difference spectra. The residual absorbance, $\Delta Abs(T)$, between the absorbance spectra at temperature T, $Abs(T)$, and the initial spectrum at 30 °C, $Abs(30)$, was calculated by:

$$\Delta Abs(T) = Abs(T) - Abs(30) \quad (5.6)$$

In the difference spectra plots (Figure 5.6), if the residual absorbance is positive, the bands are attributed to developing structures, whereas if the residual absorbance is negative, the bands are attributed to diminishing structures. A control sample whose structure was not changing during the scans was used to illustrate the effect of temperature alone as well. To serve as a control sample, BA was annealed to remove the bound water and it was crystallized during the annealing, so no thermal transitions occur in the temperature range below $T_g(2)$. The residual absorbance, $\Delta Abs_{control} = Abs(T_g(2)) - Abs(30)$, for the control sample is shown in Figure 5.6(b) (orange traces). Compared to the conformational change of the silk-water system, the thermal effect alone on the sample is relatively small.

By observing the difference spectra, the conformational change of the secondary structure can be seen more clearly. As shown in **Figure 5.6**, when the temperature increased from 30 to 220 ºC, in amorphous samples, such as B, BA, HBA_2, HBA, HAB_2, and HAB_3, the IR absorbance centered around 1650 cm^{-1} and 1550 cm^{-1} decreased dramatically, corresponding to the vanishing random coils and alpha helices structures [30, 46, 50]. In semicrystalline samples, such as A and HBA_3, the IR absorbance centered around 1617 cm^{-1}, 1650 cm^{-1} and 1533 cm^{-1} decreased, corresponding to the reduction of side chain vibrations [4, 49], the shifting of the beta sheet band [46], and the loss of random coils and alpha helices structures [30, 46, 50]. The bands centered around 1718 cm^{-1} and 1696 cm^{-1} increased during heating from 30 to 220 ºC in all samples, and this indicates the development of new structures. The peak at 1718 cm^{-1} increases dramatically when the temperature is above $T_g(2)$, and it is usually assigned to the

oxidation peak of proteins [50]. The peak at 1696 cm^{-1} increased during heating as well, and it indicates the development of beta turns [4, 28, 50]. Thus, in the heating process, some mobile random coils and alpha helices transformed into more stable conformations, such as beta turn structures, and at high temperature, the samples oxidized in air.

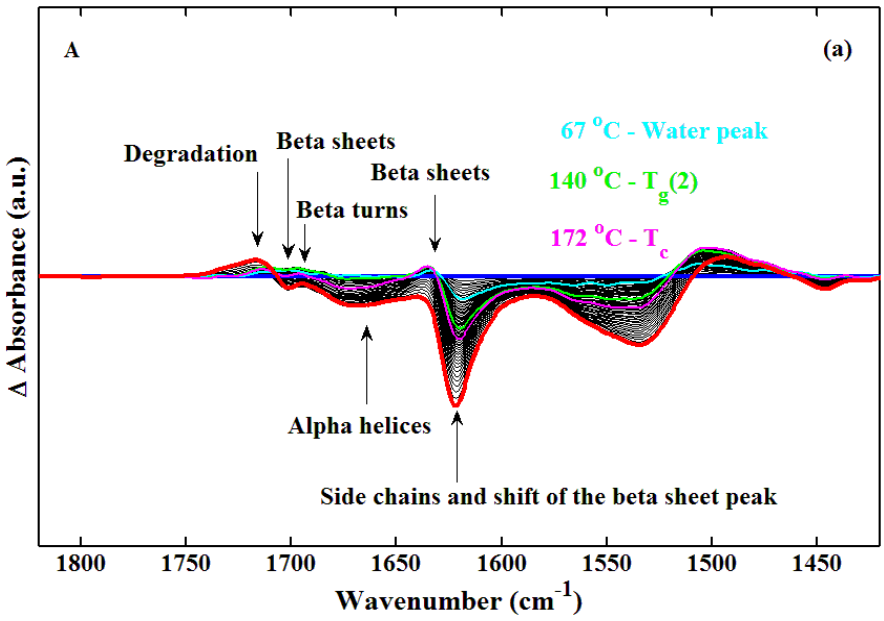

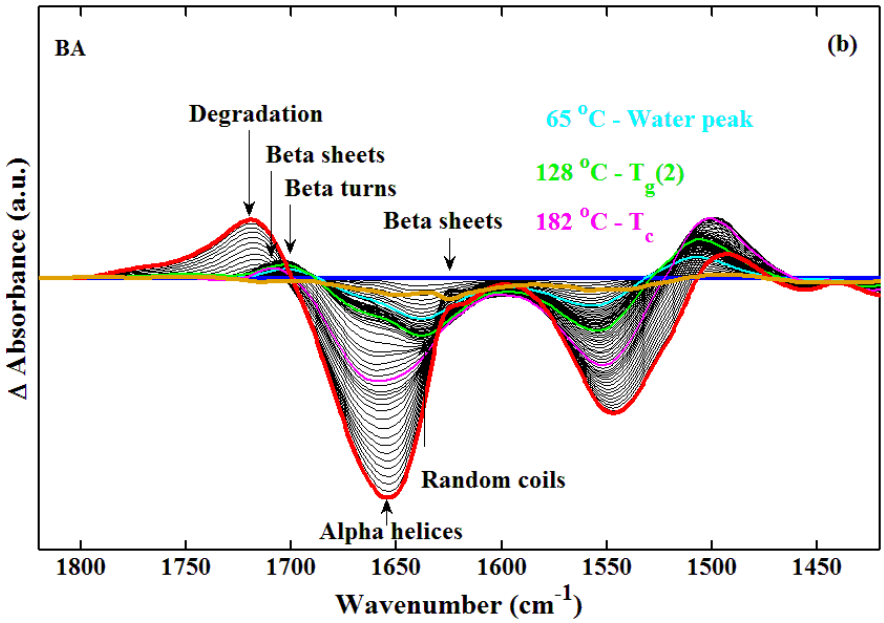

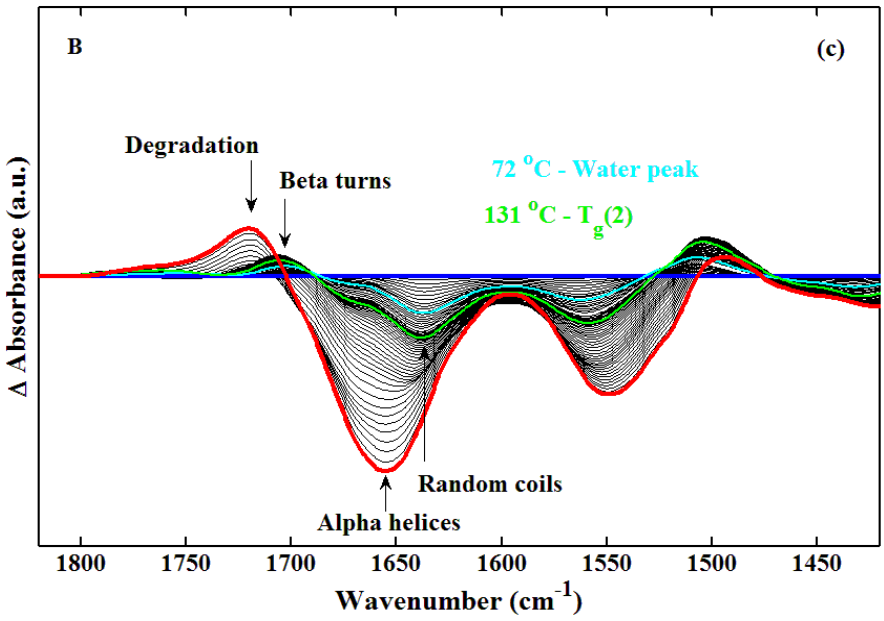
B
(c)
Degradation
Beta turns
72 °C - Water peak
131 °C - Tg(2)
Random coils
Alpha helices
Δ Absorbance (a.u.)
1800
1750
1700
1650
1600
1550
1500
1450
Wavenumber (cm-1)

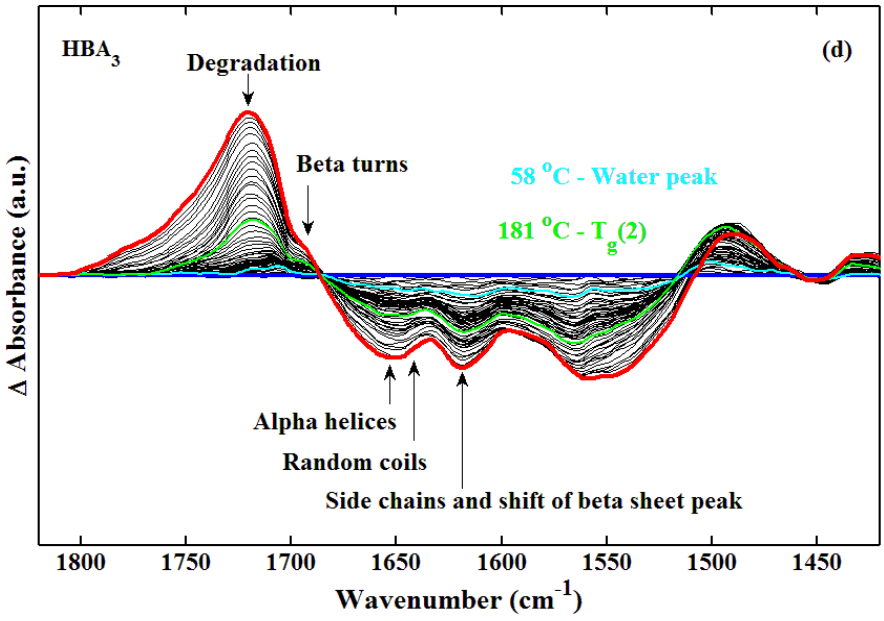
HBA3
Degradation
(d)
Beta turns
58 °C - Water peak
181 °C - Tg(2)
Alpha helices
Random coils
Side chains and shift of beta sheet peak
Δ Absorbance (a.u.)
1800
1750
1700
1650
1600
1550
1500
1450
Wavenumber (cm-1)

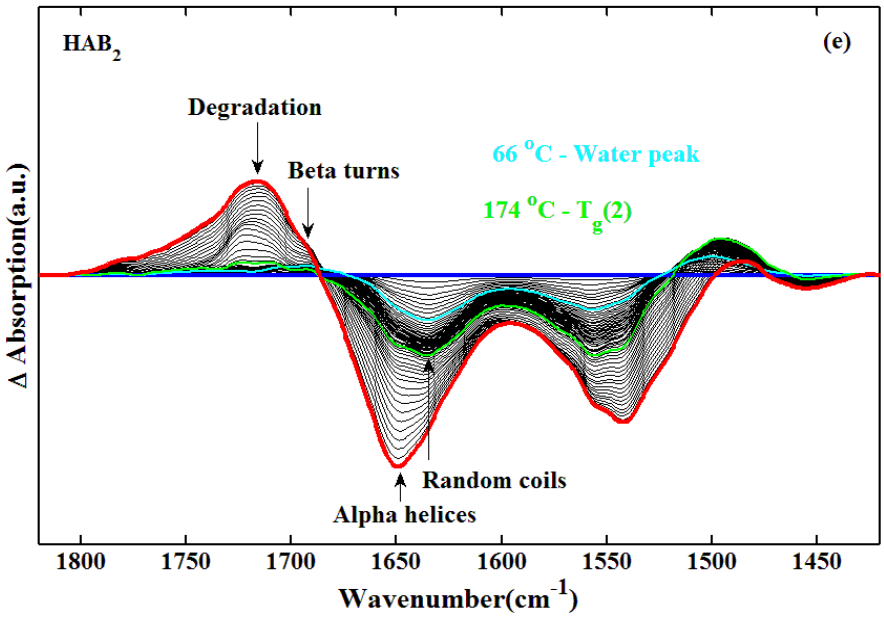

Figure 5.6 Real-time FTIR residual absorbance spectra of recombinant spider silk-like block copolymers films: (a) A, (b) BA, (c) B, (d) HBA_3, and (e) HAB_2 during heating at 2 °C/min. HBA_2, HBA, HAB_2, and HAB_3 show a similar trend as B. Keys: Blue curve – 30 °C; turquoise curve – water peak; green curve - $T_g(2)$; red curve - 220 °C; and orange curve in (b) – example of the thermal effect on spectra below $T_g(2)$. Residual absorbance is calculated from equation 5.6.

To investigate the secondary structural conformation change during the glass transition, the kinetics of the formation of beta turns and the loss of random coils and alpha helices were studied using the normalized *ΔAbs* vs. temperature plots. The normalized *ΔAbs* are calculated by the *ΔAbs* values divided by the absolute value of the maximum change of *ΔAbs* in that temperature range. The conformational transitions at $T_g(1)$ and $T_g(2)$ are investigated separately by using amorphous samples and are illustrated in **Figure 5.7** and **Figure 5.8** by BA and HBA, respectively. As shown in

Figure 5.7 (a - b) and Figure 5.8 (a - b), with the increase of the temperature around $T_g(1)$ region, the bands at 1640 cm^{-1} decreased, while the bands at 1696 cm^{-1} increased. The decrease of the 1640 cm^{-1} band is due to the vanishing of random coil structure and the removal of the bound water, and the increase of the 1696 cm^{-1} indicates the formation of beta turns. As shown in Figure 5.7 (c - d) and Figure 5.8 (c - d), with the increase of the temperature around $T_g(2)$ region, the bands at 1662 cm^{-1} decreased, while the bands at 1696 cm^{-1} increased, which indicates a diminishing of the alpha helices and increase of the beta turns.

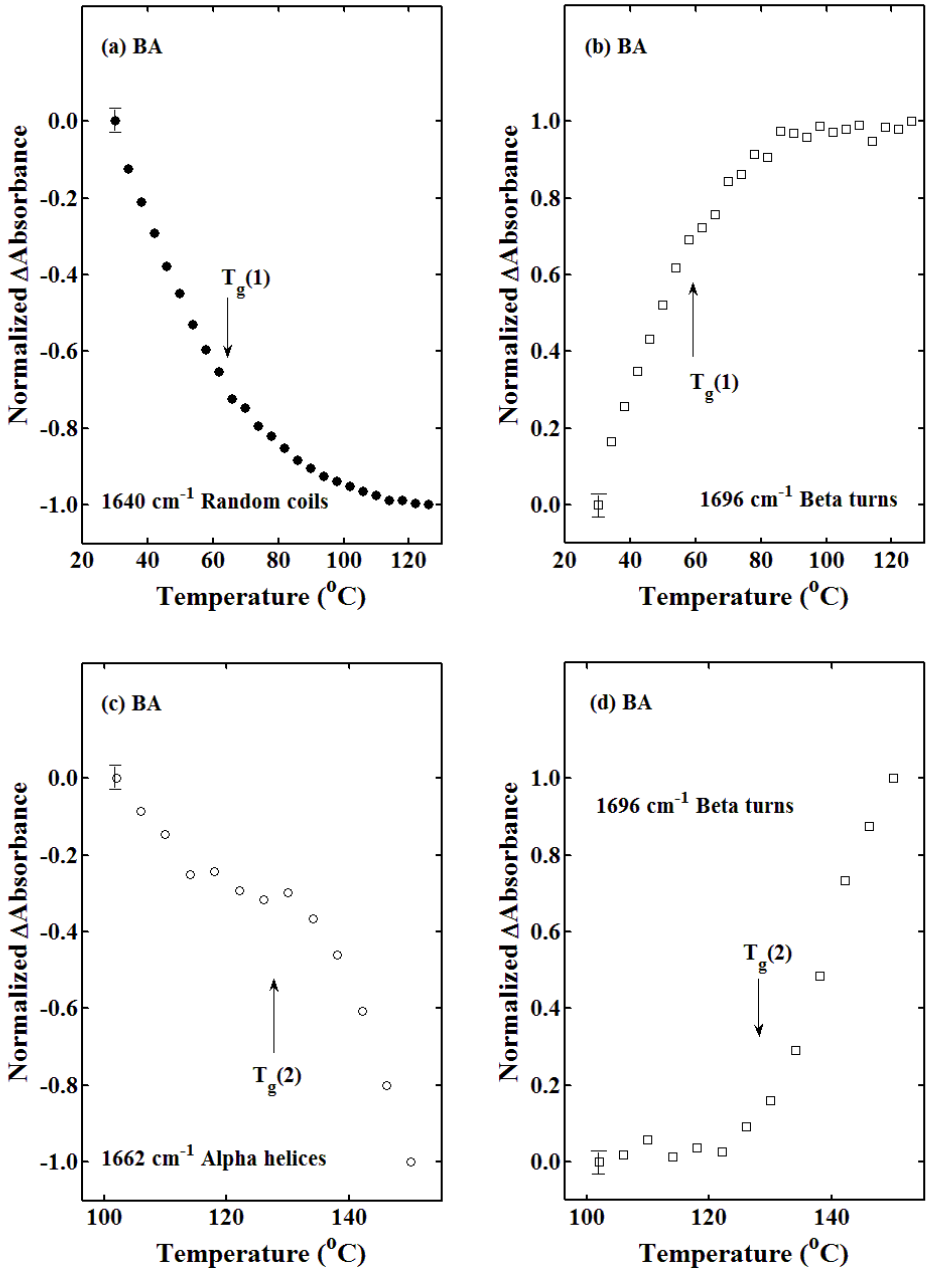

Figure 5.7 Normalized residual absorbance spectra of recombinant spider silk-like block copolymers films during heating at 2 °C/min, illustrated by BA. (a) Change of 1640 cm^{-1} band in $T_g(1)$ region; (b) Change of 1696 cm^{-1} band in $T_g(1)$ region; (c) Change of 1662 cm^{-1} band in $T_g(2)$ region; and (d) Change of 1696 cm^{-1} band in $T_g(2)$ region.

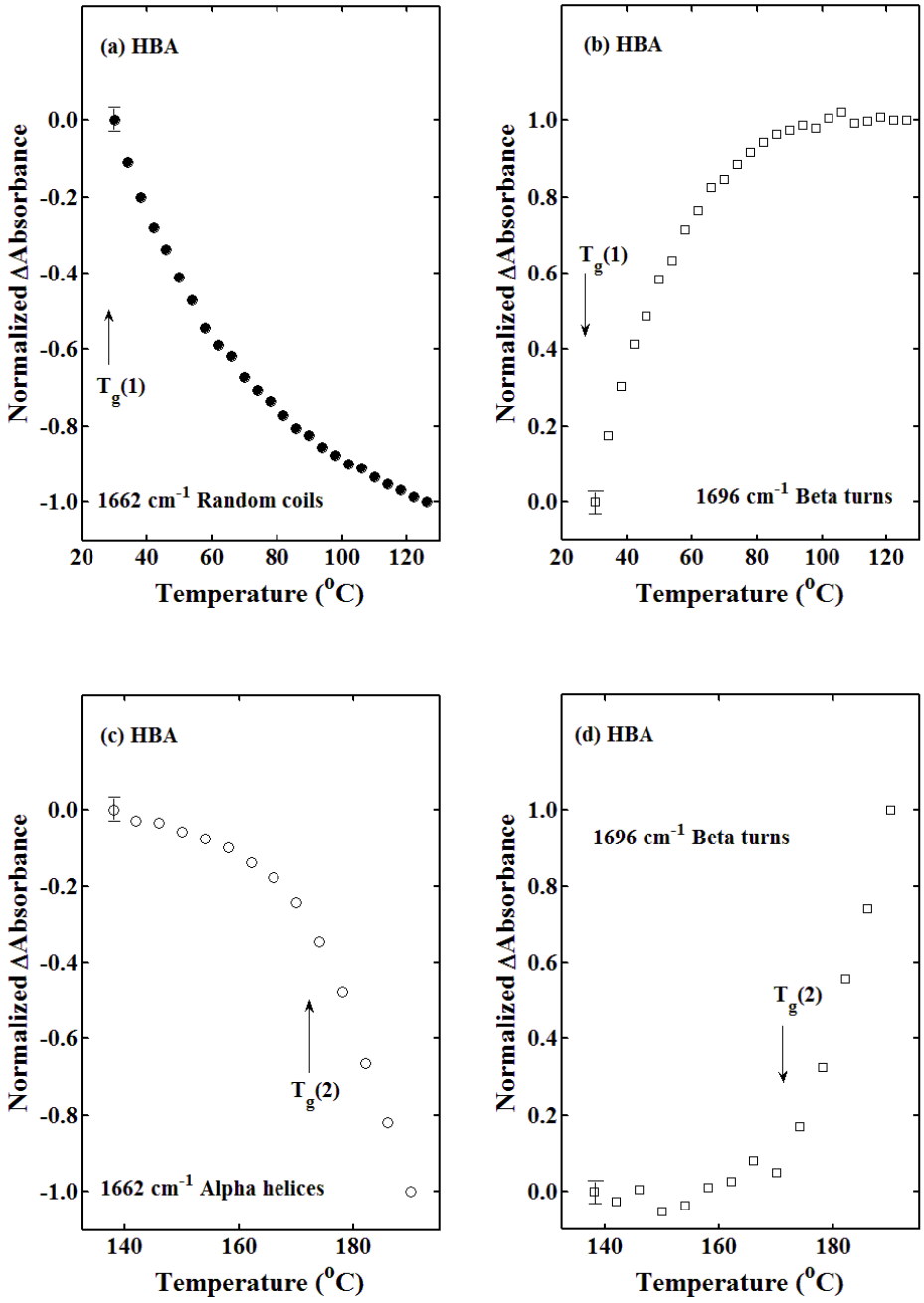

Figure 5.8 Normalized residual absorbance spectra of recombinant spider silk-like block copolymers films during heating at 2 °C/min, illustrated by HBA. (a) Change of 1640 cm^{-1} band in $T_g(1)$ region; (b) Change of 1696 cm^{-1} band in $T_g(1)$ region; (c) Change of 1662 cm^{-1} band in $T_g(2)$ region; and (d) Change of 1696 cm^{-1} band in $T_g(2)$ region.

The rate of change in the band is suggested by the slope of the normalized *ΔAbs* curve. In the $T_g(1)$ region, the bound water molecules initially expanded the accessible conformational space and acted as a "mobility enhancer" of the protein chains. When the bound water is removed from the protein, the free volume in between the protein chain was reduced, which caused a conformational transition of loosely packed random coil structure to beta turns in all samples. As shown in Figure 5.7 (a - b) and Figure 5.8 (a - b), the rate of this conformation change increases with increasing temperature. Because the $T_g(1)$ region overlaps the bound water removal region, the rate is related to not only the glass transition but also to how fast the bound water is removed from the protein chain. During $T_g(2)$, the now dry amorphous protein chains themselves transformed from a glassy state to a rubbery state. The rate of change significantly increases at the glass transition temperature, and during this thermal transition, alpha helices change to the beta turn conformation.

5.3.3 Morphology Analysis

The morphology of recombinant spider silk-like block copolymers was exanimated by SEM. The protein chain configurations can be classified into three different groups, as shown in **Figure 5.9**: (1) a hydrophobic head (A-block) with one hydrophilic tail (HB-block), such as BA, HBA_3, HBA_2 and HBA, (2) a hydrophobic head (A-block) with two hydrophilic tails (His-tag and B-block), such as HAB_2, and HAB_3, and (3) hydrophobic or hydrophilic block alone, such as A and B.

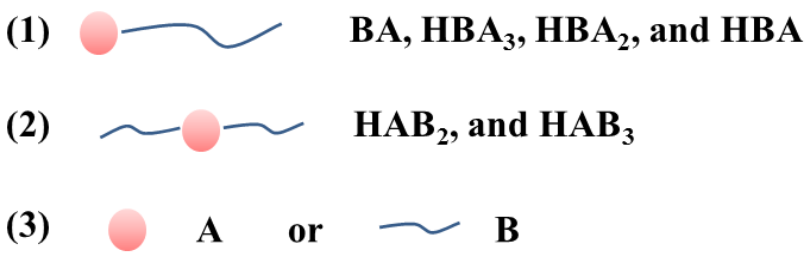

Figure 5.9 The protein chain configurations of spider silk-like block copolymers.

The hydropathy plot is calculated using the ExPASy ProtScale protein analysis tool [51], and illustrated by HBA_3 and HAB_3 as shown in **Figure5.10**. The calculation is based on the value obtained by Wolfenden *et.al.* [52], from which a positive number corresponds to a hydrophobic amino acid sequence and a negative number corresponds to a hydrophilic amino acid sequence.

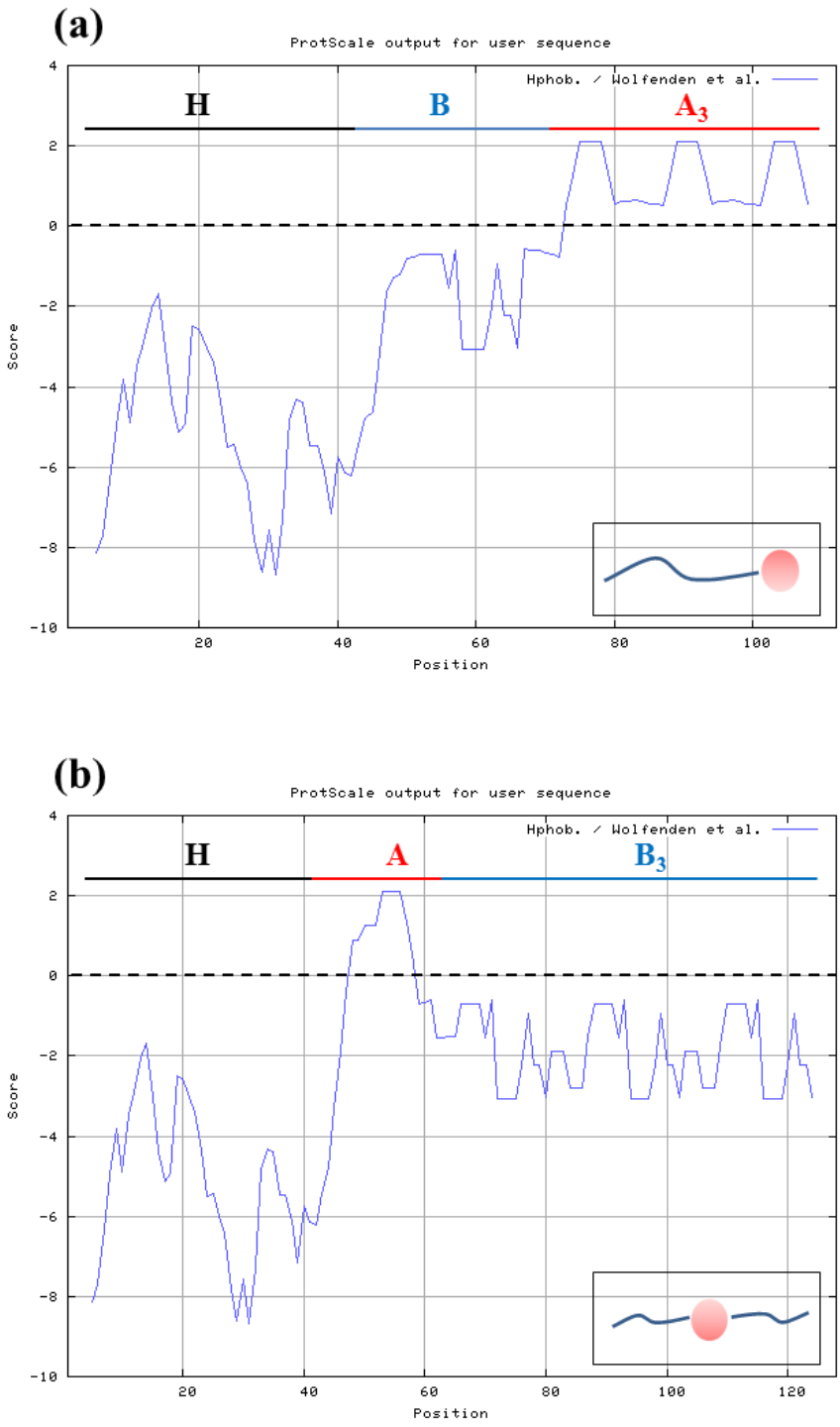

Figure 5.10 Hydropathy plots for (a) HBA_3 and (b) HAB_3 calculated based on references [51, 52].

Because the A-block is hydrophobic and the B-block is hydrophilic, the spider silk-like block copolymers behave as amphiphilic molecules, and self-assemble into various structures in water solution. As shown in **Figure 5.11**, several distinct morphologies were observed: in A, layer-like structure was formed; in BA, B, HBA, HAB_2, and HAB_3, no ordered structure was observed; and in HBA_2 and HBA_3, vesicle structures and fibrillar structures were observed. It is known that to form spherical micelles, cylindrical micelles, bilayer and vesicle structures, the volume fraction of the hydrophobic block is critical [53]. By increasing the volume fraction of hydrophobic block, f_A, to HBA_2 (f_A = 29%), the vesicle structures can be observed. The samples films were also heat treated to above the $T_g(2)$, and the morphologies formed after the heat treatment were check by SEM as well. As can be seen in Figure 5.11, the morphologies formed after heat treatment are quite similar to those formed before the heat treatment. This result indicates that relaxation occuring in amorphous region do not affect the film morphology, and the self-assembly micro-structures are stable even above the dry protein glass transition.

(a)

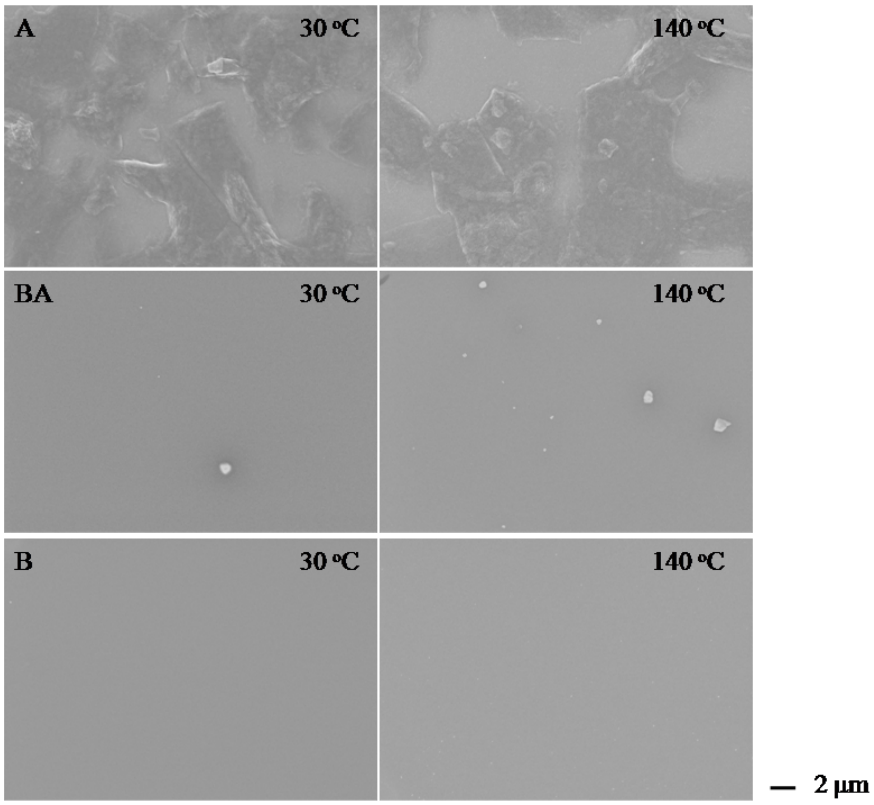

(b)

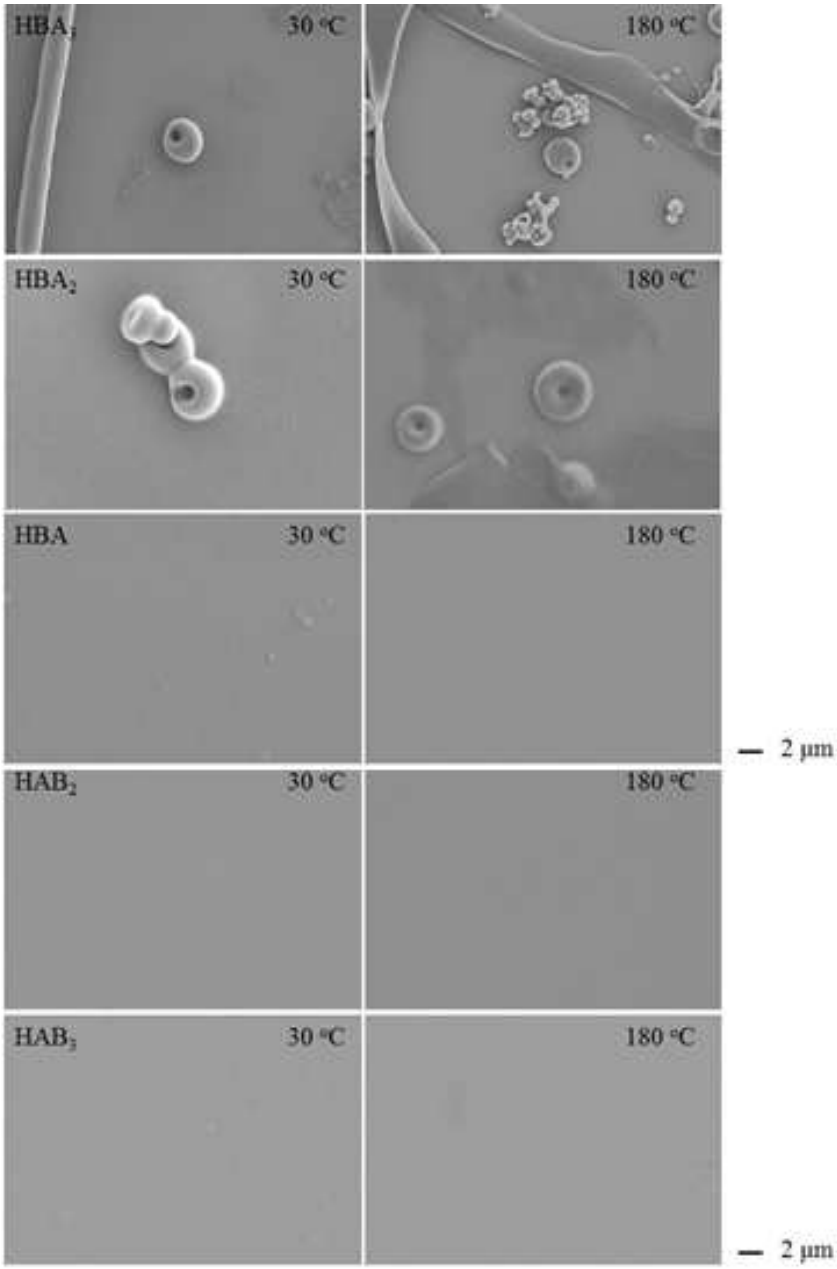

Figure 5.11 SEM morphology of recombinant spider silk-like block copolymers films: (a) A, BA, B at 30 °C and 140 °C, and (b) HBA_3, HBA_2, HBA, HAB_2, and HAB_3, at 30 °C and 180 °C. The same scale bar on the right side applies to all parts of the figure.

5.4 Conclusions

A family of recombinant spider silk-like block copolymers were characterized. These proteins were inspired by the genetic sequences found in the dragline silk of *Nephila clavipes*, comprising of an alanine-rich hydrophobic block, A, a glycine-rich hydrophilic block, B, and a C-terminus or a His-tag, H. Advanced thermal analysis methods using temperature modulated differential scanning calorimetry (TMDSC) in combination with thermogravimetric analysis (TGA) were employed to capture the thermal transitions in water cast protein films. With the help of the theoretical baselines of the specific reversing heat capacity of the protein-water system, $C_p(T)$, along with the TMDSC measurements show that two glass transitions formed in all samples during heating. The low temperature glass transition, $T_g(1)$, is related to both the bound water removal induced conformational change and the hydrophobicity of the protein sequences, while the high temperature glass transition, $T_g(2)$, refers to the now dry protein. Real-time Fourier transform infrared spectroscopy (FTIR) confirmed that different conformational changes occurred during the two glass transitions. A random coils to beta turns transition dominates during $T_g(1)$, and alpha helices to beta turns transition dominates during $T_g(2)$. The thermal stability of the self-assembly morphology formed by the spider silk-like block copolymer were also investigated by SEM. Result indicates the morphology is not changing during $T_g(1)$ and $T_g(2)$.

This study provides a deeper understanding of the protein-water relationships and the conformational changes in protein-water system during heating with implications for the thermal induced structural transitions of other protein base materials.

5.5 References

1. Kuntz ID, Brassfie.Ts, Law GD, and Purcell GV. *Science* 1969; 163(3873): 1329-1331.
2. Kuntz ID. *Journal of the American Chemical Society* 1971; 93(2): 514-516.
3. Hu X, Kaplan D, and Cebe P. *Thermochimica Acta* 2007; 461(1-2): 137-144.
4. Hu X, Kaplan D, and Cebe P. *Macromolecules* 2008; 41(11): 3939-3948.
5. Pyda M, Hu X, and Cebe P. *Macromolecules* 2008; 41(13): 4786-4793.
6. Nicholls A, Sharp KA, and Honig B. *Proteins-Structure Function and Genetics* 1991;11(4):281-296.
7. Zhang XQ, Burgar I, Do MD, and Lourbakos E. *Biomacromolecules* 2005; 6(3): 1661-1671.
8. Zayas JF. *Functionality of proteins in food. Berlin*; New York: Springer, 1997.
9. Semenova MG, Belyakova LE, Polikarpov YN, Ii'in MM, Istarova TA, Anokhina MS, and Tsapkina EN. *Biomacromolecules* 2006; 7(1): 101-113.
10. Kim YS, Dong LM, Hickner MA, Glass TE, Webb V, and McGrath JE. *Macromolecules* 2003; 36(17): 6281-6285.
11. Santagapita PR, Brizuela LG, Mazzobre MF, Ramirez HL, Corti HR, Santana RV, and Buera MP. *Biomacromolecules* 2008; 9(2): 741-747.
12. Pyda M. *Macromolecules* 2002; 35(10): 4009-4016.
13. Pyda M. *Journal of Polymer Science Part B-Polymer Physics* 2001; 39(23): 3038-3054.
14. Jin HJ, Park J, Karageorgiou V, Kim UJ, Valluzzi R, and Kaplan DL. *Advanced Functional Materials* 2005; 15(8): 1241-1247.

15. Hu X, Shmelev K, Sun L, Gil E-S, Park S-H, Cebe P, and Kaplan DL. *Biomacromolecules* 2011; 12(5): 1686-1696.
16. Dicko C, Knight D, Kenney JM, and Vollrath F. *Biomacromolecules* 2004; 5(6): 2105-2115.
17. Sapede D, Seydel T, Forsyth VT, Koza MA, Schweins R, Vollrath F, and Riekel C. *Macromolecules* 2005; 38(20): 8447-8453.
18. Krishnaji ST, Huang WW, Rabotyagova O, Kharlampieva E, Choi I, Tsukruk VV, Naik R, Cebe P, and Kaplan DL. *Langmuir* 2011; 27(3): 1000-1008.
19. Kluge JA, Rabotyagova U, Leisk GG, and Kaplan DL. *Trends in Biotechnology* 2008; 26(5): 244-251.
20. Work RW. *Textile Research Journal* 1977; 47(10): 650-662.
21. Savage KN, Guerette PA, and Gosline JM. *Biomacromolecules* 2004; 5(3): 675-679.
22. Simmons A, Ray E, and Jelinski LW. *Macromolecules* 1994; 27(18): 5235-5237.
23. Hayashi CY, Shipley NH, and Lewis RV. International Journal of Biological *Macromolecules* 1999; 24(2-3): 271-275.
24. Eles PT and Michal CA. *Macromolecules* 2004; 37(4): 1342-1345.
25. Li X, Eles PT, and Michal CA. *Biomacromolecules* 2009; 10(5): 1270-1275.
26. Chow D, Nunalee ML, Lim DW, Simnick AJ, and Chilkoti A. *Materials Science & Engineering R-Reports* 2008; 62(4): 125-155.
27. Rabotyagova OS, Cebe P, and Kaplan DL. *Biomacromolecules* 2009; 10(2): 229-236.
28. Huang WW, Krishnaji S, Hu X, Kaplan D, and Cebe P. *Macromolecules* 2011; 44(13): 5299-5309.

29. Jackson M and Mantsch HH. *Critical Reviews in Biochemistry and Molecular Biology* 1995; 30(2): 95-120.

30. Barth A. *Biochimica Et Biophysica Acta-Bioenergetics* 2007; 1767(9): 1073-1101.

31. Rabotyagova OS, Cebe P, and Kaplan DL. *Biomacromolecules* 2011; 12(2): 269-289.

32. Lee KY and Ha WS. *Polymer* 1999; 40(14): 4131-4134.

33. Hodge RM, Bastow TJ, Edward GH, Simon GP, and Hill AJ. *Macromolecules* 1996; 29(25): 8137-8143.

34. Motta A, Fambri L, and Migliaresi C. *Macromolecular Chemistry and Physics* 2002; 203(10-11): 1658-1665.

35. Agarwal N, Hoagland DA, and Farris RJ. *Journal of Applied Polymer Science* 1997; 63(3): 401–410.

36. Hu X, Kaplan D, and Cebe P. *Macromolecules* 2006; 39(18): 6161-6170.

37. Ghosh K and Dill KA. *Proceedings of the National Academy of Sciences of the United States of America* 2009; 106(26): 10649-10654.

38. Huang W, Krishnaji S, Kaplan D, and Cebe P. *Journal of Thermal Analysis and Calorimetry* 2011; 109(3): 1193-1201.

39. Bruylants G, Wouters J, and Michaux C. *Current Medicinal Chemistry* 2005; 12(17): 2011-2020.

40. Downing JW and Newell JA. *Journal of Applied Polymer Science* 2004; 91(1): 417–424.

41. Pyda M, Hu X, and Cebe P. *Macromolecules* 2008; 41(13): 4786-4793.

42. Ma Q, Mao B, and Cebe P. *Polymer* 2011; 52(14): 3190-3200.

43. Taylor LS, Langkilde FW, and Zografi G. *Journal of Pharmaceutical Sciences* 2001; 90(7): 888-901.

44. Hu X, Kaplan D, and Cebe P. *Journal of Thermal Analysis and Calorimetry* 2009; 96(3): 827-834.

45. Fischer S and Verma CS. *Proceedings of the National Academy of Sciences of the United States of America* 1999; 96(17): 9613-9615.

46. Barth A and Zscherp C. *Quarterly Reviews of Biophysics* 2002; 35(4): 369-430.

47. Snyder RW, Sheen CW, and Painter PC. *Applied Spectroscopy* 1988; 42(3): 503-508.

48. Tamm LK and Tatulian SA. *Quarterly Reviews of Biophysics* 1997; 30(4): 365-429.

49. Barth A. *Progress in Biophysics and Molecular Biology* 2000; 74(3-5): 141-173.

50. Tian K, Shao Z, and Chen X. *Journal of Applied Polymer Science* 2012; 124(4): 2838–2845.

51. **Ex**pert **P**rotein **A**nalysis **Sy**stem (ExPASy) proteomics server, http://expasy.org/, 2012

52. Wolfenden R, Andersson L, Cullis PM, and Southgate CCB. *Biochemistry* 1981; 20(4): 849–855.

53. Jones RAL. *Soft condensed matter*. Oxford; New York: Oxford University Press, 2002.

`

Chapter VI. Tunable Self-assembly, Crystallization and Degradation of Spider Silk-like Block Copolymer

This chapter studied the thermodynamic properties, structural changes and morphological features of spider silk-like block copolymer system with respect to protein amino acid sequence under various treatments.

6.1 Introduction

Amphiphilic block copolymers (ABCs) have the ability to self-assemble in solution into multiple morphologies with features on the nanometer length scale. Depending on the relative volume fractions of the hydrophobic and hydrophilic blocks, the self-assembled morphology can vary from spherical micelles, to rods, lamellae, vesicles or large compound micelles [1-5]. In recent years, ABCs are of great interest in drug and gene delivery systems [6, 7] as well as templating applications for the synthesis of nanostructured materials [8]. Among the synthetic, hybrid peptidic-synthetic, and protein-based ABCs, recombinant protein-based amphiphilic block copolymers expressed by using techniques of molecular biology have gained increasing attention in current material science studies [9-14]. Unlike synthetic polymers, recombinant proteins are usually bio-tailored to possess specific hydrophobicity patterns or secondary structures to form ABCs through the appropriate selection and positioning of amino acid residues mimicking the remarkable designs in Nature. Therefore, recombinant protein-based

`

ABCs have a number of advantages compared to other types of ABCs. First, they possess precisely defined amino acid sequences which would be extremely useful for discovering the relationship between sequence, structure, and protein bulk physical properties. Second, they are monodisperse which greatly facilitates the precise control of self-assembled supramolecular architecture. Third, and most importantly, they are biocompatible and biodegradable because of their natural origin. Thus, recombinant protein-based ABCs are superior to synthetic copolymers in many respects for biomedical research and applications.

Silks are some of the most interesting bio-block copolymers which can serve as the templates to inspire the design of recombinant protein-based ABCs. In general, silks are modular in nature. For example, in *B. mori* cocoon silk fibroin, detailed study shows that twelve repeating regions along the fibroin chain are connected by eleven non-repetitive, less ordered regions in the fibroin heavy chain component [15, 16]. The highly repetitive GAGAGS hexa-amino acid sequences in *B. mori* silk fibroin are responsible for the formation of the beta sheet crystalline regions, and the non-repeating amino acid sequences are responsible for the formation of the non-crystalline, less ordered regions. In *Nephila Clavipes* spider drag line silks, two different major motifs with an N-terminus and C-terminus exist in major ampullate dragline silk protein 1 (MaSp1) [17, 18]. The GA/A_n motif forms beta sheets crystalline regions, and the GG*X* motif forms the α helical less ordered regions. Using molecular biology, there has been considerable progress in mimicking the amino acid sequences in the natural silk structural motifs and recombining these motifs into new functional ABCs [9, 10, 12, 14]. By investigating recombinant protein block copolymers, details are revealed which are useful to solve fundamental

`

issues in polymer science, such as the mechanisms of nanostructure self-assembly [5], the relationships of protein sequence to structure [19], and microphase separation [20] of bio-polymers, as well as to inspire new biomedical engineering applications for gene transfer therapy [13, 21] and drug delivery [6, 13].

In our research, we characterized a family of novel recombinant protein-based ABCs inspired by the genetic sequences found in *Nephila Clavipes* spider dragline silk. The proteins are produced using recombinant DNA technology. A di-block copolymer model system based on MaSp1 motifs was chosen as the building template with A-block (hydrophobic) mimicking the GA/A_n poly-alanine region and B-block (hydrophilic) mimicking the GG*X* glycine rich region. The goals of our research are first, to study the self-assembly morphology and mechanism of recombinant spider silk-like protein block copolymers with different volume faction of hydrophobic and hydrophilic blocks using scanning electron microscopy (SEM). Our second goal is to investigate crystallization kinetics, degradation profiles, and the relationship of their physical properties with specific amino acid motifs by temperature modulated differential scanning calorimetry (TMDSC) and Fourier transform infrared spectroscopy (FTIR). We demonstrate that beta sheet crystalline structures play an important role in the protein self-assembly and degradation processes. Aside from the fundamental perspective, we also anticipate that these results will provide a roadmap for the design and control of biocompatible and biodegradable recombinant protein-based ABCs for drug delivery systems and smart functional silk-based materials.

`

6.2 Experimental Section

6.2.1 Materials

Two amino acid sequences from *Nephila Clavipes* spider dragline silk were selected as the building blocks of our recombinant spider silk-like block copolymers. A-block is a hydrophobic poly-alanine block which is responsible for the formation of beta sheet crystalline regions. B-block is a hydrophilic glycine rich block which is responsible for the formation of disordered, non-crystalline regions. The di-block copolymers also contain a His-tag, H, for purification purposes. The synthesis method of these protein-based ABCs was described in detail in our previous publications [10, 11]. In brief, after constructing the cloning vector, cloning silk modules into a modified pET30L vector, expressing and purifying, recombinant spider silk-like block copolymers, HBA_6, HBA_3, HBA_2, HBA, HAB_2 and HAB_3 were obtained in solid form after lyophilization. Protein identification was confirmed by matrix assisted laser desorption ionization time of flight (MALDI–TOF) mass spectrometry.

6.2.2 Real-time Fourier Transform Infrared Spectroscopy (FTIR)

Real-time FTIR was carried out on a Jasco infrared microscope IRT-5000 in transmission mode with a liquid nitrogen cooled Mercury-Cadmium-Telluride (MCT) detector. A Mettler optical microscopy hot stage (FP90) was incorporated with FTIR to control the sample temperature. Sample films cast on calcium fluoride (CaF_2) discs were inserted into the hot stage and heated at a rate of 5 °C/min from 30 to 340 °C for real-time FTIR measurements. The absorbance spectra in the frequency range from 400 to 4000 cm^{-1} were obtained by averaging 32 scans with a resolution of 4.0 cm^{-1}. The air

`

background spectra were subtracted from the sample scans. Before the experiments, the temperature of the hot stage was calibrated with a thermocouple.

6.2.3 Temperature Modulated Differential Scanning Calorimetry (TMDSC)

TMDSC studies were performed on a TA Instruments Q100 DSC with dry nitrogen gas at a flow rate of 50 mL/min. Materials were solubilized in hexafluoroisopropanol, HFIP, and cast into films by solvent evaporation. Dried HFIP-cast samples were sealed into aluminum pans and heated in the DSC cell at a heating rate of 5 °C/min with oscillation amplitude of 0.318 °C and a modulation period of 60 s. The empty aluminum pan with the same weight as the sample pan was used as reference in all the runs. The temperature and heat flow of the TMDSC were calibrated using indium standard before experiments.

6.2.4 Scanning Electron Microscopy (SEM)

The surface morphologies of the solution-cast recombinant spider silk-like block copolymers films were imaged using a Zeiss Supra55VP SEM and a Zeiss Ultra55 SEM in the Center for Nanoscale Systems at Harvard University. All samples were cast on silicon surfaces and allowed to dry overnight at room temperature. After drying, samples were sputter-coated with platinum- palladium. Images were taken using SE2 and InLens detectors at 5.00 kV.

`

6.3 Results and Discussion

6.3.2 Crystallization Kinetics

The secondary structure of silk films can be affected by certain solvents [16, 22, 23]. HFIP is a strong polar organic solvent, and serves as hydrogen-bond acceptor to dissolve synthetic or natural polymers, especially silks [23]. After treatment with HFIP, alpha helical structures are induced [23, 24], and beta sheets are dissolved in recombinant silk films. Therefore, the secondary structure of HFIP-treated silk films and water-cast silk films are different. **Table 6.1** summarizes the alpha helix content in HFIP-treated and water-cast spider silk-like block copolymers at room temperature; the alpha helix content of methanol (MeOH)-treated films is also listed for reference.

Table 6.1 Alpha Helix Content of HFIP-treated, Water cast and MeOH-treated Spider Silk-like Block Copolymers at Room Temperature

Sample	φ_{α_HFIP} **± 0.02**	φ_{α_water} **± 0.02**	φ_{α_MeOH} **± 0.02**
HBA_6	0.25	0.12	0.11
HBA_3	0.26	0.15	0.13
HBA_2	0.30	0.16	0.13
HBA	0.30	0.16	0.14
HAB_2	0.30	0.17	0.19
HAB_3	0.30	0.17	0.19

`

By treating spider silk-like block copolymers with HFIP, their crystallization kinetics can be analyzed. The secondary structure changes in the Amide I and the Amide II regions of HFIP-treated recombinant spider silk-like block copolymers during heating are exanimated by real-time FTIR absorbance studies. The recombinant protein films were obtained first by casting protein/HFIP solutions on polydimethylsiloxane (PDMS) substrates. After evaporating HFIP, the free standing films were gently peeled off from the PDMS substrates and transferred onto an IR transparent CaF_2 substrate which served as a support to prevent the film from breaking during heating. **Figure 6.1** shows real-time FTIR spectra of HFIP-treated recombinant spider silk-like block copolymers during heating at 5 °C/min from 30 to 220 °C. As observed in Figure 6.1, alpha helical structure dominated at room temperature. When the temperature increases, the spider silk-like block copolymer behaves differently depending upon their volume fractions of the hydrophobic and hydrophilic blocks. During heating, the samples, HBA_6, HBA_3, and HBA_2, which have a higher volume fraction of the poly(alanine) hydrophobic block (A-block), crystallized, and HBA_6 had a highest final crystallinity upon non-isothermal heating. HBA, HAB_2 and HAB_3, which have a lower volume fraction of the A-block maintained a non-crystalline disordered structure. HAB_2 and HAB_3 exhibited similar heating profiles as HBA, thus only HBA is shown in Figure 6.1.

`

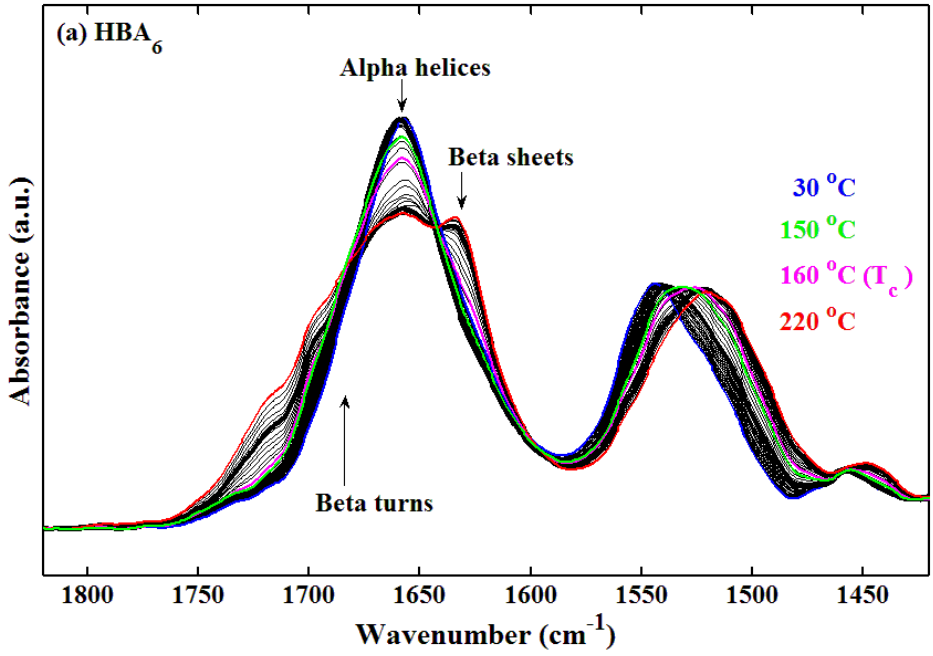
(a) HBA6
Alpha helices
Beta sheets
Beta turns
30 °C
150 °C
160 °C (Tc)
220 °C
Absorbance (a.u.)
1800
1750
1700
1650
1600
1550
1500
1450
Wavenumber (cm-1)

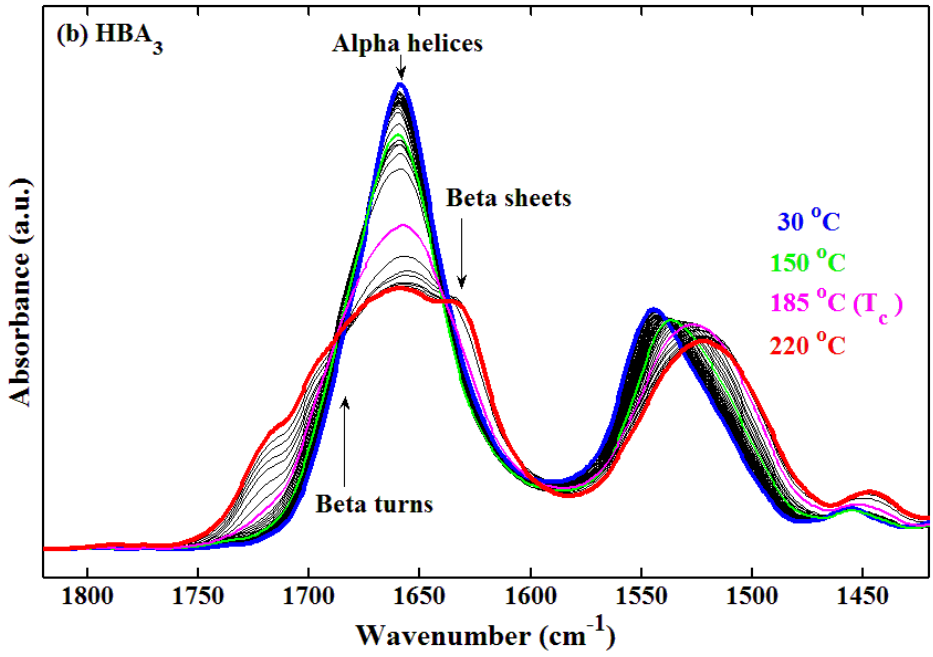
(b) HBA3
Alpha helices
Beta sheets
Beta turns
30 °C
150 °C
185 °C (Tc)
220 °C
Absorbance (a.u.)
1800
1750
1700
1650
1600
1550
1500
1450
Wavenumber (cm-1)

`

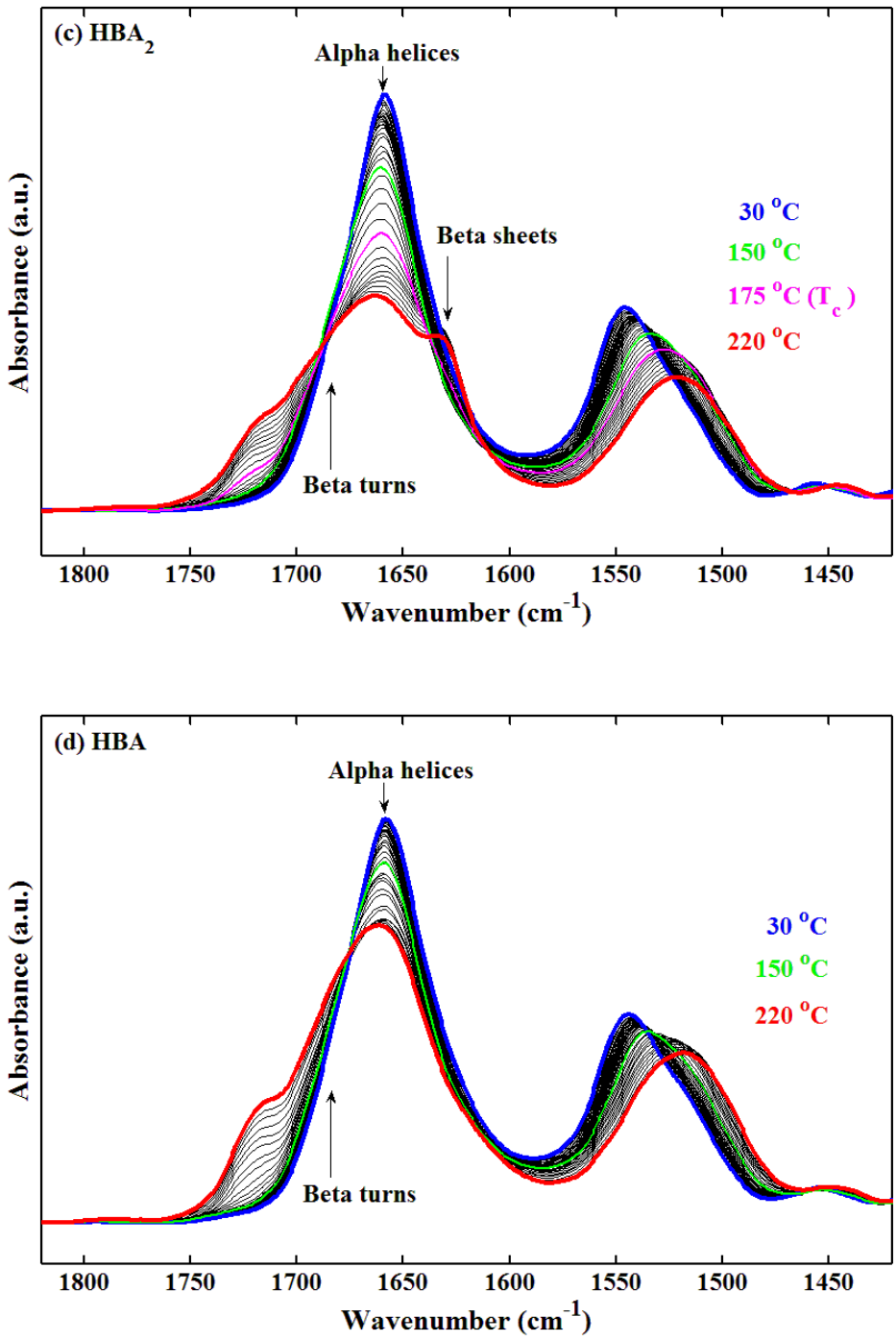

Figure 6. 1 Real-time FTIR spectra in the Amide I and II regions of recombinant spider silk-like block copolymers films treated with HFIP: a) HBA_6, (b) HBA_3, (c) HBA_2, and (d) HBA, during heating at 5 °C/min from 30 (blue) to 220 °C (red).

`

The changes of secondary structure can be examined more easily by using the difference spectra. The residual absorbance, *ΔAbs(T)*, between the absorbance spectra at temperature *T*, *Abs(T)*, and the initial spectrum at 30 °C, *Abs(30)*, was calculated by:

$$\Delta Abs(T) = Abs(T) - Abs(30) \tag{6.1}$$

As shown in **Figure 6.2**, a random coil to beta turns transition occurred during the HFIP evaporation process at around 60 ºC. During the glass transition process at about 150 ºC, an alpha helix to beta turns transition occurred. Above the glass transition, HBA_6, HBA_3, and HBA_2 crystallized upon heating, as seen by the alpha helix to beta sheets transition from above 160 ºC to about 200 ºC.

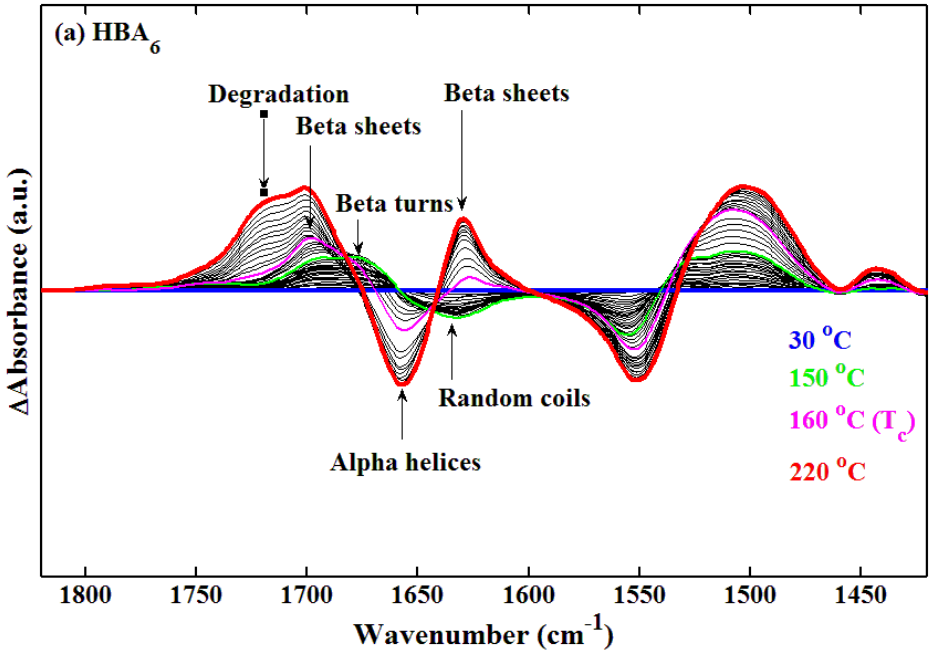

`

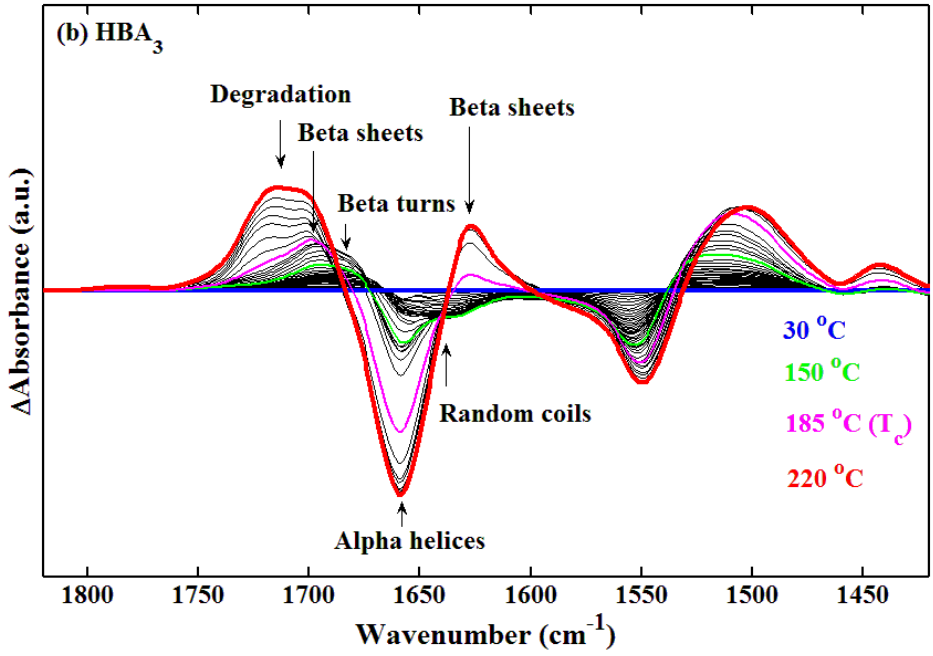
(b) HBA3
Degradation
Beta sheets
Beta sheets
Beta turns
Random coils
Alpha helices
30 °C
150 °C
185 °C (Tc)
220 °C
ΔAbsorbance (a.u.)
1800
1750
1700
1650
1600
1550
1500
1450
Wavenumber (cm-1)

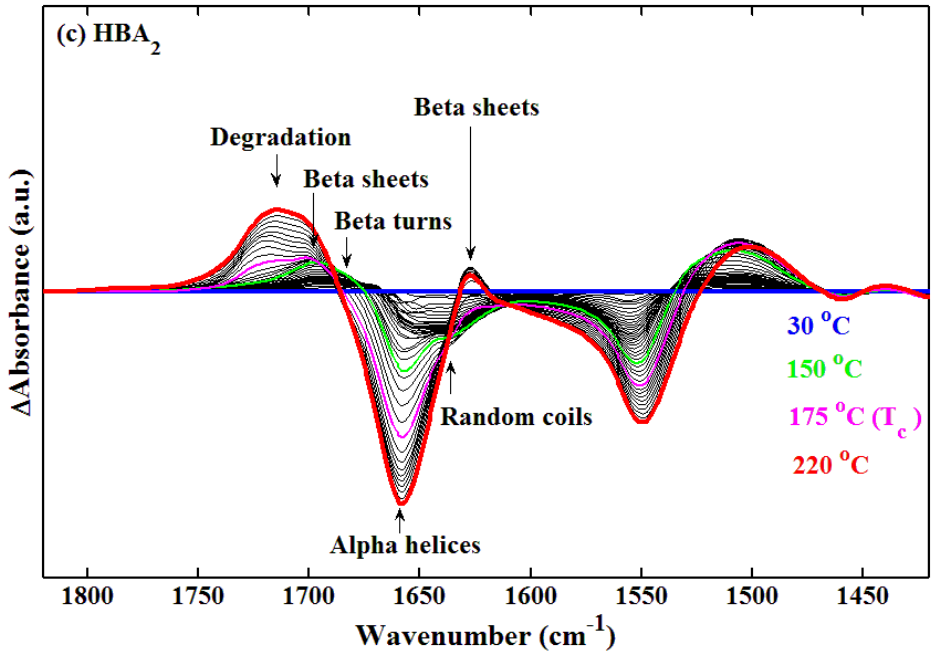
(c) HBA2
Beta sheets
Degradation
Beta sheets
Beta turns
Random coils
Alpha helices
30 °C
150 °C
175 °C (Tc)
220 °C
ΔAbsorbance (a.u.)
1800
1750
1700
1650
1600
1550
1500
1450
Wavenumber (cm-1)

`

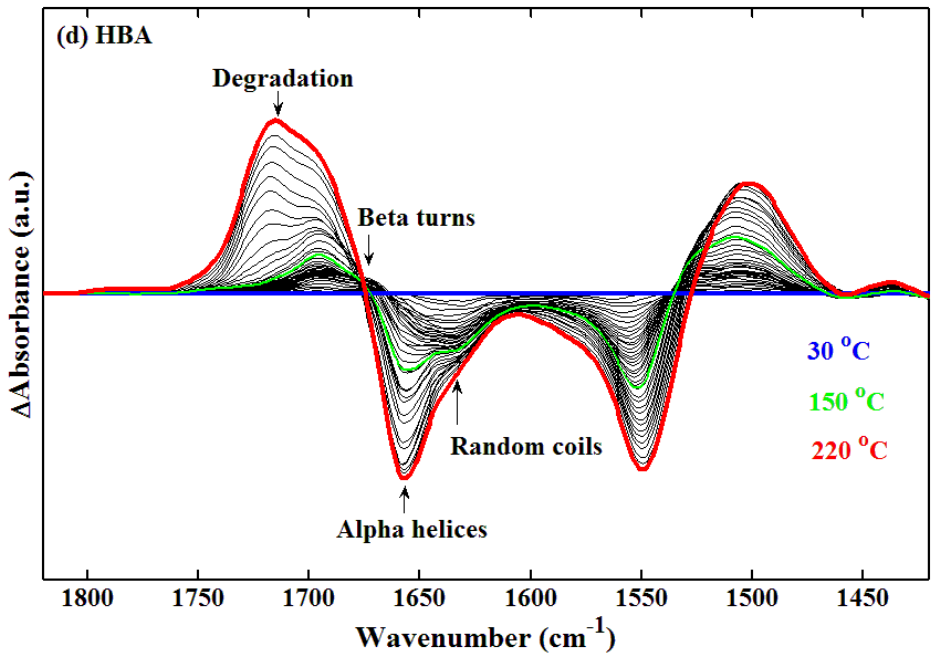

Figure 6.2 Real-time FTIR residual absorbance spectra in the Amide I and II regions of recombinant spider silk-like block films: (a) HBA_6, (b) HBA_3, (c) HBA_2, and (d) HBA, during heating at 5 °C/min from 30 to 220 °C.

The crystallization kinetics of HBA_6, HBA_3 and HBA_2 were studied in the crystallization temperature region by using the normalized *ΔAbs* vs. temperature plots as illustrated by HBA_6 in **Figure 6.3**. The normalized *ΔAbs* were calculated by dividing *ΔAbs* values by the absolute value of the maximum change of *ΔAbs* in that temperature range. As shown in **Figure 6.3**, during crystallization, the alpha helical structures are vanishing, and the beta sheet crystals are developing. The crystallinities, φ, during heating were calculated by Fourier self-deconvolution (FSD) over the amide I peaks, and the results are summarized in Table **6.2**. HBA_6 developed the highest crystallinity by

`

both the thermal treatment and MeOH treatment, while HBA_2 has the lowest crystallinity among the three samples, HBA_6, HBA_3 and HBA_2.

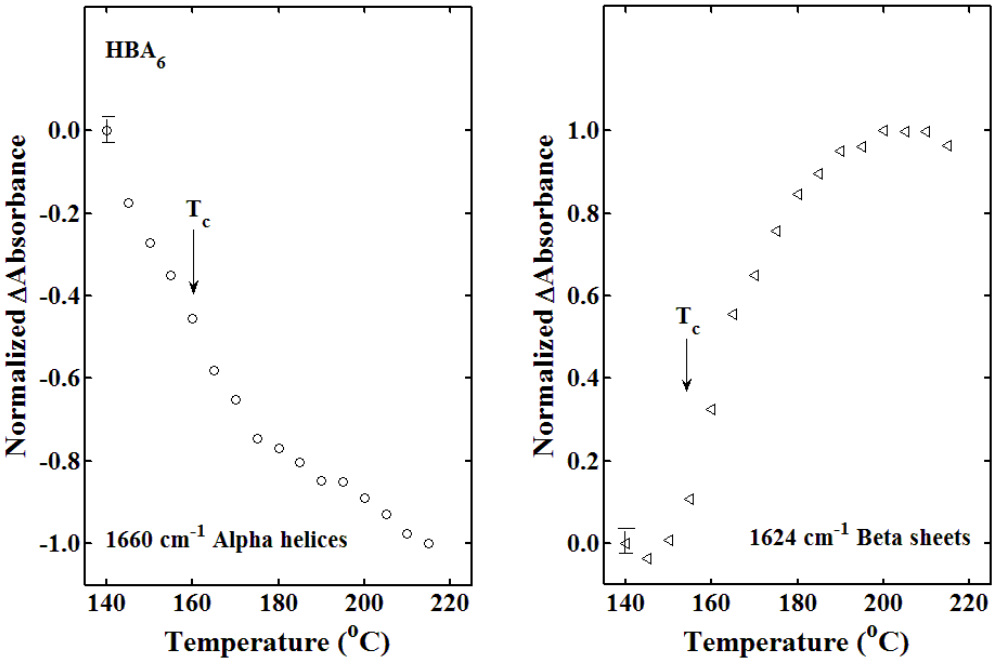

Figure 6.3 Crystallization kinetics of HBA_6. During heating, the alpha helical structures are vanishing and the beta sheet crystals are developing.

`

Table 6.2 Crystallinity[a] of HFIP-treated Spider Silk-like Block Copolymers During Heating

Sample	$\varphi_{\beta\_HFIP\_160C}$ ± 0.02	$\varphi_{\beta\_HFIP\_180C}$ ± 0.02	$\varphi_{\beta\_HFIP\_200C}$ ± 0.02	$\varphi_{\beta\_HFIP\_220C}$ ± 0.02	φ_{β_MeOH}[b] ± 0.02
HBA_6	0.09	0.10	0.10	0.15	0.32
HBA_3	0.00	0.03	0.10	0.14	0.28
HBA_2	0.00	0.06	0.11	0.12	0.25
HBA	0.00	0.00	0.00	0.00	0.21
HAB_2	0.00	0.00	0.00	0.00	0.08
HAB_3	0.00	0.00	0.00	0.00	0.07

[a] From FTIR analysis of the Amide I region

[b] Determined at room temperature after MeOH exposure

To capture the thermal transitions, and further analyze the crystallization kinetics of recombinant spider silk-like block copolymers, the thermal properties of the HFIP-cast films were examined by TMDSC. **Figure 6.4** shows the total heat flow vs. temperature curves of recombinant spider silk-like block copolymers: HBA_6, HBA_3, HBA_2, HBA, HAB_2 and HAB_3, with heating rates of 5 °C/min from 30 to 340 °C. Solvent evaporation peaks centered around 78 °C can be observed in all of the samples, which indicates residual HFIP existed in the silk films. After the glass transition temperature region of dry film, around 150 °C, broadened non-isothermal crystallization exothermal peaks were also observed in HBA_6, HBA_3, and HBA_2. As known from the real-time FTIR results,

`

HBA did not crystalize during heating, the exothermal heat flow in HBA is due to the cross-linking or aggregation. No exotherm was observed in HAB_2 or HAB_3. Degradation peaks, centered around 300 °C, were observed in all samples. Thermal Properties of recombinant spider silk-like block copolymers are summarized in **Table 6.3**.

Table 6.3 Thermal Properties[a] of Recombinant Spider Silk-like Block Copolymers from TMDSC

Sample	**HFIP Peak Position (°C) ± 1**	**T_g (°C) ± 1**	**Degradation Peak Position (°C) ± 1**
HBA_6	76	161	300
HBA_3	75	165	300
HBA_2	78	162	296
HBA	78	136	292
HAB_2	75	166	290
HAB_3	78	175	290

[a] Determined from TMDSC heating at 5 °C/min.

`

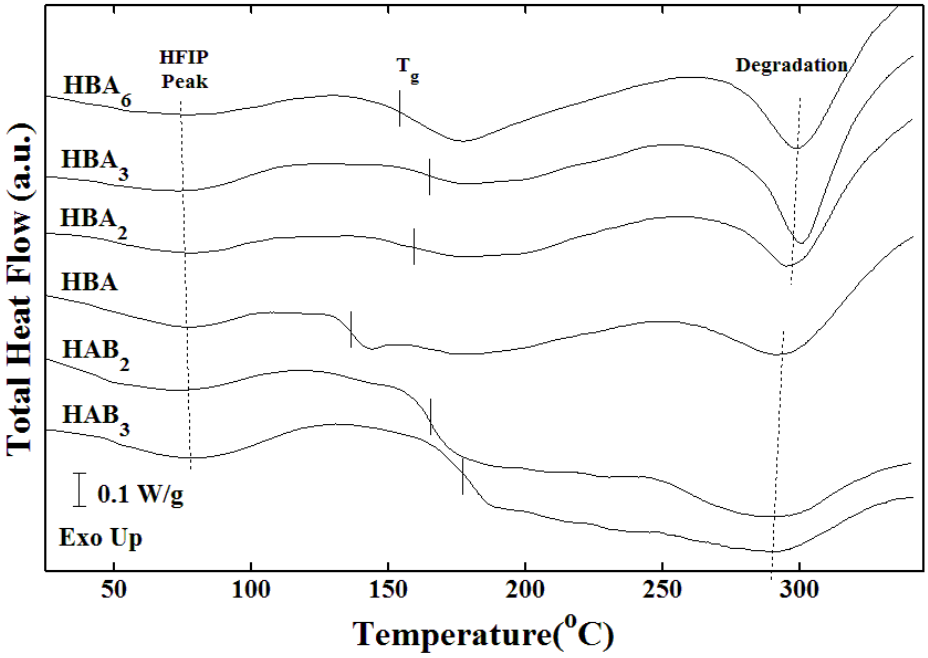

Figure 6.4 TMDSC total heat flow scans of recombinant spider silk-like block copolymers: HBA_6, HBA_3, HBA_2, HBA, HAB_2 and HAB_3, with heating rate of 5 °C/min from 30 to 340 °C. Short lines mark the midpoint of the glass transition step.

6.3.2 Degradation Mechanism

Figure 6.5 shows the secondary structure change during the degradation process in air, illustrated by the semicrystalline sample, HBA_3, and non-crystalline sample, HBA. Alpha helices begin to degrade even below 250 °C, while beta sheets degrade around 290 °C. When the temperature is above 300 °C, beta turn structures begin to decompose. By comparison with the TMDSC results shown in Figure 6.4, the degradation peak from TMDSC increases 10 °C from HAB_3 to HBA_6. Results indicate that beta sheets act as a physical cross-linker to stabilize the protein films.

`

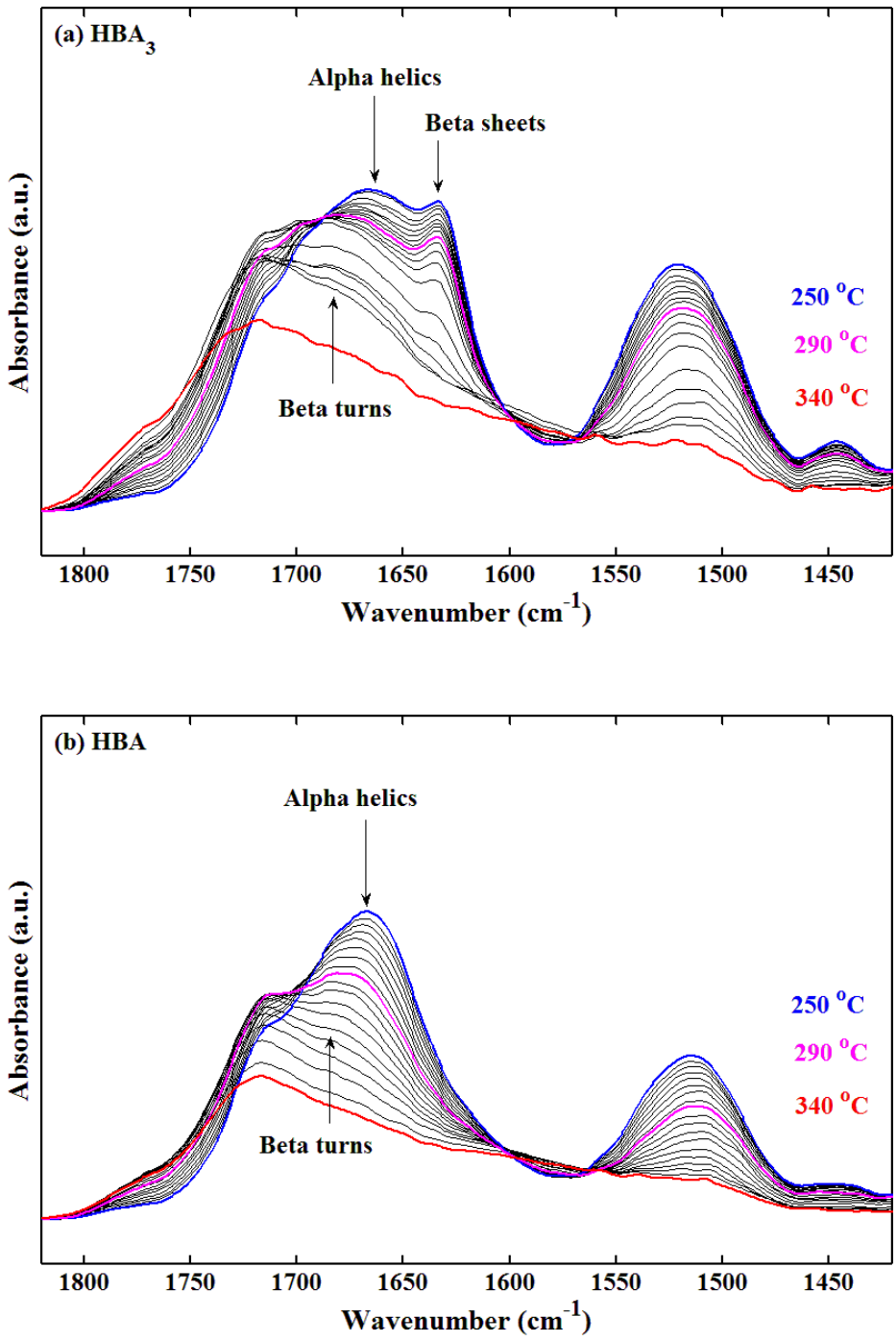

Figure 6.5 Real-time FTIR spectra in the Amide I and II regions of recombinant spider silk-like block films: (a) HBA_3, and (b) HBA, during heating at 5 °C/min from 250 to 340 °C.

`

The degradation kinetics of spider silk-like block copolymers were studied in the temperature range from 250 to 340 °C using the normalized *ΔAbs* vs. temperature plots as illustrated by HBA_3 and HBA in **Figure 6.6**. As shown in Figure 6.6, during degradation, the alpha helical structures are diminishing even below 250 °C. The rate of change in the 1660 cm^{-1} band is suggested by the slope of the normalized *ΔAbs* curve. As can be observed in Figure 6.6, the diminishing of the alpha helical structure is much slower in the semicrystalline silk film, HBA_3, than in the non-crystalline silk film, HBA, when the temperature is below 300 ºC. This result also indicates that beta sheets act as a physical cross-linker which stabilizes the protein films at high temperature.

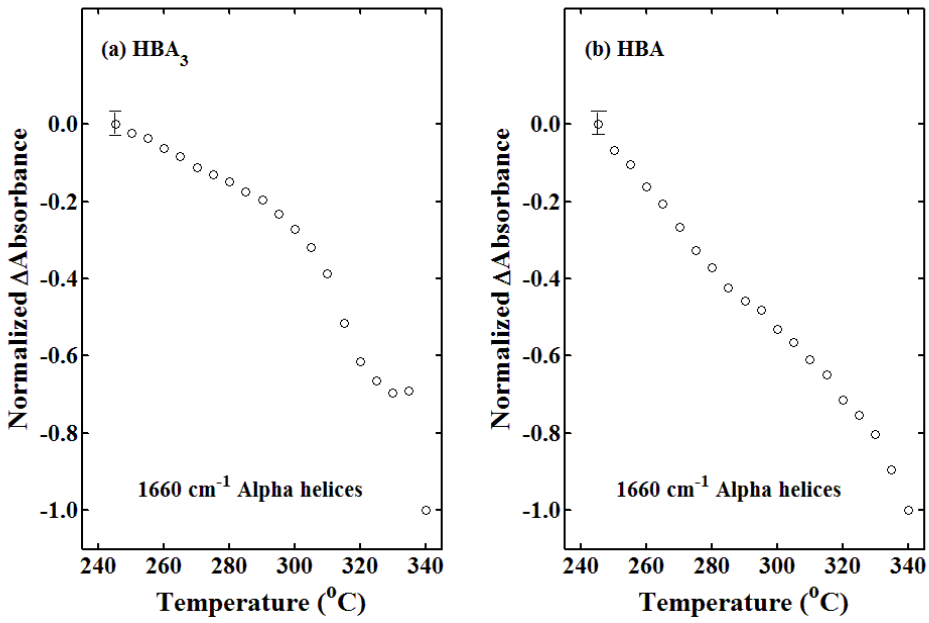

Figure 6.6 Degradation kinetics studied by the change of 1660 cm^{-1} FTIR absorbance band of recombinant spider silk-like block copolymer films during heating at 2 °C/min, illustrated (a) HBA_3 (semicrystalline) and (b) HBA (non-crystalline).

`

6.3.3 Self-assembly Morphology and Mechanism

Lyophilized spider silk block copolymers were treated with different solvents and/or thermal methods. FTIR absorbance spectra of HFIP-treated, thermally-treated (heating at 5 ºC/min to 220 ºC), or MeOH-treated films are shown in **Figure 6.6**. Samples become non-crystalline upon HFIP treatment. When samples are treated by either thermal treatment or MeOH exposure, beta sheets formed in A-block, and the secondary structures of the A-block and B-block in the block copolymers become different.

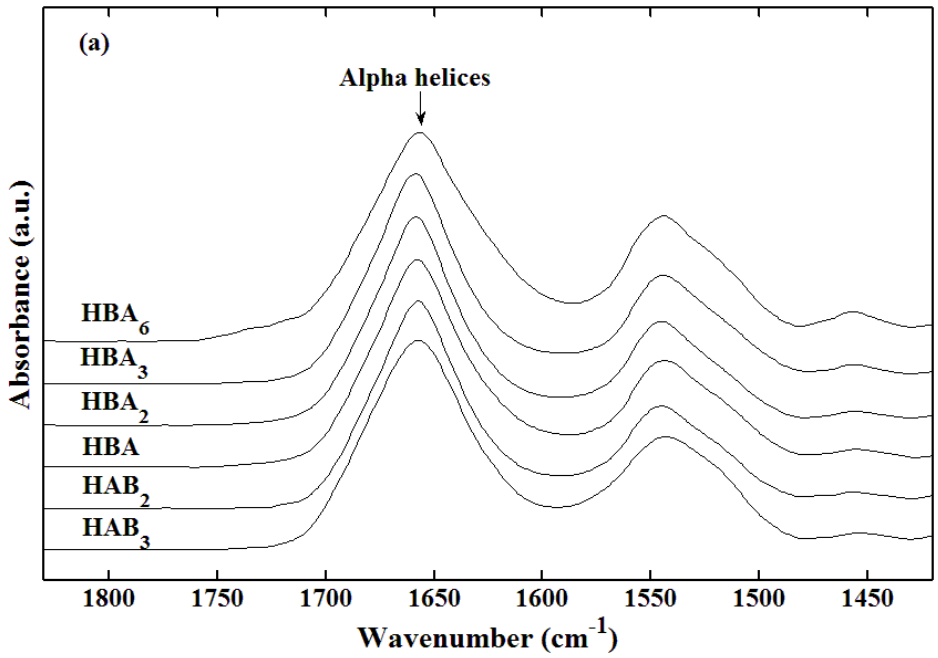

`

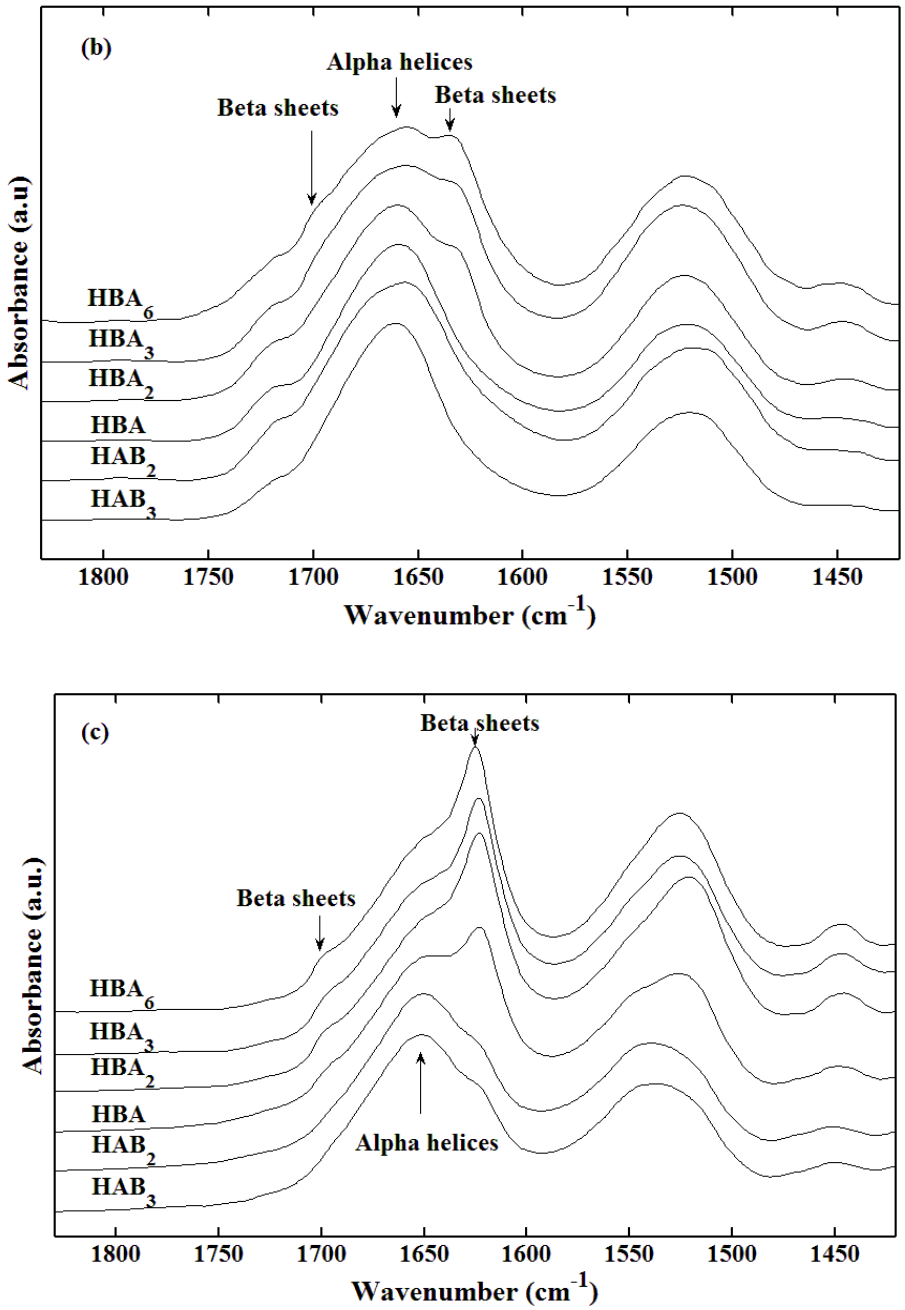

Figure 6.7 FTIR spectra of recombinant spider silk-like block copolymers films, HBA_6, HBA_3, HBA_2, HBA, HAB_2 and HAB_3 after different treatments: (a) HFIP-cast films examined at room temperature, (b) HFIP-cast films heated from 30 to 200 °C at 5 °C/min and measured at 200 °C, and (c) MeOH-cast films examined at room temperature.

`

The morphologies of recombinant spider silk-like block copolymers films, HBA_6, HBA_3, HBA_2, HBA, HAB_2 and HAB_3 obtained by using different treatments were imaged using SEM. As shown in **Figure 6.7**, aggregated micelles are observed in heat-treated HBA_6, HBA_3 and HBA_2; large hollow vesicles in MeOH-treated HBA_6, HBA_3 and HBA_2, and fibrils were observed in were observed in MeOH-treated HBA_3, HBA_2 and HBA. A magnified insert picture of the small fibrils formed in HBA is also shown in Figure 6.7. No obvious surface morphology is formed in HFIP-treated films or in HAB_2 and HAB_3 films. **Figure 6.8** shows the cross section of the HBA_6 vesicles formed in MeOH (top) which was then cut open by focused ion beam milling. The SEM picture confirmed that a hollow centered vesicle structure formed in MeOH-treated HBA_6.

It is known that to form spherical micelles, cylindrical micelles, bilayer and vesicle structures, the volume fraction of the hydrophobic block is critical [25]. The conditions for the formation of various shapes of micelles are listed below:

Spherical micelles: $$\frac{v}{l_c a_0} \leq \frac{1}{3}$$

Cylindrical micelles: $$\frac{1}{3} < \frac{v}{l_c a_0} \leq \frac{1}{2}$$

Bilayer and vesicles: $$\frac{v}{l_c a_0} > \frac{1}{2}$$

Where a_0 is the optimal head group area, v is the volume of a linear hydrocarbon chain, and l_c is the critical chain length (length of the hydrocarbon chain if it is fully extended). By treating our silk ABCs with different solvents or by thermal methods, the protein chains adopt different secondary structures, and the $v/l_c a_0$ value varies. Therefore, a variety of morphologies was observed in Figure 6.7.

`

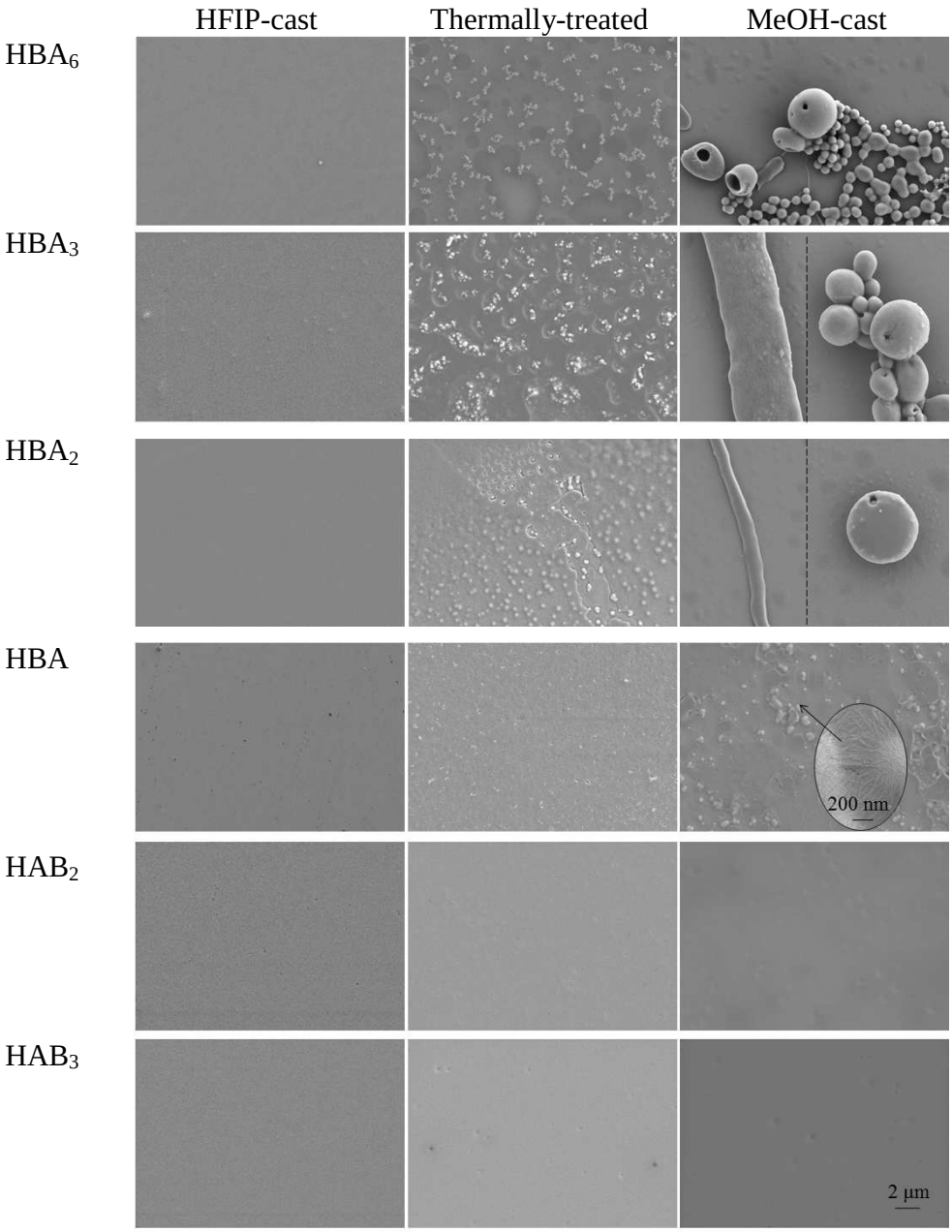

Figure 6.8 SEM morphology of recombinant spider silk-like block copolymer films, HBA_6, HBA_3, HBA_2, HBA, HAB_2 and HAB_3, obtained by different treatments: first column - HFIP-cast films, second column - HFIP-cast films heated from 30 to 200 °C at a heating rate of 5 °C/min, and third column - MeOH-cast films. Images were taken at room temperature. The scale bar applies to all images, except for the magnified insert plot of MeOH-cast HBA. The scale bar for the insert represents 200nm.

`

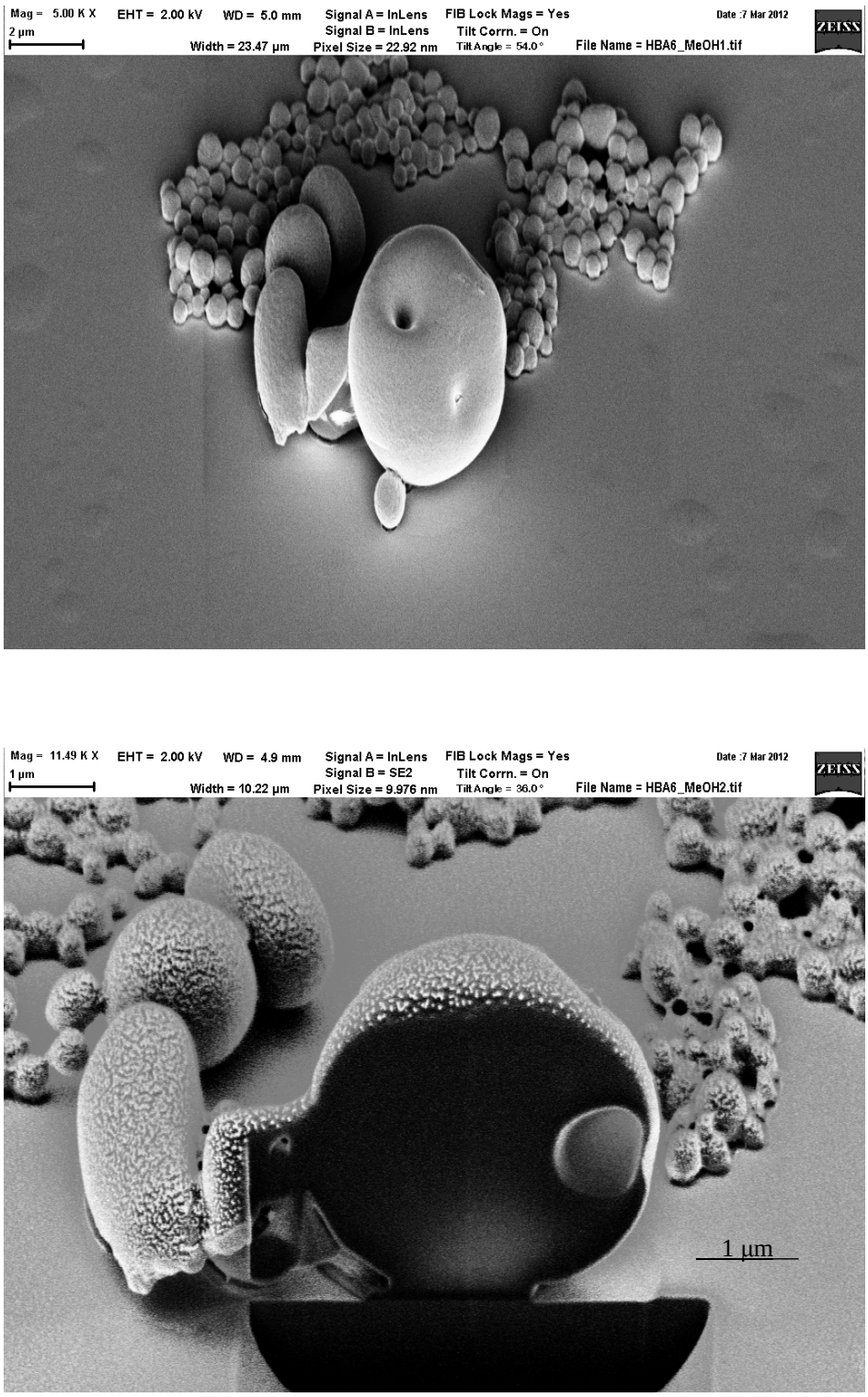

Figure 6.9 SEM morphology of vesicles in MeOH-treated HBA_6 before (top) and after (bottom) cutting by using a focused ion beam.

`

6.4 Conclusions

We studied a family of silk-based block copolymers patterned after *Nephila Clavipes* spider dragline silk. The block copolymers are of the form HBA_m (m=1, 2, 3, 6) and HAB_n (n=2, 3), where B is a hydrophilic block, A is a hydrophobic block, and H is a histidine-tag. Thin films were prepared either from solutions of hexafluoroisopropanol (HFIP), or from methanol (MeOH) which served as a control. Secondary structure and crystallinity of the films were monitored by Fourier transform infrared spectroscopy during heating from 30 - 340 ^{o}C. Thermal properties were determined by differential scanning calorimetry. Using scanning electron microscopy, micelles were observed in thermally-treated HBA_6, HBA_3, HBA_2 and HBA films. Hollow vesicles and fibrillar networks were observed in methanol-cast HBA_6, HBA_3, HBA_2 and HBA sample films, while no micro-structures were formed in HFIP-cast films or in HAB_2 and HAB_3, indicating that morphology and crystallinity can be tuned by not only the block length and also the thermal/chemical treatments.

Results indicate when we increase the number of repeating units of A-block in the protein, sample films crystallize more easily. When the volume fraction of A –block is increased, more beta sheets form upon thermal treatment, and because beta sheets acted as a cross-link between protein chains, the sample films became more thermally stable. Moreover, when samples crystallize, the secondary structure of the A-block and B-block become different, thus favoring of formation of bilayer structures which could fold into vesicles and tube structures during drying.

`

6.5 References

1. Mayes AM and Delacruz MO. *Macromolecules* 1988; 21(8): 2543-2547.
2. Zhang LF and Eisenberg A. *Science* 1995; 268(5218): 1728-1731.
3. Gebhardt KE, Ahn S, Venkatachalam G, and Savin DA. *Langmuir* 2007; 23(5): 2851-2856.
4. Lin WR, Zheng C, Wan XH, Liang DH, and Zhou QF. *Macromolecules* 2010; 43(12): 5405-5410.
5. de Kruif CG, Huppertz T, Urban VS, and Petukhov AV. *Advances in Colloid and Interface Science* 2012; 171-172: 36–52.
6. Adams ML, Lavasanifar A, and Kwon GS. *Journal of Pharmaceutical Sciences* 2003; 92(7): 1343–1355.
7. Kwon GS and Forrest ML. *Drug Development Research* 2006; 67(1): 15-22.
8. Forster S. *Colloid Chemistry: Topics in Current Chemistry* 2003; 226: 1-28.
9. Minich EA, Nowak AP, Deming TJ, and Pochan DJ. *Polymer* 2004; 45(6): 1951-1957.
10. Rabotyagova OS, Cebe P, and Kaplan DL. *Biomacromolecules* 2009; 10(2): 229-236.
11. Krishnaji ST, Huang WW, Rabotyagova O, Kharlampieva E, Choi I, Tsukruk VV, Naik R, Cebe P, and Kaplan DL. *Langmuir* 2011; 27(3): 1000-1008.
12. Xia XX, Xu QB, Hu X, Qin GK, and Kaplan DL. *Biomacromolecules* 2011; 12(11): 3844-3850.
13. Rabotyagova OS, Cebe P, and Kaplan DL. *Biomacromolecules* 2011; 12(2): 269-289.

`

14. Vargo KB, Parthasarathy R, and Hammer DA. *Proceedings of the National Academy of Sciences of the United States of America* 2012; 109(29): 11657–11662.

15. Ha SW, Gracz HS, Tonelli AE, and Hudson SM. *Biomacromolecules* 2005; 6(5): 2563–2569.

16. Hu X, Kaplan D, and Cebe P. *Macromolecules* 2006; 39(18): 6161-6170.

17. Huang WW, Krishnaji S, Hu X, Kaplan D, and Cebe P. *Macromolecules* 2011; 44(13): 5299-5309.

18. Huang WW, Krishnaji S, Kaplan D, and Cebe P. in preparation to submit to *Macromolecules* 2012.

19. Rabotyagova OS, Cebe P, and Kaplan DL. *Macromolecular Bioscience* 2010; 10(1): 49-59.

20. Hu X, Lu Q, Kaplan DL, and Cebe P. *Macromolecules* 2009; 42(6): 2079-2087.

21. Tian Z, Li H, Wang M, Zhang A, and Feng Z-G. *Journal of Polymer Science Part a-Polymer Chemistry* 2008; 46(3): 1042–1050.

22. Valluzzi R, He SJ, Gido SP, and Kaplan D. *International Journal of Biological Macromolecules* 1999; 24(2-3): 227-236.

23. Spiess K, Ene R, Keenan CD, Senker J, Kremer F, and Scheibel T. *Journal of Materials Chemistry* 2011;21(35): 13594-13604.

24. Huemmerich D, Slotta U, and Scheibel T. *Applied Physics a-Materials Science & Processing* 2006; 82(2): 219-222.

25. Jones RAL. *Soft condensed matter*. Oxford; New York: Oxford University Press, 2002.

Chapter VII. Conclusions and Future Works

This chapter is the conclusion of this thesis and outlines some possible future work in silk studies.

7.1 Conclusions

Due to the potential biomedical and high-tech applications [1-4], silks have been investigated extensively in recent decades. In this project, we wanted to characterize a new family of silk proteins made by recombinant DNA technology. The goal of this thesis was to use this new family of silk-based block copolymers as novel model materials with specific motifs to understand and then control the thermal, structural, and morphological features of recombinant proteins. The conclusions from this thesis are summarized as follows:

a. Heat Capacity of Spider Silk-like Block Copolymers

Among the many different stimuli-sensitive delivery systems, temperature-sensitive drug delivery systems offer great potential due to their tunability of phase transition temperatures, and non-toxic trigger for in vivo drug release [5, 6]. Therefore, thermal property studies of protein-based material are very crucial because of the potential use of these materials in biomedical applications in controlled drug delivery [5, 6]. The heat capacities below and above T_g of our spider silk-like block copolymer were studied from both theoretical and experimental perspectives.

The reversing C_p of recombinant spider silk-like proteins were modeled, based on summation of the contributions of the underlying molecular motions of the individual

amino acids, and then experimentally measured by TMDSC. However, not all twenty of the amino acids have their heat capacity data known from prior measurements of their poly(amino acids). Therefore, to model the heat capacities of the unknown amino acids, we developed an additive scheme using the chemical side group equivalence between amino acids with known and unknown heat capacities. Excellent agreement was found between the measured and calculated values of the heat capacity, showing that this method can serve as a standard by which to assess the C_p for other biologically inspired block copolymers.

The fraction of beta sheet crystallinity of spider silk block copolymers was also determined by using the predicted ΔC_p, and was verified by WAXD and FTIR. These biomaterials degrade at temperatures just above T_g, and display no endothermic heat of fusion in the DSC scan. So the heat of fusion method to determine degree of crystallinity, which is used extensively in polymer science, could not be used for our materials. Our result indicates the ΔC_p model can be used to accurately determine the crystallinity of biomaterials, providing the first quantitative measure of this property in silk copolymers.

The glass transition temperatures of spider silk block copolymer were fitted by Kwei's equation, which indicates attractive interaction exists between A-block and B-block, while intermolecular interactions exist between A-block and the His-tag.

b. Determining the Effect of Water on Spider Silk-like Block Copolymer Glass Transition

Since silk and other naturally occurring fibrous proteins are often processed in water, we embarked on a program of study to determine the impact of residual water on

the structure and thermal properties of our silk-based block copolymers. By studying the effect of bound water acting as a plasticizer in water-cast protein films, a fuller understanding of the protein-water interactions with respect to the protein amino acid sequence was obtained. By analogy with synthetic polymers, the plasticization (lowering of the glass transition temperature) of silk copolymers by water was investigated.

A theoretical model based on molecular motions along with the TMDSC measurements show that two glass transitions were observed in all silk samples during heating. The lower temperature glass transition, $T_g(1)$, is related both to the bound water removal induced conformational change, and to the hydrophobicity of the protein sequences. The higher temperature glass transition, $T_g(2)$, refers to the now-dry protein glass transition.

The conformational changes occurring during the two glass transitions were also monitored by real-time FTIR, which indicates a random coils to beta turns transition occurs during $T_g(1)$, and alpha helices to beta turns transition occurs during $T_g(2)$.

c. Tunable Self-assembly, Crystallization and Degradation of Recombinant Spider Silk-like Block Copolymer

Due to the hydrophobic and hydrophilic nature of the individual blocks, the spider silk block copolymers tend to self-assemble into various microstructures from their water solutions. It is not unusual for block-copolymers to exhibit different morphologies depending upon volume fraction, and indeed this is commonly observed in synthetic block copolymers [7-9]. However, synthetic polymers lack the secondary structures present in protein-based copolymers. We expect difference in the phase behavior in our

silk copolymers, which would most likely depart from the traditional copolymer phase diagram. The morphological features formed by spider silk-like block copolymers under various thermal and chemical treatments were studied.

Using SEM, micelles were observed in thermally-treated HBA_6, HBA_3, HBA_2 and HBA films. Hollow vesicles and fibrillar networks were observed in methanol-cast HBA_6, HBA_3, HBA_2 and HBA sample films, while no micro-structures were formed in HFIP-cast films or in HAB_2 and HAB_3. Result indicates the secondary structure of the A-block and B-block become different when samples crystallize. Thus it will be easier to form bilayer structures which could fold into vesicles and tube structures during drying. Results also suggest that the morphology and crystallinity can be tuned by not only by the block length but also by using the thermal or chemical treatments. Thermal annealing and MeOH treatment induce beta sheet crystal in silk samples, while HFIP stabilizes the alpha helical structures and breaks down the beta sheet structure in silks.

Using real-time FTIR, we conclude that when we increase the number of repeating units of A-block in the protein, sample films crystallize more easily (i.e., the sample has a higher final crystallinity upon thermal or chemical treatment). Real-time FTIR result also indicates the beta sheets acted as a cross-link between protein chains, and postpone the films degradation during heating. However, unlike many synthetic polymers, the beta sheet crystals are not thermo-reversible.

7.2 Future Work

In this thesis, the thermal, structural and morphological properties of spider silk-like block copolymers were studied in detail. However, the mechanical properties were not discussed in this thesis because of the extremely low mechanical strength of the films formed by these block copolymers. During the film formation process by solution casting method, we discovered that these films are very brittle and can be easily broken even during very gently handling. A possible explanation for the low mechanical properties is that the molecular weight of the recombinant proteins (10 kDa on average) is too low compared to the native silk proteins (250-320 kDa) [10]. It is known that the entanglement density of a polymer chain scales with molecular weight. The reduced molecular weight of our materials reduces the entanglement density, and makes the materials more brittle than native silks. Therefore, a suggested future experiment is to make recombinant proteins either with larger molecular weights, or with chemical cross-linking sites, to produce tougher fibers with high mechanical strength and modulus.

In this thesis, the self-assembly morphologies of spider silk-like block copolymers were observed by SEM. However, the locations of each block in those micro-structures are left unknown. Neutron scattering has been used to reveal the molecular structure of both crystalline and disordered materials. In recent decades, it was further applied to study the order-disorder transition [11], self-assembly [12] and microphase separation [13] of block copolymers and polymer blends. Therefore, another suggested future investigation is to study morphological and structural features of silk-based block copolymers and silk-base polymer blends by small angle neutron scattering.

7.3 References

1. Yang Y, Chen X, Ding F, Zhang P, Liu J, and Go X. *Biomaterials* 2007; 28(9): 1643-1652.
2. Lammel A, Schwab M, Hofer M, Winter G, and Scheibel T. *Biomaterials* 2011; 32(8): 2233–2240.
3. Pritchard EM. *Silk biomaterials for controlled drug delivery*. Tufts University, 2011; 1-59 .
4. Hwang S-W, Tao H, Kim D-H, Cheng H, Song J-K, Rill E, Brenckle MA, Panilaitis B, Won SM, Kim Y-S, Song YM, Yu KJ, Ameen A, Li R, Su Y, Yang M, Kaplan DL, Zakin MR, Slepian MJ, Huang Y, Omenetto FG, and Rogers JA. *Science* 2012; 337(6102): 1640-1644.
5. McGrath K and Kaplan D. *Protein-based materials*. Boston: Birkhäuser, 1997: 103-132.
6. Bikram M and West JL. *Expert Opinion on Drug Delivery* 2008; 5(10): 1077-1091.
7. Bates FS and Fredrickson GH. *Annual Review of Physical Chemistry* 1990; 41: 525-557.
8. Fredrickson GH and Bates FS. *Annual Review of Materials Science* 1996; 26: 501-550.
9. Bates FS and Fredrickson GH. *Physics Today* 1999; 52(2): 32-38.
10. Xia XX, Qian ZG, Ki CS, Park YH, Kaplan DL, and Lee SY. *Proceedings of the National Academy of Sciences of the United States of America* 2010; 107(32): 14059-14063.

11. Hardy CM, Bates FS, Kim MH, and Wignall GD. *Macromolecules* 2002; 35(8): 3189-3197.
12. de Kruif CG, Huppertz T, Urban VS, and Petukhov AV. *Advances in Colloid and Interface Science* 2012; 171: 36–52.
13. Smith SD, Spontak RJ, Satkowski MM, Ashraf A, Heape AK, and Lin JS. *Polymer* 1994; 35(21): 4527-4536.

Appendix A. *Nephila Clavipes* Spidroin 1 (MaSp1) mRNA, Partial cds

LOCUS: NCU20329; 1726 bp; mRNA; linear; INV 17-OCT-2007

DEFINITION: Nephila clavipes spidroin 1 mRNA, partial cds.

ACCESSION: U20329

VERSION: U20329.1; GI: 2911273

SOURCE: Nephila clavipes

ORIGIN

1 gtggatatgg aggtcttggt ggacaaggtg ccggacaagg agctggtgca gccgccgcag

61 cagcagctgg tggtgccgga caaggaggat atggaggtct tggaagccaa ggtgctggac

121 gaggtggaca aggtgcaggc gcagccgcag ccgcagctgg aggtgctggt caaggaggat

181 acggaggtct tggaagccaa ggtgctggac gaggaggatt aggtggacaa ggtgcaggtg

241 cagcagcagc agctggaggt gtcggacaag gaggactagg tggacaaggt gctggacaag

301 gagctggagc agctgctgca gcagctggtg gtgccggaca aggaggatat ggaggtctcg

361 gaagccaagg tgcaggacga ggtggatcag gtggacaagg ggcaggtgca gcagcagcag

421 cagctggagg tgccggacaa ggaggatatg gaggtcttgg aagccaaggt gcaggacgag

481 gtggattagg tggacagggt gcaggtgcag cagcagcagc agcagccgga ggtgctggac

541 aaggaggata cggtggtctt ggtggacaag gtgccggaca aggtggctat ggaggacttg

601 gaagccaagg tgctggacga ggaggattag gtggacaagg tgcaggtgca gcagcagcag

661 ctggaggtgc cggacaagga ggactaggtg gacaaggagc tggagcagcc gctgcagcag

721 ctggtggtgc cggacaagga ggatatggag gtcttggaag ccaaggtgct ggacgaggtg

781 gacaaggtgc aggcgcagcc gcagcagcag ccggaggtgc tggacaagga ggatacggtg

841 gacaaggtgc cggacaagga ggctatggag gacttggaag ccaaggtgct ggacgaggag

901 gattaggtgg acaaggtgca ggtgcagcag cagcagcagc agcagctgga ggtgccggac

961 aaggaggatt aggtggacaa ggtgcaggtg cagcagcagc agcagctgga ggtgctggac

1021 aaggaggatt aggtggacaa ggtgctggac aaggagctgg agcagccgct gcagcagccg

1081 ctgcagcagc tggtggtgtt agacaaggag gatatggagg tcttggaagc caaggtgctg

1141 gacgaggtgg acaaggtgca ggcgcagccg cagcagcagc cggaggtgct ggacaaggag

1201 gatatggtgg tcttggtgga caaggtgttg gacgaggtgg attaggtgga caaggtgcag

1261 gcgcagcggc agctgttggt gctggacaag gaggatatgg tggtgttggt tctggggcgt

1321 ctgctgcctc tgcagctgca tcccgtttgt cttctcctca agctagttca agagtttcat

1381 cagctgtttc caacttggtt gcaagtggtc ctactaattc tgcggccttg tcaagtacaa

1441 tcagtaatgt ggtttcacaa ataggcgcca gcaatcctgg tctttctgga tgtgatgtcc

1501 tcattcaagc tcttctcgag gttgtttctg ctcttatcca gatcttaggt tcttccagca

1561 tcggccaagt taactatggt tccgctggac aagccactca gatcgttggt caatcagttt

1621 atcaagccct aggttaaatg taaaatcaag agttgctaaa acttaatgaa tcgggctgtt

1681 aaatttgtgt tagttttaaa atattttcaa taaatattat gcatat

//

REFERENCE: 1 (sites)

AUTHORS: Xu,M. and Lewis,R.V.

TITLE: Structure of a protein superfiber: spider dragline silk

JOURNAL: Proc. Natl. Acad. Sci. U.S.A. 87 (18), 7120-7124 (1990)

PUBMED: 2402494

REFERENCE: 2 (bases 1346 to 1634)

AUTHORS: Arcidiacono,S., Mello,C., Kaplan,D., Cheley,S. and Bayley,H.

TITLE: Purification and characterization of recombinant spider silk expressed in Escherichia coli

JOURNAL: Appl. Microbiol. Biotechnol. 49 (1), 31-38 (1998)

PUBMED: 9487707

REFERENCE: 3 (bases 1 to 1726)

AUTHORS: Beckwitt,R., Arcidiacono,S. and Stote,R.

TITLE: Evolution of repetitive proteins: spider silks from Nephila clavipes (Tetragnathidae) and Araneus bicentenarius (Araneidae)

JOURNAL: Insect Biochem. Mol. Biol. 28 (3), 121-130 (1998)

PUBMED: 9654736

REFERENCE: 4 (bases 1 to 1726)

AUTHORS: Beckwitt,R.

TITLE: Direct Submission

JOURNAL: Submitted (26-JAN-1995) Richard Beckwitt, Biology, Framingham State College, 100 State Street, Framingham, MA 01701, USA

* Information from http://www.ncbi.nlm.nih.gov/nuccore/U37520.1

Appendix B. *Nephila Clavipes* dragline silk fibroin spidroin 2 (MaSp2) mRNA, 3' end

LOCUS: NEPFIBPR; 1981 bp; mRNA; linear; INV 26-APR-1993

DEFINITION: Nephila clavipes dragline silk fibroin (spidroin 2) mRNA, 3' end.

ACCESSION: U20329

VERSION: M92913.1; GI:159713

SOURCE: Nephila clavipes

ORIGIN

1 cctggaggat atggaccagg acaacaaggc ccaggaggat atggccctgg acaacaagga

61 ccatctggac ctggcagtgc cgctgcagca gcagcagccg ccgcagcagg acctggagga

121 tatggccctg gacaacaagg acccggagga tatggaccag gacaacaagg acccggaaga

181 tatggaccag gacaacaagg accatctgga cctggcagtg ccgctgcagc cgcagcagga

241 tctggacaac aaggcccagg aggatatgga ccacgtcaac aaggtccagg aggttatgga

301 caaggacaac aaggaccatc tggaccaggc agtgcagccg cagcctcagc cgcagcctca

361 gcagaatctg gacaacaagg cccaggaggt tatggaccag gtcaacaagg cccaggaggt

421 tatggaccag gtcaacaagg tcctggagga tatggaccag gacaacaagg accatctgga

481 ccaggtagtg ccgctgcagc agccgccgcc gcatcaggac ctggacaaca aggaccagga

541 ggatatggac caggtcaaca aggtcctgga ggatatggac caggacaaca aggaccatct

601 ggaccaggta gtgccgctgc agccgccgcc gccgcatcag gacctggaca acaaggacca

661 ggaggatatg gaccaggtca acaaggtcca ggaggttatg gaccaggaca acaaggacta

721 tctggaccag gcagtgcagc tgcagcagcc gcagcaggac ctggacaaca aggacccgga

781 ggatatggac caggacaaca aggaccatct ggacccggta gtgccgctgc agcagcagcc

841 gccgcagcag gacctggagg atatggccct ggacaacaag gacccggagg atatggacca

901 ggacaacaag gaccatctgg agcaggcagt gcagcagcag cagccgcagc aggacctgga

961 caacaaggat taggaggtta tggaccagga caacaaggtc caggaggata tggaccagga

1021 caacaaggtc caggaggata tggaccaggt agtgcatctg cagcagcagc cgcagcagga

1081 cctggacaac aaggaccagg aggatatgga cctggacaac aaggaccatc tggaccaggc

1141 agtgcatctg cagcagcagc cgcagccgca gcaggaccag gaggatatgg accaggacaa

1201 caaggtccag gaggatatgc accaggacaa caaggaccat ctggaccagg cagtgcatct

1261 gcagcagcag ccgcagccgc agcaggacca ggaggatatg gaccaggaca acaaggtcca

1321 ggaggatatg caccaggaca acaaggacca tctggaccag gcagtgcagc agcagcagca

1381 gctgctgcag caggacctgg tggatatgga ccagcgcaac agggaccatc tggtcctgga

1441 atcgcagctt cagctgcttc agcaggacct ggaggttatg gaccagcaca acaaggacca

1501 gctggatatg ggcctggaag cgcagtagca gcctctgccg gtgcaggatc tgcaggttat

1561 gggccaggtt ctcaagcttc cgctgcagct tctcgtctgg cttctccaga ttcaggcgct

1621 agagttgcat cagctgtttc taacttggta tccagtggcc caactagctc tgctgcctta

1681 tcaagtgtta tcagtaacgc tgtgtctcaa attggcgcaa gtaatcctgg tctctctggt

1741 tgcgatgtcc tcattcaagc tctcttggaa atcgtttctg cttgtgtaac catcctttct

1801 tcatccagca ttggtcaagt taattatgga gcggcttctc agttcgccca agttgtcggc

1861 caatctgttt tgagtgcatt ttaattgaaa aatttattaa aatatgcatg gattttctag

1921 cctgggcaac taattgctcg tactatgtaa ttttttttta ataaaattct ttgcaacttc

1981 t

//

REFERENCE: 1 (bases 1 to 1981)

AUTHORS: Hinman,M.B. and Lewis,R.V.

TITLE: Isolation of a clone encoding a second dragline silk fibroin. Nephila clavipes dragline silk is a two-protein fiber.

JOURNAL: J. Biol. Chem. 267 (27), 19320-19324 (1992)

PUBMED: 1527052

* Information from http://www.ncbi.nlm.nih.gov/nuccore/M92913.1

Appendix C. Matlab Program of Reversing Heat Capacity Calculation

This matlab program is to evaluate the specific heat capacity from TMDSC measurements using a “three run method”. This program is developed by Dr. Hui Xu, and recorded in his Ph.D thesis. It was updated by Dr. Qian Ma and Wenwen Huang for the calculation of C_p of various polymers and biopolymers.

```
**************************************************************************
function result=Cpcomputation()
fnameAl=input('please input Al pans file name:','s');
fnameSapp=input('please input sapphire file name:','s');
fnameSample=input('please input sample file name:','s');
load([fnameAl '.txt']);
load([fnameSapp '.txt']);
load([fnameSample '.txt']);
load SapphireLiter.txt;
m=input('please input the mass of Sapphire for Sapphire run(mg):','s');
massSapp=str2num(m);
m=input('please input the mass of Sample for Sample run(mg):','s');
massSample=str2num(m);
Al=eval(fnameAl);
Sapp=eval(fnameSapp);
```

```
Sample=eval(fnameSample);
[a,b]=size(Al);
CpSapp(:,1)=Sapp(:,2);
CpSapp(:,2)=spline(SapphireLiter(:,1),SapphireLiter(:,2),Sapp(:,2));
for j=1:a
   Kprime(j,1)=(1/30)*(massSapp*CpSapp(j,2))/abs((Sapp(j,3)-Al(j,3)));
end
for k=1:a
   CpSample(k,1)=Sample(k,2);
   CpSample(k,2)=abs((Sample(k,3)-Al(k,3)))*Kprime(k,1)/((1/30)*massSample);
end
plot(CpSample(:,1),CpSample(:,2),'k'),hold on;
result=CpSample;
end
```

Appendix D. Heat Capacity of Sapphire Standard

Temperature (ºC)	**Specific c_p (J/g ºC)**	**Temperature (ºC)**	**Specific c_p (J/g ºC)**	**Temperature (ºC)**	**Specific c_p (J/g ºC)**
-183.15	0.0949	6.85	0.7343	206.85	1.0247
-173.15	0.1261	16.85	0.7572	216.85	1.0330
-163.15	0.1603	26.85	0.7788	226.85	1.0409
-153.15	0.1968	36.85	0.7994	236.85	1.0484
-143.15	0.2349	46.85	0.8188	246.85	1.0557
-133.15	0.2739	56.85	0.8373	256.85	1.0627
-123.15	0.3134	66.85	0.8548	266.85	1.0692
-113.15	0.3526	76.85	0.8713	276.85	1.0756
-103.15	0.3913	86.85	0.8871	286.85	1.0817
-93.15	0.4291	96.85	0.902	296.85	1.0876
-83.15	0.4659	106.85	0.9161	306.85	1.0932
-73.15	0.5014	116.85	0.9296	316.85	1.0987
-63.15	0.5356	126.85	0.9423	326.85	1.1038
-53.15	0.5684	136.85	0.9545	336.85	1.1089
-43.15	0.5996	146.85	0.966	346.85	1.1137
-33.15	0.6294	156.85	0.977	356.85	1.1183
-23.15	0.6579	166.85	0.9875	366.15	1.1228
-13.15	0.6848	176.85	0.9975	376.15	1.1271
-3.15	0.7103	186.85	1.007	386.15	1.1313
0.00	0.718	196.85	1.0161	396.15	1.1353

* Data from D. A. Ditmars, et. al., *J. Res. Nat. Bur. Stand.* 1982; 87 (2): 159-163.

Appendix E. Heat Capacity of Glassy Water

Temperature (ºC)	**Specific c_p (J/g ºC)**	**Temperature (ºC)**	**Specific c_p (J/g ºC)**	**Temperature (ºC)**	**Specific c_p (J/g ºC)**
-173.15	0.8471	-83.15	1.5914	6.85	2.1582
-163.15	0.9342	-73.15	1.6641	16.85	2.2104
-153.15	1.0214	-63.15	1.7341	26.85	2.2614
-143.15	1.1074	-53.15	1.8018	76.85	2.4946
-133.15	1.1929	-43.15	1.8668	126.85	2.7038
-123.15	1.2767	-33.15	1.9295	176.85	2.8992
-113.15	1.3489	-23.15	1.9900	226.85	3.0885
-103.15	1.4488	-13.15	2.0477	326.85	3.4771
-93.15	1.5165	-3.15	2.1038		

* Data from Pyda M., *Journal of Polymer Science Part B-Polymer Physics* 2001; 39(23): 3038-3054.

Appendix F. Supplement for Chapter IV

The degree of crystallinity of A, B and BA was determined from the TMDSC measurements and the heat capacity model by

$$\varphi_C = 1 - \varphi_M = 1 - (\Delta C_p / \Delta C_{p0})|_{T_g}$$

where the ΔC_p is the heat capacity step measured at T_g from TMDSC (shown as line ON in **Figure F.1** and line ON overlap line MN in Figure F.1 (b) and (c)), and the ΔC_{p0} is the calculated heat capacity step at T_g based on the number of mobile units for 100% amorphous sample (shown as line MN in Figure F.1).

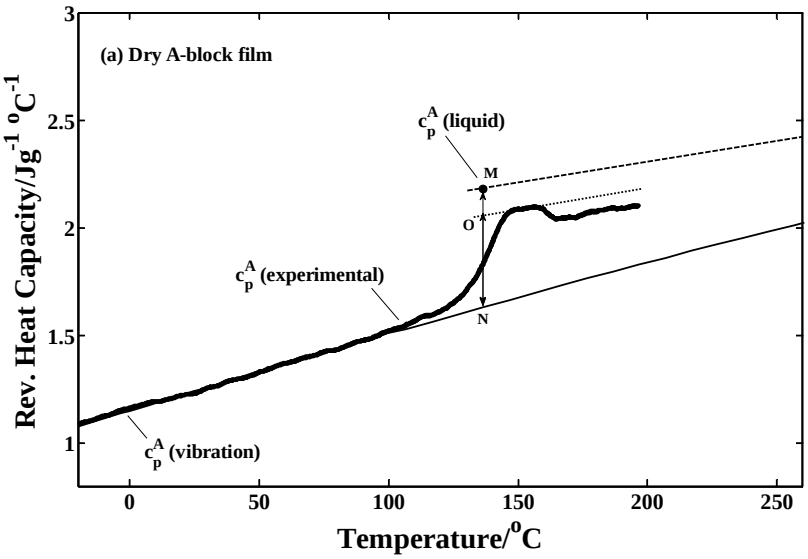

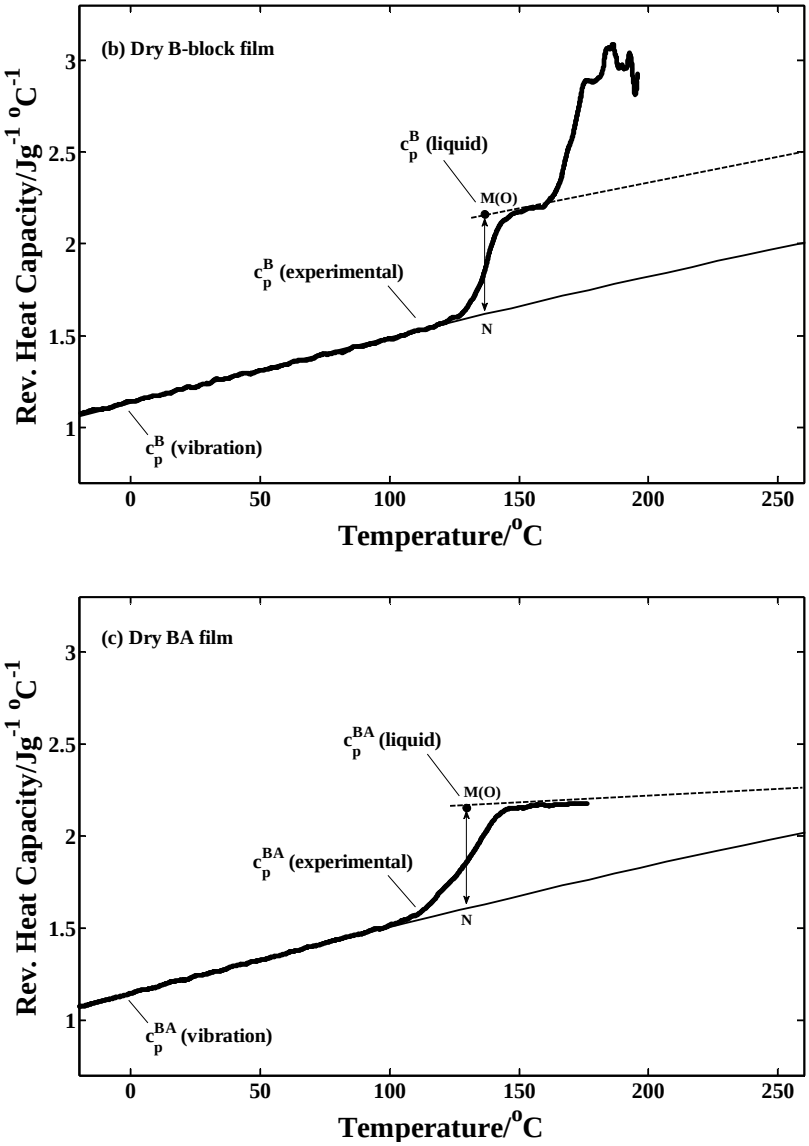

Figure F.1 The measured and calculated apparent reversing heat capacity vs. temperature, after annealing at 120 °C, for dry films of: (a) A-block, (b) B-block, and (c) BA. Heavy curve -- c_p*(experimental)*; thin solid curve -- c_p*(vibrational)*; filled circles -- c_p*(liquid)* calculated at T_g taken at half height of the heat capacity step. Dashed lines are extrapolated best fit lines to experimental curve above T_g. Line *ON* is the measured heat capacity step, ΔC_p, at T_g from TMDSC and line *MN* is the calculated heat capacity ste,p ΔC_{p0}, at T_g based on the number of mobile units for 100% amorphous sample.

To verify the heat capacity model, WAXD was also employed to determine the crystallinity index of A-block, B-block and BA. The inset plots of **Figure F.2** (a), (b) and (c) show the 2-D WAXD pattern of A-block, B-block and BA, respectively. The 2-D WAXD patterns were then radially integrated into 1-D WAXD intensity. In Figure F.2 (a), three major crystalline peaks were observed for A-block film at q = 12.09 nm^{-1}, 14.51 nm^{-1}, and 17.06 nm^{-1} corresponding to lattice distances of β sheet d_{200} = 0.520 nm, d_{120} = 0.433 nm and d_{121} = 0.371 nm, respectively.

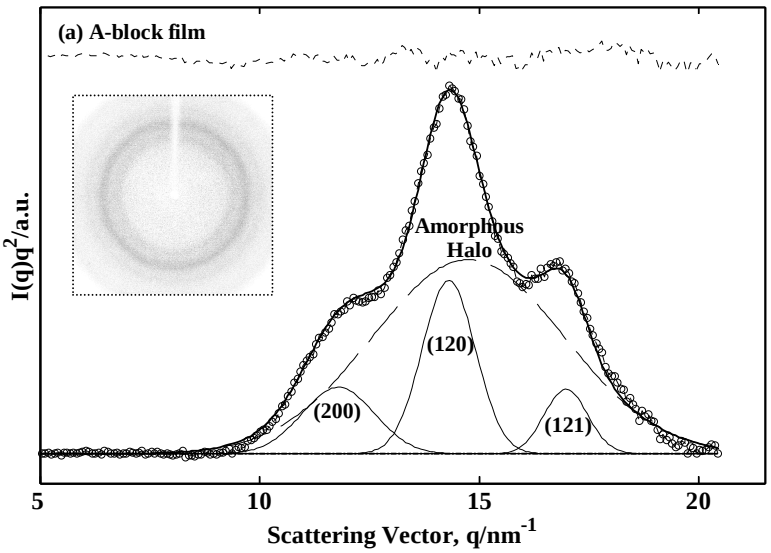

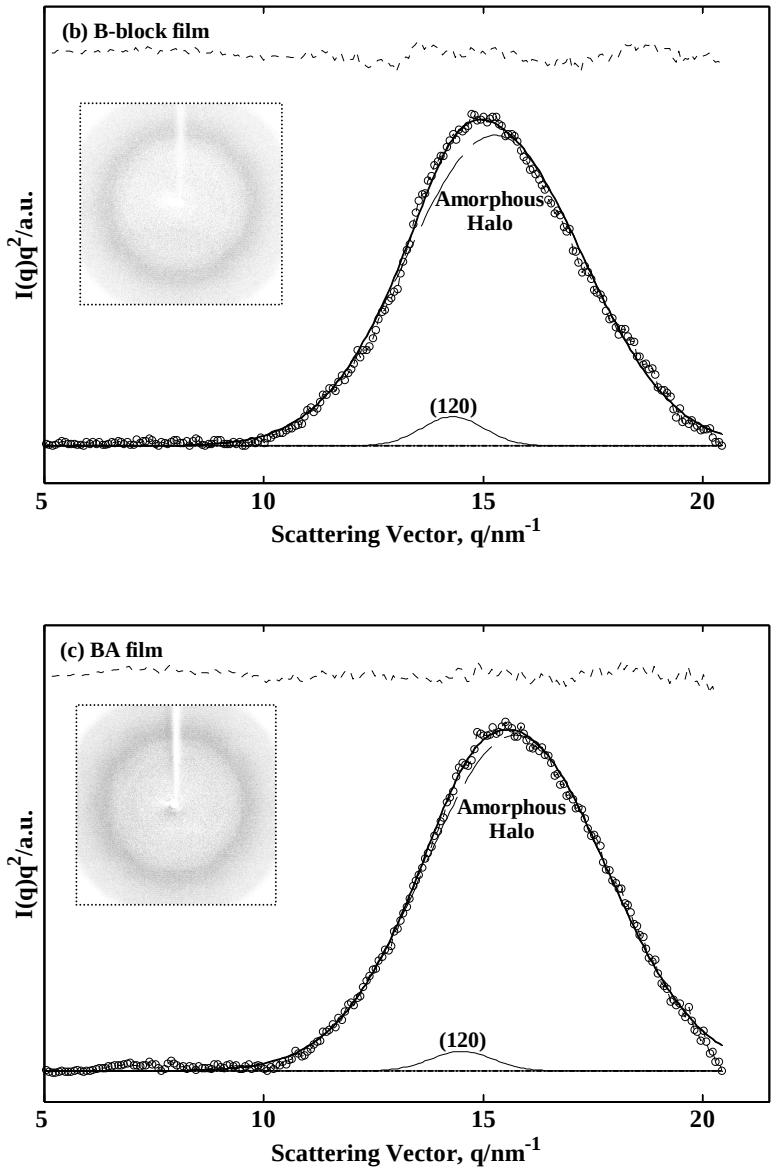

Figure F. 2 Deconvolution of the Lorentz-corrected WAXD intensity, *I(q)q2* vs. *q*, using Gaussian wave functions for (a) A-block, (b) B-block and (c) BA (Open circles - measured data; heavy curves - summation of Gaussian peaks; thin solid curves - individual crystalline Gaussian peaks; dashed curves - amorphous Gaussian peaks; dotted lines at the top - the residual between the fitted curve and measured curve). The inserts shows the 2-D WAXD patterns.

Appendix G. Supplement for Chapter V

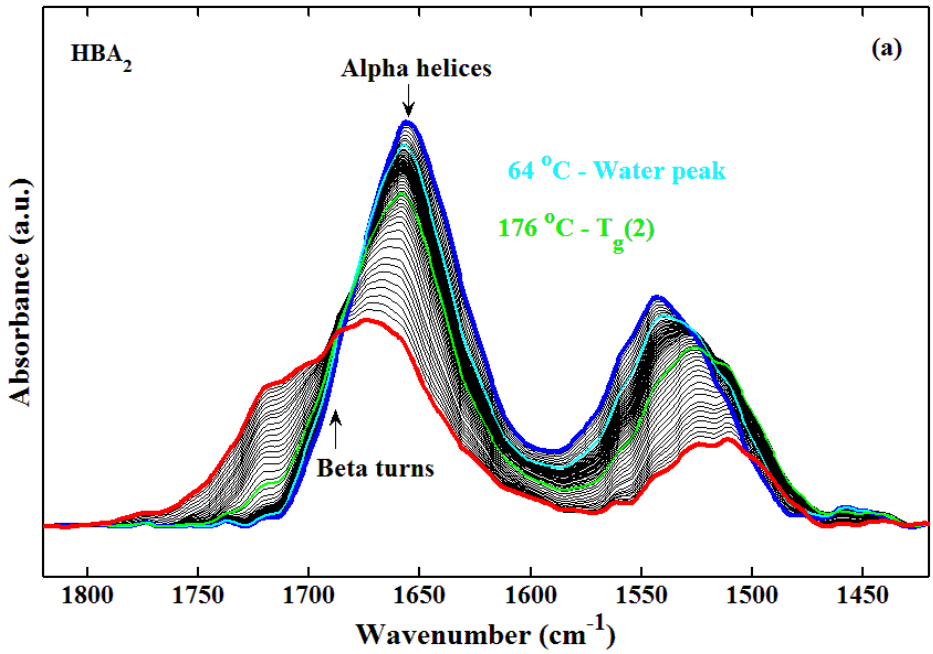

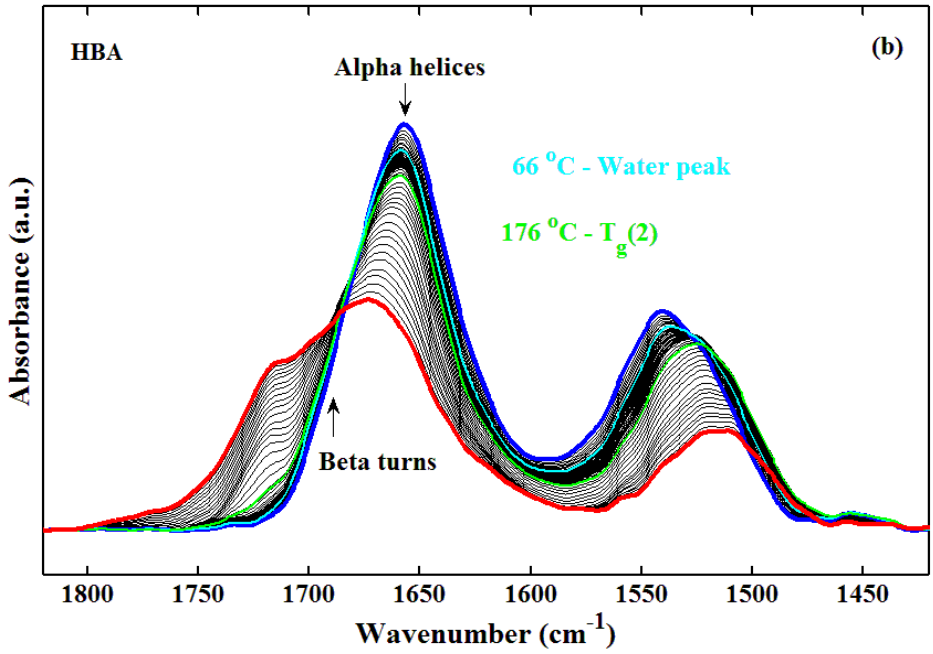

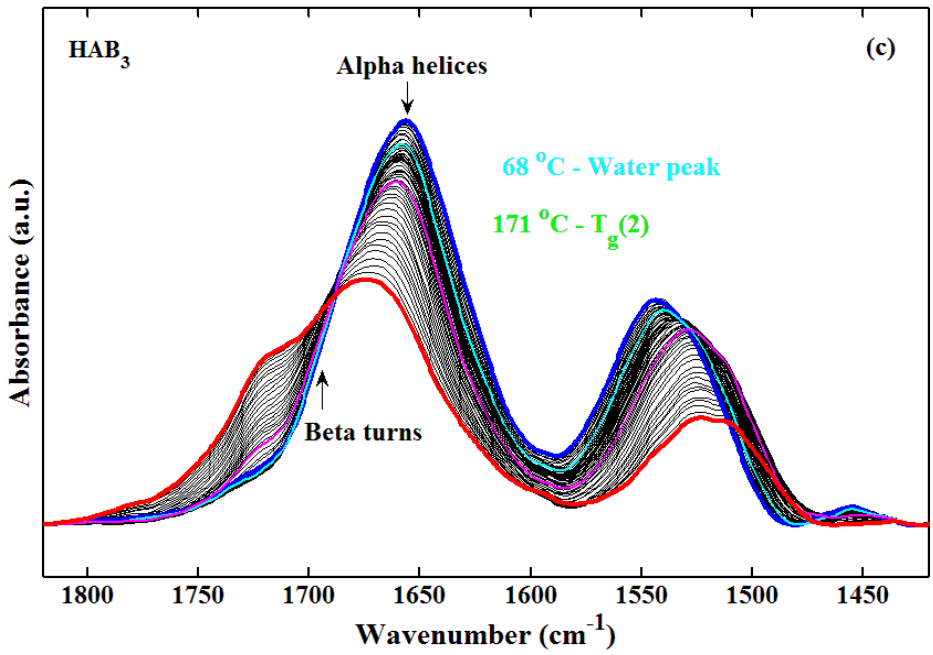

Figure G.1 Real-time FTIR spectra of recombinant spider silk-like block copolymers films: (a) HBA_2, (b) HBA, and (c) HAB_3, during heating at 2 °C/min from 30 to 220 °C. Keys: Blue curve - 30 ºC, Red curve - 220 ºC.

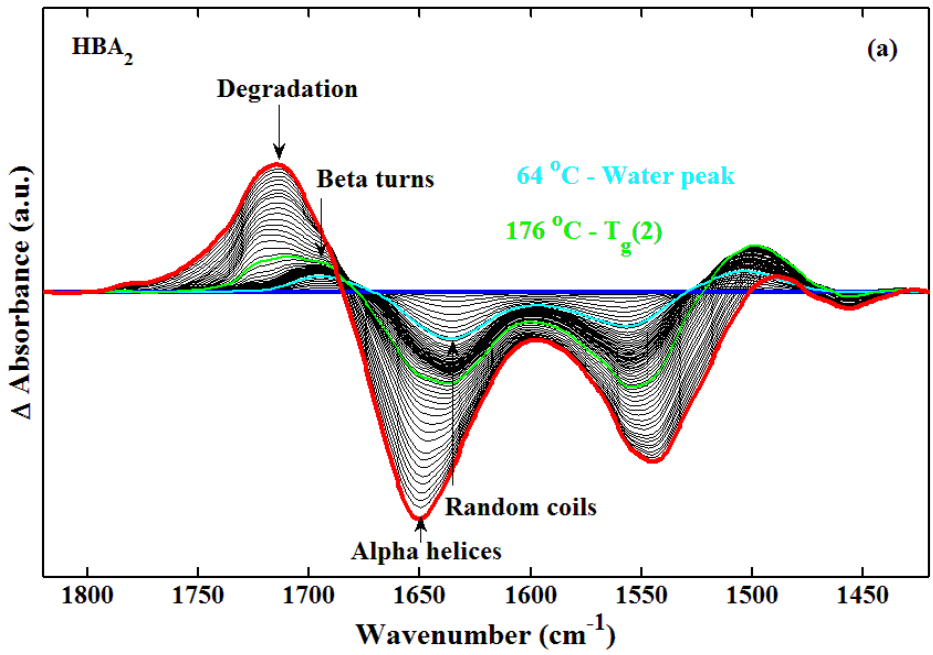
HBA2
(a)
Degradation
Beta turns
64 °C - Water peak
176 °C - Tg(2)
Random coils
Alpha helices
Δ Absorbance (a.u.)
1800
1750
1700
1650
1600
1550
1500
1450
Wavenumber (cm-1)

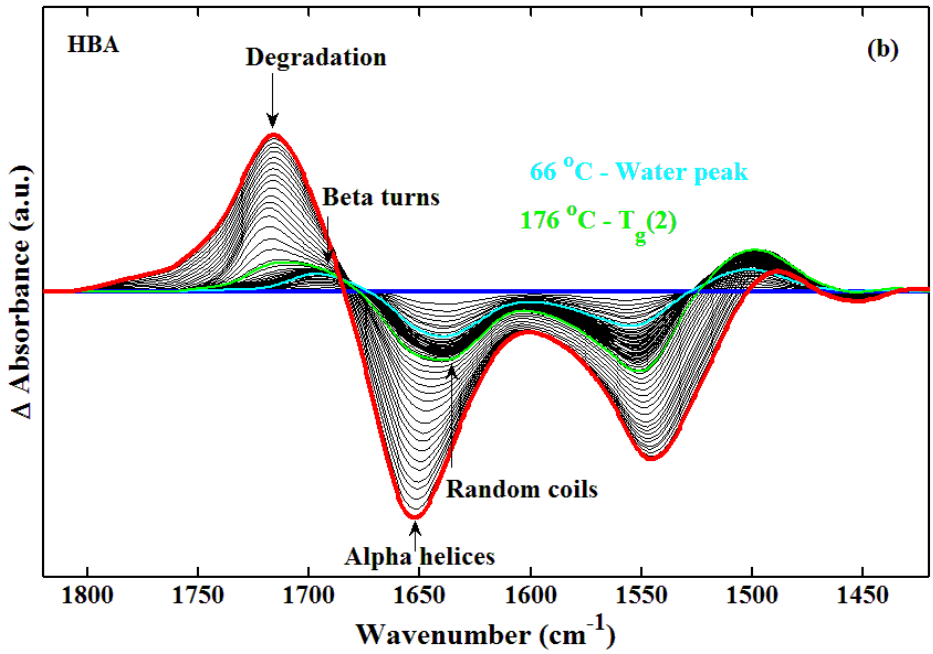
HBA
(b)
Degradation
Beta turns
66 °C - Water peak
176 °C - Tg(2)
Random coils
Alpha helices
Δ Absorbance (a.u.)
1800
1750
1700
1650
1600
1550
1500
1450
Wavenumber (cm-1)

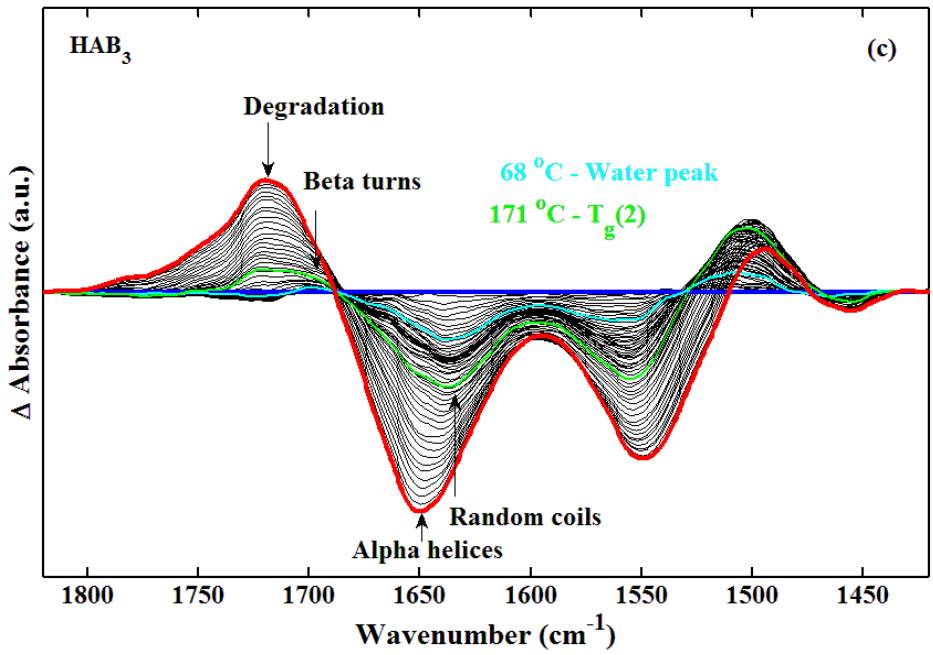

Figure G. 2 Real-time FTIR residue spectra of recombinant spider silk-like block copolymers films: (a) HBA_2, (b) HBA, and (c) HAB_3, during heating at 2 °C/min from 30 to 220 °C. Keys: Blue curve - 30 ºC, Red curve - 220 ºC.

Appendix H. Supplement for Chapter VI

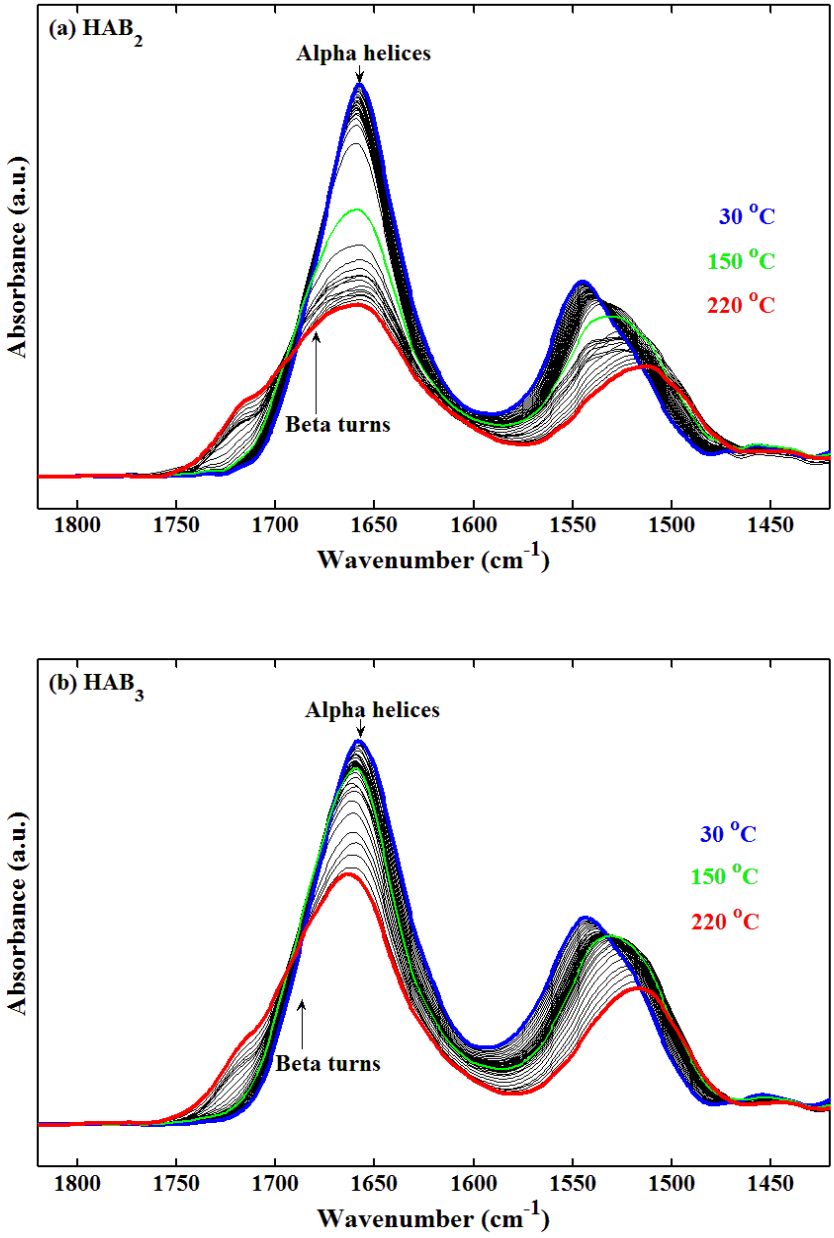

Figure H.1 Real-time FTIR spectra of recombinant spider silk-like block copolymers films treated with HFIP: (a) HAB_2, and (b) HAB_3, during heating at 5 °C/min from 30 to 220 °C.

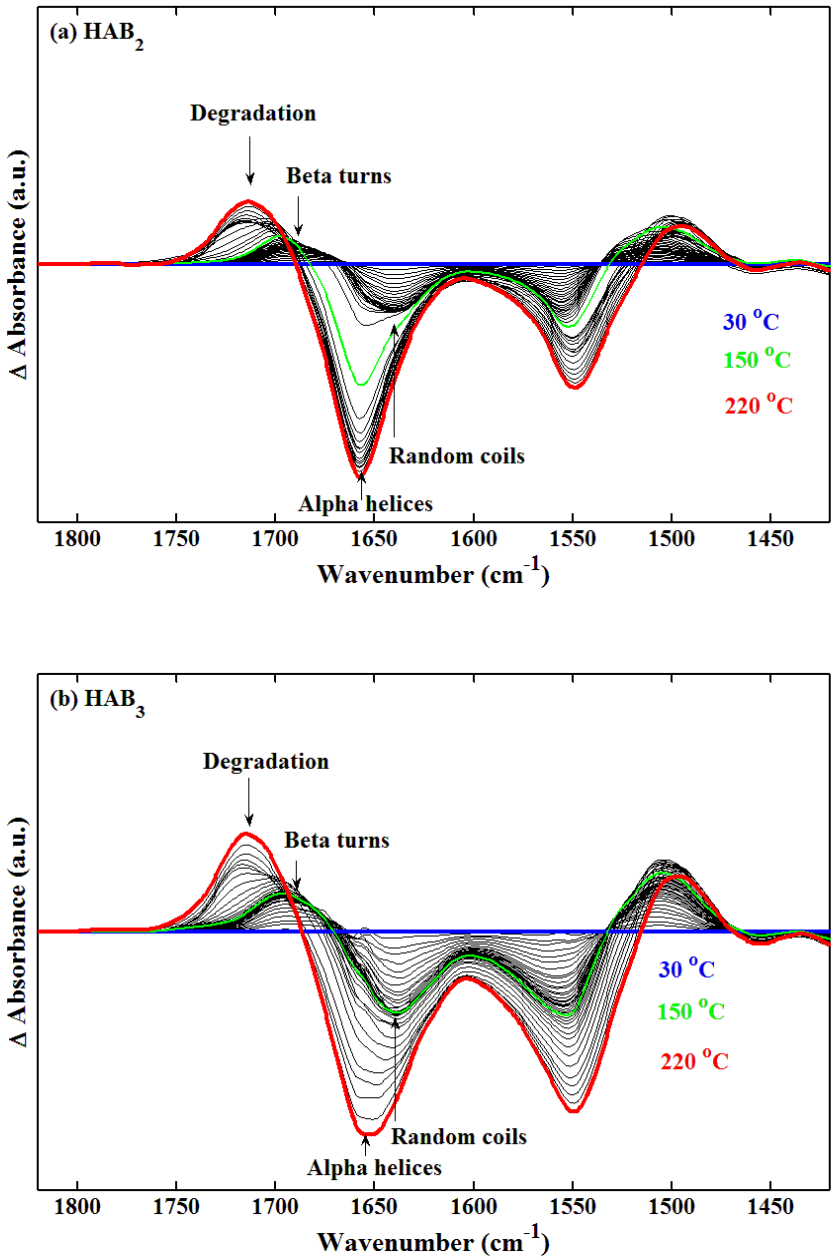

Figure H. 2 Real-time FTIR residual spectra of recombinant spider silk-like block copolymers films treated with HFIP: (a) HAB_2, and (b) HAB_3, during heating at 5 °C/min from 30 to 220 °C.

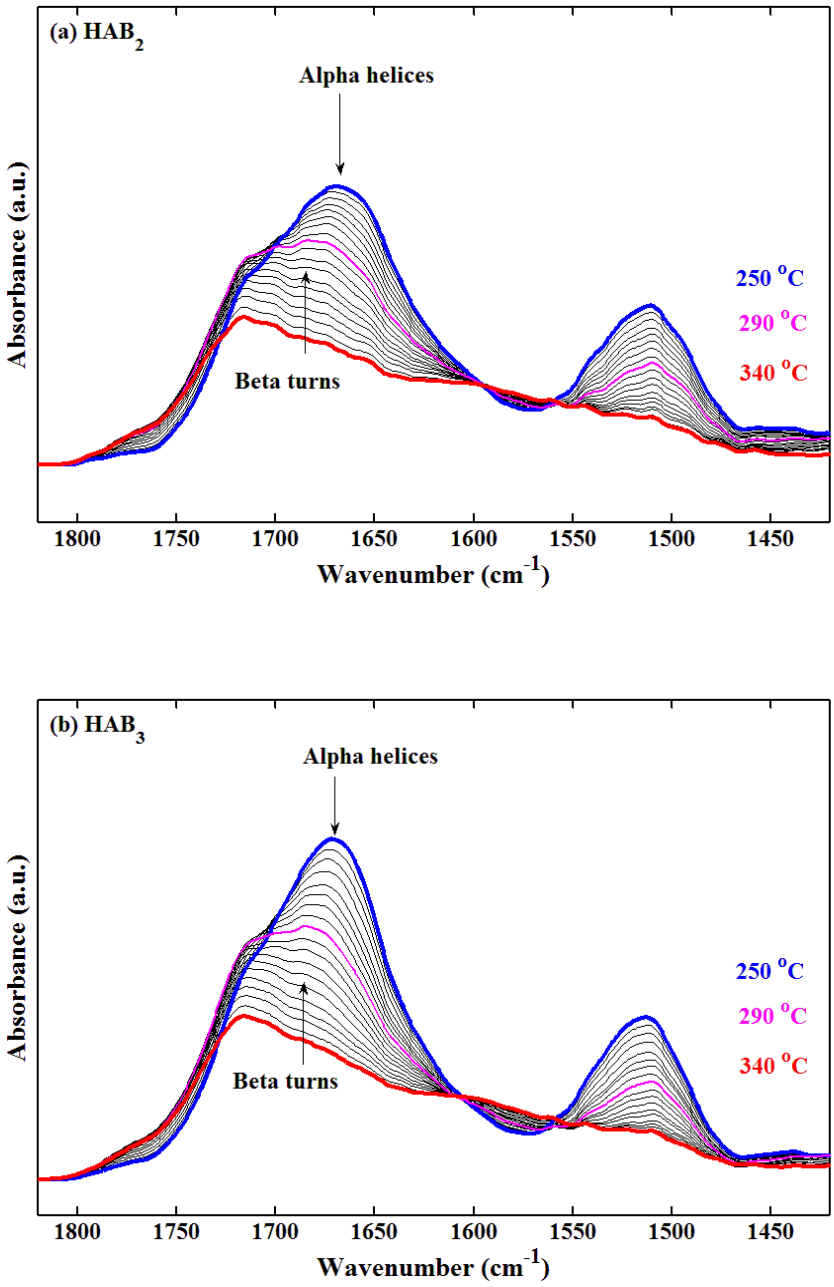

Figure H. 3 Real-time FTIR spectra of recombinant spider silk-like block films treated with HFIP: (a) HAB_2, and (b) HAB_3, during heating at 5 °C/min from 250 to 340 °C.

Appendix I. Nanocomposites of Poly(vinylidene fluoride) with Multi-walled Carbon Nanotubes

1. Introduction:

Poly(vinylidene fluoride) (PVDF) is one of the most important thermoplastics used in a variety of modern engineering application such as in sensors, actuators, and energy transducers [1]. A wide range of studies of PVDF have been reported due to its good mechanical properties, and attractive piezoelectric and pyroelectric properties [1-9]. PVDF crystallizes into five crystallographic forms. The two major forms of interest of our present work are: the polar *tttt* beta phase (form I) and the non-polar tg^+tg^- alpha phase (form II) [2, 3].

In 1969, Kawai first discovered the piezoelectric property in PVDF [4]. Shortly after that, in 1971, pyoelectric property was discovered in PVDF by Bergman, *et al.*[5]. Their studies show when stressed or under changes in temperature, PVDF undergoes a change in electric polarization. The beta PVDF crystal is polarized and transduces electric energy into motion (or vice versa) thus is technologically preferred, while the alpha PVDF crystal does not. Normally alpha PVDF crystal is more easily obtained. To obtain the beta PVDF crystal, special treatments are commonly used: 1.) uniaxial mechanical drawing alpha PVDF film at temperature between 80ºC and 140ºC [6], 2.) crystallizing from N,N-dimethylformamide (DMF) or N,N- dimethylacetamide (DMAc) solutions below 70 ºC [7], and 3.) modifying the polymer with nanoparticle addition [8, 9]. Using method 1, one can seldom get complete alpha-beta conversion. Approximately

20% of alpha PVDF will remain, depending on the drawing temperature. Method 2 can form almost exclusively beta PVDF film, but the film is brittle and with high degree of porosity. Method 3 was the most intensively studied one, not only because it can form almost exclusively beta phase PVDF film, but also it can improve the thermal and mechanical properties of the polymer. For PVDF nanocomposite with more than 0.5 wt% organically modifies silicate clay, the beta phase dominates, and the glass transition temperature and storage modulus are also higher than in the homopolymer [9].

Ever since the discovery of carbon nanotubes (CNTs) by Iijima in 1991 [10], the use of CNTs as a nano-filler for polymers, such as polystyrene, poly(vinylidene fluoride), poly(methyl methacrylate), polycaprolactam (nylon-6) and isotactic poly(propylene), has been receiving increasing attention [11-15]. Two forms of CNTs exist: single-walled carbon nanotubes (SWCNTs) and multi-walled carbon nanotubes (MWCNTs). SWCNTs comprise a single sheet of graphite rolled into a cylinder; multiwalled carbon nanotubes (MWCNT) consist of concentric cylinders around a hollow center with constant wall to wall separation of 0.34nm [16]. The Young's modulus of MWCNT is about 1.8 TPa [17], and appears to be a function of the number of walls, as reported by both theoretical and experimental works [16, 18]. The thermal conductivity of MWCNT can be more than 3000 W/m-K [19]. By dispersing MWCNT into polymer matrix, it is expected that polymer properties can be enhanced with a higher thermal conductivity, higher electrical conductivity, and large Young's modulus. Another advantage for MWCNT use as a nano-filler is its large surface area and high aspect ratio, which induce a better adhesion of polymer. However, despite the attractive properties mentioned above, using CNTs as nanofillers has its own draw back in producing polymer nanotube composites: dispersing

the nanotubes uniformly into the polymer matrix is difficult due to the Van de Waal's force existing in between the carbon nanotubes, and due to their small size. Several methods have been studied to overcome this problem, including chemical modification of the surface of CNTs, grafting polymer on to CNTs, solution method, and direct mixing in melt processing [20].

In our present work, we report a characterization study of PVDF/MWCNT films prepared from solution over a wide composition range, from 0.1% to 5.0% MWCNT by weight. The MWCNT was purified by acid treatment. Effect of uniaxial orientation by zone drawing on these nanocomposites is also discussed and compared with unoriented compression molded films. The purpose of this study is to determine separate effects of uniaxial drawing and the MWCNT modification of PVDF on the phase transition from alpha phase to beta phase in PVDF, and their effect on the thermal and mechanical properties of the PVDF/MWCNT films. The projects resulted in publication in Journal of Applied Polymer Science [21].

2. Experimental section:

2.1 Sample preparation

PVDF used in our present study was a KYNAR® poly(vinylidene fluoride) resin grade 740 commercially obtained from ATOFINA Chemicals, Inc. in pellet form. MWCNTs were purchased from MER Corporation with a nominal diameter about 140 nm and length ranging from 5μm to 9μm. To purify the MWCNTs, they were suspended in a mixture of concentrated sulfuric acid and nitric acid (3:1 vol. ratio) and ultra-sonicated in a water bath for several hours, then washed with deionized water and filtered

through a 400 nm pore PTFE membrane until the water passing through the filter had a pH between 6 and 7. After this treatment, the MWCNTs had been functionalized and reach a purity of 95% [22].

To achieve uniformly mixed PVDF/MWCNT solutions with desired weight percentages of MWCNT, a two step method was used. First, two stock solutions were prepared: PVDF was dissolved and MWCNTs were separately dispersed in dimethylacetamide (DMAc) solution with stirring for about 3 days at 30 - 40 °C. Then, two stock solutions were mixed to achieve the desired weight percentages of MWCNTs from 0.1% to 5%. The PVDF/MWCNT solutions were stirred for 2 days at 30 - 40°C and then ultra-sonicated in water bath for 10 minutes. To remove the DMAc solvent, PVDF/MWCNT solutions were poured into uncovered preheated glass Petri dishes and uniformly heated at 60°C for 1 day. Curly films formed after evaporation of DMAc, and could be easily lifted from the glass Petri dishes. Because MWCNTs are black in color, the films containing more MWCNTs look darker: film colors varied from tan (0% MWCNT) to light grey (1% MWCNT) to dark black (5% MWCNT). Uniform color was observed, an indication of good distribution (i.e., little or no large scale aggregation) of MWCNTs in the polymer matrix. To achieve flat bulk films, about 100 micrometers thick, all compositions were compression molded using a Carver hydraulic hot press at a pressure of 12MPa, at 200°C for 3 min, well above the melting point of PVDF (178ºC) and then were air cooled. **Figure I.1** shows a scanning electron microscope (SEM) image of MWCNTs after purification and evaporation of DMAc, which showed that those treatments did not change the morphology of MWCNTs compared to the untreated

MWCNTs (not shown for the sake of brevity).

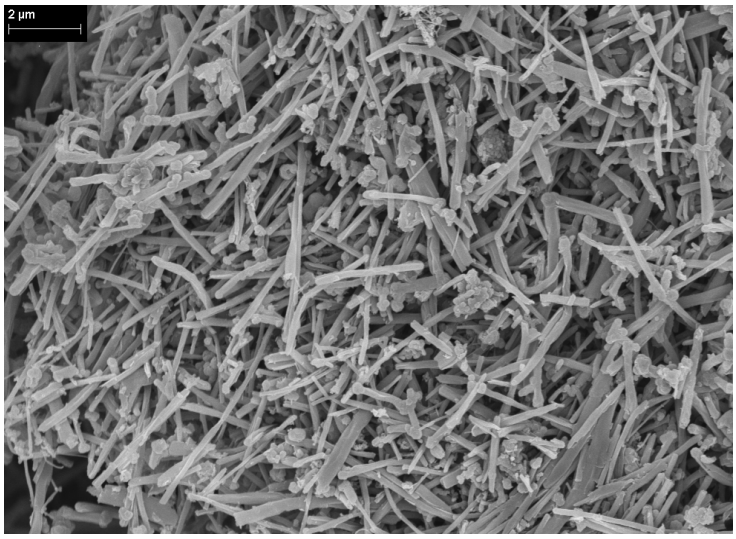

Figure I. 1 Scanning Electron Microscope (SEM) image of MWCNT powder after acid treatment and evaporation of DMAc.

Zone drawing experiments [23, 24] were performed at a fixed temperature, 105 ± 5°C, with an almost constant applied stress, 2.3 kg/m^2. During this process, the samples became oriented so that the crystallographic c-axis and molecular chain axes were partially aligned along the zone drawing direction. The a-axis and b-axis were randomly oriented in the plane perpendicular to the draw direction. The draw ratio, λ, was calculated from:

$$\lambda = L_f/L_i \qquad \text{(I.1)}$$

where L_f is the final length of the film after drawing and L_i is the initial length of the film. Though there was a large standard error (± 12.5%) of the draw ratio for each composition, which may due to non-uniformity of the film thickness, the draw ratio for all the samples we investigated was in the range of 4.7 ± 0.3.

2.2 Analysis methods

Room temperature two-dimensional (2-D) wide angle X-ray scattering (WAXS) was performed on a Bruker GADDS D8 X-ray diffractometer, with wavelength $\lambda = 0.154$ nm, operated at 40 kV and 20 mA. Scattering angle, 2θ, was calibrated by using silicon powder reference standard with silicon (111) peak at 28.444º, for all the undrawn and drawn films. The scan time used was 600s per sample. The scattering angle, 2θ, ranged from 5º to 30°. The air background was subtracted from the original scan for each sample. To compare the peak position and identify the crystalline content, the 2-D WAXS patterns were converted to a one-dimensional pattern by integrating over a sector. The crystallinity index, $\phi_{ci,}$ the fraction of alpha, ϕ_{alpha}, and the fraction of beta phase, ϕ_{beta}, were calculated using the area of crystal peaks and area of amorphous halo by fitting the Lorentz-corrected WAXS peak intensity using Gaussian wavefunctions as described previously [9].

Room temperature Fourier transform infrared spectroscopy (FTIR) studies were performed using a Jasco FT/IR-6200 with a TGS detector in attenuated total reflection (ATR) mode. The absorbance spectra were obtained by averaging 64 scans with a resolution of 4.0 cm^{-1}. The background spectra were collected under the same conditions and subtracted from the scan for each sample. The wavenumbers investigated ranged from 600 to 4000 cm^{-1}.

Differential scanning calorimetry (DSC) was performed on a TA Instruments 2920 temperature modulated differential scanning calorimeter (TMDSC) in standard mode. The same heating/cooling method was used for all samples: they were heated at a rate of 10°C/min from 50 to 200°C and then cooled at a rate of 10°C/min from 200 to

50°C. Aluminum sample pans were used to encapsulate the sample. A nitrogen purge gas was used at a flow rate of 50 ml/min. The sample weights were in the range between 7.5 mg and 12.0 mg.

Thermogravimetric analysis (TGA) was performed on a TA Instruments Q500 thermogravimetric analyzer at a heating rate of 10°C/min from room temperature to 1000°C in a nitrogen gas flow (60.0 ml/min). The initial sample weight was in the range between 7.0 mg and 11.0 mg.

Polarizing optical microscopy (POM) studies were performed on a Nikon eclipse E600 polarized optical microscope with a Linkam THMS600 hotstage. The heating/cooling method used was the same as the method used for DSC studies.

Dynamic mechanical analysis (DMA) studies were performed on a TA Instruments RSA3 dynamic mechanical analyzer using frequency/temperature sweep test at a strain of 0.1%, with four different frequencies, 0.1, 1.0, 10 and 50 Hz. The temperature ranged from -100 to 30 °C with an increase of 3°C per step and a soak time of 45 s per step.

Tensile tests were performed at room temperature on unoriented samples, using an Instron 3366 with a 100N capacity load cell. Crosshead displacement rates of 2 and 10 mm/min were used. Sample specimens were cut into dog bone shapes with a sharp-edged die ASTM-D-638-5-1MP from ODC Tooling & Molds. Each sample type was run at least three times, and average values are reported.

3. Result and Discussion

3.1 Phase Identification

The crystal structure of our films was evaluated by static 2-D WAXS as shown in **Figure I. 2** (a) and (b) for the unoriented film and oriented zone drawn film, respectively, exemplified by 1.0 wt% MWCNT. As can be seen, the (h00), (0k0) and (hk0) reflections lie on the equator, while the (0kl) reflection is quadrantal for the oriented sample. By the Laue formula, we can conclude that the ab plane is perpendicular to the sample surface and the drawing direction. The crystallographic c axis is along the drawing direction. The zone drawing process orientated the crystals with polymer molecular chain along the fiber axis (draw direction).

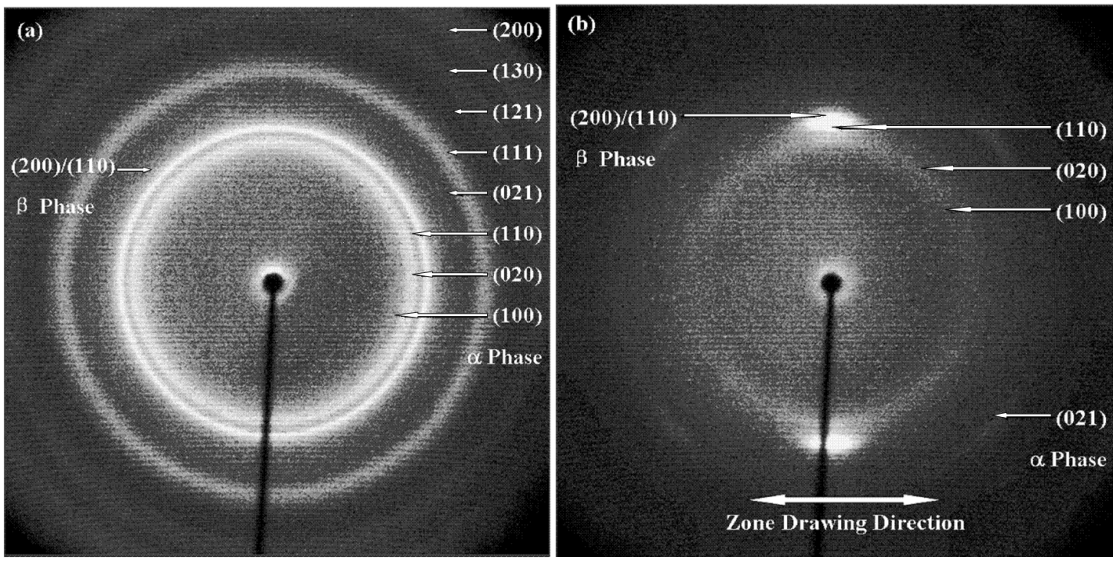

Figure I. 2 2-D WAXS patterns of nanocomposites of PVDF with MWCNT, exemplified by 1.0 wt% MWCNT. (a) Unoriented sample, formed by hot pressing, (b) Oriented sample, formed by hot pressing and then zone drawing. The white arrow at the bottom represents the drawing direction. Miller indices for alpha and beta PVDF are marked.

To compare the peak positions of each sample, the intensity was integrated from χ = 90º to 270º (the upper half sector) and normalized to 1 by dividing by the greatest intensity for each composition. **Figure I.3** (a) and (b) compare the 1-D WAXS pattern for all unoriented and oriented samples with different MWCNT compositions. For the unoriented PVDF /MWCNT films, Figure I.3 (a), the major peaks for all compositions were observed at 2θ = 17.8º, 18.5º, 20.1º, 26.8º, 28.1º, for $d_{100}(\alpha)$= 0.497 nm, $d_{020}(\alpha)$= 0.480 nm, $d_{110}(\alpha)$= 0.443 nm, $d_{021}(\alpha)$= 0.334 nm, and $d_{111}(\alpha)$= 0.318 nm, respectively.[9] These reflections belong to orthorhombic alpha PVDF which has lattice constants of a = 0.496 nm, b = 0.964 nm, c = 0.462 nm [25]. For films with 0.1 wt% to 5.0 wt% MWCNT, a small shoulder can also be observed at 2θ = 20.8º for $d_{200/110}(\beta)$ = 0.427 nm corresponding to pseudo-hexagonal polar beta PVDF crystal which has lattice constants of a = 0.858 nm, b = 0.491 nm, c = 0.256 nm [3, 26]. For oriented PVDF/MWCNT films, Figure I.3 (b), the peak intensity at 2θ = 20.8º increases remarkably while all other peak intensities decrease significantly compared to unoriented samples. This result shows the increase of MWCNTs has no strong effect on forming beta phase crystal for unoriented samples. However, the uniaxial zone drawing process has the very clear effect of transforming alpha phase crystals to beta phase, which has been reported previously [26]. MWCNT did not hinder the alpha to beta crystal transformation in PVDF during zone drawing either.

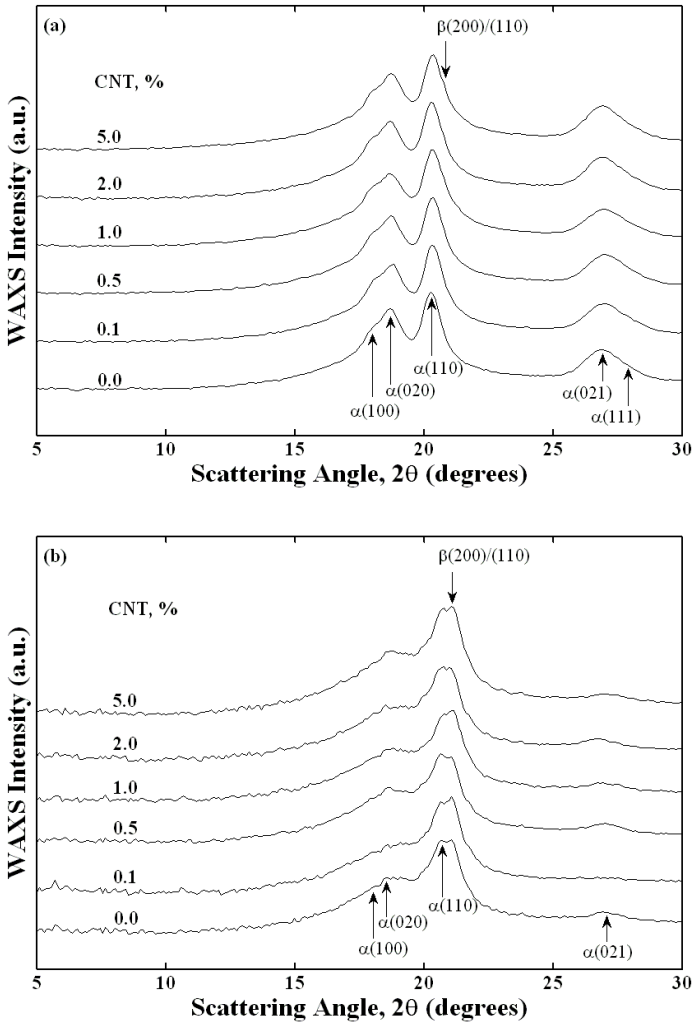

Figure I. 3 Normalized WAXS Intensity vs. scattering angle, 2θ, for nanocomposites of PVDF with MWCNT with composition as indicated. (a) Unoriented samples, (b) Oriented zone drawn samples. Miller indices for alpha and beta PVDF are marked [9].

To estimate the crystallinity index, $\phi_{ci,}$ the fraction of alpha, ϕ_{alpha}, and the fraction of beta phase, ϕ_{beta}, of PVDF/MWCNT films, the Lorentz-corrected WAXS peak intensities were fitted with Gaussian peaks and a quadratic baseline [9]. **Figure I. 4** illustrates the fitting for 1.0 wt% PVDF/MWCNT film.

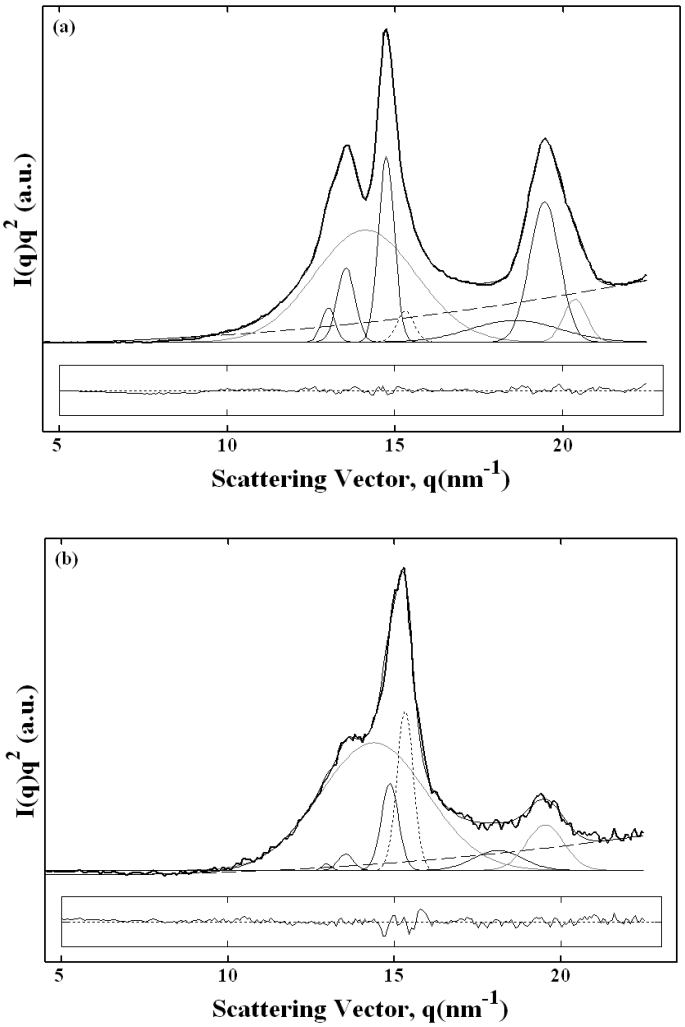

Figure I. 4 Peak deconvolution of Lorentz-corrected WAXS peak intensity, $I(q)q^2$ vs q, using Gaussian wavefunction and quadratic baseline, for nanocomposites of PVDF with MWCNT exemplified by 1.0 wt%. (a) Unoriented sample, (b) Oriented zone drawn sample. The heavy curve represents the measured data; the grey lines represent the amorphous halos; the solid lines represent the alpha peaks; the dotted lines represent the beta peak; and the dash lines represent the corrected baseline. The insert shows the residual between the fitted curve and measured curve. The dotted line in each insert plot represents the zero position.

The crystallinity index, $\phi_{ci,}$ was estimated by dividing the area of crystal peaks by the total area of the coherent scattering, which is the sum of the areas of amorphous halo and crystal peaks. This approach has been applied to crystallinity determination in unoriented [9] and oriented samples [27, 28]. The fraction of alpha (or beta), ϕ_{alpha} (or ϕ_{beta}), was estimated by dividing the sum of the alpha (or beta) crystal peaks by the total area. The dependence of alpha fraction, beta fraction, and crystallinity index, on MWCNT concentration is shown in **Figure I. 5** (a), (b) and (c), respectively, for all unoriented samples (filled triangles) and oriented samples (open squares). The scattering peak for MWCNT, occurring at $2\theta = 26.29^{o}$ and corresponding to $d_{002} = 0.34$ nm, is neglected due to the small peak intensity [29, 30]. We observed from Figure I.5 that the beta fraction and crystallinity index increase slightly, and the alpha fraction varies around a constant, with MWCNT addition. This result suggests that MWCNT addition increases crystallinity slightly through enhanced nucleation (POM results show spherulites become smaller with MWCNT addition). On the other hand, MWCNT may also reduce the chain mobility which would hinder the crystallization process. The competition between those two effects of MWCNT makes the trend for crystallinity index hard to predict. From our data, the former one prevails. The maximum beta to alpha ratio, $\phi_{beta} / \phi_{alpha}$, occurred at 1.0 wt% for unoriented films which is in agreement with previous work by Carroll [12], while the maximum beta to alpha ratio occurred at 2.0 wt% for oriented samples. The decrease of the beta to alpha ratio at higher MWCNT concentration is possibly due to reaggregation within the polymer matrix as the MWCNT concentration increases [12]. We also observed that the alpha fraction and crystallinity index are lower, and beta fraction is higher, for the oriented sample compared to the

unoriented sample. This result suggests that the crystalline structure of alpha phase is partially destroyed by the zone drawing process, and all original alpha phase is not completely transformed to beta phase; some was converted to the amorphous phase.

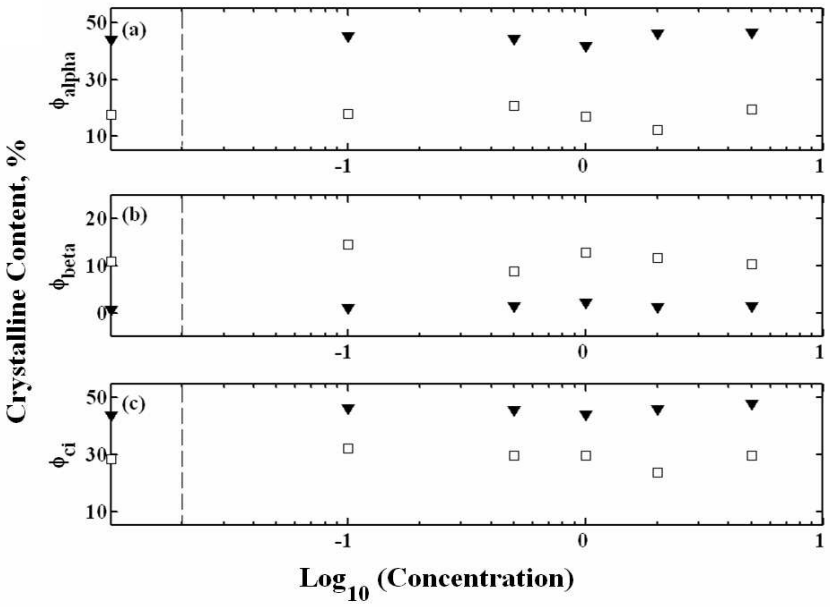

Figure I. 5 Crystalline content vs. MWCNT concentration for nanocomposites of PVDF with MWCNT calculated from Lorentz-corrected WAXS peak intensity fitting analysis, for unoriented samples (black triangles) and oriented samples (white squares). (a) alpha PVDF content, $\phi_{alpha,}$ (b) beta PVDF content, $\phi_{beta,}$ (c) crystalline index, $\phi_{ci} = \phi_{alpha} + \phi_{beta}$. The crystalline content for homopolymer PVDF is marked on the y axis for comparison. The error bar is within each data point.

The crystal structure was also investigated by static Fourier transform infrared spectroscopy (FTIR). **Figure I. 6** (a) and (b) shows the FTIR absorbance spectra for unoriented samples and oriented samples, respectively. We observe that the alpha

absorption bands at 1383, 976, 764, and 613 cm^{-1}, exist in all compositions. Those peaks correspond to bending and wagging motion of CH_2 (1383 cm^{-1}), twisting motion of CH_2 (976 cm^{-1}), bending motion of CF_2 and skeletal bending of CF-CH-CF (764 cm^{-1}), and bending motion of CF_2 and skeletal bending of CH-CF-CH (613 cm^{-1}) [31]. Peaks at 764 cm^{-1} and 613 cm^{-1} were decreased as a function of wt% of MWCNT, which suggest the vibration modes for CF_2 were weakened. This is because hydrogen bonds exist between the carboxyl group on acid treated MWCNT walls and the fluorine atoms in PVDF. A rough estimate of the energy of the O-H···F hydrogen bond is 3 kcal mol^{-1} [32]. Fluorine atoms in PVDF tend to be attracted to MWCNT exterior walls due to this strong hydrogen bond, and the vibrations of CF_2 are thus hindered, which effect was also demonstrated in PVDF nanocomposites with silicates [33]. Whereas in the case of PVDF/silicate nanocomposites there was complete conversion of alpha phase gauche bonds to beta phase all trans [33], in our case with MWCNTs, the effect is less, and the beta fraction only increases slightly.

The alpha fraction estimated by FTIR is almost constant. The beta absorption peaks at 1274 and 840 cm^{-1} increased slightly with MWCNT addition and reached a maximum beta fraction at above 1 % MWCNT in both cases. These peaks correspond to symmetric stretching motion of CF_2 and CC, and skeletal bending motion of CF-CH-CF (1274 cm^{-1}), and rocking motion of CH_2 and antisymmetric stretching motion of CF_2 (840 cm^{-1}) [31]. This result suggests that the MWCNT served as a nucleation agent for beta phase, which cause beta phase to increase slightly in both cases. The zone drawing studies show the beta phase grew at the expense of reducing the alpha phase. This conclusion is consistent with that from 2-D WAXS. FTIR absorption peaks for purified

MWCNTs are located at 3409, 1708 and 1200 cm^{-1} corresponding, respectively, to OH (3409 cm^{-1}), C=O (1708 cm^{-1}) and C-O (1200 cm^{-1}) stretching in the carboxylic group [29]. These peaks do not overlap with any characteristic peaks for PVDF alpha and beta phase.

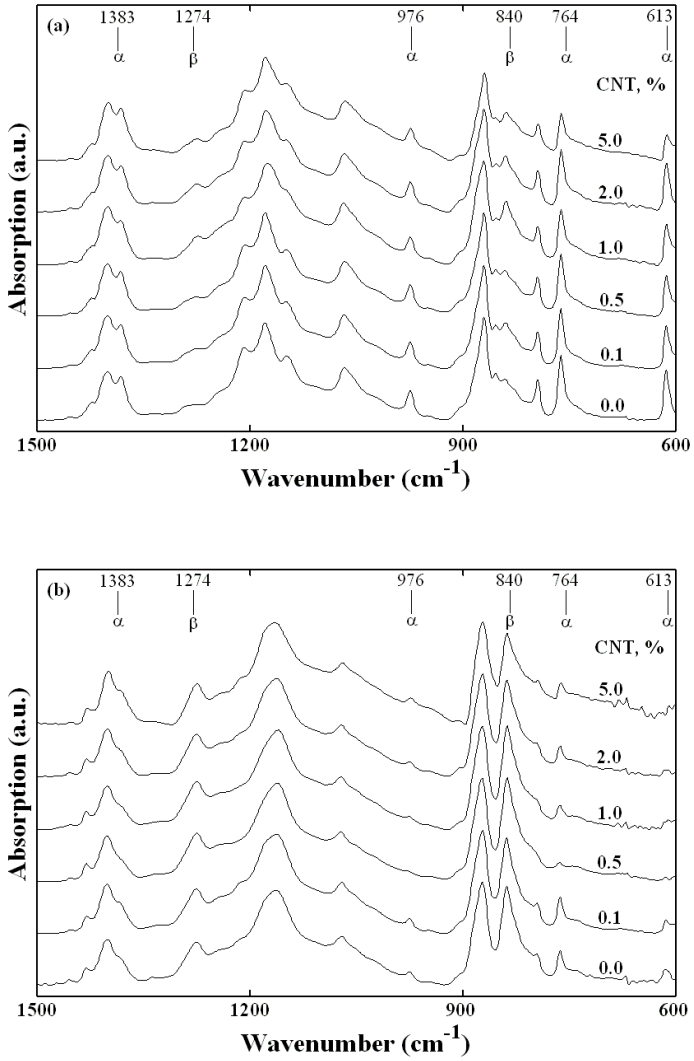

Figure I.6 Normalized infrared absorption vs. wavenumber for nanocomposites of PVDF with MWCNT. (a) Unoriented samples, (b) Oriented zone drawn samples. Absorption bands for alpha and beta PVDF are marked.

3.2 Thermal properties

DSC scans of unoriented samples during cooling at 10 °C/min from 200 to 50°C are shown in **Figure I. 7**. As MWCNT content increases, the crystallization exothermal extrapolated onset and peak position systematically shift to a higher temperature. The extrapolated onset shifted upward 8°C and the crystallization peak shifted 16°C. This means the sample film with the highest concentration of MWCNTs crystallized first during cooling. DSC scans confirm that the MWCNT acts as nucleation agent. This behavior was also observed by POM studies and is summarized in **Table I.1**, column 4.

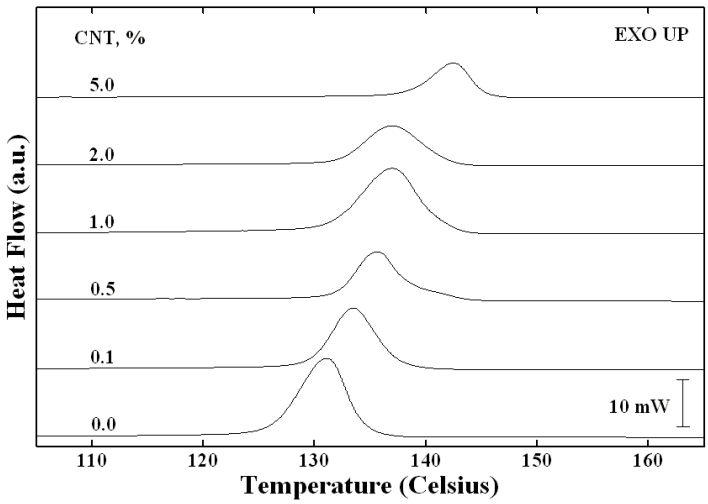

Figure I.7 Normalized heat flow vs. temperature for nanocomposites of PVDF with MWCNT during DSC cooling from 200 ºC at 10ºC/min. The exothermal peaks represent the crystallization peaks, at temperature T_c.

The degree of crystallinity of PVDF/MWCNT film, χ_c, summarized in Table I.1 column 6, was determined from the area of endotherm peak using:

$$\chi_c = \Delta H_f / \Delta H_{f\,(100\%)} \quad \text{(I.2)}$$

where ΔH_f is the measured heat fusion of the PVDF/MWCNT films, and $\Delta H_{f(100\%)}$ = 104.6 J/g [9] is the heat fusion of 100% crystalline PVDF. This result is consistent with crystallinity index, $\phi_{ci,}$ from 2-D WAXS, showing the crystal portion of the sample will increase with the concentration of MWCNT.

Table I.1 Thermal Parameters for Nanocomposites of PVDF with MWCNT.

Sample[a] (MWCNT wt %)	**T_c [b] (±0.5°C)**	**T_c [c] (±0.5°C)**	**T_c [d] (±2°C)**	**ΔH_f [e] (±1.5 J/g)**	**χ_c [f] (±1)**	**ϕ_{ci} [g] (±1)**
0.0	131.0	140.7	144	46.2	44	44
0.1	133.4	143.9	147	48.5	46	47
0.5	135.6	144.9	145	47.0	45	46
1.0	136.7	146.2	146	48.1	46	44
2.0	138.6	147.5	152	51.0	49	47
5.0	142.5	148.3	153	50.1	48	48

[a] PVDF/MWCNT unoriented film

[b] Crystallization peak temperature from DSC at cooling rate of 10 °C/min

[c] Crystallization onset temperature from DSC at cooling rate of 10 °C/min

[d] Crystallization onset temperature from POM at cooling rate of 10 °C/min

[e] Heat of fusion from DSC at heating rate of 10 °C/min

[f] Degree of crystallinity calculated by Equation 1

[g] Crystallinity index from 2-D WAXS

Thermogravimetic analysis of unoriented sample films is shown in **Figure I. 8**. A major weight loss occurred in the region between 400 and 470 °C for all samples. This is related to the degradation of PVDF and also to oxidization of MWCNT at around 450 °C [34]. As can be seen, when the wt % of MWCNT increases, to obtain the same weight loss, higher temperature is needed for PVDF/MWCNT films in this region, which is shown in the insert plot of Figure I. 8 as a systematic shift of the thermogravimetic curve. The thermal stability of PVDF/MWCNT films was improved with MWCNT loading, a trend similar to what was observed by Liu's group [35]. A small weight loss, about 1 % from 100°C to 170°C was also observed. This can be attributed to the evaporation of absorbed moisture and DMAc residue.

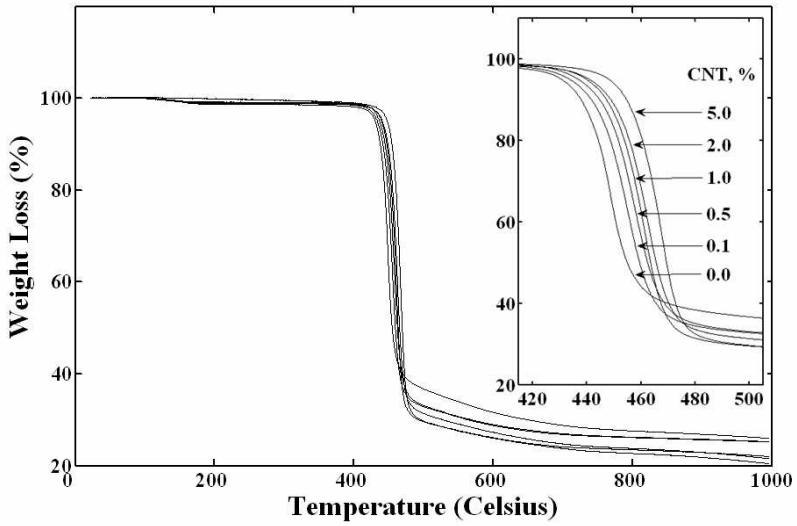

Figure I. 8. Thermogravimetic curve of weight loss vs. temperature for nanocomposites of PVDF with MWCNT. The insert plot of weight loss vs. temperature is a magnification of the region between 400 and 500 ºC.

Residual weight percent remaining at different temperatures for PVDF/MWCNT is summarized in **Table I.2**. In Table I.2 column 6, the weight percent remeining after major degradation at 500 to 1000°C was higher for PVDF than for PVDF/MWCNT films. This indicates MWCNT accelerates the degradation of PVDF at high temperature, above 500°C. One reason for this acceleration is that the HF monomer and a small amount of $C_4H_3F_3$ formed as a degradation product of PVDF [36] acted with MWCNT or its residue and caused a further degradation of the residual portion of the nanocomposites.

Table I.2 Thermogravimetric Results for Residual Weight Percent Remaining at Different Temperatures for PVDF/MWCNT Nanocomposites.

Sample	**Weight Remaining (%), ± 0.5 %**				
(wt %)	**400°C**	**450°C**	**500°C**	**600°C**	**1000°C**
0.0	99.3	65.8	38.0	33.0	27.7
0.1	99.7	81.3	34.1	29.9	26.4
0.5	99.9	84.5	34.0	30.0	26.1
1.0	99.6	87.7	30.5	27.0	22.9
2.0	99.4	89.5	32.2	28.1	22.5
5.0	99.4	94.6	30.0	26.4	20.8

3.3 Mechanical properties

For unoriented films, the storage modulus increases with an increase in MWCNT concentration, and the glass transition is unaffected by adding MWCNT into the polymer matrix. This was observed by Liu's group as well, even though they used a different sample preparation method [35]. **Figure I. 9** (a) shows the storage modulus, E', vs. temperature for all unoriented samples. Because MWCNTs have a higher Young's

modulus, by bonding to MWCNT, PVDF becomes stiffer (higher E'). This is further evidence that hydrogen bonds exist between MWCNT and PVDF [13, 37].

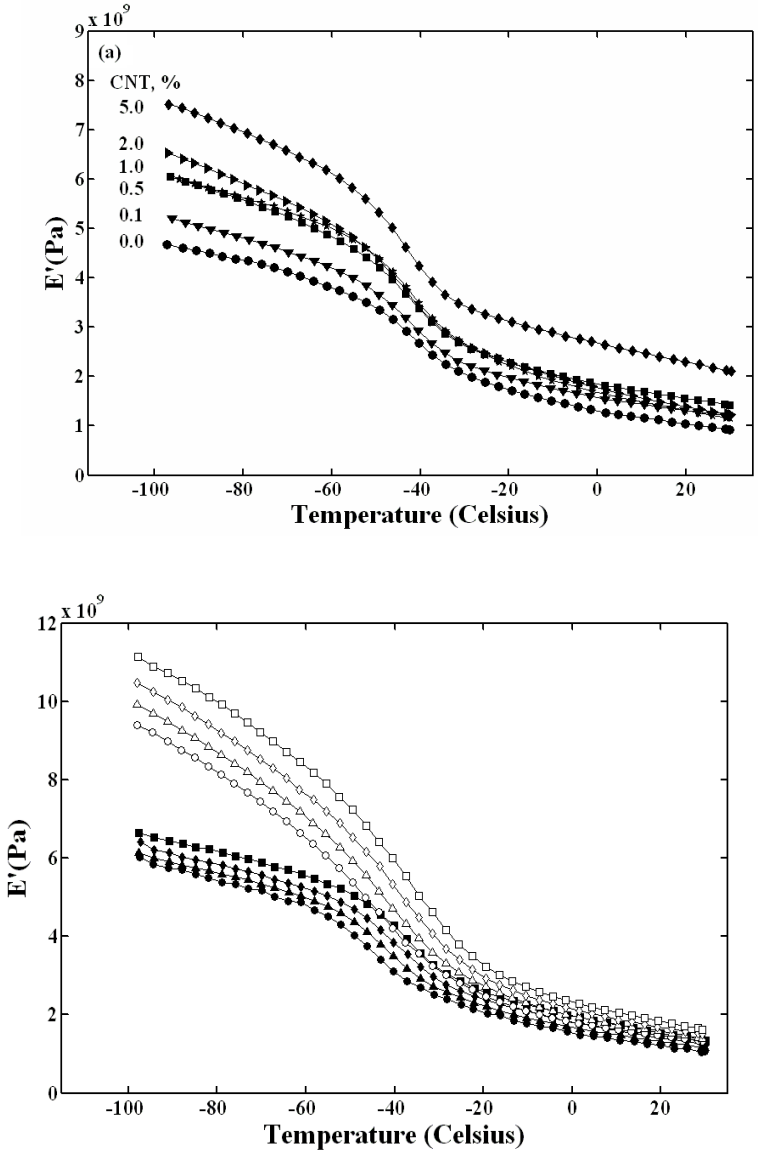

Figure I. 9 Storage modulus, E', vs. temperature for nanocomposites of PVDF with MWCNT. (a) Unoriented sample, (b) Unoriented samples (black) and oriented zone drawn samples (white) at different frequencies, 0.1 Hz (circle), 1.0 Hz (triangle), 10Hz (diamond) and 50 Hz (square), exemplified by 0.5 wt%.

For oriented films, E' measured along the drawing direction is larger, as compared to unoriented films. Figure I. 9 (b) shows a comparison of E's for unoriented and oriented samples at different frequencies, exemplified by 0.5 wt%. The mechanical response of PVDF nanocomposite to the oscillating strain along the drawing direction is smaller for oriented samples and causes a higher E'. This result shows that the zone drawing process rotates the gauche bond to trans bond whose energy is relatively lower, causing a permanent change of dipole in PVDF/MWCNT nanocomposites, and aligning the polymer chain in the drawing direction.

The dielectric relaxation that occurred in PVDF/MWCNT [38] has also been studied by dynamic mechanical analysis. The loss factor, tan δ, can be obtained by:

$$\tan \delta = E''/E' \qquad \text{(I.3)}$$

where E' is the storage modulus related to the elastic deformation, and E'' is the loss modulus related to the viscous deformation and energy absorption [39].

The peak position of tan δ is assigned to glass transition, the segmental motions of polymer chain in the amorphous regions, and usually labeled as the β-transition [40]. Glass transition is a quasi-second order phase transition involving no latent heat. Above the glass transition temperature, T_g, there is sufficient mobility inside the polymer matrix, so that large scale reorganization of polymer chains can occur in response to an applied mechanical force. Below T_g the chains are frozen in position, and only small scale vibrational motion is possible. **Figure I. 10** (a) compares the tan δ peak position for all compositions for unoriented samples, and Figure I. 10 (b) compares the tan δ peak for unoriented samples and oriented samples at different frequencies, exemplified by 0.5 wt%. A major relaxation was observed between -60 and -10°C. The peak position of

tanδ, referring to T_g, is independent of the concentration of MWCNT in both cases we studied, as shown in Figure I. 10 (a). A slight shift of T_g, about 3 °C, to a higher temperature from unoriented sample to oriented sample is observed, as shown in **Table I.3**. For oriented sample, the volume of amorphous region is larger, but it is more confined by aligned polymer chains ($\lambda \sim 5$) and MWCNT, thus a higher temperature is needed for the relaxation. We also observe that T_g increases with the frequency, which shows a phase delay in mechanical response of films at a higher frequency.

Table I.3 Tan δ peak position at different frequencies for PVDF/MWCNT nanocomposites.

Sample	**Unoriented (±1°C)**			**Oriented (±1°C)**			
(wt %)	**1.0 Hz**	**10 Hz**	**50 Hz**	**0.1 Hz**	**1.0 Hz**	**10 Hz**	**50 Hz**
0.0	-39.9	-36.1	-32.6	-40.5	-37.0	-33.6	-31.3
0.1	-40.5	-37.1	-34.5	-40.5	-37.1	-34.3	-31.1
0.5	-39.9	-37.1	-34.3	-40.7	-37.7	-34.3	-31.4
1.0	-40.5	-37.5	-34.1	-41.9	-37.5	-34.3	-31.5
2.0	-40.3	-37.1	-34.3	-40.3	-36.9	-31.2	-29.6
5.0	-40.3	-37.3	-34.3	-43.5	-37.5	-34.5	-31.3

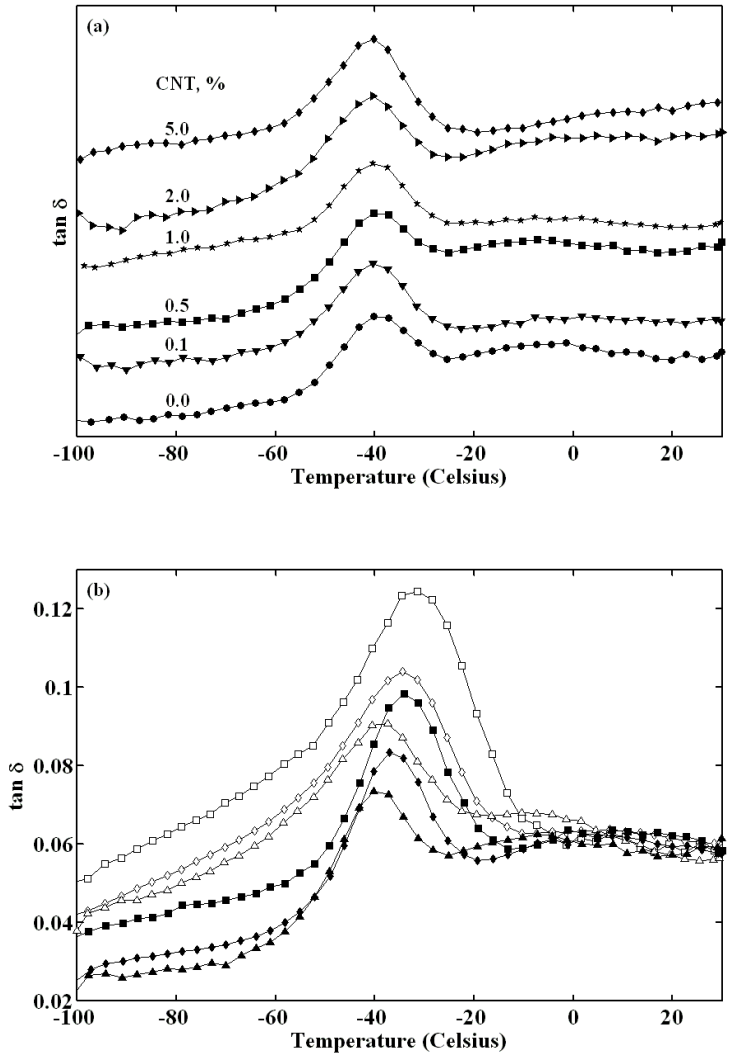

Figure I. 10. Loss factor, tan δ, vs. temperature for nanocomposites of PVDF with MWCNT. (a) Unoriented sample, (b) Unoriented samples (black) and oriented zone drawn samples (white) at different frequencies, 1.0 Hz (triangle), 10Hz (diamond) and 50 Hz (square), exemplified by 0.5 wt%.

The relaxation time for the β-transition follows Vogel-Fulcher-Tamman-Hesse (VFTH) equation [41, 42].

$$\tau = \tau_0 \exp [B / k(T- T_0)] \qquad (I.4)$$

where τ is the relaxation time for β-transition, $k = 1.38 \times 10^{-23}$ JK^{-1} is Boltzmann's constant, T_0 is the Vogel temperature (T_0 = 170 K for PVDF [41]), which is usually 30-70 K below T_g, and B is a constant activation energy. Molecules must acquire an extra amount of energy in order to pass the energy barrier from state a to state b.

The activation energy for unoriented PVDF and oriented PVDF has been estimated using both DSC and DMA data. DSC heating rate was transformed to an equivalent frequency [43, 44]. By fitting logarithm frequency from DSC and DMA with reciprocal glass transition temperature (determined by tan δ peak position in DMA), we obtained best fit lines in an Arrhenius plot (not shown in the interest of brevity). The slope of the best fit lines is the activation energy. **Figure I. 11** depicts the estimated activation energy from Arrhenius plots versus MWCNT concentration. The activation energy is in the range of 0.08-0.17 eV.

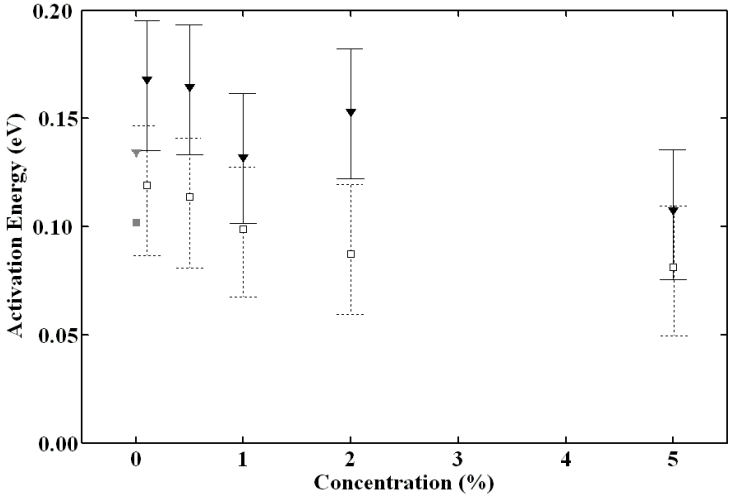

Figure I. 11 Activation energy vs. concentration for unoriented (solid triangle) and oriented (empty square) nanocomposites of PVDF with MWCNT. Pure PVDF was marked in grey for reference.

Mechanical properties were also evaluated by tensile testing at room temperature. The modulus of elasticity (Young's modulus) was calculated using least squares fitting within the low strain (linear) portion of stress-strain curve, which follows Hooke's law:

$$\sigma_e = E\,\varepsilon_e \tag{I.5}$$

where σ_e is the stress applied, ε_e is the strain, and E is Young's modulus of the sample. The proportional limit was determined by offsetting a line parallel to the tangency line by 0.02% strain. The intersection of the offset line and the stress-strain curve is used to estimate the proportional limit [45]. The ultimate tensile strength (UTS) was determined by the highest stress value over the entire stress-strain curve from elongation until failure. In **Table I.4**, as expected, the nanocomposites with the greater weight percent of MWCNT have greater Young's moduli and greater proportional limits. The nanocomposite with highest weight percent of MWCNT, 5wt%, has the highest average Young's modulus and UTS of 1.82±0.05GPa and 44.7±0.5MPa, respectively, at a crosshead speed of 2mm/min. The average Young's modulus and UTS of pure PVDF are 1.46±0.05GPa and 42.0±0.5MPa, respectively. The strain at UTS decreases as weight percentage of MWCNT increases. Typical stress-strain curves at 2mm/min for all nanocomposites in the low strain region are shown in **Figure I. 12**. The tests with crosshead speed of 10mm/min (not shown for the sake of brevity) presented a similar graph. This result shows that the high weight percent nanocomposite is stiffer than pure PVDF. By adding nanofiller with large Young's modulus, the mechanical properties of the polymer nanocomposite were also improved.

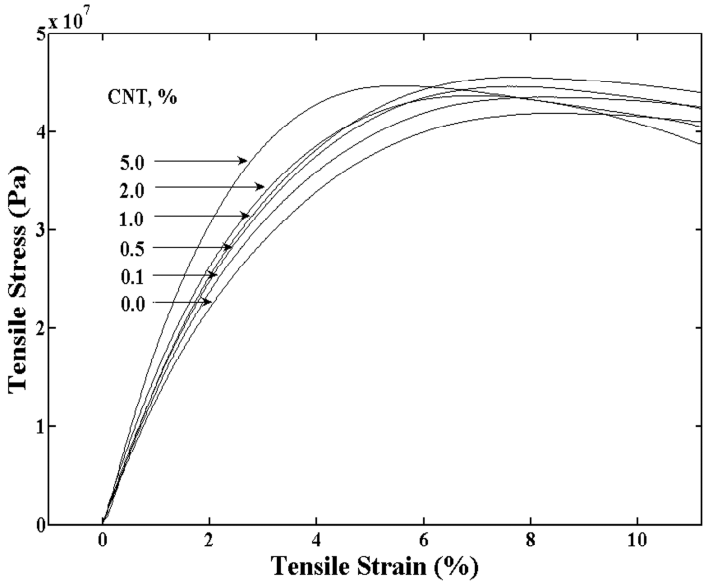

Figure I.12 Stress–strain curves at room temperature in the low strain region at a cross head speed of 2 mm/min for nanocomposites of PVDF with MWCNT.

Table I.4 Mechanical Properties from Tensile Testing at Room Temperature for PVDF/MWCNT Nanocomposites, at Various Crosshead Speeds[a]

Sample (wt %)	Young's Modulus, GPa, (±0.05)		Proportional limit, MPa, (±0.5)		UTS (Ultimate Tensile Stress), MPa (±0.5)		Strain at UTS, % (±1.0)	
	2	10	2	10	2	10	2	10
0.0	1.46	1.25	7.0	9.1	4.2	4.3	8.5	9.6
0.1	1.46	1.47	8.5	11.4	4.4	4.7	8.1	8.0
0.5	1.52	1.48	9.7	13.0	4.5	4.6	7.3	7.6
1.0	1.61	1.58	10.2	12.1	4.5	4.7	7.3	7.6
2.0	1.70	1.52	11.7	12.2	4.4	4.7	6.7	6.7
5.0	1.82	1.76	11.9	11.0	4.5	4.6	5.5	6.4

[a] Crosshead speeds of 2 or 10 mm/min

4. Conclusions

Nanocomposites of poly (vinylidene fluoride) (PVDF) with mutiwalled carbon nanotubes (MWCNTs) have been investigated over a wide composition range, from 0.1% to 5.0% MWCNT by weight. The effect of zone drawing on these nanocomposites is also studied by comparing the oriented samples with unoriented samples. The conclusions are summarized as follows:

1. MWCNTs have negligible effect on forming beta crystal in PVDF (inducing only a tiny portion of beta phase crystal (1-2 %) in the PVDF/MWCNT films). Zone drawing causes a significant alpha to beta transition in PVDF/MWCNT strips. In this process the beta phase grew at the expense of alpha phase, but the total degree of crystallinity decreased.
2. MWCNT acts as nucleation agent during crystallization and slightly increases the degree of crystallinity of both unoriented and oriented PVDF/MWCNT films. Crystallization temperature, $T_{c,}$ for PVDF/MWCNT films increases with MWCNT concentration.
3. The lower temperature thermal stability for PVDF/MWCNT is also improved (nanocomposites show a higher degradation temperature below 500 °C) when MWCNT concentration increases.
4. The glass transition temperature, $T_{g,}$ measured by the peak position of tan δ does not change with MWCNT concentration, but a higher T_g can be obtain by zone drawing.
5. Dynamic storage modulus, E', was improved when MWCNT concentration increases in unoriented PVDF/MWCNT film. Zone drawing also generally increases E'.

6. Young's modulus and the proportional limit from stress-strain curves increase, while strain at the point of ultimate tensile stress decreases, as MWCNT concentration increases.

Acknowledgments

The authors thank the National Science Foundation, Polymers Program of the Division of Materials Research, for support of this research through grant DMR-0704056. Undergraduate summer interns K. Edenzon, L. Fernandez, S. Razmpour, and J. Woodburn performed the research at Tufts University. The author thanks Mr. J. Kluge for the help with mechanical test experiments and analyses, Dr. H. Chen for the help with SEM work, and Prof. Georgi Georgiev (Assumption College) for purification of the MWCNTs.

References

1. Lang SB and Muensit S. *Applied Physics a-Materials Science & Processing* 2006; 85(2): 125-134.
2. Lovinger AJ. *Science* 1983; 220(4602): 1115-1121.
3. Hasegawa R, Tadokoro H, and Kobayash.M. *Polymer Journal* 1972; 3(5): 591-600.
4. Kawai H. Japanese *Journal of Applied Physics* 1969;8(7):975-980.
5. Bergman JG, McFee JH, and Crane GR. *Applied Physics Letters* 1971; 18(5): 203-210.
6. Branciforti MC, Sencadas V, Lanceros-Mendez S, and Gregorio R. *Journal of Polymer Science Part B-Polymer Physics* 2007; 45(19): 2793-2801.

7. Gregorio R and Cestari M. *Journal of Polymer Science Part B-Polymer Physics* 1994; 32(5): 859-870.

8. Priya L and Jog JP. *Journal of Polymer Science Part B-Polymer Physics* 2003; 41(1): 31-38.

9. Buckley J, Cebe P, Cherdack D, Crawford J, Ince BS, Jenkins M, Pan JJ, Reveley M, Washington N, and Wolchover N. *Polymer* 2006; 47(7): 2411-2422.

10. Iijima S. *Nature* 1991; 354(6348): 56-58.

11. Safadi B, Andrews R, and Grulke EA. *Journal of Applied Polymer Science* 2002; 84(14): 2660-2669.

12. Levi N, Czerw R, Xing SY, Iyer P, and Carroll DL. *Nano Letters* 2004; 4(7): 1267-1271.

13. Jin ZX, Pramoda KP, Goh SH, and Xu GQ. *Materials Research Bulletin* 2002; 37(2): 271-278.

14. Rangari VK, Yousuf M, Jeelani S, Pulikkathara MX, and Khabashesku VN. *Nanotechnology* 2008; 19(24): 9-19.

15. Bikiaris D, Vassiliou A, Chrissafis K, Paraskevopoulos KM, Jannakoudakis A, and Docoslis A. *Polymer Degradation and Stability* 2008; 93(5): 952-967.

16. Tu ZC and Ou-Yang Z. P*hysical Review B* 2002; 65(23): 4-10.

17. Treacy MMJ, Ebbesen TW, and Gibson JM. *Nature* 1996; 381(6584): 678-680.

18. Tang WZ, Santare MH, and Advani SG. *Carbon* 2003; 41(14): 2779-2785.

19. Kim P, Shi L, Majumdar A, and McEuen PL. *Physical Review Letters* 2001; 87(21): 4-14.

20. Wang M, Shi JH, Pramoda KP, and Goh SH. *Nanotechnology* 2007; 18(23): 7-15.

21. Huang WW, Edenzon K, Fernandez L, Razmpour S, Woodburn J, and Cebe P. *Journal of Applied Polymer Science* 2010; 115(6): 3238-3248.
22. Chen H, Liu Z, and Cebe P. *Polymer* 2009; 50(3): 872-880.
23. Aihara Y and Cebe P. *Polymer Engineering and Science* 1994; 34(16): 1275-1286.
24. Berns DM, Oyebode E, Dair B, Cebe P, and Capel M. *Journal of Applied Polymer Science* 2001; 82(14): 3492-3504.
25. Bachmann MA and Lando JB. *Macromolecules* 1981; 14(1):40-46.
26. Matsushige K, Nagata K, Imada S, and Takemura T. *Polymer* 1980; 21(12): 1391-1397.
27. Gutierrez MCG, Alfonso GC, Riekel C, and Azzurri F. *Macromolecules* 2004; 37(2): 478-485.
28. Freimuth H, Sinn C, and Dettenmaier M. *Polymer* 1996; 37(5): 831-836.
29. Yang ZL, Chen HZ, Cao L, Li HY, and Wang M. *Materials Science and Engineering B-Solid State Materials for Advanced Technology* 2004; 106(1): 73-78.
30. Wang YH, Li YN, Lu J, Zang JB, and Huang H. *Nanotechnology* 2006; 17(15): 3817-3821.
31. Kobayashi M, Tashiro K, and Tadokoro H. *Macromolecules* 1975; 8(2): 158-171.
32. Crabtree RH, Eisenstein O, Sini G, and Peris E. *Meeting of the Groupe-d-Etude-en-Chimie-Organometallique/Concertation-en-Chimie-de-Coor dination (GECOM-CONCOORD 97)*. France, 1997; 7-11.
33. Minh NQ. *Journal of the American Ceramic Society* 1993; 76(3): 563-588.
34. Hou PX, Bai S, Yang QH, Liu C, and Cheng HM. *Carbon* 2002; 40(1): 81-85.

35. Chen D, Wang M, Zhang WD, and Liu TX. *Journal of Applied Polymer Science* 2009; 113(1): 644-650.

36. Zulfiqar S, Zulfiqar M, Rizvi M, Munir A, and McNeill IC. *Polymer Degradation and Stability* 1994; 43(3): 423-430.

37. Tran MQ, Shaffer MSP, and Bismarck A. *Macromolecular Materials and Engineering* 2008; 293(3): 188-193.

38. Singh R, Kumar J, Singh RK, Kaur A, Sinha RDP, and Gupta NP. *Polymer* 2006; 47(16): 5919-5928.

39. Sencadas V, Lanceros-Mendez S, and Mano JF. *Thermochimica Acta* 2004; 424(1-2): 201-207.

40. Liu ZH, Marechal P, and Jerome R. *Polymer* 1997; 38(19): 4925-4929.

41. Ozkazanc E, Guney HY, Oskay T, and Tarcan E. *Journal of Applied Polymer Science* 2008; 109(6): 3878-3886.

42. Mijovic J, Ristic S, and Kenny J. *Macromolecules* 2007; 40(14): 5212-5221.

43. Huo PPT and Cebe P. *Symp on Advances in Polymer Matrix-Based Composites, at the Meeting of the American Chemical Soc. San Francisco, Ca*: Elsevier Sci Ltd, 1992; 696-704.

44. Hensel A, Dobbertin J, Schawe JEK, Boller A, and Schick C. *Journal of Thermal Analysis* 1996; 46(3-4): 935-954.

Appendix J. PVDF-based Polymer Blend Films for Fuel Cell Membranes

1. Introduction:

Polymer Electrolyte membrane (PEM) fuel cells (FC) have attracted much attention as the power sources of electric vehicles. The most commonly used membranes in PEM fuel cell is Nafion by the DuPont Company [1]. Most PEMs function below 80 - 90 °C, which is the dehydration temperature of Nafion. In this work, we fabricated conduction membranes of binary blend films of poly(vinylidene fluoride) (PVDF) and poly(1-ethyl-3-vinylimidazolium) doped with trifluoromethylsulfonylimide salt ($PVIm^+TFSI^-$). The potential utility of such materials is in capacitive electronic devices, especially in proton exchange membrane fuel cells.

Poly(vinylidene fluoride) (PVDF) is a technologically important semicrystalline polymer widely used in modern engineering applications, such as in piezoelectric sensors, energy transducers, electrical wires, and filtration membranes, because of its light weight, high chemical resistance, good thermal stability, and excellent mechanical properties. PVDF crystallizes into five crystallographic forms [2]. The two major forms of interest to our present research are the polar beta phase (with chain conformation TTTT) and the non-polar alpha phase (TGTG'). Beta phase PVDF presents a porous structure formed by spherulites with a diameters between 3 and 6 μm, while alpha phase PVDF forms banded spherulites with diameters between 20 and 40 μm [3]. In the binary blend PVDF/$PVIm^+TFSI^-$ films, the amorphous $PVIm^+TFSI^-$ is thought to occupy the

boundary regions of the PVDF spherulites, and form a tortuous, but continuous, electrical conducting pathway. When working in capacitive electronic devices, such as in PEMFC, the alpha phase is relatively stable. The alpha PVDF crystal will maintain after cooling from the melt, but the beta PVDF crystal will melt if the temperature goes above about 160 °C and alpha PVDF will form after cooling. Thus, the alpha phase is the preferred crystallographic phase of PVDF in polymer blend films for PEMFCs. In this study, we cast PVDF/PVIm$^+$TFSI$^-$ films from dimethly formamide (DMF) solution. The polar beta phase of PVDF crystals dominates in as-cast films. After heat treatment at 200 °C in an inert atmosphere, only the non-polar alpha phase is observed after cooling from the melt. PVDF imparts mechanical strength and chemical stability to the blends, and because of its high crystal melting point (T_m > 160 °C), serves to improve the high temperature stability of resulting films. This work has published in MRS Proceedings [4].

2. Experimental Section

Sample preparation PVDF used in our present study was a KYNAR® 301F poly(vinylidene fluoride) resin obtained in fine powder form. Poly(1-ethyl-3-vinylimidazolium trifluoromethylsulfonylimide) (PVIm$^+$TFSI$^-$) was derived from ionic liquid imidazolium monomers [5]. The chemical structures are shown in **Figure J. 1**.

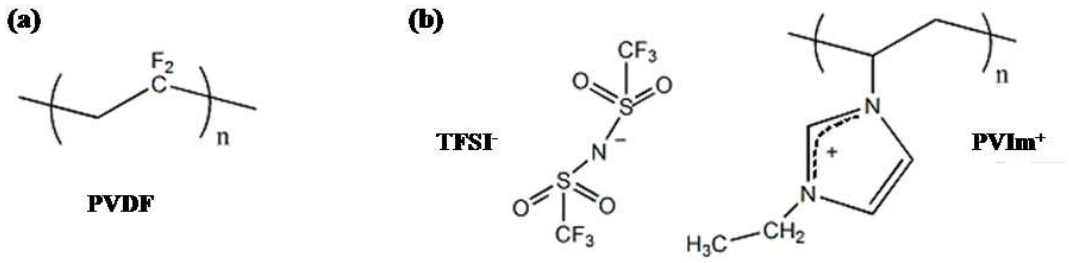

Figure J. 1 The chemical structures of (a) PVDF and (b) PVIm$^+$TFSI$^-$.

PVDF and $PVIm^+TFSI^-$ were separately dissolved in dimethly formamide (DMF) solution at room temperature and stirred overnight to make a 15 wt.% PVDF stock solution and a 5 wt.% $PVIm^+TFSI^-$ stock solution. Then, the two stock solutions were mixed to achieve polymer blends with 4:1 or 3:1 weight ratio of PVDF: $PVIm^+TFSI^-$. To obtain a thin film with thickness of 30 ~ 40 μm, the mixed solutions were doctor bladed at 50 °C on a pre-cleaned glass substrate and dried at 100 °C.

Fourier transform infrared spectroscopy (FTIR) studies were performed using a Jasco FT/IR-6200 with a TGS detector. The absorbance spectra were obtained by averaging 32 scans with a resolution of 4.0 cm^{-1}. The background spectra were collected under the same conditions and subtracted from the scan for each sample.

Wide angle X-ray diffraction (WAXD) was performed with a Phillips PW1830 X-ray generator, operated at 40 kV and 45 mA. Free standing films were examined in reflection mode, using a step scan interval of 0.01° and a scan time of 2.4 s/step.

Differential scanning calorimetry (DSC) was performed on a TA Instruments Q100 temperature modulated DSC. Samples with mass in the range of 2 to 3 mg were encapsulated into aluminum pans and heated from 100 to 200 °C, then cooled from 200 to 100 °C and then reheated to 200 °C at a rate of ±10 °C/min. A nitrogen purge gas was used at a flow rate of 50 mL/min.

Thermogravimetric analysis (TGA) was performed on a TA Instruments Q500 thermogravimetric analyzer at a heating rate of 20 °C/min from room temperature to 800 °C in a nitrogen gas flow of 50 mL/min.

Dynamic mechanical analysis (DMA) was performed on a TA Instruments RSAIII dynamic mechanical analyzer using frequency/temperature sweep test at a strain

of 0.1%, with four different frequencies, 0.1, 1.0, 10, and 50 Hz. The temperature ranged from −100 °C to 30 °C with an increase of 3 °C per step and a soak time of 45 s per step.

3. Discussion

Phase identification

Figure J. 2 shows the phase structure of PVDF identified using FTIR. According to Gregorio [3], solution cast films result in beta phase PVDF spherulites with diameters between 3 and 6 μm, and forming an incompletely filled, or porous, structure with large gaps between adjacent spherulites. On the other hand, when films are heat treated from the melt, the alpha phase PVDF forms banded spherulites with diameters between 20 and 40 μm which are more completely space filling [3]. Beta phase crystals, which are formed after solution evaporation at relatively low drying temperatures, are metastable, and will tend to reorganize during any subsequent excursion to higher temperature. The alpha phase spherulites, grown by cooling from the melt, will be stable to higher temperatures during use. In our binary blend PVDF/PVIm^{+}TFSI^{-} films, the PVIm+TFSI- component will be rejected to the boundaries of the alpha phase PVDF spherulites and will facilitate formation of conduction channels at the spherulite boundaries. Thus, on the basis of thermal stability, the melt crystallized alpha phase is preferred to the solution cast beta phase in capacitive electronic devices applications.

As can be seen form Figure J. 2, the beta absorption peaks at 1273 and 1175 cm^{-1} [2, 6-8] were observed in doctor bladed as-cast films in all compositions. After heat treatment at 200 °C in the inert atmosphere glove box filled with argon gas, the beta phase melted and alpha phase formed after cooling from the melt. The alpha absorption

bands at 976 and 764 cm^{-1} [2, 6-8] were observed in heat treated films for all compositions. WAXD confirmed the phase structure determined from FTIR. This result suggests that $PVIm^{+}TFSI^{-}$ will not change the crystallographic phase of PVDF. The beta PVDF can be obtained by crystallization from DMF solution at 100 °C, and the alpha PVDF can be obtained by melting and subsequent cooling at room temperature [3]. The $PVIm^{+}TFSI^{-}$ blend component was completely amorphous which was confirmed by WAXD.

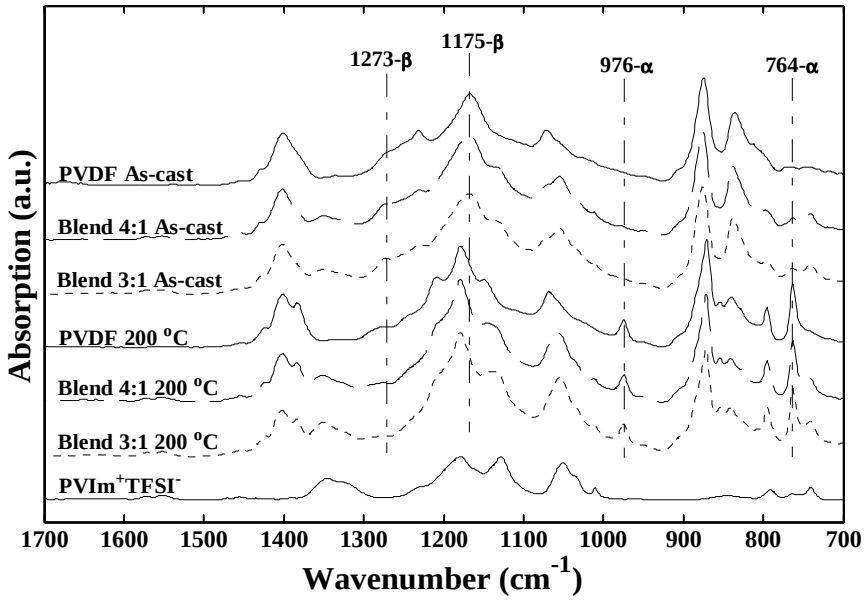

Figure J. 2 Normalized infrared absorption versus wavenumber of PVDF/$PVIm^{+}TFSI^{-}$ films.

Thermal properties

Figure J. 3 shows the DSC scans of PVDF homopolymer and blend films PVDF/$PVIm^{+}TFSI^{-}$ with ratio 4:1 and 3:1 PVDF to $PVIm^{+}TFSI^{-}$. Upper three curves are as cast, while the lower three curves are films heat treated at 200 °C and cooled quickly.

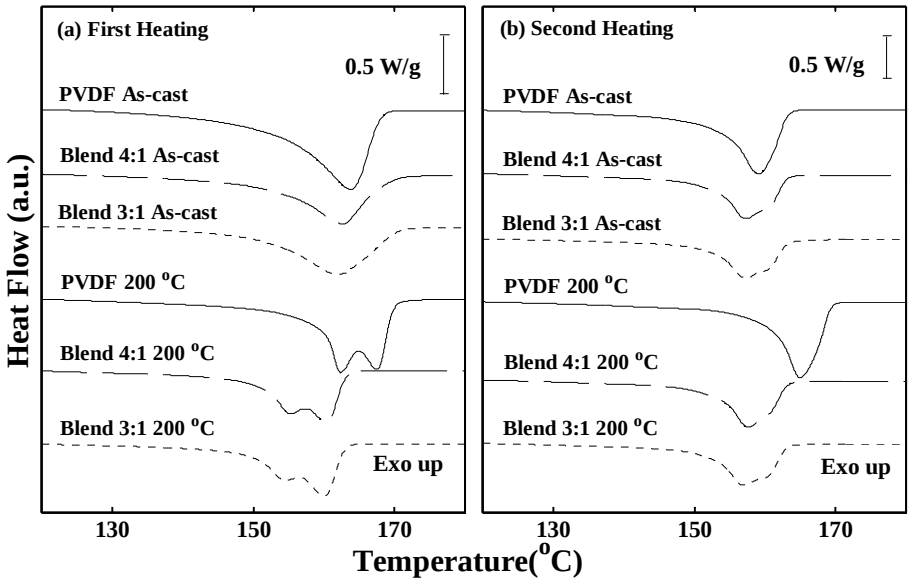

Figure J. 3 DSC Heat flow versus temperature scans for PVDF/PVIm$^+$TFSI$^-$ films during (a) the first heating ramp and (b) the second heating ramp with a heating/cooling rate of 10 °C/min.

In the first heating ramp, shown in Figure J. 3a, the doctor bladed as-cast films have only a single melting peak at about 164 °C, which can be attributed to the melting of beta crystals of PVDF. The heat treated films have doublet melting peaks in the temperature range of 150 to 170 °C, which can be attributed to the melting of alpha PVDF. In the second heating ramp shown in Figure J. 3b, the melting temperature, T_m, of homopolymer PVDF is about 160 °C, and the T_m of PVDF/PVIm$^+$TFSI$^-$ blend films are about 158 °C with a small shoulder at about 160 °C. The first heat of beta phase shows a long period of endothermic heat flow, due to an unstable baseline, which confirms that the beta is reorganizing, while the second heat showing that alpha is more stable, giving a better, flatter baseline. Result indicates that as the PVDF content decreases, melting endotherm peak positions systematically shift to a lower temperature,

and PVDF serves to improve the high temperature stability of resulting blend films because of its high crystal melting point (T_m > 160 °C).

Figure J. 4 shows the TGA scans of percent weight remaining vs. temperature for PVDF homopolymer and blend films of PVDF/PVIm$^+$TFSI$^-$. In the blend films, weight loss begins at 315 °C due to the degradation of PVIm$^+$TFSI$^-$, and major weight loss occurred in the region between 400 and 500 °C for all samples. Results indicate the degradation temperature of the films is well above the working temperature for PEMFC.

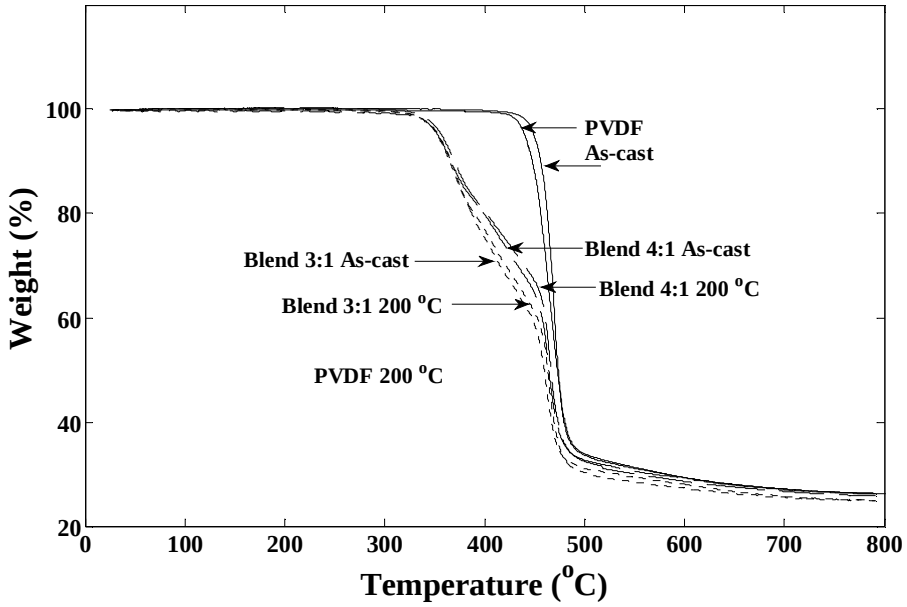

Figure J. 4 Thermogravimetric curve of weight remaining versus temperature for PVDF/PVIm$^+$TFSI$^-$ films with a heating rate of 20 °C/min.

Mechanical properties

Figure J. 5 shows the storage modulus, E', and the loss factor, tan δ, versus temperature for PVDF/PVIm^{+}TFSI^{-} films. The storage modulus increases with an increase in PVDF content. This indicates that the blend films becomes stiffer (higher *E*') when PVDF content increases relative to the PVIm^{+}TFSI^{-} component. The glass transition, determined by the peak position of tan δ, is slightly increased, about 2 °C, and the amplitude of the relaxation peak increases as well, as the PVDF fraction increased. By increasing the PVDF content, the blend film will have a higher damping capacity for viscoelastic vibration. Results indicate that an increase of PVDF serves to improve the mechanical properties of resulting blend films.

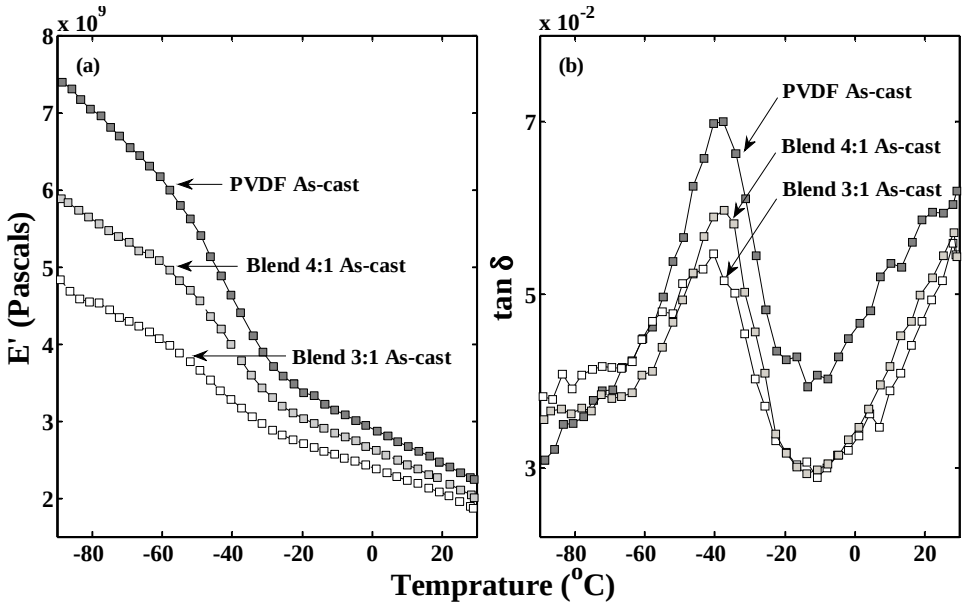

Figure J. 5 (a) Storage modulus, E', and (b) loss factor, tan δ, versus temperature for PVDF/PVIm^{+}TFSI^{-} films (exemplified by as cast films at oscillation frequency of 10 Hz).

4. Conclusions

We report the preparation and characterization of binary blend films of PVDF/PVIm$^+$TFSI$^-$. Thin PVDF/ PVIm$^+$TFSI$^-$ films were fabricated from DMF solutions by doctor blading. The polar beta phase of PVDF crystals dominates in as-cast films, while the non-polar alpha phase is observed after cooling from the melt. PVDF imparts mechanical strength and chemical stability to the composite films, and because of its high crystal melting point (T_m > 160 °C), serves to improve the high temperature stability of resulting films.

5. Acknowledgement

Support was provided from the National Science Foundation grant DMR 0906455.

6. References

1. K.A. Mauritz, R.B. Moore, *Chemical Reviews*, 2004; 104: 4535-4585.
2. J. Buckley, P. Cebe, D. Cherdack, J. Crawford, B.S. Ince, M. Jenkins, J.J. Pan, M. Reveley, N. Washington, N. Wolchover, *Polymer*, 2006;47: 2411-2422.
3. R. Gregorio, *Journal of Applied Polymer Science*, 2006; 100: 3272-3279.
4. W.W. Huang, M. Zhao, F. Yang, P. Haghighi, L. Farovitch, L.J. Macisco, T. Swob, T. Smith, P. Cebe, "PVDF-based Polymer Blend Films for Fuel Cell Membranes". *MRS Proceedings*, 2011, 1384, b05-02.
5. T.W. Smith, D.J. Luca, S. Kaplan, M.A. Abkowitz, *Abstracts of Papers of the American Chemical Society*, 1998; 215: U353-U353.

6. W.W. Huang, K. Edenzon, L. Fernandez, S. Razmpour, J. Woodburn, P. Cebe, *Journal of Applied Polymer Science*, 2010; 115: 3238-3248.
7. B.S. Ince-Gunduz, R. Alpern, D. Amare, J. Crawford, B. Dolan, S. Jones, R. Kobylarz, M. Reveley, P. Cebe, *Polymer*, 2010; 51: 1485-1493.
8. B.S. Ince-Gunduz, K. Burke, M. Koplitz, M. Meleski, A. Sagiv, P. Cebe, *Journal of Macromolecular Science Part a-Pure and Applied Chemistry*, 2010; 47: 1208-1219.